Simulating short lived carbonaceous compounds with an atmospheric chemistry general circulation model

Dissertation

zur Erlangung des Grades ,
“Doktor der Naturwissenschaften”

am Fachbereich Physik der

Johannes Gutenberg-Universitat
in Mainz

Andrea Pozzer

geb. in Verona

Mainz, 2007

Abstract

A newly developed atmospheric chemistry general circulation model (*ECHAM5/MESSy1*) has been used to study the chemistry and transport of ozone precursors, with particular focus on non-methane hydrocarbons and oxidation products. For this purpose the model has been extensively evaluated using observations from different data sources. This analysis indicates that the model realistically predicts the distribution of ozone, both the abundance and the seasonal cycle. At the tropopause the model accurately simulates stratosphere-troposphere exchange without prescribed fluxes or concentrations. The model simulates the ozone related precursors with different degrees of correlation with observations. While alkanes are well reproduced, some discrepancies are present for alkenes. For oxygenated compounds, the model accurately reproduces formaldehyde (HCHO), while the correlation between observations and model results for methanol (CH_3OH) and acetone (CH_3COCH_3) are much lower. To increase the ability of the model *ECHAM5/MESSy1* to simulate oxygenated compounds, some sensitivity studies have been conducted. These species are influenced by oceanic emission/deposition, and the gas exchange of these gases is associated with relative large uncertainties. To improve the simulation results of *ECHAM5/MESSy1* , the new submodel **AIRSEA** has been developed within the MESSy framework. This submodel takes into account ocean-atmosphere gas exchange including oxygenated organic compounds. **AIRSEA**, which requires knowledge of the liquid phase concentration of the gases in the ocean near the surface, has been extensively tested. The application of the new submodel improves somewhat the representation of acetone and methanol, although the use of a prescribed liquid phase concentration largely limits the success of this approach due to the lack of observations. This work revealed new insights about organic compounds. It highlights the importance of the coupling between the ocean and the atmosphere for the budgets of many gases.

Zusammenfassung

Ein neu entwickeltes globales Atmosphärenchemie- und Zirkulationsmodell (*ECHAM5/MESSy1*) wurde verwendet um die Chemie und den Transport von Ozonvorläufersubstanzen zu untersuchen, mit dem Schwerpunkt auf Nichtmethankohlenwasserstoffen. Zu diesem Zweck wurde das Modell durch den Vergleich der Ergebnisse mit Messungen verschiedenen Ursprungs umfangreich evaluiert. Die Analyse zeigt, daß das Modell die Verteilung von Ozon realistisch vorhersagt, und zwar sowohl die Menge als auch den Jahresgang. An der Tropopause gibt das Modell den Austausch zwischen Stratosphäre und Troposphäre ohne vorgeschriebene Flüsse oder Konzentrationen richtig wieder. Das Modell simuliert die Ozonvorläufersubstanzen mit verschiedener Qualität im Vergleich zu den Messungen. Obwohl die Alkane vom Modell gut wiedergeben werden, ergibt sich einige Abweichungen für die Alkene. Von den oxidierten Substanzen wird Formaldehyd (HCHO) richtig wiedergegeben, während die Korrelationen zwischen Beobachtungen und Modellergebnissen für Methanol (CH_3OH) und Aceton (CH_3COCH_3) weitaus schlechter ausfallen. Um die Qualität des Modells im Bezug auf oxidierte Substanzen zu verbessern, wurden einige Sensitivitätsstudien durchgeführt. Diese Substanzen werden durch Emissionen/Deposition von/in den Ozean beeinflußt, und die Kenntnis über den Gasaustausch mit dem Ozean ist mit großen Unsicherheiten behaftet. Um die Ergebnisse des Modells *ECHAM5/MESSy1* zu verbessern wurde das neue Submodell **AIRSEA** entwickelt und in die MESSy-Struktur integriert. Dieses Submodell berücksichtigt den Gasaustausch zwischen Ozean und Atmosphäre einschließlich der oxidierten Substanzen. **AIRSEA**, welches Informationen über die Flüssigphasenkonzentration des Gases im Oberflächenwasser des Ozeans benötigt wurde ausgiebig getestet. Die Anwendung des neuen Submodells verbessert geringfügig die Modellergebnisse für Aceton und Methanol, obwohl die Verwendung einer vorgeschriebenen Flüssigphasenkonzentration stark den Erfolg der Methode einschränkt, da Meßergebnisse nicht in ausreichendem Maße zu Verfügung stehen. Diese Arbeit vermittelt neue Einsichten über organische Substanzen. Sie stellt die Wichtigkeit der Kopplung zwischen Ozean und Atmosphäre für die Budgets vieler Gase heraus.

Contents

Chapter 1

Introduction

Ozone has generally been recognised for its importance in atmospheric chemistry. It is essential for protecting the Earth from high energetic solar rays (UV-c with a wavelength of $\approx$ 200-280 nm, thanks to the the "ozone layer", and preventing our planet to become inhabitable (Diffey, 1991; van der Leun and de Gruijl, 2002). On the other hand, ozone itself is a toxic gas which can have detrimental effects on humans and crops (Lippmann, 1989; McKee, 1993; Longstreth et al., 1995). Hence monitoring the level of ozone in the troposphere is essential for preventing effects on human health.

Before the 1970s it was believed that tropospheric ozone was transported from the stratosphere and destroyed at the Earth's surface (Regener, 1957; Junge, 1962). During the 1970s, it has been discovered that ozone is produced and destroyed in the troposphere through a catalytic cycle with nitrogen oxides (NO and $\mathrm{NO_2}$; Crutzen (1972, 1973, 1974); Chameides and Walker (1973)). Additionally, it has been discovered that ozone is the main precursor for the hydroxyl radical OH (Levy, 1971). This radical is often called "the detergent of the atmosphere" because it is the dominant sink for methane, carbon monoxide and many organic substances. Thus, ozone in the troposphere is indirectly responsible for the cleansing capacity of the atmosphere through the formation of hydroxyl radicals. Model studies and observations have shown that although ozone is decreasing in the stratosphere, in the troposphere it has increased ($\approx 100\%$) over large parts of the Northern Hemisphere since preindustrial times (Crutzen and Zimmermann, 1991; Lelieveld and Dentener, 2000; Volz and Kley, 1988).

Following recent studies (Jöckel et al., 2006; Kentarchos and Roelofs, 2003), only 20-35% of the tropospheric ozone originates from the stratosphere, while the rest is created directly in the troposphere. Although 90% of the ozone formed in the troposphere is photochemically destroyed, the remaining 10% contribute to 65-80% of the total tropospheric ozone budget. It is hence extremely important to understand the formation and destruction process of ozone; under certain conditions, in fact, the close balance between formation and destruction is perturbed, creating the well known phenomenon of "ozone smog", recognized since the 1950s (Haagen-Smit, 1952; Leighton, 1961).

Organic compounds, together with nitrogen oxides, play a key role in the production (and destruction) of ozone in the troposphere; being emitted in huge quantities by forest and in populated locations, it is essential to develop modeling tool to understand the interactions between ozone, nitrogen oxides, hydroxyl radicals and the organic compounds.

Due to the complexity of the system and the needs to solve complex sets of chemical equations, the use of numerical atmospheric chemistry models is necessary. Only numerical models, in fact, are able to simulate this highly non-linear system. Additionally, they can also realistically represent the meteorology that influences the chemistry of the atmosphere.

Thanks to these powerful tools, a deep understanding of the connections between organics and other chemical compounds in the atmosphere is possible. The models often explain behaviour that "a priori" is not obvious. In fact, many phenomena in atmospheric chemistry are not intuitive due to their non-linear nature.

Several aspects have to be kept in mind when interpreting the model calculations. Due to the enormous complexity of the system, simplifications are commonly applied for computational reasons. Moreover many coefficients used in the models are derived from laboratory measurements and include uncertainties. These aspects contribute to uncertainties in the model results, and therefore appropriate caution has to be taken in the interpretation of the results. In general, numerical studies give indications and not proofs. At present, no uncertainties (in the classical mathematical sense) are quantifiable from a model simulation and it is responsibility of the scientist to analyse the results with particular attention.

In summary, models in conjunction with observations are essential to test our knowledge in atmospheric chemistry. Models and observations are essentially two faces of the same coin, and both have to be used to achieve real scientific progress.

This study mainly employs a three-dimensional global scale atmospheric chemistry general circulation model to study the photochemistry of the troposphere, especially considering the non-methane hydrocarbon (NMHC) chemistry . The main objective of this thesis is to improve the simulation of these trace gases in the model.

In this Chapter a brief overview on tropospheric chemistry is given, needed to underpin the following work. In the first part of Chapter 2, the model *ECHAM5/MESSy1* is presented; the basics features of this new model are given, together with a detailed description of the set-up used to integrated a reference simulation. In the second part of Chapter 2, the reference simulation is evaluated with observations, focusing especially on organic compounds in the troposphere. This analysis shows the weak and the strong points of the model; some hypotheses to explain the discrepancies between model results and the observations are also given.

The **AIRSEA** submodel is presented in the first part of Chapter 3; this submodel has been developed to improve the representation of ocean-atmosphere gas exchange, with particular focus on oxygenated volatile organic compounds. In addition, this submodel has also been tested with different gases (namely CO_2, DMS and isoprene) as shown in the second part of Chapter 3.

A new feature of the Lagrangian representation in *ECHAM5/MESSy1* is presented in Chapter 4, with the description of some processes implemented in this representation.

In the first part of Chapter 5 the hypotheses derived in Chapter 2 are tested, by a series of sensitivity simulations. This allows better comprehensions of what can be improved in the model to achieve a more realistic simulation of the organic compounds. In the second part, the effect of the **AIRSEA** submodel is analysed, and some conclusions about this process are drawn. Finally, in Chapter 6, the main results of this thesis are summarized together with some suggestions for future studies.

1.1 Tropospheric chemistry

1.1.1 Ozone and radicals in the troposphere

The oxidation of many compounds in the atmosphere is controlled by the hydroxyl radical OH. This radical is mainly formed by the photolysis of ozone (O_3) at wavelengths shorter than 320 nm followed by the reaction with water vapour (Levy, 1971):

$$\begin{array}{lcll} O_3 + h\nu & \longrightarrow & O\left(^1D\right) & \text{R1} \\ O\left(^1D\right) + H_2O & \longrightarrow & 2OH & \text{R2} \end{array}$$

$h\nu$ represents the energy of the photon, h is the Planck constant and ν is the frequency of the photon. Only a small portion of $O\left(^1D\right)$ (1-10%) reacts with water vapour. In the troposphere the rest quickly recombines with molecular oxygen (O_2), to form ozone again. Ozone also reacts with nitrogen oxides (NO and NO_2) in the troposphere:

$$\begin{array}{lcll} NO + O_3 & \longrightarrow & NO_2 + O_2 & \text{R3} \\ NO_2 + h\nu & \longrightarrow & O\left(^1D\right) + NO & \text{R4} \\ O\left(^1D\right) + O_2 & \longrightarrow & O_3 & \text{R5} \end{array}$$

This is a *null cycle*: neither ozone nor NO_2 and NO are destroyed or created. Moreover, due to the fast reactions between NO and NO_2, these two tracers are often regarded as one tracer "family" $NO_x = NO_2 + NO$.

The main terminating reaction for the NO_x cycle is:

$$OH + NO_2 \longrightarrow HNO_3 \quad \text{R6}$$

Nitric acid (HNO_3) is very soluble and is moderately reactive, therefore it is very likely to be deposited and thus lost from the atmosphere before it can release back the NO_2.

1.1.2 CO oxidation

The simplest case of degradation is the case of CO. Due to its abundance, carbon monoxide provides the most important sink for OH (Lelieveld et al., 2002; Logan et al., 1981; Thompson, 1992).

In regions with low concentrations of NO_x the following reactions occur:

$$\begin{array}{lcll} CO + OH\ (+O_2) & \longrightarrow & CO_2 + HO_2 & \text{R7} \\ HO_2 + O_3 & \longrightarrow & OH + 2O_2 & \text{R8} \\ \hline \text{net: } CO + O_3 & \longrightarrow & CO_2 + 2O_2 & \text{R9} \end{array}$$

In regions with high concentration of NO_x:

$$\begin{array}{lcll} CO + OH(+O_2) & \longrightarrow & CO_2 + HO_2 & \text{R7} \\ HO_2 + NO & \longrightarrow & NO_2 + OH & \text{R10} \\ NO_2 + h\nu & \longrightarrow & NO + O\left(^1D\right) & \text{R4} \\ O\left(^1D\right) + O_2 & \longrightarrow & O_3 & \text{R5} \\ \hline \text{net: } CO + 2O_2 & \longrightarrow & CO_2 + O_3 & \text{R11} \end{array}$$

It is important that the radicals OH and HO_2 as well as NO and NO_2 are not affected by this reaction sequence. Similar to NO_x, OH and HO_2 form a tracer family: $HO_x = OH + HO_2$.

Reaction 10 competes with reaction 8. Hence the availability of NO_x is very important in determining whether net production or destruction of O_3 occurs, together with the concentration of HO_x.

Moreover, the reaction

$$OH + O_3 \longrightarrow HO_2 + O_2 \qquad R12$$

contributes to ozone destruction in the troposphere.

A schematic of the CO oxidation reactions is shown in Fig. 1.1

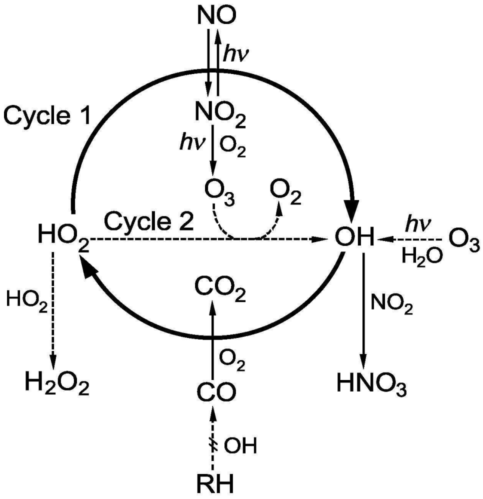

Figure 1.1: Schematic of CO oxidation. Cycle 1 is dominant at high concentrations of NO_x and cycle 2 at low concentrations of NO_x (Lelieveld et al., 2002).

1.2 Organic compounds in atmospheric chemistry

Following the **IUPAC**[1] recommendations, for nomenclature purposes " a structure containing at least one carbon atom is considered to be an organic compounds". However, it is common use to define organic compound as those whose molecules contain carbon and hydrogen. The organic compounds present in the atmosphere are generally named according to the following conventions:

- **V**olatile **O**rganic **C**ompounds (**VOC**) include all organic compounds (in the gas phase) present in the atmosphere.
- The VOC without methane are called **N**on-**M**ethane **V**olatile **O**rganic *C*ompounds (**NMVOC** or **NMOC**).
- Excluding the partially oxidized species, the remaining NMVOC are named **N**on **M**ethane **H**ydro**C**arbons (**NMHC**).
- **O**xygenated **V**olatile **O**rganic **C**ompounds (**OVOC**) refer to oxygen containing **VOC**

---

[1] **I**nternational **U**nion of **P**ure and **A**pplied **C**hemistry

1.2.1 $\mathrm{CH_4}$ oxidation

A typical oxidation chain is that of methane, the simplest VOC; this reaction chain can be considered as typical for the oxidation of the organic compounds (Crutzen, 1972, 1973, 1974).

Under low NO_x conditions:

$$\begin{array}{lcll}
CH_4 + OH + (+O_2) & \longrightarrow & CH_3O_2 + H_2O & R16 \\
CH_3O_2 + HO_2 & \longrightarrow & CH_3O_2H + O_2 & R13 \\
CH_3O_2H + OH & \longrightarrow & HCHO + H_2O + OH & R14 \\
\hline
\text{net: } CH_4 + HO_2 + OH & \longrightarrow & HCHO + 2H_2O & R15
\end{array}$$

Under high NO_x conditions:

$$\begin{array}{lcll}
CH_4 + OH\ (+O_2) & \longrightarrow & CH_3O_2 + H_2O & R16 \\
CH_3O_2 + NO & \longrightarrow & CH_3O + NO_2 & R17 \\
CH_3O + O_2 & \longrightarrow & HCHO + HO_2 & R18 \\
HO_2 + NO & \longrightarrow & NO_2 + OH & R10 \\
2(NO_2 + h\nu + (+O_2)) & \longrightarrow & NO + O_3 & R4 \\
\hline
\text{net: } CH_4 + 4O_2 & \longrightarrow & HCHO + H_2O & R19
\end{array}$$

Net reaction (R19) is catalysed by HO_x and NO_x. In both sequences the reactions of CH_3 and CH_3O with oxygen are so fast that they are assumed to be instantaneous. Furthermore, the gas phase oxidation of formaldehyde (HCHO) to CO occurs via one of the two following pathways:

$$\begin{array}{lcll}
HCHO + OH & \longrightarrow & CO + H_2O + HO_2 & R20 \\
HCHO + h\nu + (+O_2) & \longrightarrow & CO + 2HO_2 & R21
\end{array}$$

and CO finally forms CO_2 with (Sect. 1.1.2, R9-R11).

The tropospheric reactions of methane and carbon monoxide are the dominant loss processes for the HO_x radical concentrations in the "clean" background troposphere, and an increase in tropospheric methane concentration generally reduces the HO_x radical concentration (Houghton, 1996).

1.2.2 The oxidation of Non Methane HydroCarbons (NMHC)

Although differences occur in the oxidation of NMHC, still a generalised oxidation scheme can be described, as presented in Fig. 1.2. Generally the NMHC oxidation is similar to the methane oxidation (see 1.2.1), with the peroxy radicals (RO_2) playing a major role in this reaction chain.

The repetition of this chain leads to CO, and hence to CO_2 (see Sect. 1.1.2), the final fate of all the VOC present in the atmosphere. A more detailed description is present in Jenkin and Clemitshaw (2000), Atkinson and Arey (2003) and Atkinson (2000).

The initial reaction with OH (partly also with NO_3 or halogens) leads to alkyl radicals, which rapidly combine with oxygen (O_2) to produce the peroxy radical (RO_2).

The peroxy radicals can react with:

- HO_2 producing hydroperoxide (ROOH)
- other peroxy radicals (RO_2) producing carbonlys (e.g. aldehydes) or alcohols (ROH)

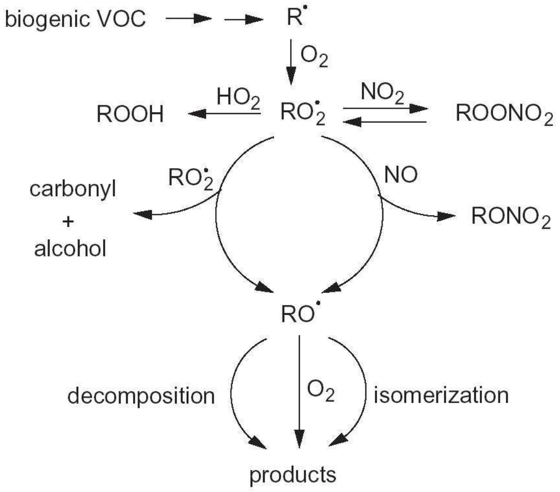

Figure 1.2: Typical oxidation process for Volatile Organic Compounds (Atkinson and Arey, 2003).

- NO producing mainly NO_2 and alkoxy-radicals (RO, which can react via isomerization, decomposition or with O_2), plus a small fraction of alkyl-nitrates($RONO_2$)
- NO_2 forming peroxy nitrates ($ROONO_2$). These compounds are very unstable and decompose rapidly at room temperature. A case of special interest is the formation of peroxy acetyl nitrate PAN.

The peroxy radicals produced in the oxidation of NMHC can sequester NO_x into an inactive form which can then be transported away from the production regions. A typical example (and the most stable and abundant of these nitrate compounds) is peroxy acetyl nitrate (PAN) formed by the peroxy acetyl radical $CH_3C(=O)O_2$ + NO_2. PAN is rapidly decomposed at room temperature and surface pressure, but becomes very stable with decreasing pressure and temperature. In the upper troposphere, for example, concentrations of PAN exceeding those of NO_x species have been measured (Singh et al., 1992). PAN can hence be transported to and decomposed at locations with low concentrations of NO_x, providing an additional (and important) source of NO_x in regions where direct emissions are absent (Crutzen, 1979; Singh and Hanst, 1981; Singh et al., 1985; Moxim et al., 1996).

The effect of NMHC on ozone production is strong in polluted regions where high concentrations of NO_x are present. In fact, since CH_4 and CO are readily available even in remote regions of the atmosphere, ozone production from these hydrocarbons is largely limited by the availability of NO_x. In locations where NO_x is available the oxidation of CH_4 and CO reaches easily a saturation level (VOC limited region). In this case the ozone production depends also on the production rate of the peroxy radicals (HO_2, RO_2), which can be greatly enhanced by NMHC oxidation.

Net photochemical formation or loss of O_3 is determined by the reactions

$$\begin{array}{lcll} HO_2 + NO & \longrightarrow & OH + NO_2 & \mathrm{R10} \\ RO_2 + NO & \longrightarrow & RO + NO_2 & \mathrm{R22} \end{array}$$

versus the reactions

$$
\begin{array}{lcll}
HO_2 + HO_2 & \longrightarrow & H_2O_2 + O_2 & \text{R23} \\
HO_2 + O_3 & \longrightarrow & OH + 2O_2 & \text{R8} \\
OH + O_3 & \longrightarrow & HO_2 + O_2 & \text{R12}
\end{array}
$$

Hence the overall production of O_3 in the troposphere is determined by the ratio of NO_x versus VOC. As shown in Fig.1.3, the isopleths of O_3 depend on the ratio of VOC and NO_x.

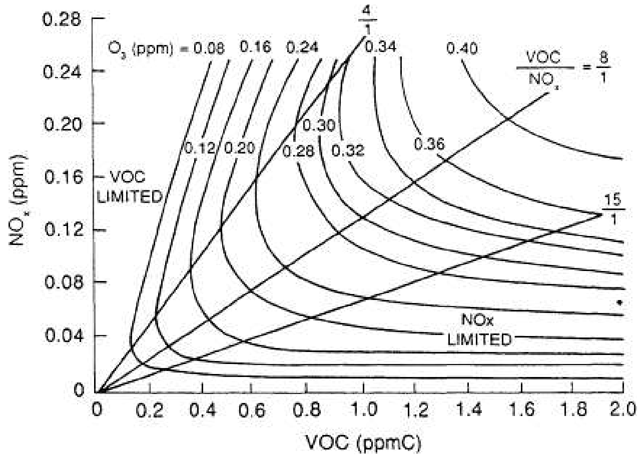

Figure 1.3: Isopleths of ozone depending on the concentrations of VOC and NO_x based on a box model study for urban conditions (Kelly, 1991).

Based on the presence of NO_x two regimes can be defined:

- In polluted regions the oxidation of NMVOC is important for O_3 formation. This is called "VOC limited" and there is a net production of O_3. In the troposphere this case generally implies $[\mathrm{NO}] > 10{-}30 \times 10^{12}$ mol/mol.
- In unpolluted regions, with low NO_x, the chemical regime is generally NO_x limited, and there is a net phtochemical destruction of O_3 due to the OH radical. In the troposphere this case generally occurs at $[\mathrm{NO}] < 10{-}30 \times 10^{12}$ mol/mol.

1.2.3 Oxygenated VOC

Many oxygenated compounds (OVOC), different from the other VOC, can photolyse. This is very important in the upper troposphere (UT), where the photolysis rate is generally higher and OVOC are more efficiently destroyed by solar radiation (Atkinson et al., 2005b). Their photolysis leads to production of HO_x, which is not so abundant in the UT region (due to the lower water content). Jaeglé et al. (2001) calculated that these sources are very important for vapour mixing ratios less than 100 nmol/mol.

As we have seen for formaldehyde (HCHO, the simplest OVOC):

$$HCHO + h\nu + (+O_2) \longrightarrow CO + 2HO_2 \quad \text{R21}$$

As other example, Wennberg et al. (1998) and Folkins and Chatfield (2000) show that without the acetone (CH_3COCH_3) photolysis, the concentration of HO_x in the UT is underestimated by a factor of

2. Moreover, in the flight corridors (with elevated NO_x) acetone tends to double the production of ozone compared to normal NO_x chemistry (Brühl et al., 2000).

The relative contribution on HO_x from different OVOC, however, is still not very clear (Prather and Jacob, 1997; Jaeglé et al., 1997, 2000; Collins et al., 1997; Müller and Brasseur, 1995).

1.3 Summary

NMVOC have a strong impact in the chemistry of the atmosphere, and their influence on the concentration of other tracers is highly dependent on the local chemical-physical conditions.

The main effects are:

- formation of peroxy radicals, which produce ozone in regions with high NO_x concentrations: the peroxy radicals (RO_2) convert NO into NO_2 which leads to the production of O_3 through reactions R22 and R4. Anthropogenic VOC are generally emitted into a NO_x-rich atmosphere. If exchange with clean air is suppressed or limited (due to the meteorological conditions), this process can generate photochemical smog.
- decrease of HO_x: in locations with low concentrations of NO_x the VOC react with HO_x, providing a sink for this tracer family.
- HO_x formation in the upper troposphere (UT) directly from photolysis of several OVOC.
- transformation of reactive nitrogen to a non-reactive form, decreasing the available NO_x.
- formation of NO_x through the dissociation of these nitrogen oxide reservoir tracers.

Chapter 2

Description and evaluation of the model

In this chapter the atmospheric chemistry general circulation model *ECHAM5/MESSy1* is described and evaluated, based on numerous observations. First the model is briefly described (Sect. 2.1), followed by a description of the observational datasets used for the evaluation (Sect. 2.2). Finally (Sect. 2.3) the comparison of the model results with the observations in the troposphere is presented, with a focus on ozone and various organic precursor gases.

2.1 The ECHAM5/MESSy model

2.1.1 ECHAM5

The dynamical core of *ECHAM5/MESSy1* is the 5^{th} generation general circulation model ECHAM (from now on *ECHAM5*) developed at the **M**ax **P**lanck **I**nstitute (MPI) for Meteorology in Hamburg (Roeckner et al., 2003, 2006; Manzini et al., 2006; Roesch and Roeckner, 2006; Hagemann et al., 2006; Wild and Roeckner, 2006). *ECHAM5* is based on the weather forecasting model of the **E**uropean **C**entre for **M**edium-range **W**eather **F**orecasting (**ECMWF**), which has been modified into a climate model.

ECHAM5 simulates the dynamics and thermodynamics of the atmosphere, solving the basic equations of atmospheric dynamics. The solutions of the basic equations are obtained with the "spectral transform method" using grid and spectral representations. The model resolution depends on the (triangular) truncation of the waves in the spectral space. Technically every truncation is possible, but for practical reasons only some of them are used. A hybrid pressure grid describes the vertical coordinate. This implies a terrain-following profile at the surface, and constant pressure levels in the stratosphere. In a standard configuration the vertical axis reaches up to 10 hPa (mid of uppermost layer), with 19 or 31 levels, whereas in the "middle atmosphere" (MA) configuration, the model describes the atmosphere up to 0.01 hPa (mid of uppermost layer), with 39 or 90 vertical layers. The horizontal and vertical resolution also defines the maximum time step applicable. To avoid numerical instabilities, the CFL criterion (Courant et al., 1928) has to be satisfied. The possible resolutions are resumed in Tab. 2.1.

Advection of constituents is calculated with a flux form semi-lagrangian (FFSL) scheme (Lin and Rood, 1996). Convection is calculated following the Tiedtke (1989) scheme, with some additions by Nordeng (1994).

spectral truncation	No. of longitudes	No. of latitudes	horizontal resolution [°×°]	horizontal resolution [km×km]	max timestep [s]
T21	64	32	5.6×5.6	621×621	2400
T31	96	48	4.2×4.2	467×467	1800
T42	128	64	2.8×2.8	311×311	1200
T63	192	96	1.8×1.8	233×233	720
T85	256	128	1.4×1.4	156×156	480
T106	320	160	1.1×1.1	122×122	360

Table 2.1: Triangular truncation and associated number of Gaussian latitudes (and longitudinal number of grid points). The corresponding horizontal resolutions and the maximum time step available for each resolution are also listed.

A “leapfrog-scheme” is used as integration scheme. This is a semi-implicit integration scheme, with two time levels. Due to the presence of a numerical (undesired) solution associated with this integration scheme, the Robert-Asselin time filter (Robert, 1969; Asselin, 1972) is also applied.

In order to push the model toward the observed state, an assimilation data procedure called NUDGING (Jeuken et al., 1996; van Aalst et al., 2004), is available in *ECHAM5*. The information about temperature, surface pressure, vorticity and divergence have to be introduced from an external source, typically the **ECMWF** analysis or reanalysis data (ERA15, ERA40). The model assimilates these quantities by adding an additional tendency $(\partial X/\partial t)_{nudge}$ to the respective variables in the spectral space; this tendency is the difference of the input data and the simulated values, multiplied by a relaxation coefficient $G(X)$ (Lelieveld et al., 2006; Bucholz, 2005).

$$\left(\frac{\partial X}{\partial t}\right)_{nudge} = G(X)\,[X_{ECMWF} - X]$$

However, if the added tendency is too big the model tends to deviate from its “natural state”, leading to instabilities or unrealistic model states (Bengtsson et al., 2004; Hagemann et al., 2002). The relaxation coefficient is hence a critical parameter and different relaxation coefficients are applied to different vertical levels to avoid such inconsistencies .

2.1.2 MESSy

The *ECHAM5* code has been further developed at the MPI for Chemistry in Mainz, and it has been connected with the **M**odular **E**arth **S**ystem **M**odel (*MESSy*) interface. The *MESSy* interface implies a rigorous modularisation and coding standard (Jöckel et al., 2005); it is easily expandable and very flexible. In the *MESSy* framework, thanks to its modularity, numerous submodels which simulate various aspects of the atmospheric chemistry have been connected forming a comprehensive **A**tmospheric **C**hemistry **G**eneral **C**irculation **M**odel (**AC-GCM**). The submodels are also improving some important dynamic aspect of the atmospheric chemistry. These submodels have been developed at the MPI in Mainz with contributions from the **D**eutsches Zentrum für **L**uft und **R**aumfahrt (DLR).

The *MESSy* interface is structured in four layers:

- **B**ase **M**odel **L**ayer (BML) consisting of the base model (currently *ECHAM5*).
- **B**ase **M**odel **I**nterface **L**ayer (BMIL), which includes the central management interface of the *MESSy* submodels and allows data exchange between the submodels.
- **S**ub **M**odel **I**nterface **L**ayer (SMIL), which performs the data transfer to and from the individual submodels.
- **S**ub **M**odel **C**ore **L**ayer (SMCL), which contains the representation of the individual processes.

A graphical representation of the layers is presented in fig. 2.1

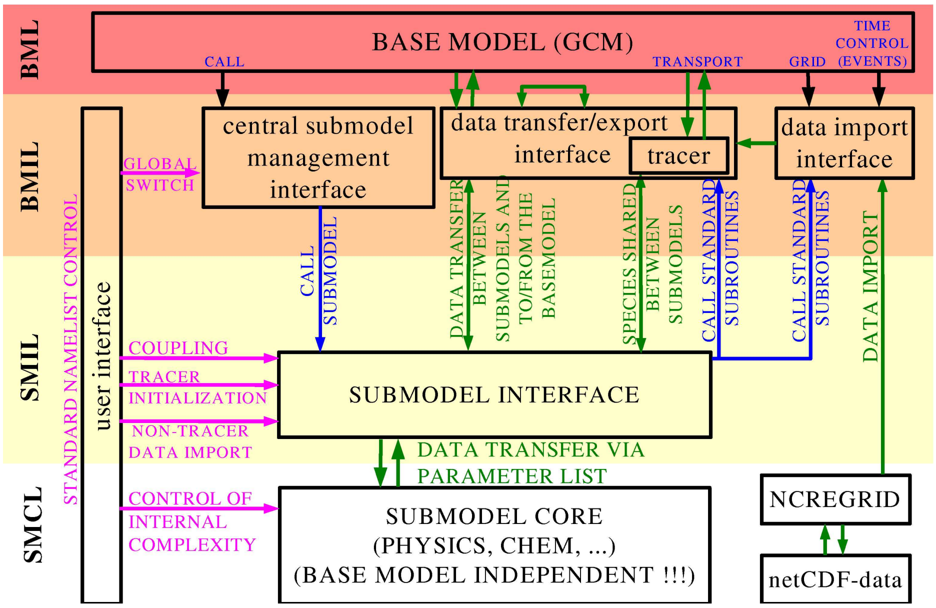

Figure 2.1: The four layers defining the *MESSy* interface, from Jöckel et al. (2005).

2.1.2.1 The evaluation simulatio *S1*

The *ECHAM5/MESSy1* (version 1.1), used for this work, has been officially released in January 2006, and it has been extensively evaluated (Jöckel et al. (2006); Pozzer et al. (2006)).

ECHAM5 with a resolution of T42L90MA (see Sect. 2.1.1) has been chosen for the reference simulation (from now on called *S1*).

Apart from surface pressure and the prescribed Sea Surface Temperature (SST), the model has been nudged only in the free troposphere, between 700 and 100 hPa towards analysis data from the **ECMWF** operational model (see Sect. 2.1.1). Additional transition levels very weakly nudged (i.e. with low relaxation coefficients) are present at the boundaries of this “nudged” region. This “forces” the model to reproduce the “observed” meteorology, so that a direct comparison of the model output with measurement data is possible.

The time step of the model in this resolution is 900 s, and an output frequency of 5 hours (instantaneous field) has been selected. This permits to cover a typical diurnal cycle within 5 days of integration.

The simulation aimed to reproduce the year 2000, and a simulation of seven years (1998-2005) has been performed.

submodel name	function
CLOUD	**CLOUD** model
CONVECT	**CONVECT**ion processes
CVTRANS	**C**on**V**ective tracer **TRANS**port
DRYDEP	**DRY DEP**osition of gases and aerosol
H2O	Water vapor feedback
HETCHEM	**HET**erogoneous **CHEM**istry
JVAL	photolysis calculations
LNOX	**L**ightning NO_X formation
MECCA	chemistry reactions calculations
OFFLEM	**OFF**-line **EM**issions
ONLEM	**ON**-line **EM**issions
PSC	**P**olar **S**tartospheric **C**louds
PTRAC	**P**assive **TRAC**ers
QBO	**Q**uasi **B**iennial **O**scillation nudging
RAD4ALL	**RAD**iation calculation and feedback with chemistry
SCAV	**SCAV**enging of gases and aerosol
SEDI	**SEDI**mentation of aerosols
TNUDGE	**T**racer **NUDG**ing
TROPOP	**TROPOP**ause calculation

Table 2.2: MESSy submodels used in the reference simulation

2.1.2.2 The submodels in the reference simulation

The submodels used in the reference simulation *S1* are listed in Tab. 2.2, and they are shortly described here.

CLOUD contains the original *ECHAM5* (Lohmann and Roeckner, 1996; Tompkins, 2002) algorithm for cloud processes, recoded according to the *MESSy* standard.

CONVECT uses the *ECHAM5* algorithm to calculate the convection and convective precipitation (Tiedtke, 1989). Please refer to Tost (2006, and references therein) for more information.

CVTRANS calculates the tracer transport due to the convection (Lawrence and Rasch, 2005).

DRYDEP calculates the dry deposition for different gas and aerosol species following the big leaf approach (Kerkweg et al., 2006a; Ganzeveld and Lelieveld, 1995; Ganzeveld et al., 1998).

H2O defines H_2O as a tracer, provides its initialisation in the stratosphere and mesosphere from satellite data, and controls the feedback with the specific humidity of *ECHAM5* .

HETCHEM calculates the heterogeneous reaction rates on stratospheric nitric acid trihydrate (NAT), ice, super-cooled ternary solutions (STS), and on stratospheric and tropospheric (sulfate) aerosols. Monthly climatologies of stratospheric $\mathrm{H_2SO_4}$ mixing ratios for the years 1960 to 1999 (derived from the Stratospheric Aerosol and Gas Experiment (SAGE) data) and tropospheric sulfate aerosol surface for present day conditions (Kerkweg, 2005) are provided. In the reference simulation the $\mathrm{H_2SO_4}$ climatology (monthly averages) of the year 1999 has also been used for the years 2000-2005 in the stratosphere. This submodel calculates the heterogeneous reaction rates only outside the **P**olar **S**tratospheric **C**loud region (see **PSC** later).

JVAL provides the photolysis rates of different tracers, based on the Landgraf and Crutzen (1998) algorithm.

LNOX calculates the lightning $\mathrm{NO_x}$ production (Price and Rind, 1992; Pickering et al., 1998). The flash frequency and the amount of produced $\mathrm{NO_x}$ per single flash has been scaled in order to obtain a global lightning $\mathrm{NO_x}$ production of $\approx 2\ \mathrm{Tg/yr}$.

MECCA (**M**odule **E**fficiently **C**alculating the **C**hemistry of the **A**tmosphere) calculates tropospheric and stratospheric chemistry (Sander et al., 2005, and references therein). In this simulation 104 gas phase species have been included with 245 reactions (see Appendix B). It comprises the ozone related chemistry of the troposphere plus NMHCs up to isoprene (von Kuhlmann et al., 2003b). Chlorine (Steil et al., 1998) and bromine (Meilinger, 2000) reactions are considered for the stratosphere. **MECCA** uses heterogeneous rate coefficients calculated by **HETCHEM** and **PSC** and photolysis rates calculated by **JVAL**.

OFFLEM (Kerkweg et al., 2006b) controls the prescribed emissions of trace gases. Some pre-calculated files with monthly emission maps (in $\mathrm{mlc/(m^2s)}$) are imported by this submodel, which then changes the tracer tendency accordingly. Offline emissions are used for CO, HCHO, HCOOOH, $\mathrm{CH_3OH}$, $\mathrm{C_2H_4}$, $\mathrm{C_2H_6}$, $\mathrm{C_3H_6}$, $\mathrm{C_3H_8}$, $\mathrm{C_4H_{10}}$, $\mathrm{CH_3CHO}$, $\mathrm{CH_3COOH}$, $\mathrm{CH_3COCH_3}$, $\mathrm{CH_3COC_2H_5}$, $\mathrm{SO_2}$, $\mathrm{NH_3}$ and anthropogenic $\mathrm{NO_x}$.

ONLEM (Kerkweg et al., 2006b) calculates surface emission fluxes based on on-line calculations. Dimethylsulfide (DMS) from ocean, isoprene from plants and NO from soils are emitted with this method. In the reference simulation, the emissions of isoprene and NO have been scaled by a factor of 0.6. This reduction yields to realistic mixing ratios of isoprene in the boundary layer (Houweling et al. (1998), Brasseur et al. (1998), von Kuhlmann et al. (2004)) and fluxes of $\mathrm{NO_x}$ are comparable to previous estimates (Houghton et al., 2001).

PSC controls the micro-physical processes which lead to the formation of super-cooled ternary solutions (STS), nitric acid trihydrate (NAT), and ice particles in the polar stratosphere (Bucholz, 2005). Denitrification and dehydration due to sedimenting solid PSC particles are calculated for each grid box depending on particle size, pressure and temperature.

PTRAC is used to define and initialise tracers which are not taking part in the chemical mechanism MECCA (for example $\mathrm{SF_6}$).

QBO is used to initialise the phase of the **Q**uasi **B**iennial **O**scillation of the zonal wind during the first year of the simulation (Giorgetta and Bengtsson, 1999; Naujokat, 1986).

RAD4ALL contains the original *ECHAM5* routines that calculate radiation, coded following the *MESSy* standard. It provides the feedback between chemistry and dynamics by coupling the tracers with the income radiation. For the aerosols the original *ECHAM5* aerosol climatology has been applied (Tanre et al., 1984).

SCAV simulates the processes of wet deposition and liquid phase reactions in droplets (Tost, 2006).

SEDI calculates the sedimentation of the aerosol particles (Kerkweg et al., 2006a) with a mass conserving algorithm.

TNUDGE (Kerkweg et al., 2006b) is used for the nudging of tracers towards prescribed fields (from **OFFLEM**). In the reference simulation the lower boundary conditions of the following tracers have been prescribed: N_2O, CH_4, $CFCl_3$, $CFCl_2$, C_2H_3Cl,CCl_4, CH_3Cl,CH_3Br, CF_2ClBr, CF_3Br,H_2, CO_2 and SF_6 using the AGAGE database (Prinn et al., 2000).

TROPOP calculates the tropopause height based on the definition of the **W**orld **M**eteorological **O**rganisation (WMO, 1992). The calculation is based on the temperature laps rate for latitudes equatorward of 30° and the potential vorticity iso-surface of 3.5 PVU at latitudes polewards of 30°. The submodel calculates also the planetary boundary layer height.

The link between chemistry and dynamics is provided in the via the following processes:

- The chemical water vapour tendency (calculated by the chemistry) is synchronized with the water vapour (by submodel **H2O**) used in *ECHAM5*;
- The incoming radiation is calculated (by **RAD4ALL**) using the on-line column concentration of the gases, the cloud cover (calculated by **CLOUD**), the water vapour, the cloud water content and cloud ice;
- The partitioning of total water to vapour, liquid and ice phase is calculated within and outside the PSC region (by **PSC** and **HETCHEM**);
- The water vapour, liquid water and ice are transported by convection (by **CONVECT**);
- Partitioning of the of total water to vapour, liquid and ice phase is calculated accordingly to the cloud droplet formation (**CLOUD**).

2.1.2.3 Chemical mechanism

The submodel **MECCA** calculates the chemical reactions in *MESSy*. The species and the reactions that have to be calculated by this submodel must be selected before the simulation, from a large set of chemical reactions (Sander et al., 2005, and references therein). After the selection of the chemical equations, the **K**inetc **P**re**P**rocessor (Damian et al., 2002; Sandu and Sander, 2006) is then used to generate the code to solve the set of differential equations.

In the reference simulation, the reaction mechanism introduced by von Kuhlmann et al. (2003a,b) (based on Lawrence et al. (1999a)), has been included for the tropospheric part. This mechanism covers reactions of VOC up to 4 carbons plus isoprene. Due to the long lifetime of these trace gases with respect to the model time step, all VOC have been transported by advection and convection, with the exception of the high reactive peroxy-radicals. More information about this chemical mechanism are present in von Kuhlmann (2001b, and references therein)

The calculation of the chemical reactions in the model requires the knowledge of the rate coefficients of all the reactions included. These reaction rates are calculated in **MECCA**, according to meteorological and chemical parameters, such as temperature, pressure and tracer concentrations. In case of photolysis reactions, the required photolysis reaction rates are imported from **JVAL**.

In Appendix B a list of the reactions used in the reference simulation is presented.

2.1.2.4 Photolysis

For oxygenated organic compounds the photolysis is also a very important sink processes (see Sect. 1.2.3).

The photolysis reaction is calculated by **MECCA**; however, the photolysis reaction rates have to be introduced from the submodel **JVAL**. Based on the work of Landgraf and Crutzen (1998), in this submodel the photolysis rate coefficients for a gas X are calculated via the integrals

$$J_X = \int_I \sigma_X(\lambda)\Phi_X(\lambda)F(\lambda)d\lambda, \tag{2.1}$$

where λ is the wavelength, σ_X the absorption cross section, Φ_X the quantum yield, and I (the integration range) is the photochemically active spectral interval $178.6\text{nm} \leq \lambda \leq 752.5\text{nm}$. Numerically, Eq.2.1 is approximated as:

$$J_X \approx \sum_{i=1}^{N} \sigma_X(\lambda_i)\Phi_X(\lambda_i)F(\lambda_i)d\lambda_i \tag{2.2}$$

In **JVAL**, the active spectral range has been subdivided in eight intervals I_i ($i = 1 \ldots 8$), with only the first in the Schumann-Runge band ($178.6\text{nm} \leq \lambda \leq 202.0\text{nm}$).

The actinic flux $F(\lambda_i)$ is influenced by the scattering by air molecules, aerosol and cloud particles. With the exception of the Schumann-Runge band, these effects are included modifying the actinic flux of a purely absorbing atmosphere ($F^a(\lambda_i)$) with a factor which is wavelength dependent (δ_i):

$$F(\lambda_i) = F^a(\lambda_i) \times \delta_i \tag{2.3}$$

Because the scattering effects can be neglected for the Schumann-Runge band (due to the strong absorption of O_2), the final approximation for the calculation of J_X is:

$$J_X \approx J^a_{1,X} + \sum_{i=2}^{8} J^a_{i,X} \cdot \delta_i \tag{2.4}$$

With these assumptions, $F^a(\lambda_i)$ can be precalculated, and only δ_i has to be calculated on-line, depending on the atmospheric conditions at the particular location. The 8 wavelengths representing the wavelength intervals have been chosen to minimize the error of Eq. 2.4 compared to Eq. 2.1.

In Tab. 2.3 the wavelength intervals are shown, as present in **JVAL**.

Interval	λ_a [nm]	λ_b [nm]	λ_i [nm]
1	178.6	202.0	
2	202.0	241.0	205.1
3	241.0	289.9	287.9
4	289.9	305.5	302.0
5	305.5	313.5	309.0
6	313.5	337.5	320.0
7	337.5	422.5	370.0
8	422.5	752.5	580.0

Table 2.3: Subdivision of the spectral range $178.6\mathrm{nm} \leq \lambda \leq 752.5\mathrm{nm}$; λ_a and λ_b are the lower and the upper wavelengths of the bands, λ_i is the fixed wavelength used in Eq.2.4. From Landgraf and Crutzen (1998).

2.1.2.5 Emissions

Four submodels are responsible for the emissions in the reference simulation (**OFFLEM**,**ONLEM**,**TNUDGE** and **LNOX**).

As already mentioned, in the **OFFLEM** submodel the emissions are independent from the state of the atmosphere while in **ONLEM** the chemical-physical conditions modify the emission fluxes.

The **OFFLEM** submodel imports external flux fields and changes the mixing ratios of the tracers accordingly. In the reference simulation *S1* emissions fields for various organic gases have been used, namely : HCHO, HCOOOH, CH_3OH, C_2H_4, C_2H_6, C_3H_6, C_3H_8, C_4H_10, CH_3CHO, CH_3COOH, CH_3COCH_3 and $CH_3COC_2H_5$.

Two emission methods are available from the **OFFLEM** submodel (Kerkweg et al., 2006b):

method 1 : The change of the mixing ratio $\Delta\mu$ in one time step Δt of the model is calculated from the prescribed emission flux F_{emiss}:

$$\frac{\Delta\mu}{\Delta t} = \frac{F_{emiss}}{z_{box}} \frac{RT}{pN_a} \tag{2.5}$$

z_{box} is the height of the grid box (m), T is the temperature K, $R = 8.314$ J mol^{-1}K^{-1} is the universal gas constant, p is the air pressure and $N_a = 6.022 \times 10^{23}$ mol^{-1}is the Avogadro constant.

method 2 : A lower boundary condition for the vertical diffusive flux F_{vdiff} is calculated from the prescribed emission.

The realistic representation of the emissions in **OFFLEM** is solely dependent on the input files, which should contain the best possible estimates of the emission fluxes. Providing these estimates (and the production of inventories that can be used by global models) is a tedious task. Large amounts of NMVOC are emitted from anthropogenic and biogenic sources (Guenther et al., 1995, 2000; Hein et al., 1997; Placet et al., 2000; Olivier et al., 1999, 1996). Literature estimates of world-wide emissions of NMVOC are $\approx 60 - 140$ TgC/yr from anthropogenic sources and ≈ 1150 TgC/yr from biogenic sources (Atkinson, 2000; Lamb et al., 1993; Guenther et al., 1995). The few estimates of the natural emissions for the simplest NMVOC are generally associated with uncertainties of up to a factor of 3 (Guenther et al., 1995), depending on the species.

In *MESSy* the anthropogenic and biomass burning emissions have been obtained from the EDGAR database, specifically compiled for the year 2000 (version 3.2 “fast-track”, van Aardenne et al. (2005)) as described by Ganzeveld et al. (2006).

The biogenic emissions, which generally are estimated with the highest degree of uncertainty, have been obtained from the inventory database GEIA, compiled by Guenther et al. (1995). To adapt such inventories, the emission fields have been multiplied by a constant factor to obtain the desired global annual emissions.

2.1.2.6 Dry deposition

The flux of a gas X to the surface in $\mathrm{mcl/m^2s}$ can be expressed as $F(X) = v_d \times C_X$, where C_X is the concentration ($\mathrm{mcl/m^3}$) of the gas X and v_d is the deposition velocity in $\mathrm{m/s}$.

To take into account that the mixing ratio used to calculate the dry deposition flux continuously decreases during the time step due to dry deposition and to avoid total depletion in one grid box for very efficiently depositing species (e.g. $\mathrm{HNO_3}$) the effective dry deposition velocity $v_{d,\mathit{eff}}$ in $\mathrm{m/s}$ is calculated from the dry deposition velocity v_d according to

$$v_{d,\mathit{eff}} = \frac{\Delta z}{\Delta t} \times \left[1 - \exp\left(v_d \, \frac{\Delta t}{\Delta z}\right)\right] \tag{2.6}$$

with Δt time step in s and Δz layer thickness in m. Hence, the flux in *ECHAM5/MESSy1* is expressed as:

$$F(X) = v_{d,eff} \times C_X .$$

In *ECHAM5/MESSy1* , the mixing ratios of trace gases are calculated, thus the flux $F(X)$ has to be calculated in $\mathrm{kg/(m^2s)}$ with:

$$F(X) \;=\; \mu(X) \times \frac{M(X)}{M_{air}} \times \frac{\Delta p}{g \, \Delta z} \times v_{d,eff}(X) \tag{2.7}$$

with $\mu(X)$ being the gas phase mixing ratio of species X in $\mathrm{mol/mol}$ and $M(X)$ and M_{air} the molar mass of species X and dry air (in $\mathrm{kg/mol}$), respectively. g is the gravitational acceleration ($\mathrm{m\,s^{-2}}$) and Δp the layer thicknesses in Pa.

The calculation of the the dry deposition velocity $v_d(X)$ of a trace gas X (in $\mathrm{m/s}$) is based on the “big leaf approach” (Ganzeveld et al., 1998):

$$v_d(X) = \frac{1}{R_a + R_{qbr}(X) + R_s(X)} \;, \tag{2.8}$$

where R_a is the aerodynamic resistance, $R_{qbr}(X)$ the quasi-laminary boundary layer resistance, and $R_s(X)$ the surface resistance (all resistances are in units of $\mathrm{s\,m^{-1}}$). R_a is a function of the physical state of the atmosphere, $R_{qbr}(X)$ is controlled by molecular diffusion and $R_s(X)$ depends on the chemical, physical and biological properties of the surface.

While R_a and $R_{qbr}(X)$ are calculated from physical properties of the tracer and of the atmosphere, the surface resistance $R_s(X)$ for a gas is approximated by scaling the deposition velocities of ozone ($\mathrm{O_3}$)

and sulfur dioxide (SO_2), which are relatively well known. Wesely (1989b), Kerkweg et al. (2006a) and Ganzeveld and Lelieveld (1995) provide more information about this parameterisation.

Because, very little is known about the dry deposition of NMVOC from direct measurements, the approach used in **DRYDEP** is justified.

In Tab. 2.4, the emission and deposition budgets for the most important organic tracers as calculated by *MESSy* are presented, together with values from the literature.

2.2 Observations

Three types of observation datasets have been used to extensively evaluate the reference simulation (*S1*) :

- Ozonesondes:

  Based on an extensive network of ozonesonde measurements (World Meteorological Organization, 1998), climatologies for ozone can be calculated for different locations on the globe (Logan, 1999a,b). All measurements are archived (and available) at the **W**orld **O**zone and **U**ltraviolet **D**ata **C**enter (**WOUDC**[1]).

  Two datasets are available from these measurements:

  Logan dataset : This dataset has been compiled from several measurements between 1980 and 1995 (Logan, 1999a, and references therein), mainly obtained from the **WOUDC**. In Fig. 2.2, the locations of these measurements are shown as blue circles. From these measurements an ozone climatology has been calculated for 22 pressure levels. To compare the model results with this dataset, we used *always* a climatological ozone mixing ratio obtained from our model, averaging the 7 years simulation of *S1*.

  SHADOZ dataset (**S**outhern **H**emisphere **A**dditional **OZ**onesondes, Thompson et al. (2003a,b)): Due to the lack of ozonesonde measurements in the tropics, in the 1998 a network of 10 ozonesonde stations has been set up in the tropical and subtropical Southern Hemisphere (SH) The data obtained from the **SHADOZ**[2] project are also archived in the **WOUDC**. In Fig. 2.2, the locations of these measurements are shown as red circles.

  Although the locations of the observations contained in this dataset are largely limited to the tropics, the measurements range from 1998 to present day and hence are better suited for a comparison with our simulation. In our comparison, measurements from 1998 to 2002 have been used. To avoid synoptical variability effects, an ozone climatology has been calculated from this dataset and it has been compared with a climatology obtained from the model, sampled at the same time and position of the measurements.

---

[1] http://www.woudc.org/

[2] http://croc.gsfc.nasa.gov/shadoz/

Table 2.4: Budgets of different tracers as calculated from the E5/M1 simulation (this work) compared to values from the literature.

tracer	emission (Tg/yr) this work	emission (Tg/yr) literature	dry deposition (Tg/yr) this work	dry deposition (Tg/yr) literature	wet deposition (Tg/yr) this work	wet deposition (Tg/yr) literature	burden (Tg) yearly averaged this work
C_2H_4	26.35	19.55^h 22.35^f 35.46^l	-	-	-	-	0.12
C_2H_6	12.46	11.95^f 12.26^h 12^i 15^l	-	-	-	-	2.51
C_3H_6	9.92	6.95^h 9.87^f 21.46^l	-	-	-	-	0.01
C_3H_8	11.97	10.18^f 11.99^h 11.73^i 11.12^l	-	-	-	-	0.66
CH_3COCH_3	47.96	95^b 80.16^h 59.64^f 46.07^g 39.95^i 53.97^l	24.48	12.96^a 9^b 8.8^e	-	-	2.23
CH_3OH	77.74	312^f 240^c 128^d	42.16	55^c 31.35^a	-	12^c	2.46
HCHO	7.78	6.97^f 2.3^l	43.35	45.73^a	1.74	31.62^a	1.05
H_2O_2	-	-	142.12	170.70^a	194.22	244.52^a	4.07
CO	see Tab. 2.10		see Sect. 2.3.3		-	-	375.93

---

[a] von Kuhlmann et al. (2003b)
[b] Jacob et al. (2002), only on land
[c] Jacob et al. (2005)
[d] Heikes et al. (2002)
[e] Arnold et al. (2005)
[f] Horowitz et al. (2003)
[g] Park et al. (2004a)
[h] Folberth et al. (2006)
[i] Bey et al. (2001)
[j] Brasseur et al. (1998)

- Aircraft measurements: Compiled by Emmons et al. (2000, and references therein), from field campaigns sponsored by **NASA/GTE**[3], **NASA/UARP** [4] and **NSF/NCAR**[5], this database is an aggregate of many measurements in order to obtain reasonable vertical profiles. The campaigns have limited time coverage but provide information about the *vertical profiles* over extended areas for many trace gases. The campaigns have been conducted between 1989 and 2001 (see Tab. 2.5). Because different tracers have been measured during different campaigns (Emmons et al., 2000, and references therein), each simulated tracer is compared with a different number of measurements.

Campaign (aircraft)	Time	Reference
TRACE-P (DC8, P3)	Feb 24-Apr 10, 2001	Jacob et al. (2003)
TOPSE (C130)	Feb 5-May23, 2000	Atlas et al. (2003)
PEM-Tropics-B (DC8)	Mar 6-Apr 18, 1999	Raper et al. (2001)
PEM-Tropics-B (P3)	Mar 11-Apr 11, 1999	Raper et al. (2001)
SONEX (DC8)	Oct 7-Nov 12, 1997	Thompson et al. (2000)
POLINAT-2 (Falcon)	Sep 19-Oct 25, 1997	Thompson et al. (2000); Ziereis et al. (2000)
PEM-Tropics-A (DC8)	Aug 24-Oct 15, 1996	Hoell et al. (1999)
PEM-Tropics-A (P3)	Aug 15-Sep 26, 1996	Hoell et al. (1999)
VOTE (DC8)	Jan 20-Feb 19, 1996	Schoeberl and Toon (2002)
TOTE (DC8)	Dec 6-22, 1995	Schoeberl and Toon (2002)
ACE-1 (C130)	Oct 31-Dec 22, 1995	Bates et al. (1998)
PEM-West-B (DC8)	Feb 7-Mar 14, 1994	Hoell et al. (1997)
TRACE-A (DC8)	Sep 21-Oct 26, 1992	Fishman et al. (1996)
PEM-West-A (DC8)	Sep 16-Oct 21, 1991	Hoell et al. (1996)
ABLE-3B (Electra)	Jul 6-Aug 15, 1990	Singh et al. (1994); Andronache et al. (1994); Harris et al. (1994)
ELCHEM (Sabreliner)	Jul 27-Aug 22, 1989	Ridley et al. (1994)

Table 2.5: Campaign data used for the model evaluation, as compiled by Emmons et al. (2000)

- Surface measurements : A large number of surface observations has been collected by von Kuhlmann et al. (2003b) from literature (Solberg et al., 1996; Lindskog and Moldanová, 1994; Bottenheim and Shepherd, 1995; Goldan et al., 1995; Wang et al., 1998a; Greenberg et al., 1996; Touaty et al., 1996; Rudolph et al., 1989; Clarkson et al., 1997). Climatologies for different tracers have been obtained from these measurements (C_2H_4, C_2H_6, C_3H_6, C_3H_8, CH_3CHO, CH_3COCH_3, HCHO, PAN).

  A specific dataset of surface measurements is provided by the **N**ational **O**ceanic and **A**tmospheric **A**dministration **C**limate **M**onitoring **D**iagnostic **L**aboratory (**NOAA/CMDL**[6], Novelli et al. (1998)). The **NOAA/CMDL** has maintained a network of sites from which samples of air are collected in flasks and shipped to a central laboratory in Boulder for analysis (Lang et al., 1992; Novelli et al., 1992; Conway et al., 1994). The CO measurements cover the period from 1988 to present day, at 50

---

[3] **G**lobal **T**ropospheric **E**xperiment (**GTE**), is a project sponsored by the **N**ational **A**eronautics and **S**pace **A**dministration (**NASA**)

[4] The **NASA** **U**pper **A**tmosphere **R**esearch **P**rogram (**UARP**)

[5] The **N**ation **C**enter for **A**tmospheric **R**esearch (**NCAR**) is an **N**ational **S**cience **F**oundation (**NFS**) funded organisation

[6] http://www.cmdl.noaa.gov/

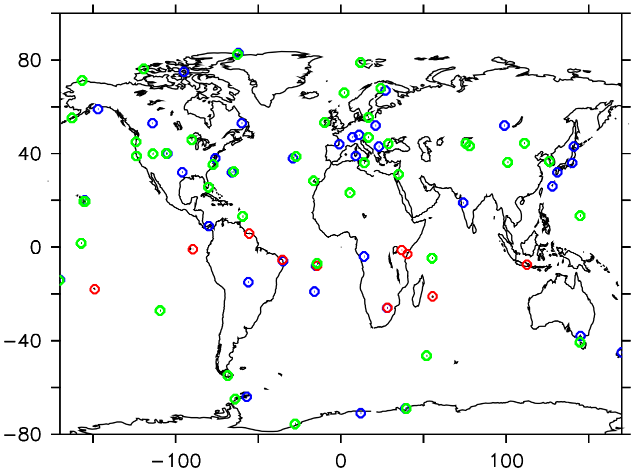

Figure 2.2: Locations of the measurements. Blue circles denote measurements from the LOGAN dataset, red circles from the SHADOZ dataset and green circles from the NOAA/CMDL dataset.

locations over the globe (from $82°N$ to $90°S$). These sites represent the marine boundary layer, the continental boundary layer and the free troposphere. In Fig. 2.2, the locations of the **NOAA/CMDL** sites are shown as green circles.

In this work, the surface and ozonesonde measurements are compared with 7 year climatological monthly averages of the model results, the aircraft observations are compared *only* with the year 2000 of the model results. The year 2000 has been chosen because the anthropogenic emissions (see Sect. 2.1.2.5) have been calculated specifically for this year, and it should hence be the optimum simulated year. The NOAA/CMDL flask measurements, finally, are compared with the corresponding monthly averages of the model results.

2.3 Evaluation of the model

2.3.1 Ozone (O_3)

2.3.1.1 Vertical profiles

The vertical profiles of ozone obtained from the Logan dataset are well reproduced by the model. In Figs. 2.3 and 2.4 model results and measurements are shown.

The model simulates the shape and magnitude of the observed vertical distribution of ozone. The correlation between model results and observations is very high at all the locations, with a linear correlation coefficient R higher than 0.9. Moreover, no bias between the model results and the observations is evident; for example in Boulder, the model simulation overestimates the observations at certain altitudes and underestimates at others. In some cases (Hilo station) the model is able to reproduce also the variability present in the observations. The uncertainties of the measurements (combination of instrumental error and variance of the measurements) generally encompasses discrepancies between the model simulation and the observations. However, from Figs. 2.3 and 2.4, at 400hPa the model seems to present the highest deviations from the observed values and a more detailed comparison will be conducted in Sect. 2.3.1.2.

Compared with the **SHADOZ** dataset (see Figs. 2.5 2.6), the model reproduces the observed vertical profile, with a very high correlation (correlation coefficient R higher than 0.9). Also here no bias can be noticed between the reference simulation *S1* and the observations.

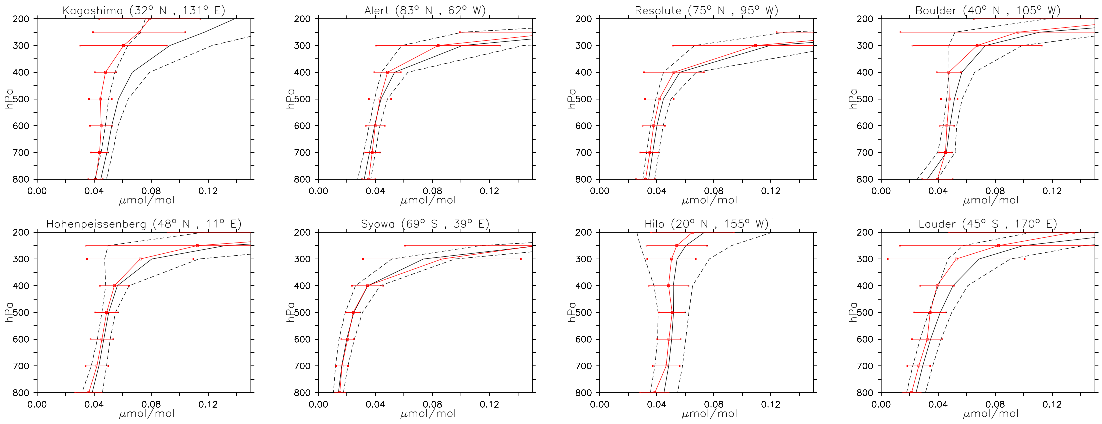

Figure 2.3: Vertical profiles of ozone in January in the troposphere for some selected stations in $\mu\mathrm{mol/mol}$ (Logan dataset). The line is the model simulation and the squares the observations. The dashed lines show the model standard deviations, and the bars the observed standard deviations.

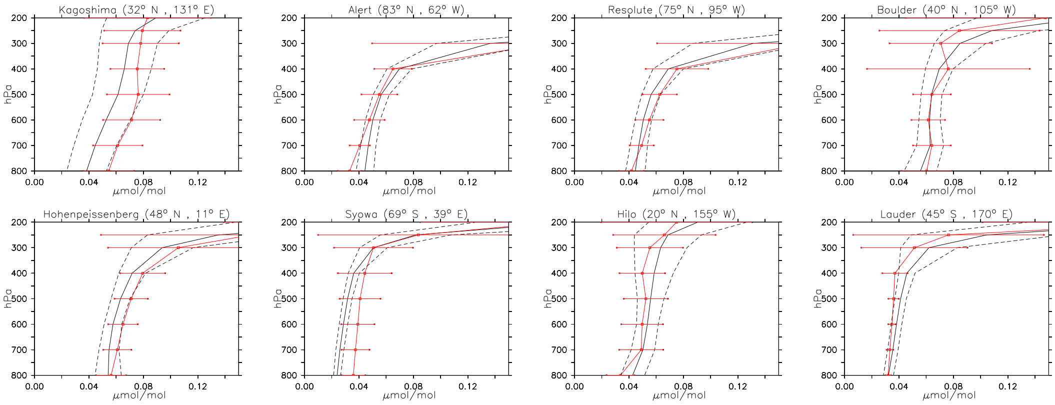

Figure 2.4: Vertical profiles of ozone in July in the troposphere for some selected stations in $\mu\mathrm{mol/mol}$ (Logan dataset). Symbols as in Fig.2.3

2.3.1.2 Seasonal cycle

In Figs. 2.7, 2.8 and 2.9, the comparisons between model results and observations (from the Logan dataset) are presented for different pressure levels (200, 400 and 600 hPa). As mentioned in Sect. 2.3.1.1, the model has difficulties in reproducing the observed mixing ratio of ozone at an altitude of ≈ 400 hPa. In few locations at this altitude (Kagoshima, Alert and Hohenpeissenberg, Fig. 2.8) the model is not able to reproduce

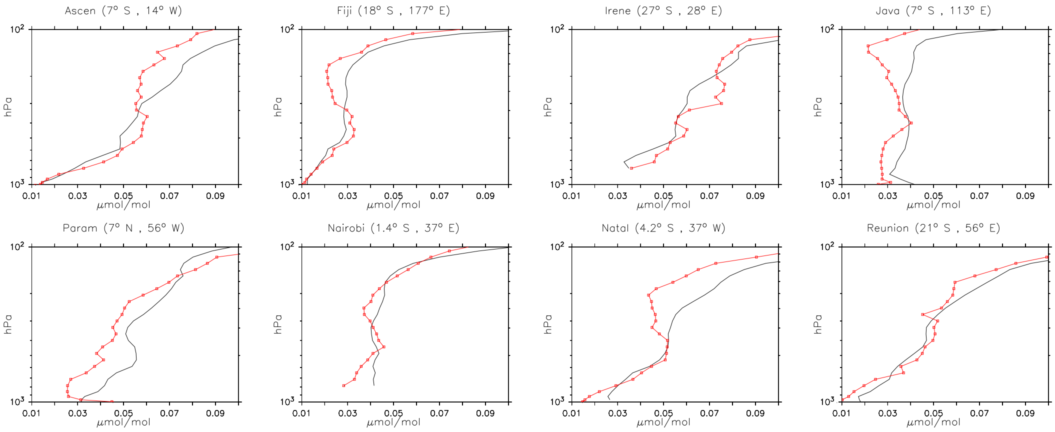

Figure 2.5: Ozone vertical profile in January for some selected region in µmol/mol. The line is the model, squares the observed values (SHADOZ database).

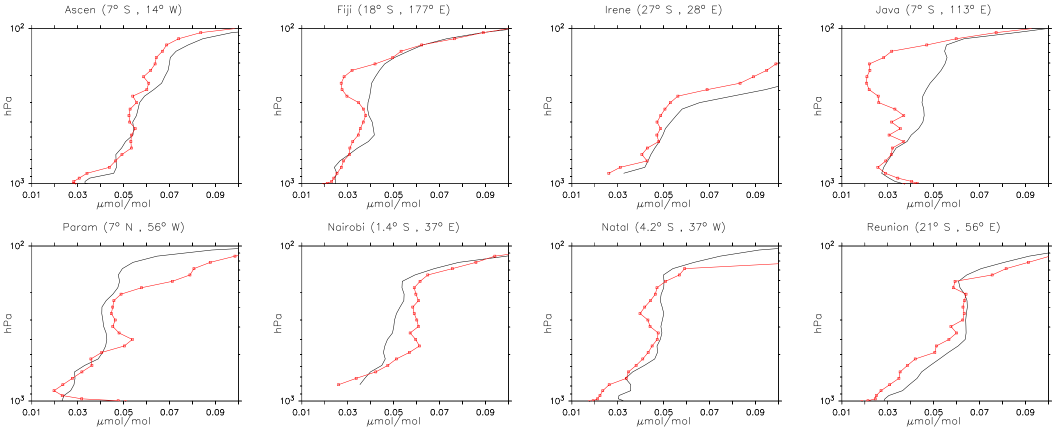

Figure 2.6: Ozone vertical profile in June for some selected region in µmol/mol. Black is the model, red squares the observed values (SHADOZ database).

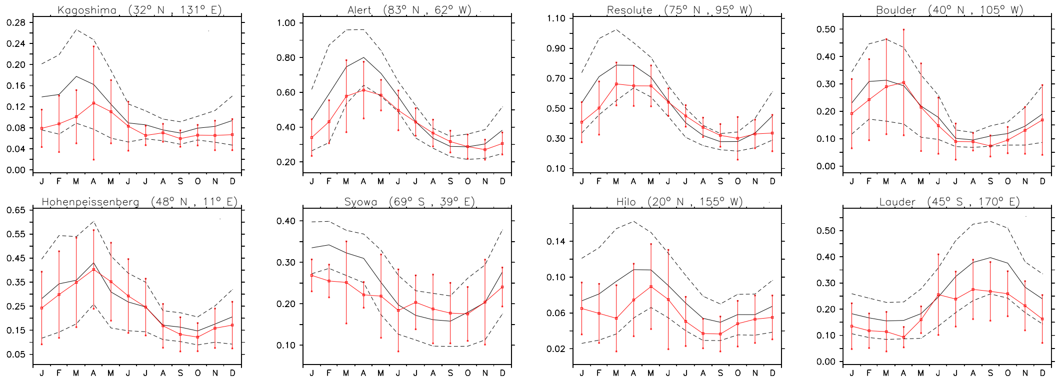

Figure 2.7: Comparison of simulated and observed O_3 mixing ratios in $\mathrm{nmol/mol}$ at 200 hPa (near tropopause), for some selected locations (Logan dataset). Symbol as in Fig.2.3

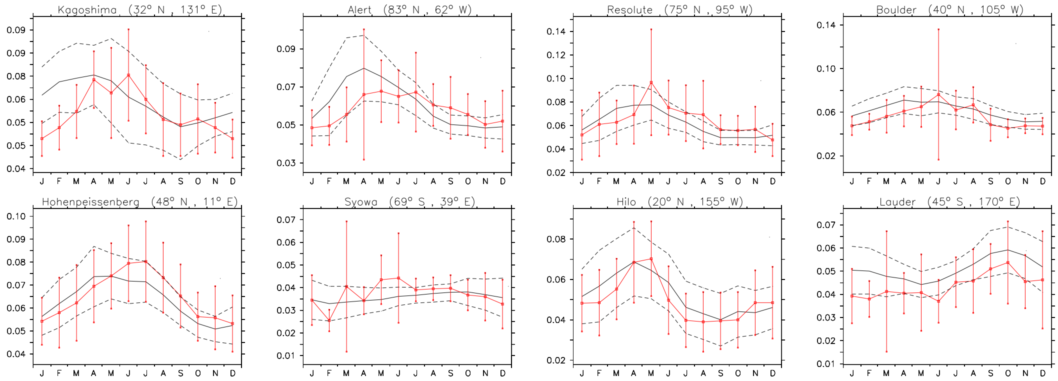

Figure 2.8: Comparison of simulated and observed O_3 mixing ratios in $\mathrm{nmol/mol}$ at 400 hPa (troposphere), for some selected locations (Logan dataset). Symbol as in Fig.2.3

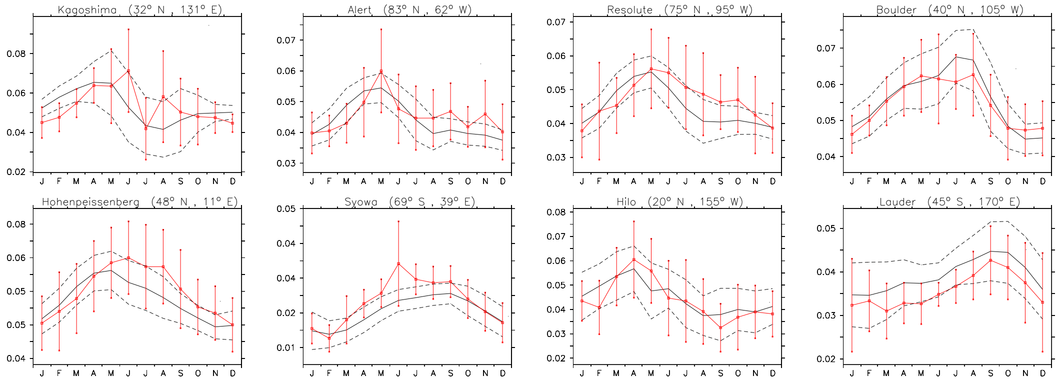

Figure 2.9: Comparison of simulated and observed O_3 mixing ratios in $\mathrm{nmol/mol}$ at 600 hPa (troposphere), for some selected locations (Logan dataset). Symbol as in Fig.2.3

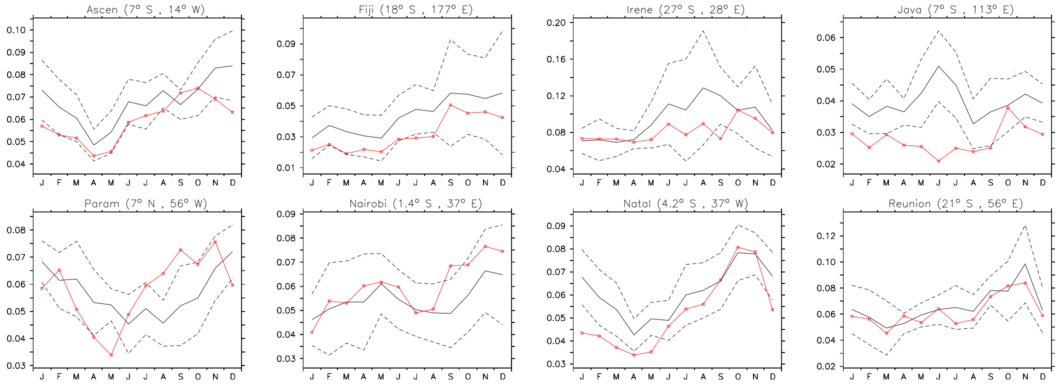

Figure 2.10: Comparison of simulated and observed O_3 mixing ratios in $\mathrm{nmol/mol}$ at 200 hPa, for some selected locations (SHADOZ dataset). The line is the model, squares the observed values and the dashed lines the model standard deviation w.r.t the monthly average.

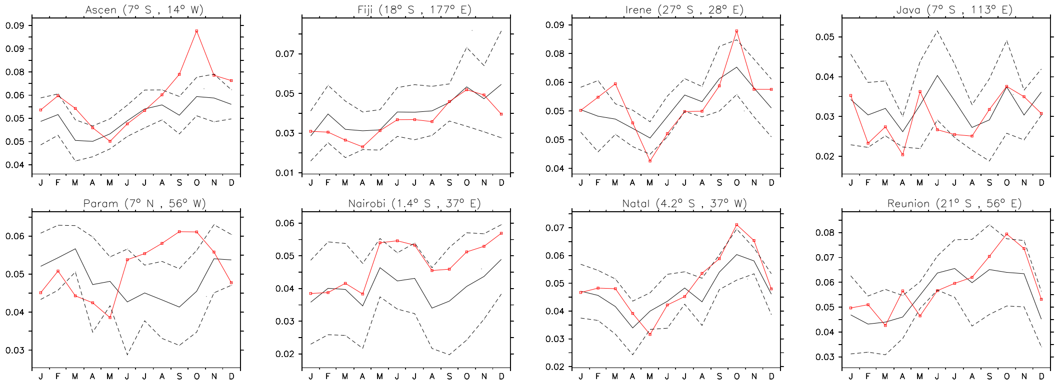

Figure 2.11: Comparison of simulated (black) and observed (red) O_3 mixing ratios in $\mathrm{nmol/mol}$ at 400 hPa, for some selected locations (SHADOZ dataset). Symbol as in Fig2.10

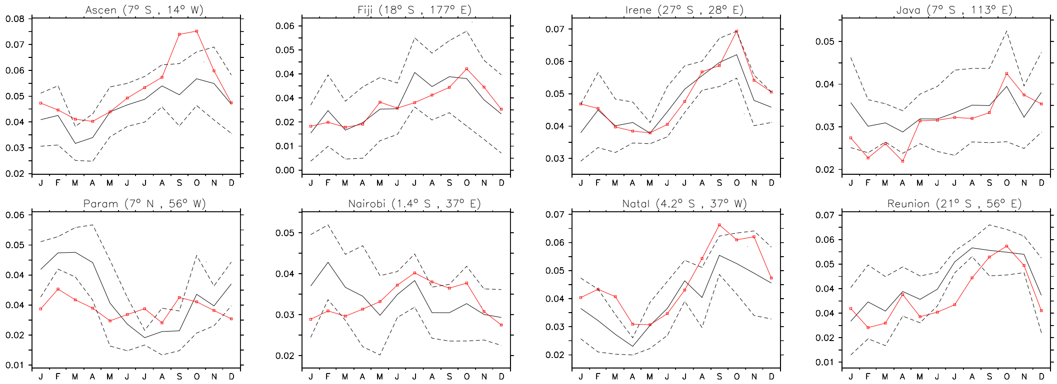

Figure 2.12: Comparison of simulated (black) and observed (red) O_3 mixing ratios in $\mathrm{nmol/mol}$ at 600 hPa, for some selected locations (SHADOZ dataset). Symbol as in Fig2.10

correctly the phase of the seasonal cycle, which is however reproduced at 200 hPa (Fig. 2.7). Moreover, while at 200 hPa a model overestimation of the ozone mixing ratios with respect to the observations is present, at 600 hPa no systematic bias can be observed, and the model reproduces the observed climatology .

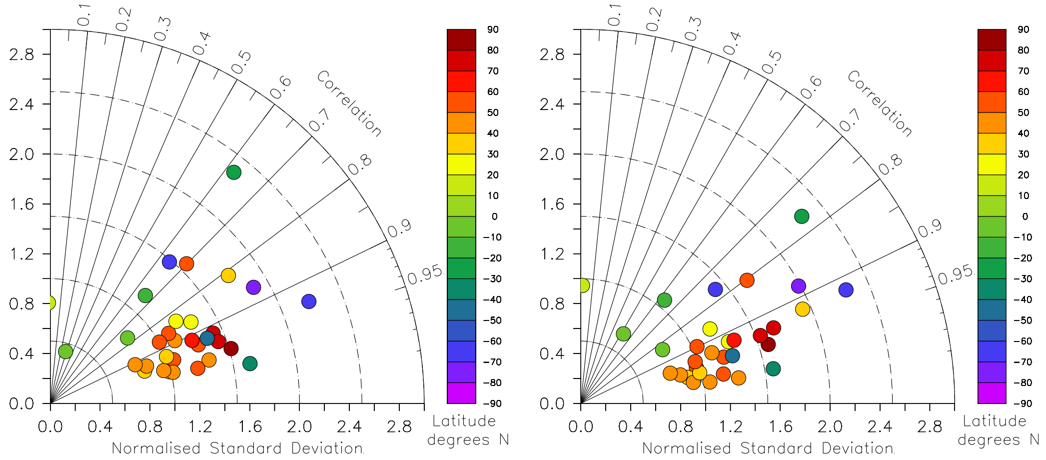

Figure 2.13: Taylor diagrams for O_3 at 200 hPa based on the Logan dataset and the 7-year climatology calculated from the reference simulation *S1*. LEFT: Taylor diagram with no uncertainties weighting RIGHT: Taylor diagram with uncertainties weighting (see Appendix A)

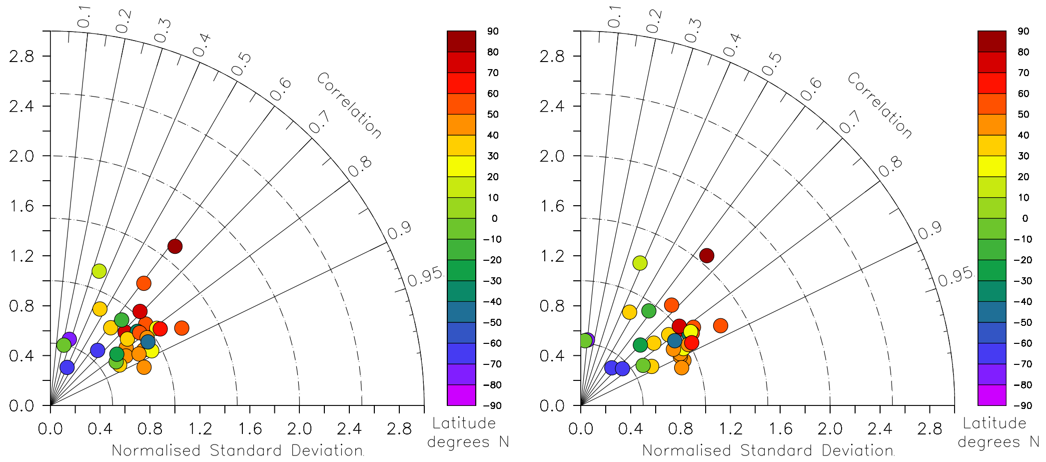

Figure 2.14: Taylor diagrams for O_3 at 400 hPa based on the Logan dataset and the 7-year climatology calculated from the reference simulation *S1*. LEFT: Taylor diagram with no uncertainties weighting RIGHT:Taylor diagram with uncertainties weighting (see Appendix A)

To combine and summarise all these findings, Taylor diagrams are presented in Figs. 2.13, 2.14 and 2.15 (left). A Taylor diagram shows the correlation between model results and observations (R) as the angle. The standard deviation of the model results normalised to the standard deviation of the observations ($\sigma_{model}/\sigma_{obs}$) is displayed in the radial direction. The observations are located at correlation 1 and nor-

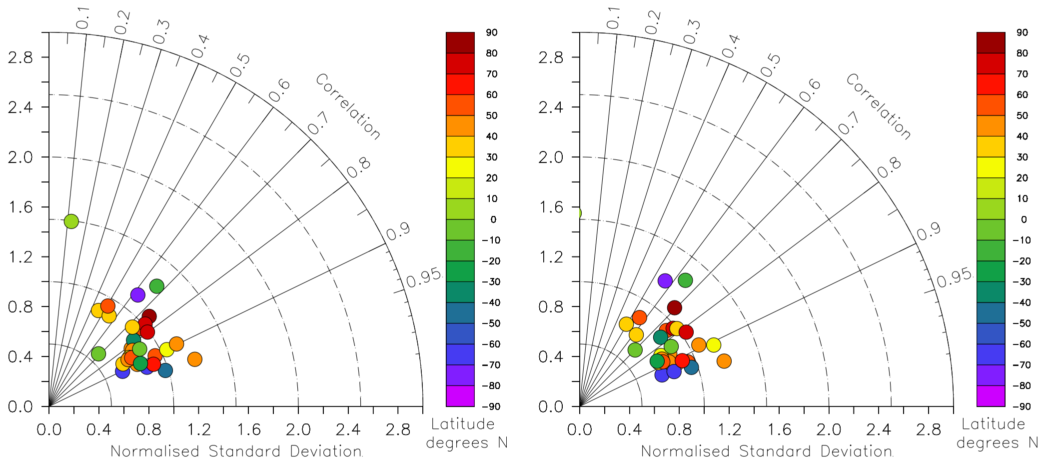

Figure 2.15: Taylor diagrams for O_3 at 600 hPa based on the Logan dataset and the 7-year climatology calculated from the reference simulation *S1*. LEFT: Taylor diagram with no uncertainties weighting RIGHT:Taylor diagram with uncertainties weighting (see Appendix A)

malised standard deviation of 1. The model is expected to be as close as possible to this "ideal" point. We refer to Taylor (2001) and the Appendix A for an extensive explanation of this diagram.

In the troposphere the (linear) correlation coefficient between model results and observations is generally higher than 0.7. The improvements of the *ECHAM5/MESSy1* model with respect to other models, where boundary conditions are prescribed either for troposphere or stratosphere, can be seen in Fig. 2.13 (left), where the Taylor diagram is presented for an altitude of 200 hPa (i.e. near the tropopause). The representation of the **S**tratosphere-to-**T**roposphere **E**xchange (**STE**) (Holton et al., 1995) is generally very difficult. In *ECHAM5/MESSy1* , the model results show a high correlation with the observations at almost all locations. The simulated mixing ratios of ozone correlate very well with observations in the extratropics ($R > 0.9$), indicating a realistic simulation of **STE**. The few sites which show poorer correlations between model results and observations ($R < 0.8$) are almost all located in the tropics; this could be related to a weakness in the representation of convection, which strongly influences the gas mixing ratio at these latitudes.

The figures also present Taylor diagrams for which the values have been weighted by their uncertainties (see Appendix A). In this case the correlations remain very high, indicating that the model results are generally inside the measurement uncertainties. Near the tropopause (at 200 hPa) the weighted correlations are generally higher than the correlations, although the points with lower correlation remain uncorrelated. The model variability and/or the measurement uncertainties can hence explain almost all the discrepancies. Finally, in the free troposphere (600 hPa), the points in the "uncertainties weighted diagram" are clustering around the normalised standard deviation of 1 with higher correlations than the unweighed calculations. This implies that the model reproduces in a satisfactory way the amplitude of the seasonal cycle of ozone at this level.

2.3.2 Aircraft and station measurements : general overview

A general overview of the model performance for the troposphere is obtained using the aircraft observations. In Tab. 2.6 the comparison between model results and aircraft observations is summarised. The Taylor diagram contained in the same table condenses graphically the same informations.

Using the approach explained in Appendix A, for further analysis, correlations and biases are recalculated using an "uncertainties" weight, maintaining the relations of the Taylor diagrams (see Tab. 2.7).

tracer	num. obs.	bias	m	b	R^2
C_2H_4	454	- 23.87	0.26	9.975	0.409
C_2H_6	473	- 174.03	0.69	78.692	0.799
C_3H_6	332	- 11.50	0.14	0.267	0.410
C_3H_8	472	- 18.82	0.92	-5.755	0.768
CH_3COCH_3	246	- 376.85	0.42	-28.717	0.385
CH_3OH	116	- 447.82	0.18	255.18	0.313
CH_3OOH	366	- 13.19	0.71	94.598	0.718
HCHO	213	6.41	0.74	55.786	0.631
H_2O_2	411	3.72	0.63	275.81	0.552
HNO_3	416	- 13.05	0.53	63.115	0.337
O_3	506	1835	1.78	-28464	0.544
PAN	395	141.97	0.71	188.99	0.268
CO	456	- 8621.8	0.51	36381	0.633
CH_4	334	-1103.6	0.66	588746	0.808

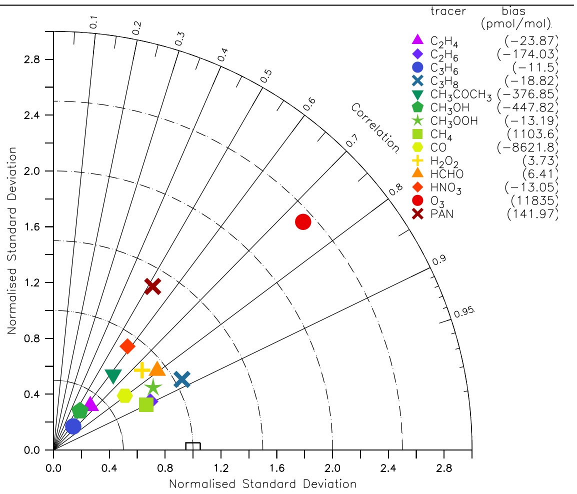

Table 2.6: Summary of the correlation coefficients and the linear regression analysis of the comparison of the model results with aircraft observations (model = m * obs + b). Bias and b coefficient in pmol/mol. Bias = model-observation.

If the weighted bias (Tab. 2.7) for any tracer is lower than one standard deviation (i.e. 1), this implies that the differences between model and measurements are inside the uncertainties, and it can be concluded that the observations are reproduced by the model. Nevertheless, a deeper analysis will be conducted for many tracers included here.

In Fig. 2.7 two trace gases are not shown (due to the very high normalised standard deviation), C_3H_6 and CH_3OH. This implies the inability of the model to reproduce the vertical distribution of these compounds.

On the other hand, the high weighted correlation and the normalised weighted standard deviation of about 1 between model results and measurements for C_3H_8 and H_2O_2, implies a realistic global representation of these tracers by the model.

The same analysis technique is applied to the surface observation database. In this case the good correlation shows that the annual cycle of these tracers is well reproduced, and that the emissions are of the correct magnitude. In Tab. 2.8, some statistical values are given for the comparison between the reference simulation and these measurements.

With the same procedure adopted for the aircraft observations, the statistical analysis (uncertainties weighted) has been repeated, following the method in Appendix A. The results are summarised in Tab. 2.9. Compared to the previously calculated correlation coefficients, the uncertainty weighted correlation coefficients are generally much higher. Although this analysis suggests that the seasonal cycles of the simulated

tracer	num. obs.	bias[a]	bias[b]	R^2
C_2H_4	454	-13.37	-921.3	0.624
C_2H_6	473	-0.76	-196.57	0.948
C_3H_6	332	-4818.8	-78982	0.996
C_3H_8	472	-0.49	-55.21	0.985
CH_3COCH_3	246	-3.46	-648.6	0.767
CH_3OH	116	-2.03	-724.54	0.599
CH_3OOH	366	0.05	10.72	0.941
HCHO	213	0.20	32.00	0.760
H_2O_2	411	0.07	36.977	0.944
HNO_3	416	-0.15	-28.12	0.767
O_3	506	0.14	3141.2	0.487
PAN	395	1.17	205.08	0.999
CO	456	-0.10	-2692.2	0.818
CH_4	334	-0.74	-11117	0.810

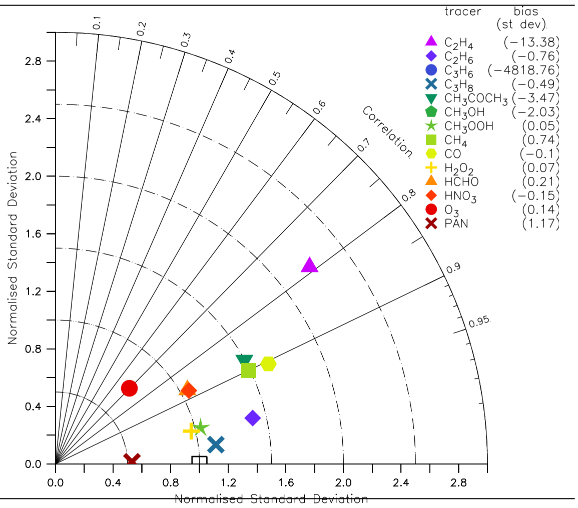

---

[a] in standard deviation units

[b] in pmol/mol (see Appendix A, Eq. A.21)

Table 2.7: Summary of the correlation coefficients and the linear regression analysis of the comparison of the model results with aircraft observations. The values have been weighted with their uncertainties (see Appendix A).

tracer	num. obs.	bias	m	b	R^2
C_2H_4	138	0.204	0.534	0.504	0.396
C_2H_6	150	0.243	0.828	0.544	0.539
C_3H_6	137	0.011	0.658	0.060	0.502
C_3H_8	150	0.607	1.130	0.508	0.424
CH_3CHO	77	0.147	0.197	0.582	0.082
CH_3COCH_3	81	- 0.078	0.528	0.459	0.508
HCHO	65	- 0.109	0.470	0.494	0.553
PAN	48	0.342	1.809	0.190	0.538
CO[a]	4224	5.675	0.976	6.499	0.672

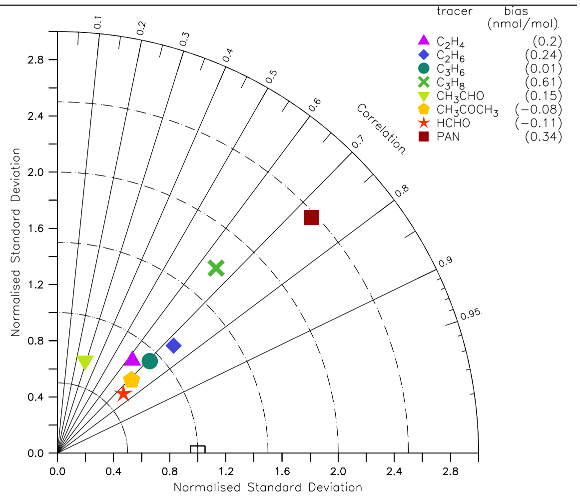

---

[a] from NOAA flask network (see Sect. 2.3.3)

Table 2.8: Summary of the correlation coefficients and the linear regression analysis of the comparison of the model results with surface station observations (model = m * obs + b). Bias and b coefficient in nmol/mol. Bias = model-observation.

trace gas concentrations at the surface (and hence most probably the emissions) are correct, a careful analysis has to be performed. In fact, some of these measurements have been performed in polluted regions with very strong influences of local sources. These cases are very difficult to predict with a global model, and the increase in the correlations could be due to the high variability of the model results (or of the observations) at these locations. A more precise analysis has hence to be conducted, comparing also graphically the simulated with the observed mixing ratios. Nevertheless, alkenes (C_2H_4 and C_3H_6) and PAN are trace gases in the model with significant biases (i.e., exceeding 1 standard deviation in Tab. 2.9) . Hence (with the exception of the mentioned tracers) the reference simulation *S1* reproduces the main feature of these tracers at the surface. A more detailed comparison will follow.

tracer	num. obs.	bias[a]	bias[b]	R^2
C_2H_4	138	2.672	0.342	0.986
C_2H_6	150	- 0.224	- 0.043	0.996
C_3H_6	137	- 6.182	- 0.149	0.890
C_3H_8	150	- 0.167	- 0.031	0.999
CH_3CHO	77	0.760	0.080	0.298
CH_3COCH_3	81	- 1.012	- 0.106	0.737
HCHO	65	- 0.929	- 0.125	0.898
PAN	48	5.199	0.381	0.891

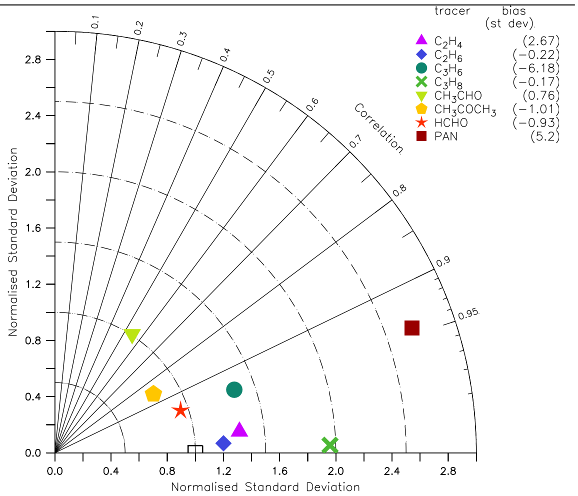

---

[a] in standard deviation units

[b] indicative in nmol/mol (see Appendix A, Eq. A.21)

Table 2.9: Summary of the correlation coefficients and the linear regression analysis of the comparison of the model results with surface station observations. The values have been weighted with their uncertainties (see Appendix A).

2.3.3 Carbon monoxide (CO)

As mentioned in Sect. 1.1.2, carbon monoxide provides the most important sink for OH (Lelieveld et al., 2002; Logan et al., 1981; Thompson, 1992). A correct simulation of this tracer is very important for studies of atmospheric oxidants. The emissions of CO applied in the present simulation have been described by Ganzeveld et al. (2006, and references therein). There are large uncertainties with respect to the amount of CO globally lost by dry deposition (e.g., $115 - 230$ Tg/yr (Sanhueza et al., 1998), 540 ± 430 Tg/yr (Moxley and Cape, 1997), 150 Tg/yr (von Kuhlmann et al., 2003b)). In a recent study Horowitz et al. (2003) estimated the global dry deposition of CO to be only around 2 Tg/yr. Following this study, in the reference simulation *S1*, the dry deposition of CO was switched off. Although the simulated CO will be influenced by taking into account the process of dry deposition, the effect is potentially significant for the budget only in very remote regions.

Thanks to the large dataset of CO observations available from the **NOAA/CMDL** (see Sect. 2.2) network, a more detailed analysis is possible for CO than for the other studied trace gases. This allows the direct comparison of 7 years (1998-2004) of monthly averages model results with the corresponding observations.

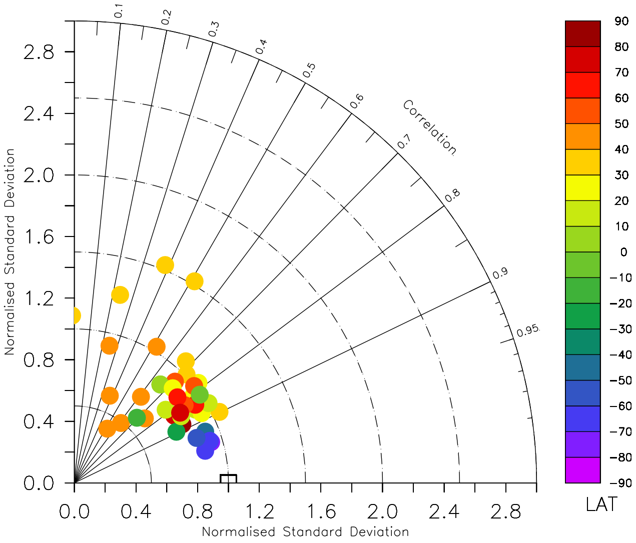

Figure 2.16: Taylor diagram comparing 7 year (1998-2004) monthly averages of CO from the model simulation with the surface observations from the **NOAA/CMDL** network (Novelli et al., 1998). The colour code denotes the geographic latitude.

It cannot be expected that the model simulation fully reproduces the inter-annual variability due to the prescribed climatological emissions for the year 2000. Nevertheless, the meteorological inter-annual variability is included through the applied nudging procedure.

The correlation between the model results and the observations is generally good (see Sect. 2.3.2) with $R^2 = 0.67$. However, thanks to the data coverage, a deeper analysis is possible to assess the quality of the simulation.

Fig. 2.17 shows the time series of observed and simulated CO mixing ratios at some selected locations.

The observed mixing ratios of CO are in some cases very well reproduced, (as example at Alert, Greenland (ALT), South Hampton, Bermuda (BMW) and Manua Loa, Hawaii (MLO)); at these locations there is a very good agreement not only with respect to the amplitude of the seasonal cycle, but also with respect to the absolute values. However, not at all locations the model results agree in the same way with the observations, although the seasonal cycle of CO is generally well simulated.

This conclusion is confirmed by the Taylor diagram in Fig. 2.16, where the high correlations of the measurements with the model results are summarised. The remote locations (south of $60°$ S) are highly correlated ($R \approx 0.9$) indicating that the main processes regulating this tracer are well represented in the model. However, locations between $20°$ N and $40°$ N are poorly correlated, due to the influence of local emissions in industrialized regions.

As pointed out by Haas-Laursea and Hartley (1997), the flask samples have been generally collected under non-polluted conditions, i.e., for stations close to local sources only certain wind directions have been

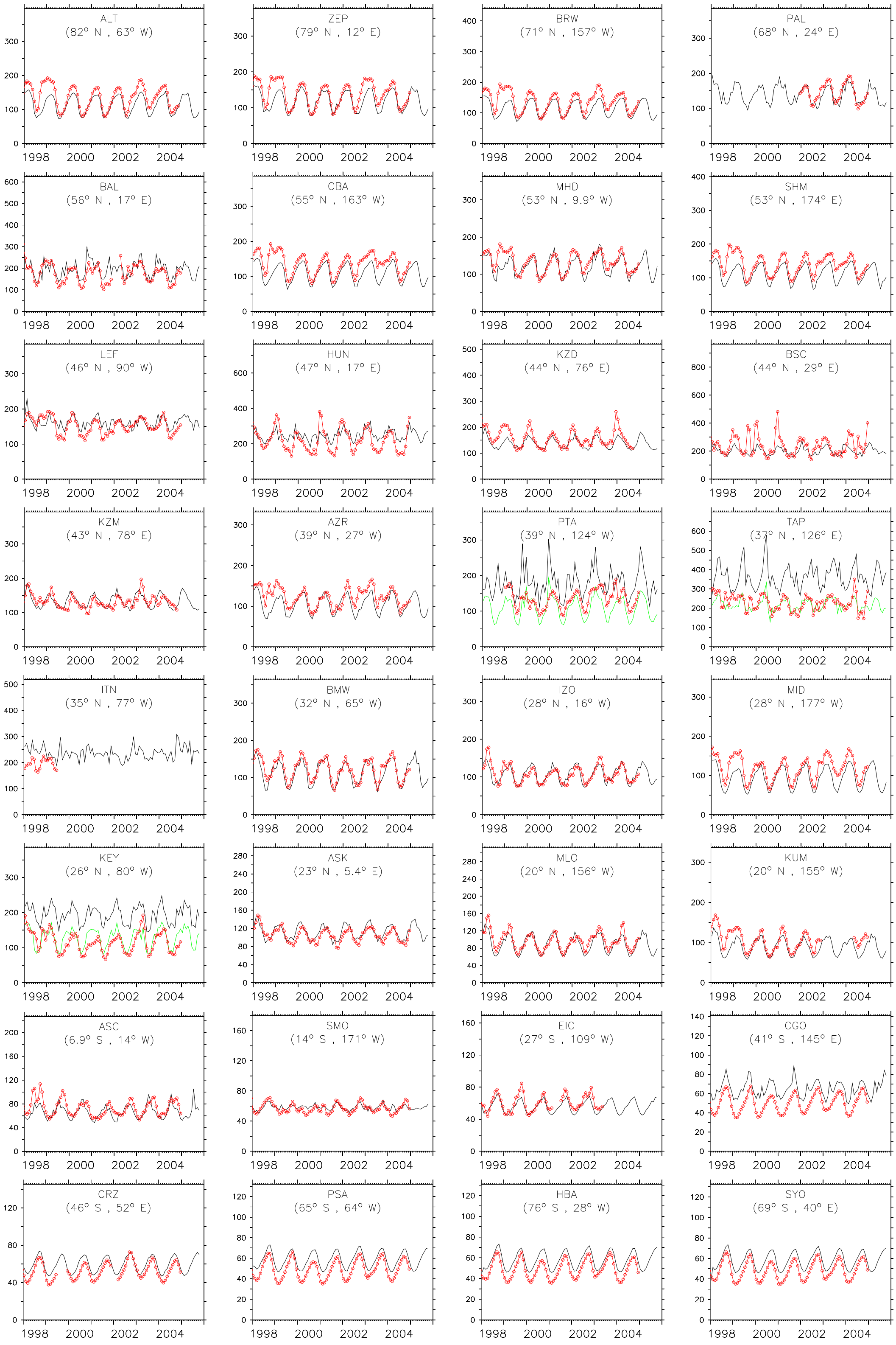

Figure 2.17: Comparison of simulated (black) and observed (red, Novelli et al. (1998)) CO mixing ratios in $\mathrm{nmol/mol}$ (ordered by latitude). The green lines show the model results sampled from the corresponding upwind grid-boxes (see text).

selected to avoid local contamination. The model results are not filtered in the same way, and at the rather low model grid resolution, local sources are sometimes located in the same grid box as the measurement station. Therefore, the simulated mixing ratios are potentially higher than the observed. For some specific cases (i.e. PTA, Point Arena, California U.S.A. , KEY, Florida, U.S.A. and TAP, Tae-ahn Peninsula, Korea), if the model results are sampled one grid-box upwind of the polluted locations, the correlation between model results and observations increases drastically and the overestimation by the model almost disappears (Fig. 2.17, green lines).

Although the amplitude of seasonal cycle is well reproduced, the model tends to underestimate its amplitude (see Fig. 2.16, standard deviation ≤ 1). In the Northern Hemisphere (NH) (e.g. Zeppelin, ZEP or Alert, Greenland, ALT) the maximum during winter seems to be systematically underestimated. More generally, the model tends to underestimate CO with respect to observations in *remote* regions in the NH. This is probably due to underestimated anthropogenic emissions, which influence the background concentration in the NH. In the simulation, as shown in Table 2.10, emissions due to fossil fuel usage are at the lower end of literature estimates, and around 25% lower than used in several other models.

	Brasseur et al. (1998)	Bey et al. (2001)	von Kuhlmann et al. (2003a)	Park et al. (2004a)	this work	range[a]
Fossil fuel	281	388	400	384	281	300-600
Biomass burning	661	522	748	746	702	300-900
Total	1218	1043	1261	1131	1096	656-1730

[a] from Bates et al. (1995)

Table 2.10: Different estimates of CO emissions in Tg/yr.

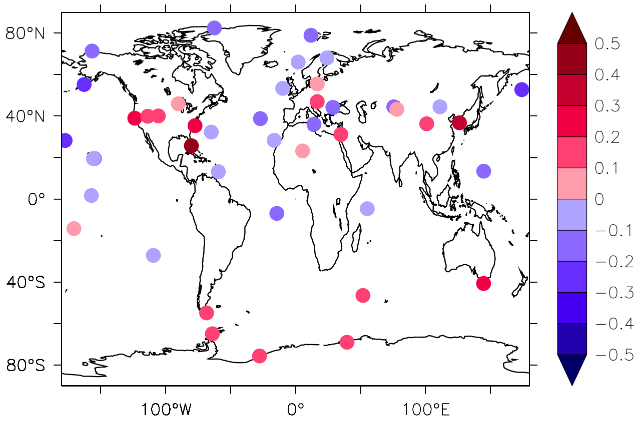

Figure 2.18: Relative differences of 7 year averaged CO between model and measurements ((mod-obs)/mod).

In the SH the model simulation produces higher mixing ratios of CO than observed (Fig. 2.18). This is particularly evident for locations south of 50°S. This significant bias is especially visible in Fig. 2.17, Palmer station, South Pole (PSA) and Halley Bay, Antarctic (HBA). This discrepancy is present in many other models (Hauglustaine et al., 1998; Wang et al., 1998b; Bey et al., 2001; von Kuhlmann et al., 2003b; Horowitz et al., 2003; Park et al., 2004b; Folberth et al., 2006) and unexplained so far.

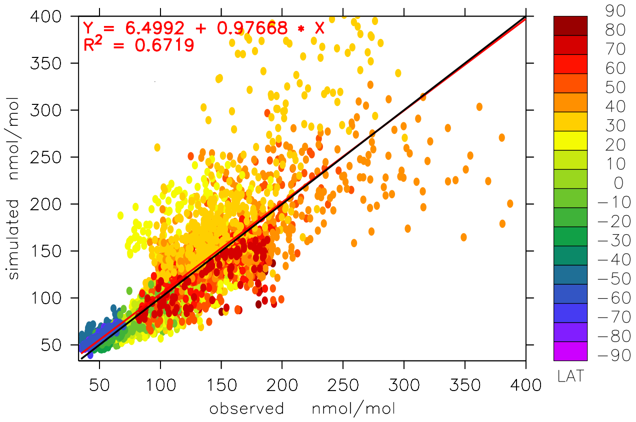

Figure 2.19: Scatter plot of all the measurements (monthly averaged) available from the **NOOA/CMDL** CO measurements database versus the results of *ECHAM5/MESSy1*, monthly averaged at the same locations as the measurements. The color code denotes the latitude of the sampling station.

The results obtained for CO from the analysis of the **NOAA/CMDL** database are summarized in Fig. 2.19. A general underestimation of the model for latitudes north of 60° N (red color) and an overestimation for latitudes between 20° and 50° N (orange) is apparent. At the same time, a general overestimation of the lower values (located south of 60° S, blue and violet) is present.

The correlation of the model results with aircraft observations is rather good ($R^2 \approx 0.6$, see Tab. 2.6) which means that the vertical profiles of CO are generally reproduced.

The hypothesis about underestimated emissions in polluted regions (i.e., primarily from fossil fuel usage) is supported by the analysis of the vertical profiles from the aircraft observations. Fig. 2.20 (TRACE-P, China or PEM-WEST-B, China) shows that CO is clearly underestimated near China, especially in the planetary boundary layer, where the influence of the emissions is largest. This underestimation is also present further downwind (PEM-WEST-B, Philippine Sea, TRACE-P, Guam), however, it almost disappears in the central Pacific region (TRACE-P, Hawaii). Interestingly, the correct representation of carbon monoxide in East Asia is a problem for many atmospheric chemistry models. Kiley et al. (2003) demonstrated that many models are underestimating CO in the western Pacific region. Wang et al. (2004, and references therein) performed an inverse modelling analysis and calculated that an increase of the CO emissions in East Asia of around 45% from the a priori estimate (Streets et al., 2003) is required to match the observations. More recently, Streets et al. (2006) estimated 116 $\mathrm{Tg/yr}$ for the year 2000 and 157 $\mathrm{Tg/yr}$ for the year 2001 of CO emissions from China with an uncertainty of 68 %.

2.3.4 Non Methane Hydrocarbons

Comparison of the simulated non-methane hydrocarbon mixing ratios with observations yields a dual picture (see Sect. 2.3.2). Some of the simulated trace gases are in particularly good agreement with the measurements (e.g., propane (C_3H_8)), while others are largely uncorrelated with measurements (e.g., ethene (C_2H_4) and propene (C_3H_6)). In the case of C_3H_6, the simulation does not reproduce the observed profiles. The simulated values are completely out of range of the observed values, even including measurement

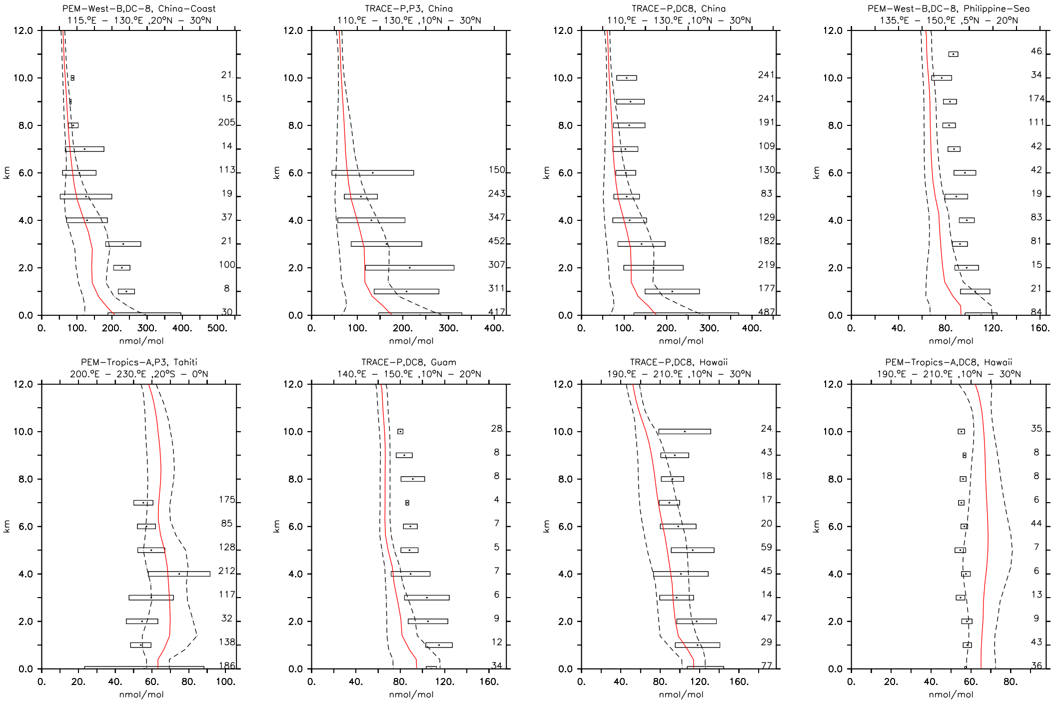

Figure 2.20: Vertical profiles of CO $(\mathrm{nmol/mol})$ for some selected campaigns from Emmons et al. (2000). Asterisks and boxes represent the average and the standard deviation (w.r.t. space and time) of the measurements in the region, respectively. The simulated average is indicated by the continuous line and the corresponding simulated standard deviation w.r.t. time and space by the dashed lines. On the right side the number of measurements is listed.

uncertainties and variability (see bias in Sect. 2.3.2). Moreover, the simulated and observed vertical profiles are uncorrelated (see Fig. 2.7), i.e., the model is unable to reproduce the shape of the profiles.

2.3.4.1 Alkanes (Ethane C_2H_6 and Propane C_3H_8)

Among all considered NMHCs, the alkanes are best reproduced by the model. The overall correlation (see Tab. 2.6) higher than 0.75 indicates a very good agreement between these simulated tracer gases and the respective observations. Tab. 2.7 shows that the model results are well within the range of the measurements.

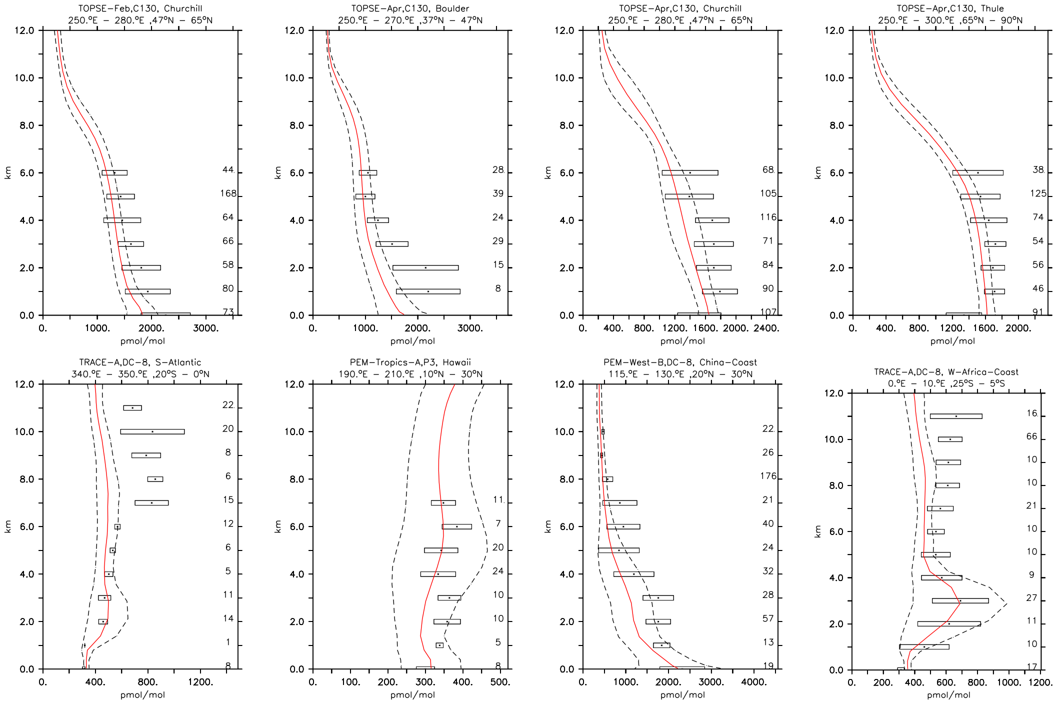

Figure 2.21: Vertical profiles of C_2H_6 (in $\mathrm{pmol/mol}$) for some selected campaigns. Symbols and colours as in Fig. 2.20.

In the case of ethane, the improvement in the results compared to other models is mainly due to different spatial distribution patterns of the emissions. For example, the total emission of C_2H_6 due to biomass burning in *ECHAM5/MESSy1* (Ganzeveld et al., 2006) is about 0.87 $\mathrm{Tg/yr}$ lower than in von Kuhlmann et al. (2003a), and the anthropogenic emissions are about 0.75 $\mathrm{Tg/yr}$ higher. Although the total is essentially unchanged, the different distribution improves the quality of the simulation. A good agreement with aircraft observations is achieved for the TOPSE campaign (Fig. 2.21), even if the model is at the low end of the measurement range. The anthropogenic emissions in the model, in fact, are not sufficient to perfectly match the observed values. This is clearly visible when the model results are compared with surface measurements (Fig. 2.22). An underestimation of ethane by the model at the surface is present in North America (Fraserdale, Lac la Flamme) mainly due to an underestimation of the emissions compiled in the EDGAR database (Jacob et al., 2002; Poisson et al., 2000). Furthermore, the amplitude of the seasonal cycle is not well reproduced at these locations, with problems mainly in reproducing the maximum in winter. The sim-

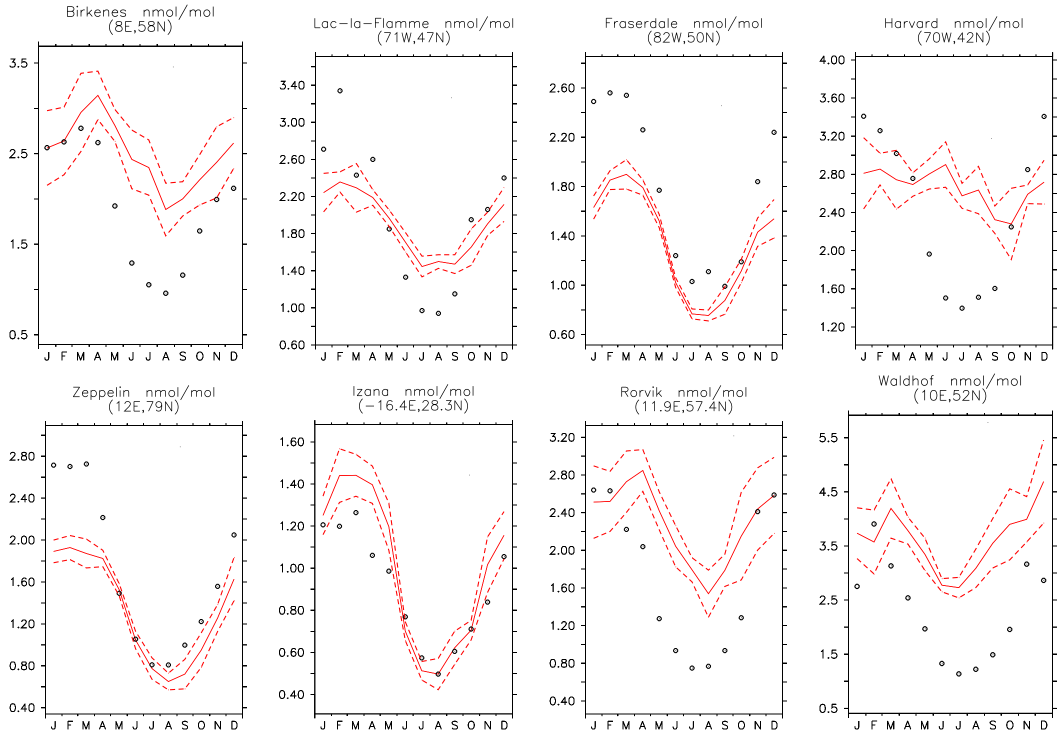

Figure 2.22: Seasonal cycle (monthly averages) of C_2H_6 (in $\mathrm{nmol/mol}$) for some selected locations at the surface (Solberg et al., 1996). Model: continuous line; model standard deviation: dashed line; measurements: circles.

ulation reproduces biomass burning plumes observed in the TRACE-A campaign (African coast, Fig. 2.21). This campaign took place in the dry season of the SH and some flight measurements were influenced by biomass burning. Problems occur in the upper troposphere, where the model underestimates the C_2H_6 mixing ratio by a factor of 2. Pickering et al. (1996) report that convection frequency during this campaign was unusually high, which could explain the disagreement between model results and observations.

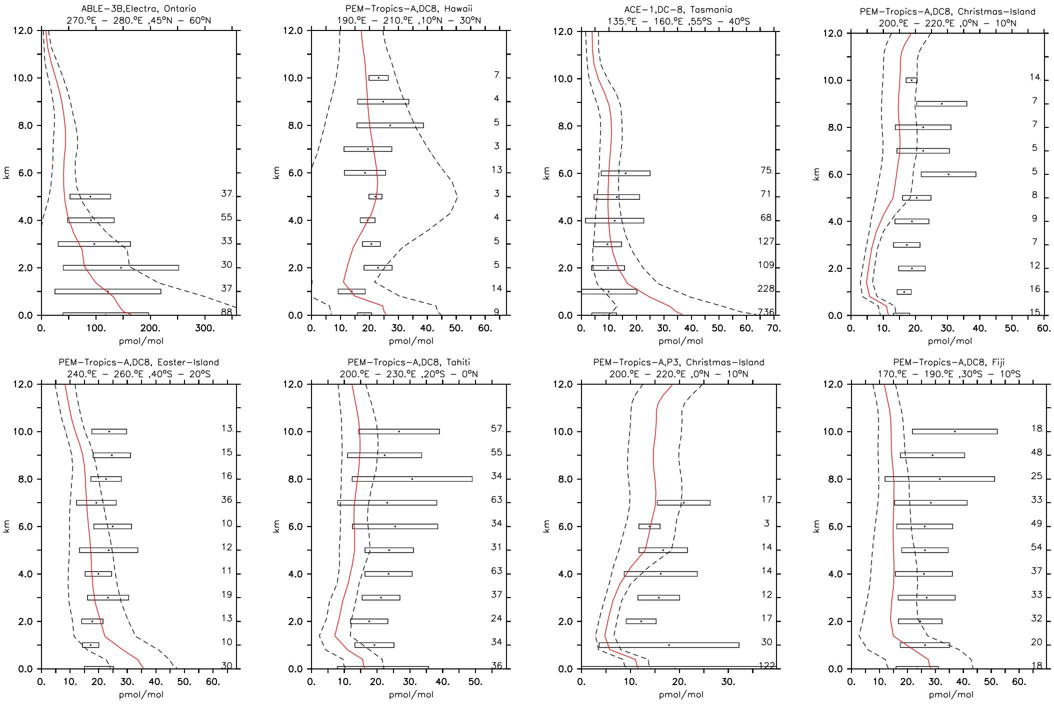

Figure 2.23: Vertical profiles of C_3H_8 (in $\mathrm{pmol/mol}$) for some selected campaigns. Symbols and colours as in Fig. 2.20.

For propane, from Tabs. 2.6 and 2.7 can be inferred that the simulated vertical profiles are in good agreement with the observations (Fig. 2.23). This agreement is mainly achieved by the realistic representation of the emissions. As pointed out by Wang and Zeng (2004), an increase of $14 \pm 5\%$ of the emission inventory used by Bey et al. (2001) ($9.66\ \mathrm{Tg/yr}$) was required to correctly match the observations, for an emission total of $11\ \mathrm{Tg/yr}$. In our simulation the total emission was $11.97\ \mathrm{Tg/yr}$ (see Tab. 2.4). This amount is still lower than suggested values present in literature (e.g., $13.46\ \mathrm{Tg/yr}$ calculated by Jacob et al. (2002)).

However, even though the emissions are in the suggested range, the simulated mixing ratios are at the low end of the measurement range (Fig. 2.23 and Tab. 2.6).

2.3.4.2 Alkenes (Ethene C_2H_4 and Propene C_3H_6)

The alkenes, in contrast to the alkanes, are generally poorly reproduced by the model. The simulated mixing ratios are usually below the measurements (Tab. 2.6).

Modelled ethene (C_2H_4) has a poor correlation, both, with surface and aircraft measurements (Tabs. 2.7 and 2.9). This low correlation is due to an overestimation of the mixing ratio at the surface (Fig. 2.26),

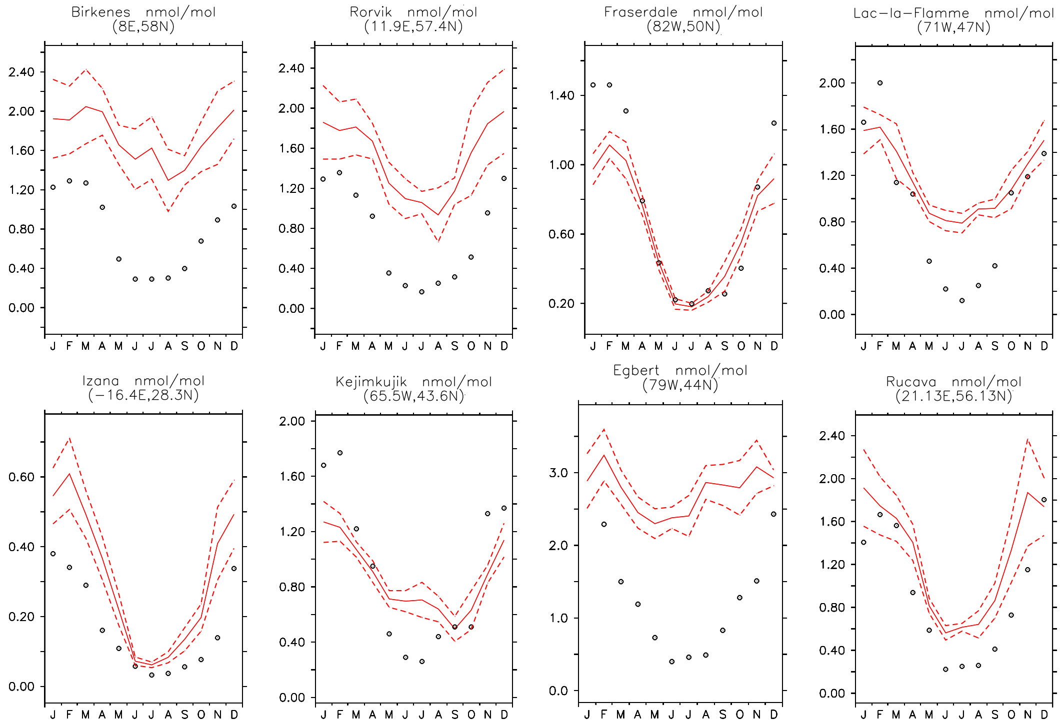

Figure 2.24: Seasonal cycle (monthly averages) of C_3H_8 (in $\mathrm{nmol/mol}$) for some selected locations at the surface (Solberg et al., 1996). Model: red continuous line; model standard deviation: red, dashed line; measurements: dots.

where the seasonal cycle is not reproduced with a peak in the mixing ratio during summer. The vertical profiles (Fig. 2.25) are mostly high biased (e.g., TOPSE-Mar, Boulder), with the largest differences between model results and observations occurring at the surface. In remote regions, where the direct influence of emissions is lower, the model is, nevertheless, at the lower end of the range of observations, with frequent underestimates (TRACE-A, Brazil Coast and South Atlantic).

The emissions from oceans appear too high (see Fig. 2.25, PEM-Tropics-B, Fiji) and a reduction in the model likely improves the simulation of ethene.

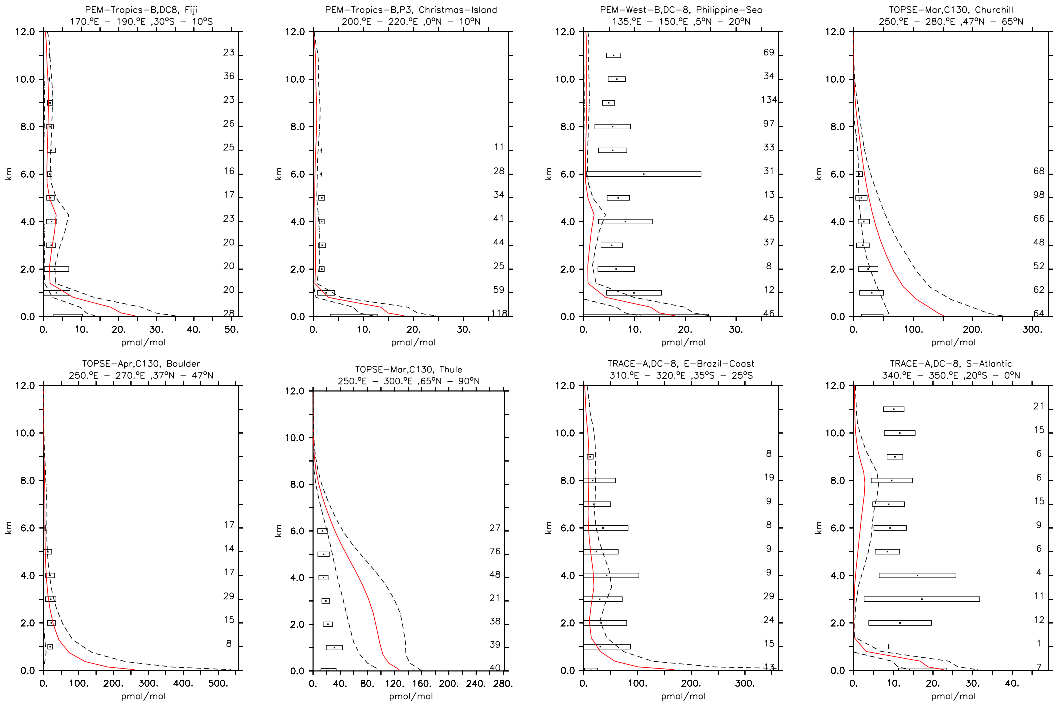

Figure 2.25: Vertical profiles of C_2H_4 (in $\mathrm{pmol/mol}$) for some selected campaigns. Symbols and colours as in Fig. 2.20.

Propene is also not very well simulated by the model. The low correlation (Tab. 2.6) indicates a wrong representation of the vertical profiles. This poor representation cannot be reconciled with the variability of the model or measurement uncertainties, since the bias in Tab. 2.7 is much larger than one standard deviation. From Fig. 2.27, the erroneous description of this trace gas in the model is evident. The very high mixing ratio in the boundary layer (2-3 times the observed one) in open ocean regions (PEM-TROPICS-A, all locations) indicates a too strong emission of this tracer from the ocean. In *ECHAM5/MESSy1* the upper limit of the suggested emission from Bates et al. (1995) has been applied (1.27 $\mathrm{Tg/yr}$).

This overestimation is less evident in continental regions more strongly influenced by anthropogenic (Fig. 2.27, PEM-WEST-B, Japan or Fig. 2.28, Izaña, Lac la Flamme) or biomass burning sources (Fig. 2.27, TRACE-A, West Africa Coast). Fig. 2.27 shows that outside the planetary boundary layer (PBL), above 2-3 km, the simulated tracer is nearly depleted, in contrast to the observations.

This points to a wrong simulation of the sinks (too fast) which could explain the low values simulated outside the PBL. However, large measurements uncertainties cannot be excluded as well for these low

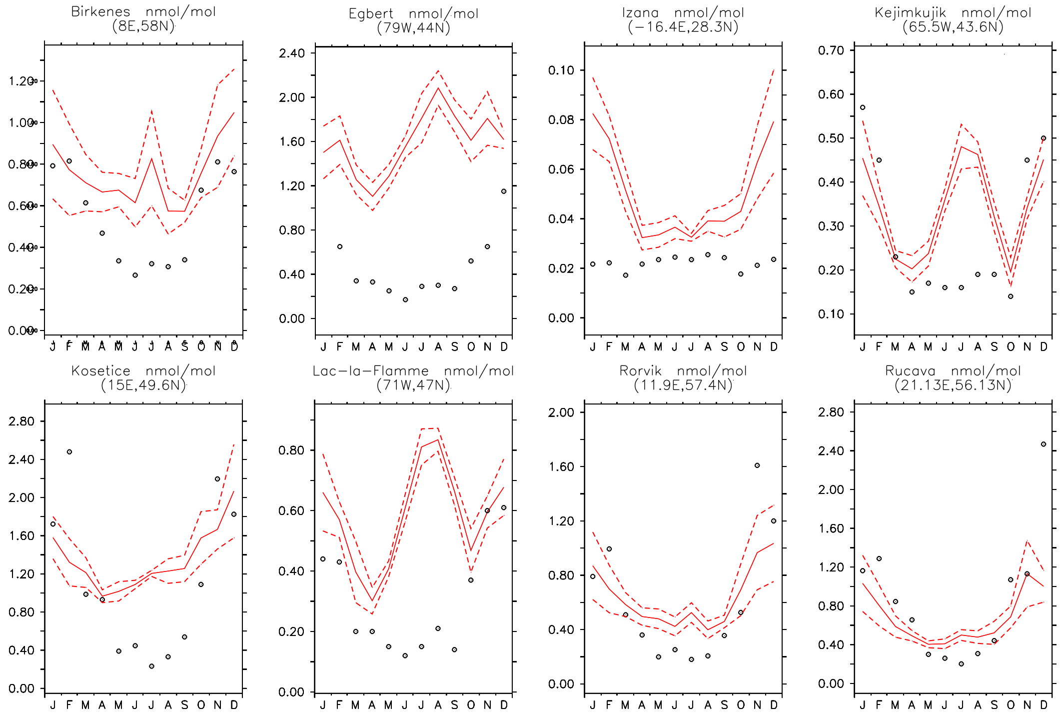

Figure 2.26: As Fig. 2.22, for C_2H_4.

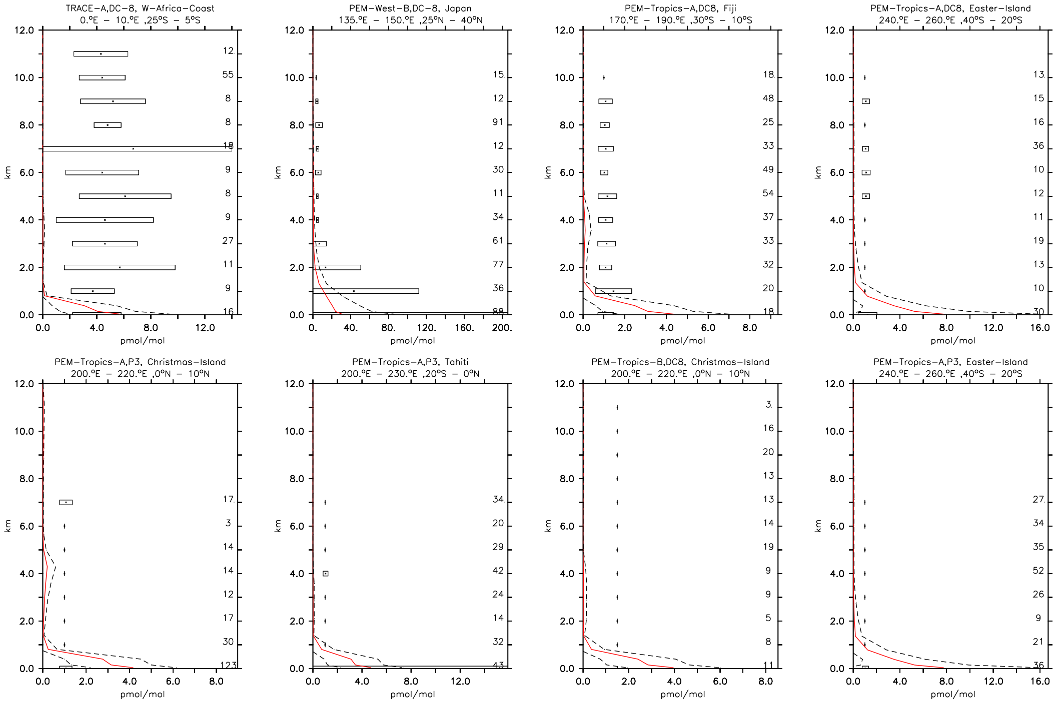

Figure 2.27: Vertical profiles of C_3H_6 (in pmol/mol) for some selected campaigns. Symbols and colours as in Fig. 2.20.

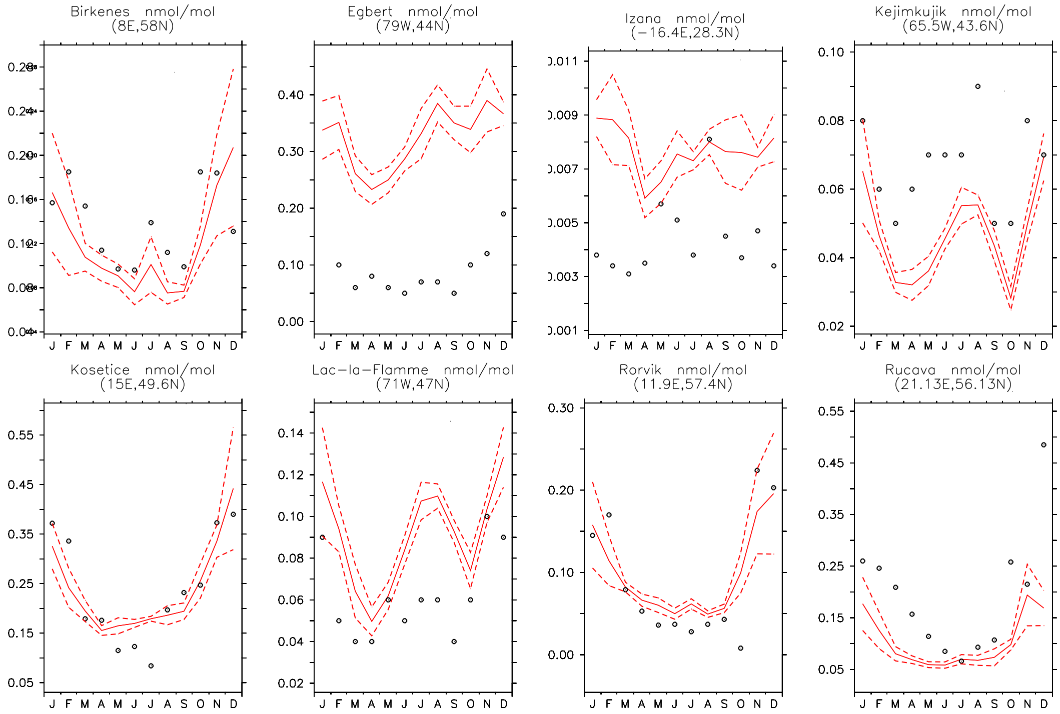

Figure 2.28: As Fig. 2.22, for C_3H_6.

mixing ratios (low ppt range) This tracer is not subject to either wet (due to its low solubility) nor dry deposition and is only removed by the reactions with OH, NO_3, or O_3, the latter two at least two orders of magnitude slower than the first. The rate coefficient used for the reaction C_3H_6 + OH is taken from the IUPAC recommendation of 1999 (Atkinson et al., 1999b, and references therein). The new recommendation suggests a slightly different dependence of the high pressure channel on temperature (Atkinson et al., 2005b; Vakhtin et al., 2003, and references therein). As shown in Fig. 2.29, the new reaction coefficient is lower than the previously estimated. This might explain the strong depletion in the free troposphere of this gas in our simulation, or vice versa, our results indirectly support the revision of the reaction coefficient.

2.3.4.3 Oxygenated compounds

Oxygenated compounds are partly soluble and are influenced by wet deposition (Tost et al., 2006) (e.g. CH_3OOH), as well as oxidation by OH, and some of them by photolysis (HCHO, CH_3CHO, CH_3OOH and CH_3COCH_3). Reproducing the vertical profiles of these tracers is therefore challenging, and the identification of the cause of discrepancies between model results and observations is difficult.

Hydroperoxide, H_2O_2

Hydrogen peroxide is produced by the self reaction of HO_2 and can photolyse to produce OH. Hence it is useful as indicator of HO_x in the troposphere.

As shown in Fig. 2.30, the vertical profiles of H_2O_2 are reasonably well reproduced by the model at different locations and for different field campaigns. Discrepancies from the observations are difficult to

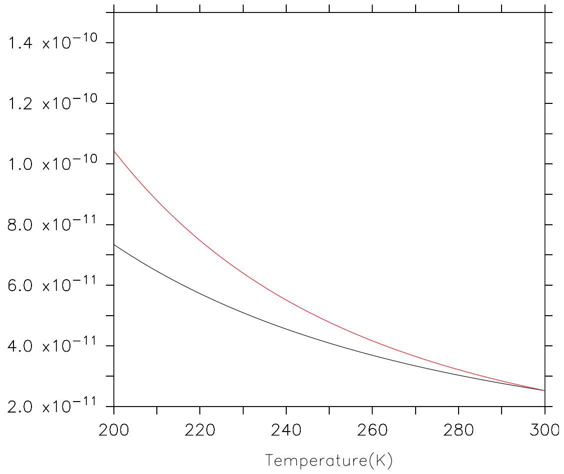

Figure 2.29: Temperature dependence of the reaction coefficient for C_3H_6 + OH (cm^3s^{-1}) according to the IUPAC recommendations (lower line: Atkinson et al. (2005b); upper line: Atkinson et al. (1999b)).

define due to its high variability. In fact, from Tab. 2.7, the correlation (uncertainty weighted calculation) between model results and measurements is very high ($R^2 \approx 0.94$), mainly because the observed H_2O_2 shows a very high variability.

Acetaldehyde, CH_3CHO

This oxygenated compound is produced from the oxidation of a variety of hydrocarbons (Lewis et al., 2005) and it can produce HO_x and PAN precursors.

The analysis shows that the model results agree within a factor of two (overestimation) with the observations, although the seasonal cycle is not well reproduced (Fig. 2.31). This is confirmed by Tab. 2.9, which shows that at the surface the amplitude of the seasonal cycle is correct (if we consider the uncertainties), but with the wrong phase ($R^2 \approx 0.298$).

Only a few aircraft measurements are available of this trace gas. Williams et al. (2001) reported a mixing ratio in Suriname in the boundary layer of about 1.7 $\mathrm{nmol/mol}$ and 0.8 $\mathrm{nmol/mol}$ in the free troposphere. The model underestimates these mixing ratios by a factor of 10. During the PEM-TROPICS-B campaign (Singh et al., 2001) over the open ocean mixing ratios between 60 and 100 $\mathrm{pmol/mol}$ have been measured, about 4 times higher than simulated. Singh et al. (2001) postulate some sources from the ocean (Zhou and Mopper, 1997), though more measurements are required to better constrain the abundance of this tracer.

Methanol, CH_3OH

Even though methanol is one of the most abundant organic trace gases in the atmosphere, its global budget is not well understood (Heikes et al., 2002; Singh et al., 2000; Jacob et al., 2005). It influences the upper tropospheric photochemistry because of its oxidation to formaldehyde (Palmer et al., 2003; Singh et al., 2003; Jacob et al., 2005). Unfortunately, the distribution and magnitude of the sources and sinks are largely unknown (Tie et al., 2003; Singh et al., 2004; Galbally and Kirstine, 2002). Due to these high uncertainties,

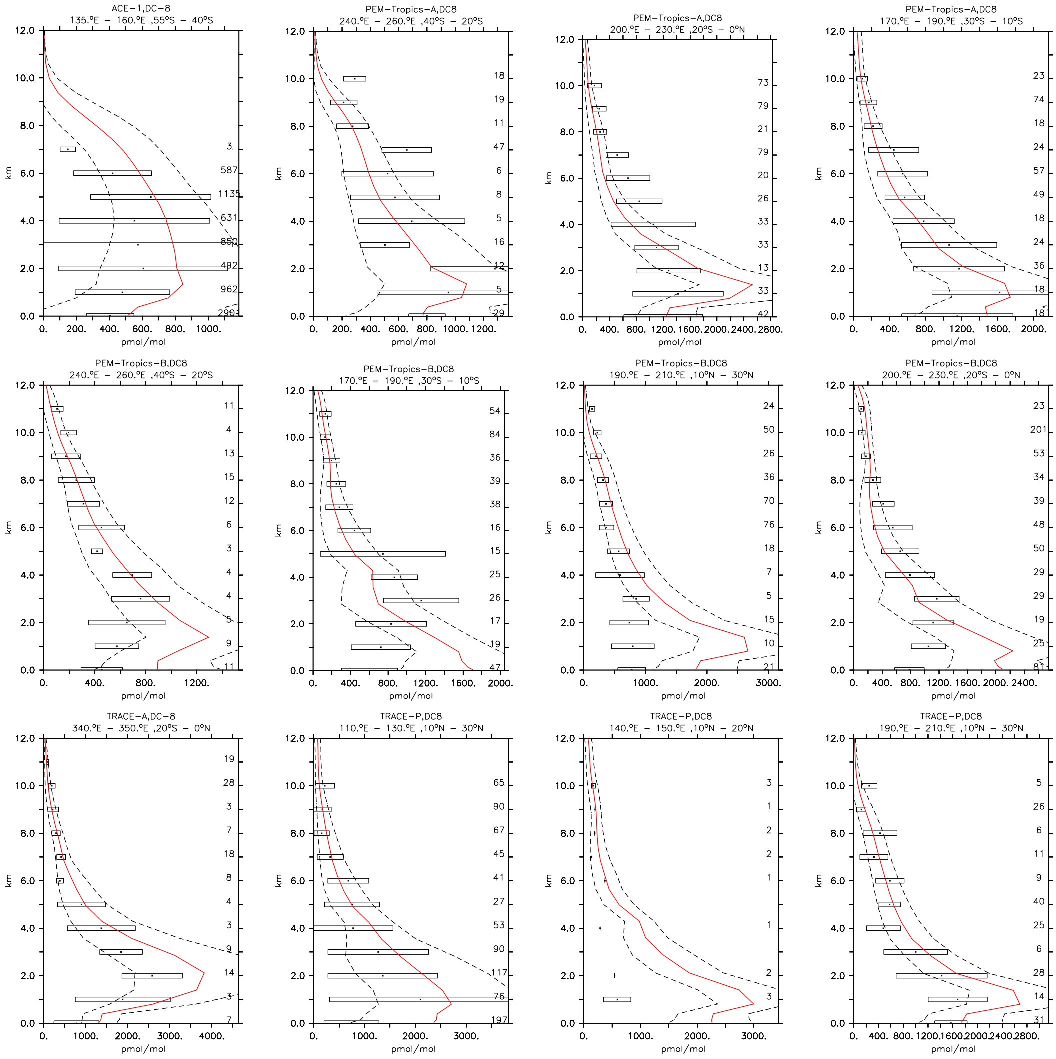

Figure 2.30: Vertical profiles of H_2O_2 (in pmol/mol) for some selected campaigns. Symbols and colours as in Fig. 2.20.

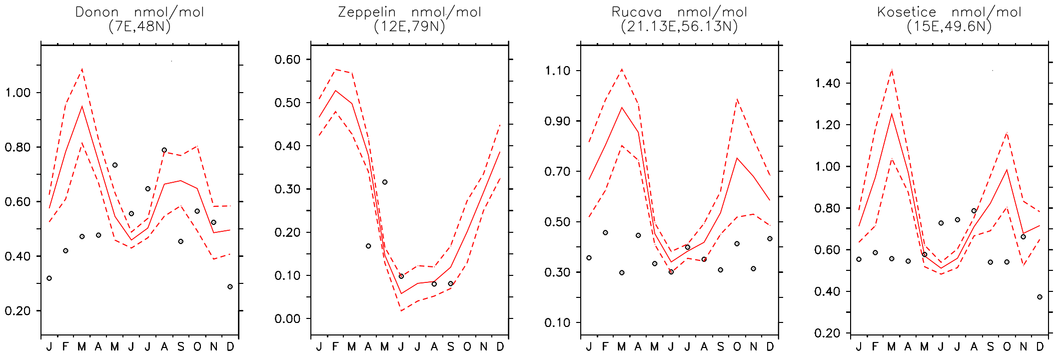

Figure 2.31: As Fig. 2.22, but for CH_3CHO.

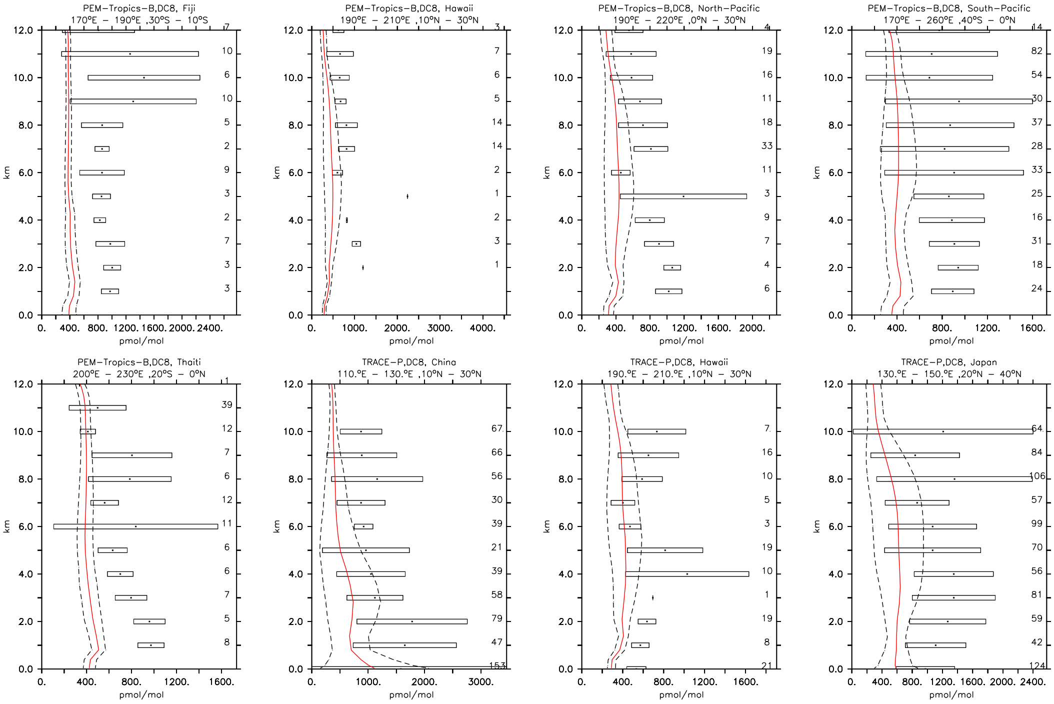

Figure 2.32: Vertical profiles of CH_3OH (in $\mathrm{pmol/mol}$) for some selected campaigns. Symbols and colours as in Fig. 2.20.

emissions from the ocean have not been included in our simulation, though indicated by previous studies (Jacob et al., 2005; Heikes et al., 2002).

Compared to other tracers, relatively few observations of methanol are available (PEM TROPICS-B and TRACE-P campaigns). As noted in Sect. 2.3.2, the correlation between model results and measurements is very low ($R^2 = 0.313$), and the vertical profiles are not reproduced by the model (Figs. 2.7 and 2.32). Wet deposition has not been taken into account for this tracer (Tost et al. (2006)), however, only small differences of $\approx 5\%$ are expected by accounting for this process (Heikes et al., 2002; Galbally and Kirstine, 2002; von Kuhlmann et al., 2003b). The simulated total dry deposition of 42.16 $\mathrm{Tg/yr}$ is well within the suggested values in the literature (e.g 35-210 $\mathrm{Tg/yr}$ (Heikes et al., 2002), 11-43 $\mathrm{Tg/yr}$ (Galbally and Kirstine, 2002), 32-85 $\mathrm{Tg/yr}$ (Tie et al., 2003), 37 $\mathrm{Tg/yr}$ (von Kuhlmann et al., 2003b) and 55 $\mathrm{Tg/yr}$ (Jacob et al., 2005)). Thus, underestimated emission fluxes or incomplete description of the chemistry are more likely responsible for the wrong representation. A total emission of 77 $\mathrm{Tg/yr}$ for CH_3OH has been used, as suggested by EDGAR (with 60 $\mathrm{Tg/yr}$ of biogenic emissions). Note, however, that a recent study by Jacob et al. (2005) recommends a total emission of 168 $\mathrm{Tg/yr}$ with 151 $\mathrm{Tg/yr}$ of biogenic emissions.

Formaldehyde, HCHO

Although formaldehyde is chemically formed by methanol, the low reaction rate from of methanol with OH ($CH_3OH + OH \rightarrow HCHO + HO_2$ $k \approx 5 \times 10^{-13}$ $\mathrm{cm^3 molec^{-1} s^{-1}}$) indicates that this reaction is not essential for a realistic simulation of formaldehyde and that the wrong representation of methanol is not strongly influencing HCHO (Stickler et al., 2006). The model, in fact, predicts the observed mixing ratios of this trace gas very well (Fig. 2.33 and Sect. 2.3.2).

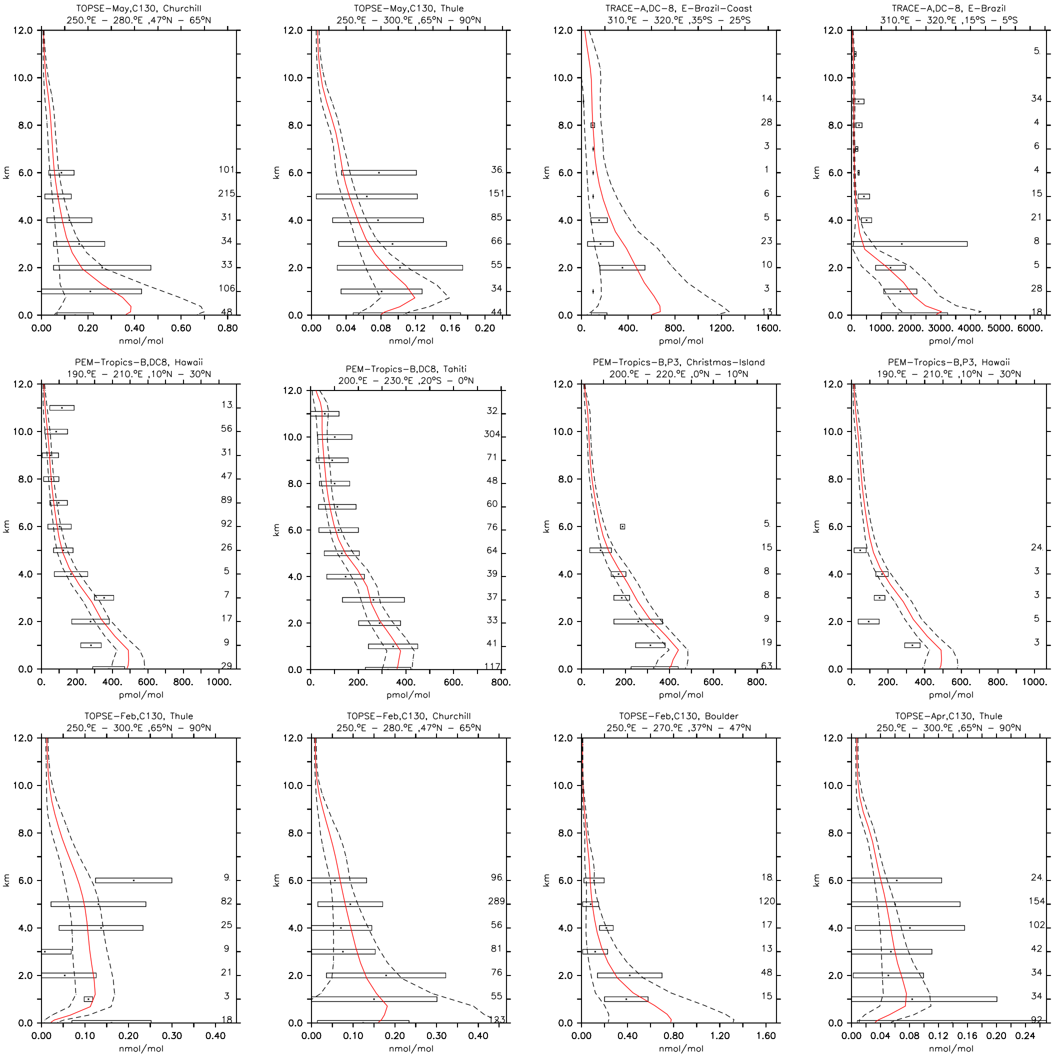

Figure 2.33: Vertical profiles of HCHO for some selected campaigns (unit in the labels). Symbols and colours as in Fig. 2.20.

The simulation is in good agreement with station measurements, and the amplitude of the seasonal cycle is reproduced well at the surface (Figs. 2.8 and 2.9), although with a smaller amplitude than observed. The Ispra site is underestimated, not only for methanol but also for other tracers. As noticed by von Kuhlmann et al. (2003b), this could be due to the location of the site, which is not suitable for comparison with large grid cells of global models.

From the comparison with the aircraft measurements (Fig. 2.33 and Sect. 2.3.2) the simulation of HCHO satisfactorily reproduces the observations. Particularly good agreement is obtained for the PEM-TROPICS-B field campaign, where more than 20 measurements per location are available. A systematic underestimation of the measurements is observed at the surface for the TOPSE-A campaign, only for the

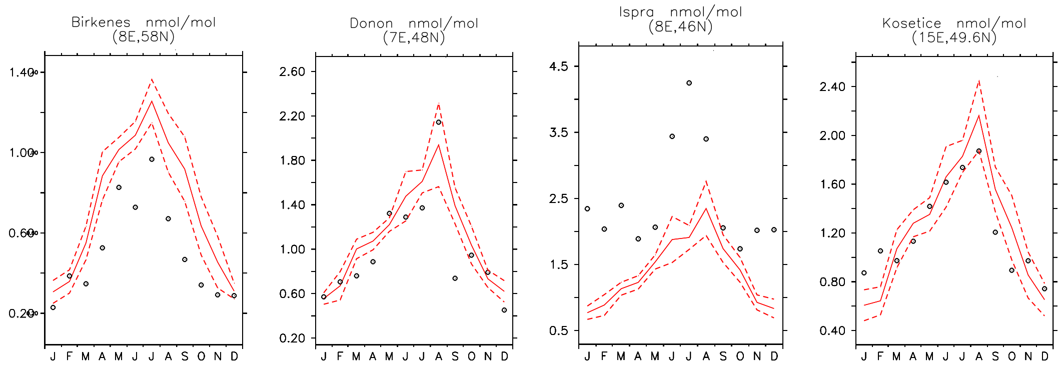

Figure 2.34: As Fig. 2.22, but for HCHO.

location Thule (Fig. 2.33). This can potentially be explained by the absence of emissions of HCHO from snow (Riedel et al., 2005, and references therein). Other models (Fried et al., 2003) also simulate large disagreements compared to measurements for the TOPSE-A campaign.

Acetone, CH_3COCH_3

Acetone (CH_3COCH_3) plays an important role in the upper tropospheric HO_x budget due to its photolysis (Singh et al., 1995; McKeen et al., 1997; Müller and Brasseur, 1995; Wennberg et al., 1998; Jaeglé et al., 2001). Moreover, this tracer is essential to correctly describe the ozone enhancement in flight corridors (Brühl et al., 2000; Folkins and Chatfield, 2000).

Comparing this simulated tracer with the station observations, at the surface this tracer is well reproduced. Problems in reproducing the seasonal cycle are evident for only two locations (see Fig. 2.35), Zeppelin and Ispra, but Tab. 2.8 shows that acetone has one of the highest correlation coefficients and lowest biases compared to other tracers. However, the annual cycle seems to be underestimated (see Figs. 2.8 and 2.9). Folberth et al. (2006) suggested biogenic emissions of 55.93 $\mathrm{Tg/yr}$, more than the 42 $\mathrm{Tg/yr}$ used in this simulation.

As also seen for HCHO, this is not the only species with which we have problems at this location, and we cannot rule out that the Ispra site is unrepresentative for the area of one model grid-box.

Although acetone is well reproduced at the surface, large discrepancies with observations are present in the vertical profiles. As shown in Sect. 2.3.2, the correlation with the aircraft measurements is low ($R^2 = 0.385$), and the vertical profile is not reproduced (bias in Fig. 2.7). Large discrepancies with observations (Fig. 2.36) are present in the free troposphere. A comparison of simulated acetone with aircraft measurements is shown in Fig. 2.37, where the colour code indicates the vertical distribution of the measurements and the corresponding model results.

The differences between model results and observations appears to increase with altitude. The shape of the simulated vertical profiles suggest a potential misrepresentation of the photolysis of this tracer. Measurements made by Blitz et al. (2004) indicate that the quantum yield (and therefore the photolysis rate) of acetone is lower than previously assumed. A reduction would increase the mixing ratio of this tracer and the simulation would then agree better with the observations. Furthermore, as shown by Arnold et al.

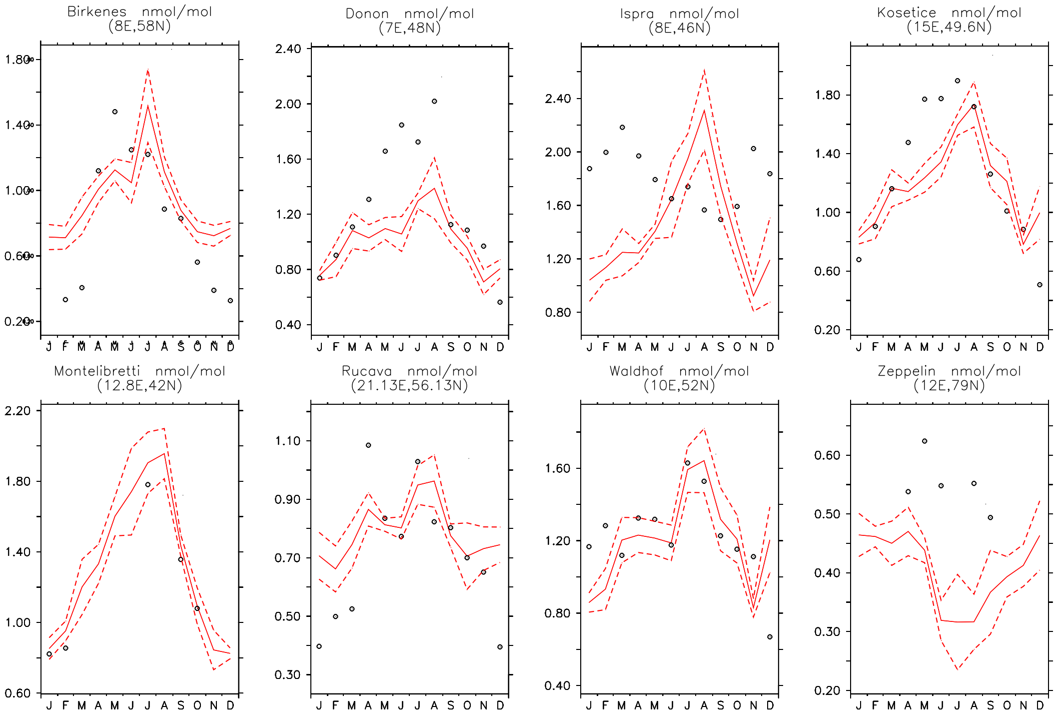

Figure 2.35: As Fig. 2.22, for CH_3COCH_3.

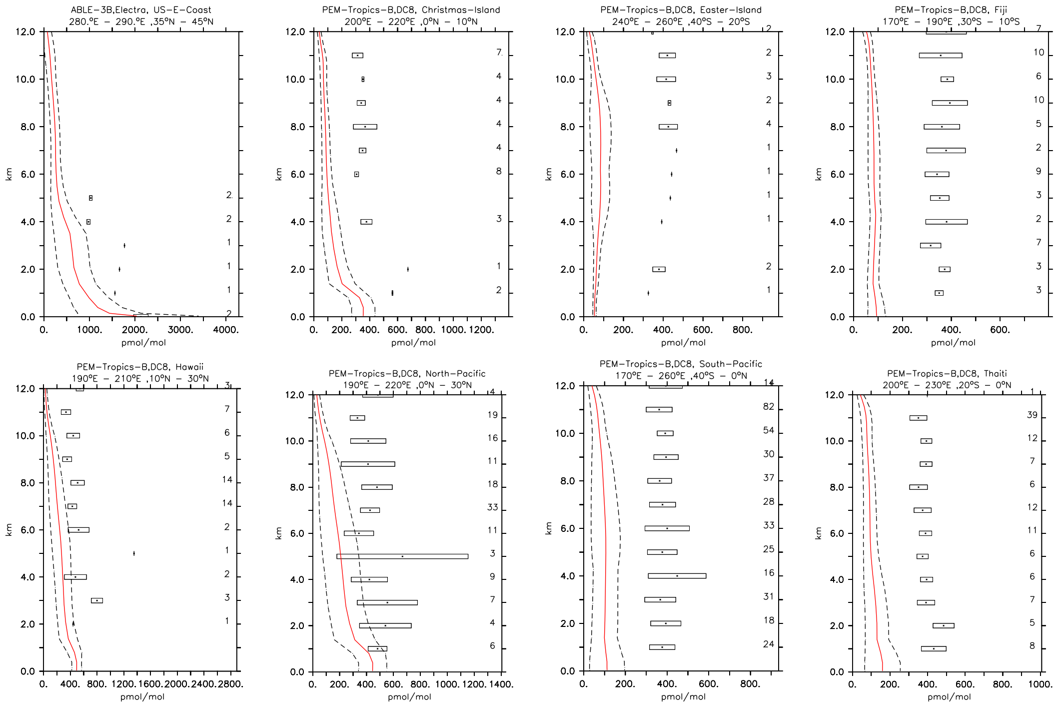

Figure 2.36: Vertical profiles of CH_3COCH_3 (in $\mathrm{pmol/mol}$) for some selected campaigns. Symbols and colours as in Fig. 2.20.

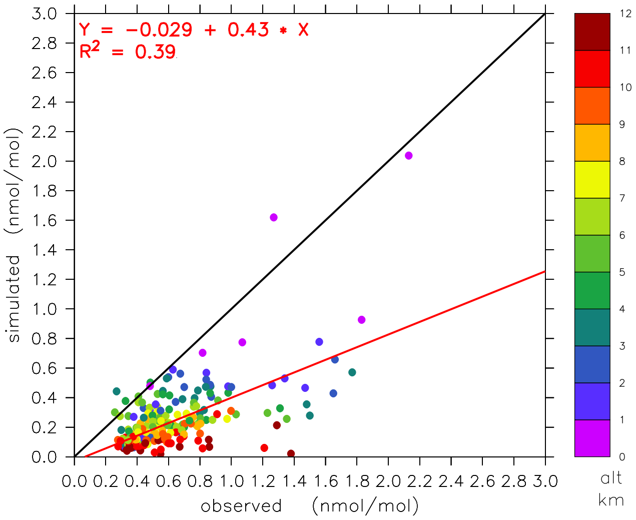

Figure 2.37: Scatter plot of simulated versus observed CH_3COCH_3, both in $\mathrm{nmol/mol}$. The regression line is shown in red, the one-by-one equivalence is drawn in black.

(2004), this new quantum yield may significantly change the contribution of CH_3COCH_3 to the HO_x budget. Arnold et al. (2005) showed that the new quantum yield decreases the global loss of acetone by a factor of ≈ 2 and by $80-90\%$ in the cold upper troposphere.

The wrong vertical distribution of acetone in our model simulation can also explain, at least partially, the poor correlation of the simulated PAN with the aircraft measurements. As for acetone, the correlation with surface measurements is high, while the simulated vertical profiles strongly deviate from the observed profiles. However, it has to be stressed that the PAN mixing ratios are generally overestimated by the model simulation (Tab. 2.7), in contrast to acetone, for which the mixing ratio is systematically underestimated by the model.

2.4 Conclusions

In this chapter the description and the evaluation of the *ECHAM5/MESSy1* model has been presented. For the first time a coherent representation of the atmosphere (from the surface to the mesosphere) has been possible, without any prescribed flux between troposphere and stratosphere. The model results have been compared with observational data from ozonesondes, aircraft field campaigns and stations measurements.

The model is reproducing in a satisfactory way the vertical profile of ozone and its seasonal cycle. In the free troposphere the model reproduces the ozone mixing ratios and the seasonal cycle in a satisfactory way. In the troposphere the comparison has been focused on organic compounds, namely CO, C_2H_4, C_2H_6, C_3H_6, C_3H_8, CH_3CHO, CH_3OH, HCHO, CH_3COCH_3, PAN plus H_2O_2.

The seasonal cycle of CO is well reproduced with a high correlation between model results and observations in remote regions. However, in the NH, the simulated CO tends to be lower than the observations, presumably due to underestimated CO emissions from fossil fuel combustion in winter.

The model reproduces also most of the observations of alkanes, while it shows discrepancies with respect to the observations of alkenes. The quality of the model results for the oxygenated organic compounds is highly dependent on the specific species. While formaldehyde (HCHO) is very well reproduced, the correlations to observations of methanol (CH_3OH), acetaldehyde (CH_3CHO) and acetone (CH_3COCH_3) are rather low.

In chapter 5 some sensitivity studies will be examined, in order to improve the model simulation of the tracers discussed here.

Chapter 3

The AIRSEA submodel

Interactions of the oceans with the atmosphere are considered important for weather and climate (e.g. for moisture and heat transport), and the exchange of carbon dioxide. Since the 1970s, it is also recognised that the oceans contributes to the exchange of organic tracers (Frank et al., 1970; Lamontagne et al., 1974; Takahashi et al., 1997; Plass-Dülmer et al., 1995, and references therein). However, only in the last decade, thanks to new measurements and improvements in atmospheric chemistry models, the role of the oceans in the atmospheric balance of OVOC (Singh et al., 2001) has been recognised. New international research initiatives have been developed, addressing the topic of atmosphere-ocean gas exchange (e.g. **S**urface **O**cean - **L**ower **A**tmosphere **S**tudy (**SOLAS**[1]) and also international projects focusing exclusively on exchange measurements of organics (e.g. **O**rganics over the **O**cean **M**odifying **P**articles in both **H**emispheres (**OOMPH**)) have been planned. This gives the great opportunity to define better the budget of the OVOC also in atmospheric chemistry models which have been generally not very accurate.

In this chapter a description of the theory of the air-sea gas transfer and its implementation as *MESSy* submodel **AIRSEA** is presented (Sect. 3.1). In the second part of this chapter (Sect. 3.2) the **AIRSEA** submodel is tested and the results discussed.

3.1 Theory and implementation in the MESSy System

3.1.1 The two layer model

The two-layer model presented by Liss and Slater (1974) has been adopted to simulate the exchange of gases between the oceans and the atmosphere. This physical model has been selected for its simplicity. Moreover, the implementation of such a model in the *MESSy* system as a submodel is straightforward. The two-layer model is based on the assumption that close to the air-sea interface each fluid is well mixed and that within the interface between water and air the exchange is solely driven by molecular diffusion. The model also postulates the presence of two films on either side of the gas/liquid interface. Diffusion of a gas X into or out from a liquid occurs across these films. Figure 3.1 depicts the physical basis of the two-layer model.

---

[1] http://www.uea.ac.uk/env/solas/

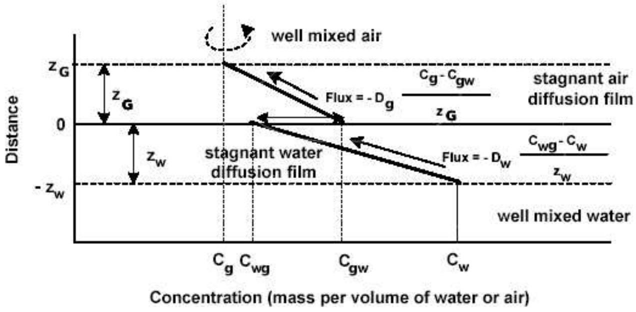

Figure 3.1: Graphical representation of the two layer model. Subscript g denotes the air phase and w denotes the water phase.

From Fick's law of diffusion, the transfer flux across each film is given by:

$$F = -D \times \frac{\partial C}{\partial z} \tag{3.1}$$

where F is the flux in $\mathrm{mol/(m^2 s)}$, D the diffusion coefficient (or diffusivity) of the gas in $\mathrm{m^2/s}$, z the vertical position in m and C the concentration of the gas X in $\mathrm{mol/m^3}$. At steady state and assuming no reactions within the films, the flux through the liquid (F_l) and gas (F_g) films will be the same, thus: $F = F_g = F_w$. Using the finite difference approximation for the partial derivative, the flux can be written as

$$F = \frac{-D_g}{z_g}\left(C_g - C_{gw}\right) = \frac{-D_w}{z_w}\left(C_{wg} - C_w\right), \tag{3.2}$$

where z_a and z_w are the thicknesses of the air and of the liquid film in m, C_{gw} and C_{wg} the concentrations in the air and in the liquid film, respectively. The subscript g denotes the gas phase and w the liquid phase. Assuming that the substance being transferred does not undergo a chemical reaction within the layer, the interface concentrations can be calculated with the Henry's Law:

$$H = C_{wg}/C_{gw} \tag{3.3}$$

The Henry's law coefficient is defined as the ratio between the aqueous phase concentration to the gas phase concentration of the tracer, expressed in this case as a dimensionless quantity. Substituting 3.3 into 3.2 yields

$$F = \frac{D_a}{z_g} \times \left(\frac{C_{wg}}{H} - C_g\right) = \frac{D_w}{z_w} \times \left(C_w - C_{wg}\right) \ , \tag{3.4}$$

solving for C_{wg}

$$C_{wg} = \frac{\left(\frac{D_w}{z_w} C_w + \frac{D_g}{z_g} C_g\right)}{\frac{D_w}{z_w} + \frac{D_g}{H z_g}} \ , \tag{3.5}$$

and substituting Eq. 3.5 in Eq. 3.2, the following equation is obtained:

$$F = \frac{1}{\frac{z_w}{D_w} + \frac{H z_g}{D_g}} \times \left(C_w - H C_g\right). \tag{3.6}$$

This is the traditional formulation used for practical proposes and can be expressed as

$$F = K_{tot} \times (C_w - HC_g)\,. \tag{3.7}$$

Since K_{tot} is always positive, the direction of the flux of C depends only on the sign of the second term in Eq. 3.7. K_{tot} (in $\mathrm{m/s}$) is called *total transfer velocity*, also known as the "piston" velocity.

From Eqs. 3.6 and 3.7, the total transfer velocity can be decomposed in *water phase transfer velocity* (K_w) and *gas phase transfer velocity* (K_g):

$$K_{tot} = \frac{1}{\left(\frac{z_w}{D_w} + \frac{Hz_a}{D_a}\right)}\,, \tag{3.8}$$

$$K_g = \frac{D_g}{Hz_g}\,, \tag{3.9}$$

$$K_w = \frac{D_w}{z_w}\,, \tag{3.10}$$

$$K_{tot} = \frac{1}{\left(\frac{1}{\alpha K_w} + \frac{H}{K_g}\right)} \tag{3.11}$$

In Eq. 3.11 the factor alpha has been introduced to take into account the acceleration of the transfer velocity due to reactions in the water phase. It is an empirical parameter, used only in case of reactive gases, for which the assumption of no reactions in the two films is only partially true.

From Eq. 3.11 two regimes can be deduced:

- $K_w > K_g/H$: the flux is controlled by the water film transfer
- $K_w < K_g/H$: the flux is controlled by the gas film transfer

3.1.2 Solubility effect on the transfer velocity

Although the dimensionless Henry's law coefficient has been used (H), in the literature it is generally common practice to use H_p, in $\mathrm{M/L}$ (i.e. $\mathrm{mol/L\,atm}$), which is defined as the ratio of the concentration in the aqueous phase of a gas X (C) and its partial pressure (p) in the gas phase:

$$H_p = C/p\,. \tag{3.12}$$

From H_p, the dimensionless Henry's law coefficient H can be easily calculated:

$$H = H_p RT\,, \tag{3.13}$$

where R is the universal gas constant (in $\mathrm{J\,mol^{-1}\,K^{-1}}$) and T is the temperature of the interface (surface temperature) in K. H_p can be transformed in the official SI units: $\frac{H_p}{[M/atm]} = 101.325 \times \frac{H_p}{[(mol/m^3)/Pa]}$.

Because the solubility (i.e. the Henry's law coefficient) of a gas is temperature dependent (Fig. 3.2), the Henry's law coefficient for standard condition (i.e. at $T = 298.15K$) is denoted as H_p^θ. The Henry's law coefficient for temperatures different from $298.15K$ can be calculated with the following formula:

$$H_p = H_p^\theta \times \left(\frac{-\Delta_{soln}H}{R}\left(\frac{1}{T} - \frac{1}{T^\theta}\right)\right) \tag{3.14}$$

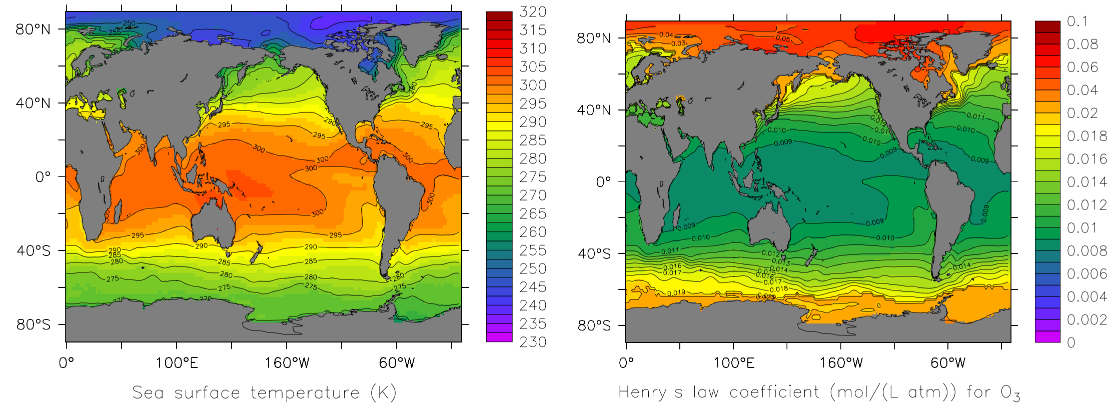

Figure 3.2: Sea surface temperature (left) and solubility (right) for O_3, as an example of the temperature dependency of the solubility. The sea surface temperature is obtained from the AMIPII data (Taylor et al., 2000) for the 1st of January 2004

where $T^{\theta} = 298.15K$ and $\Delta_{soln}H$ is the enthalpy of the solution. Both values can be measured, and a compilation of the Henry's law coefficient for different gases can be found in Sander (1999b).

The solubility of a gas in pure water is larger than that in a salty solution. This so-called salting out effect can be approximated with the Sechenov (Setchenow, Setschenow) equation (Pitzer, 1991)

$$ln\left(\frac{H}{H_0}\right) = -K_s S\,, \tag{3.15}$$

where S is the salinity of the liquid in $\mathrm{mol/L}$, K_s is the Setschenow (or salting out) constant in $\mathrm{L/mol}$ and H_0 is the Henry's law coefficient in distilled water.

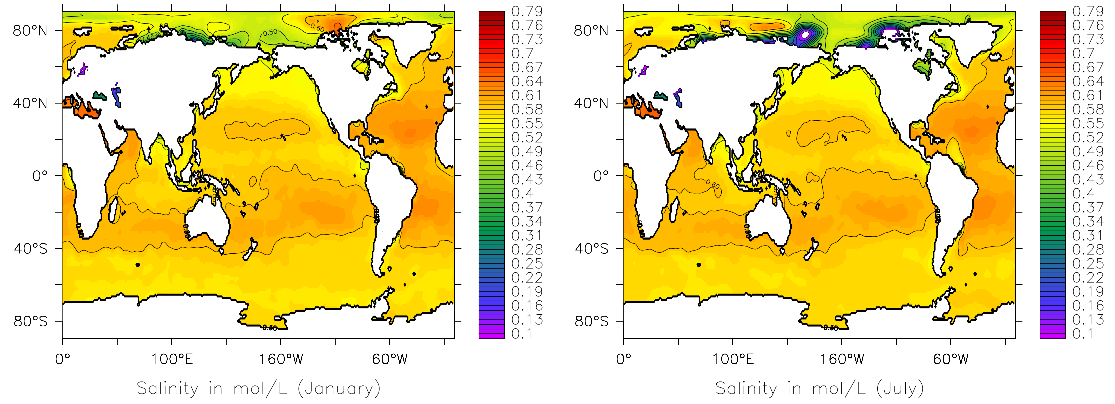

Figure 3.3: Climatological salinity field from the World Ocean Atlas (Boyer et al., 2002).

The submodel **AIRSEA** uses the climatological monthly global average maps of salinity taken from the **W**orld **O**cean **A**tlas (**WOA**[2], 2001), by Boyer et al. (2002), in a 1°× 1° resolution, imported with the **OFFLEM** submodel (Fig. 3.3).

---

[2] http://www.nodc.noaa.gov/OC5/indprod.html

Xie et al. (1997) presented a parameterisation of the Setschenow constant K_s:

$$K_s\,[\mathrm{L/mol}] = V_X\,\left[\mathrm{mol/cm^3}\right] \times 0.0018\,\left[\mathrm{cm^3 L/mol^2}\right] \tag{3.16}$$

where V_X is the molar volume at the boiling point of the tracer (in $\mathrm{cm^3/mol}$). Xie et al. (1997) showed further that this approximation (denoted as Xie and Mackay Volume calculation, XMV) leads to better estimates of K_s compared to various experimental methods, which require assumptions about several parameters (Xie et al., 1990). Nevertheless, more complex theoretical estimations of K_s are also present in the literature (e.g. electrostatic Debye MacAulay Theory (DMT) of Debye and MacAulay (1925), Conway Desnoyers Smith theory (CDST) of Conway et al. (1964), internal pressure theory (IPT) of McDevitt and Long (1952), scaled particle theory (SPT) of Masterton and Lee (1970), and internal pressure theory (XIPT) modified by Xie et al. (1985)). However, as pointed out by Ni et al. (2000), the XMV method is by far the simplest method and also one of the most accurate, with an average relative error of $\approx 11\%$ in the estimation of K_s for organic compounds. V_X is calculated using the “increment volume method” also called LeBas method (LeBas (1915); Reid et al. (1984)).

Equations 3.10 and 3.9 can alternatively be described with the so called resistance method:

$$K_{tot} = (R_g + R_w)^{-1} = \left(\frac{1}{\alpha K_w} + \frac{H}{K_g}\right)^{-1}, \tag{3.17}$$

$$\frac{H}{K_g} = R_g\,, \tag{3.18}$$

$$\frac{1}{\alpha K_w} = R_w\,. \tag{3.19}$$

The water side transfer velocity (K_w) is generally three orders of magnitude lower than the air side transfer velocity (K_g). Three regimes can be defined from Eq. 3.18 and Eq. 3.19, depending on the solubility (Henry’s law coefficient):

- H $> 10^4$: the transfer velocity is dominated by the air transfer velocity, due to very low resistance in the water. This is typical for very soluble gases.
- $10 <$ H $< 10^4$: air resistance and water resistance are of similar magnitude and *both* of them have to be considered in the calculations.
- H < 10 : the transfer velocity is dominated by the water transfer velocity due to a very high resistance in the water. This is typical for non soluble gases.

Hence, the magnitude of the total transfer velocity (K_{tot}) is mainly controlled by the solubility of tracers, i.e. the soluble gases cross the interface faster than non soluble gases. In Fig. 3.4 the Henry’s law coefficient for different tracers is shown.

3.1.3 Water phase transfer velocity

For K_w different estimates exist, primarily obtained from combinations of field and laboratory studies, based on the wind speed at a reference height of 10 m (U_{10}, in $\mathrm{m/s}$; Liss and Merlivat (1986); Wanninkhof (1992); Wanninkhof and McGills (1999); Nightingale et al. (2000); Ho et al. (2006a)). The water phase transfer velocity obtained from these parameterisations (in $\mathrm{cm/h}$) is normalised to the dimensionless

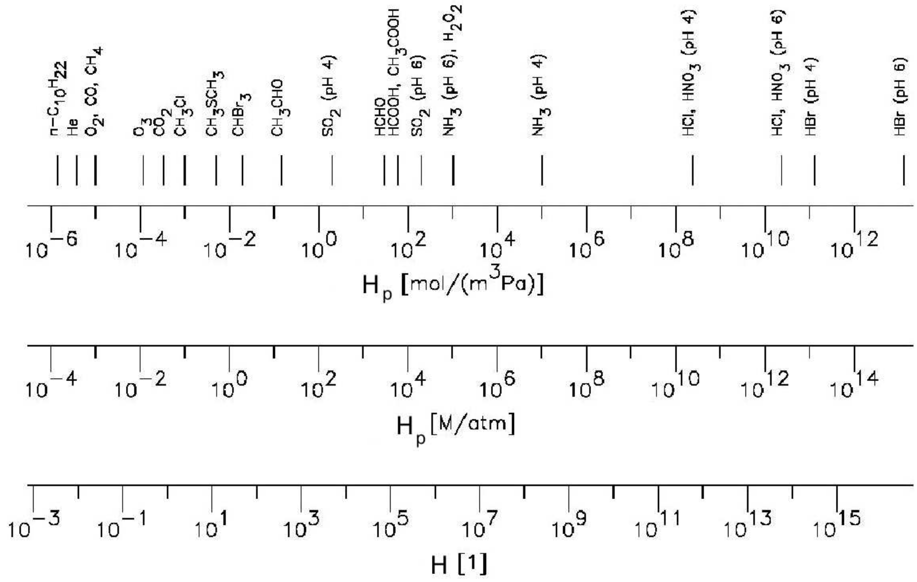

Figure 3.4: Henry's law coefficient for different tracers and for different units (from Sander,1999a)

Schmidt number (Sc_{liq}) of CO in salty water (660) and is here called $\hat{K_w}$. In Tab. 3.1 the most important parameterisations using U_{10} are reported from the literature. In Fig. 3.5 the different water phase transfer velocity ($\hat{K_w}$) parameterisations are depicted for the Schmidt number equal to 660.

Reference	relationship
Liss and Merlivat (1986)	$0.17U_{10}$ $(U_{10} < 3.6m/s)$ $2.85U_{10} - 9.65$ $(3.6 < U_{10} < 13m/s)$ $5.9U_{10} - 49.3$ $(13m/s < U_{10})$
Wanninkhof (1992)	$0.31(U_{10})^2$
Wanninkhof and McGills (1999)	$0.0283(U_{10})^3$
Nightingale et al. (2000)	$0.333(U_{10}) + 0.222(U_{10})^2$
Ho et al. (2006a)	$0.266(U_{10})^2$

Table 3.1: Different parameterisations of $\hat{K_w}$ (in $\mathrm{cm/h}$) for calculations based on instantaneous 10 meter wind speed (U_{10} in $\mathrm{m/s}$) .

$\hat{K_w}$ has then to be scaled to the actual Schmidt number and transformed to $\mathrm{m/s}$ to obtain K_w, used in Eq. 3.19:

$$K_w = \beta \times \hat{K_w} \times \left(\frac{\mathrm{Sc_{liq}}}{660}\right)^{-n}, \tag{3.20}$$

where β is 2.8×10^{-6} (necessary to convert from $\mathrm{cm/h}$ to $\mathrm{m/s}$) and $\mathrm{Sc_{liq}}$ is the dimensionless Schmidt number (in the liquid phase).

The Schmidt number is defined as ν/D, with the kinematic viscosity ν (in $\mathrm{m^2s^{-1}}$) and the molecular diffusivity D (in $\mathrm{m^2s^{-1}}$). The value of n ranges from $2/3$ for a smooth surface to $1/2$ for a rough or wavy

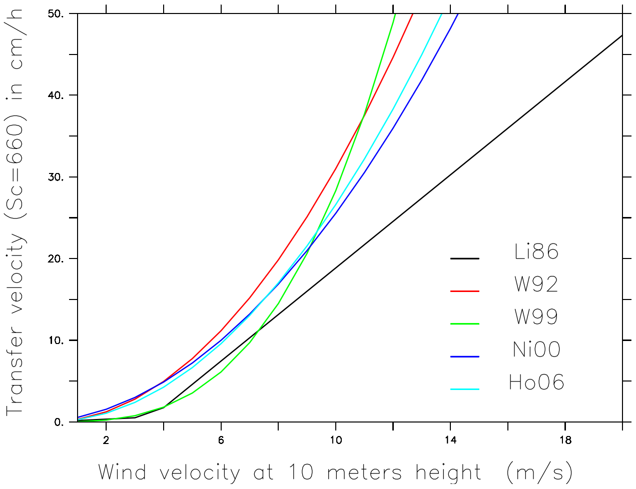

Figure 3.5: Different parameterisations of $\hat{k_w}$ as present in the literature (see Tab. 3.1). Here Li86 corresponds to Liss and Merlivat (1986) parameterisation, W92 to Wanninkhof (1992), W99 to Wanninkhof and McGills (1999), Ni00 to Nightingale et al. (2000) and Ho06 to Ho et al. (2006a).

surface (Jähne et al., 1987). In **AIRSEA** a constant value of $n = 1/2$ is used, with the exception of low-wind speed in the Liss and Merlivat (1986) parameterisation, for which $2/3$ is used. The Schmidt number in water is estimated from the Schmidt number for CO_2. This approach is preferred to other methods, e.g., from direct measurements (Saltzmann et al., 1993), because these are not always available, and also because the parameterisation of $\hat{K_w}$ has been mainly derived from CO_2 measurements. Therefore, the Schmidt number for species x is

$$Sc_x = \left(\frac{\nu}{D_x}\right) = Sc_{CO_2}\left(\frac{D_{CO_2}}{D_x}\right). \tag{3.21}$$

An expression for D_{CO_2}/D_x can be obtained (Hayduk and Laudie (1974) or Wilke and Chang (1955)) by

$$\frac{D_{CO_2}}{D_x} = \left(\frac{V_x}{V_{CO_2}}\right)^{0.6} \tag{3.22}$$

where V_x and V_{CO_2} are the molar volumes (see Sect. 3.1.2) of the tracer and of CO_2 at their boiling points at standard pressure, respectively. With this a more realistic temperature dependence of the Schmidt number on the temperature of the sea-water is achieved. Finally, the Schmidt number for CO_2 can be calculated using the relation given by Wanninkhof (1992) obtained for sea-water

$$Sc_{CO_2} = k_0 - k_1 T + k_2 T^2 - k_3 T^3 \tag{3.23}$$

with the temperature T in K and $k_0 = 2073.1$, $k_1 = 125.62(1/K)$, $k_2 = 3.6276$ $(1/K^2)$, and $k_3 = 0.043219$ $(1/K^3)$.

3.1.3.1 Bubble effect and whitecap coverage

Bubbles can enhance the transfer, and the top of the ocean layer has generally turbulent characteristics. In addition to Eq. 3.20, an alternative parameterisation for K_w with an empirical coefficient for non-clean bubbles in the presence of white-caps has been adopted (Asher and Wanninkhof, 1998a):

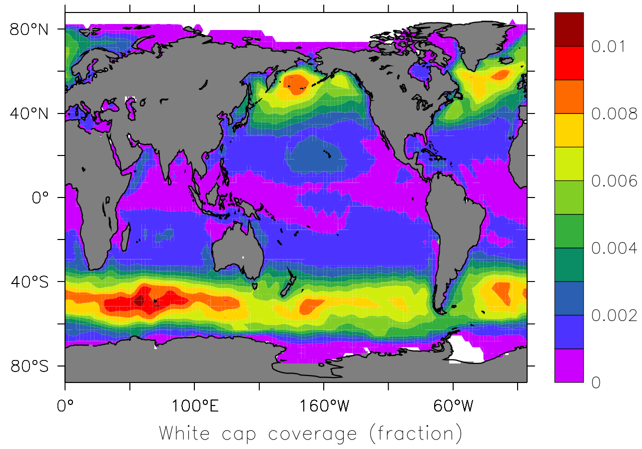

Figure 3.6: Annual average of white cap coverage predicted by *ECHAM5/MESSy1* following Eq. 3.25

$$K_w = \left[\left(\kappa U_{10} + W_c \left(115200 - \kappa U_{10} \right) \right) {Sc_{liq}}^{-1/2} + \right. \tag{3.24}$$

$$\left. W_c \left(\frac{-37}{\alpha_{ost}} + 6120 \alpha_{ost}^{-0.37} Sc_{liq}^{-0.18} \right) \right] \times 2.8 \times 10^{-6} \ \mathrm{m/s},$$

where α_{ost} is the dimensionless Ostwald number and $\kappa = 47 \ \mathrm{s/m}$. It has to be stressed that Eq. 3.24 is strictly valid only for gases far from equilibrium (Asher and Wanninkhof (1998a), Asher and Wanninkhof (1998b)) .

The fractional area coverage W_c of actively breaking white-caps is defined as (Monahan, 1993; Soloviev and Schluessel, 2002)

$$W_c = c_1 (U_{10} - c_o)^3 \tag{3.25}$$

with $c_1 = 2.56 \times 10^{-6} \ \mathrm{s^3 m^{-3}}$ and $c_0 = 1.77 \ \mathrm{ms^{-1}}$. In recent years, however, new methods for measuring whitecaps have been developed; these measurements from satellite (still in a preliminary stage) are generally by a factor of 10 higher than what is calculated with this parameterisation (Anguelova and Webster, 2006).

3.1.3.2 Rain effect

As pointed out in the previous section (Sect. 3.1.3.1), the bubble effect (with the parameterisation of white-cap coverage) can have an impact in the water-side transfer velocity. Also precipitation from to convective or large-scale clouds, can have a strong impact on the air-sea gas transfer (Schlüssel et al., 1997, and references therein).

The processes that explain the enhancement are:

- *Bubble formation* : As seen in Sect. 3.1.3.1, the bubble formation (due to the impact of the rain droplets to the ocean's surface) can increase the transfer velocity of gases, mainly controlled in the liquid phase (Houk and Green, 1976).

- *Microlayer breaking* : The impact of rain at the ocean's surface breaks-up the microlayer which is assumed to be in a steady-state. This process increases the air-gas transfer velocity (Green and Houk, 1979).

- *Change of salinity and temperature* : When large amounts of fresh water precipitate, the salinity and temperature near the ocean surface can be modified, changing the air-gas transfer velocity (Ostapoff et al., 1973; Katsaros, 1976).

Although the main physical effects of rain on the transfer velocity are well understood, no complete mathematical approach adaptable to global general circulation models can be found in literature.

The simplest approach has been proposed by Ho et al. (1997), who find that the rain effect on the transfer velocity can be parameterised as

$$K_w^{(p)} = k_d \times (k_a + k_b R_n - k_c R_n^2) \times \left(\frac{Sc_{liq}}{600}\right)^{-n}, \tag{3.26}$$

where:
$k_a = 0.929$, $k_b = 0.679\mathrm{h/mm}$, $k_c = 0.0015\mathrm{h^2/mm^2}$ and $k_d = 2.8 \times 10^{-6}$ $\mathrm{m/s}$. In equation 3.26 the superscript (p) denotes "precipitation", R_n is the rain rate in $\mathrm{mm/h}$ and $K_w^{(p)}$ is in $\mathrm{m/s}$. Following Ho et al. (2006b) this transfer velocity enhancement has to be added to the total water side transfer velocity of the air-sea interaction.

$$K_{w,tot} = K_w^{(p)} + K_w \tag{3.27}$$

and then used in Eq. 3.10.

3.1.4 Gas phase transfer velocity

3.1.4.1 General case

Based on the "resistance approach" of Wesely (1989a), the gas phase transfer velocity can be calculated as

$$K_g = \frac{1}{R_a + R_{qbr}}, \tag{3.28}$$

where R_a (in $\mathrm{s/m}$) is the aerodynamic resistance and R_{qbr} (in $\mathrm{s/m}$) the quasi-laminar boundary layer resistance (Ganzeveld and Lelieveld (1995), Ganzeveld et al. (1998) and Kerkweg et al. (2006a)). R_a is a function of the physical state of the atmosphere, whereas $R_{qbr}(X)$ is controlled by molecular diffusion. The resistances are given as follows:

1. The aerodynamic resistance R_a:

$$R_a = \frac{1}{u_{\star,wat}\,\kappa}\left[\log\left(\frac{z}{z_{0,m}}\right) - \Phi_h\right] \tag{3.29}$$

where $u_{\star,t}$ is the friction velocity, $\kappa = 0.4$ the dimensionless von Karman constant, z the reference height, and $z_{0,m}$ the momentum roughness length (both in m). For a water surface the friction velocity $u_{\star,wat}$ $(\mathrm{m/s})$ is

$$u_{\star,wat} = \sqrt{c_{m,wat}} \times |v_h|, \tag{3.30}$$

where $|v_h| = \sqrt{(u^2 + v^2)}$ is the horizontal wind speed (in $\mathrm{m/s}$), and the dimensionless drag coefficient $c_{m,wat}$ over water is the product of the neutral drag coefficient $c_{nd,wat}$, the momentum drag coefficient $c_{md,wat}$ and the exchange parameter $c_{ex,wat}$ (all dimensionless and provided by the base model):

$$c_{m,wat} = \frac{c_{nd,wat} \times c_{md,wat}}{c_{ex,wat}}. \tag{3.31}$$

The dimensionless stability function $\Phi_{h,wat}$ depends on the Monin-Obukhov-Length, and thus on the horizontal wind speed and the temperature profile. The parameterisation of Φ_h depends also on the Richardson number Ri (see e.g. Stull (1998), pp.383):

- $Ri > 0$, i.e. stable conditions:

  $$\Phi_h = 4.7 \times \frac{\Delta z}{L} \tag{3.32}$$

  where Δz in m is the layer thickness and L is the Monin-Obukhov-Length (m).

- $Ri \leq 0$, i.e neutral or unstable conditions:

  $$\begin{aligned}\Phi_h = & \left[2\log\left(\frac{1+\Psi_{h,us}}{2}\right) + \log\left(\frac{1+\Psi_{h,us}^2}{2}\right) - 2\arctan(\Psi_{h,us})\right] \\ & -\left[2\log\left(\frac{1+\Psi_{h,neut}}{2}\right) + \log\left(\frac{1+\Psi_{h,neut}^2}{2}\right) - 2\arctan(\Psi_{h,neut})\right]\end{aligned} \tag{3.33}$$

  with $\Psi_{h,neut} = 0.74$ and $\Psi_{h,us} = 0.74 \times \sqrt{1 - 9\,Ri}$.

2. The quasi-laminar boundary layer resistance R_{qbr}:

$$R_{qbr}(X) \quad = \quad \ln\left(\frac{z_{0,m}}{z_{0,X}}\right)\frac{1}{u_\star\,\kappa}\left(\frac{Sc_{air}}{Pr}\right)^{2/3} \quad , \tag{3.34}$$

where $z_{0,m}$ and $z_{0,X}$ are the surface roughness lengths (in m) of momentum and of a trace gas X, respectively, Pr is the Prandtl number (assumed to be 0.72), and Sc the Schmidt number, which is defined as the ratio of kinematic viscosity of air to the molecular diffusivity of a trace gas. Usually the influence of $R_{qbr}(X)$ is small compared to R_a.

The diffusivity (in $\mathrm{m}^2\mathrm{s}^{-1}$) of a tracer in air is calculated following the Fuller, Schettler and Giddings (FSG) method (Lyman et al., 1990)

$$D_x = k\frac{10^{-11} T^{1.75}\sqrt{\frac{M_{air}+M_x}{M_{air}M_x}}}{p\left[{V_{air}^o}^{1/3} + {V_x^o}^{1/3}\right]^2}, \tag{3.35}$$

where V_x^o is the molar volume based on the method developed by Fuller (in $\mathrm{m}^3/\mathrm{mol}$) which is equal to 0.8745 times the molar volume at boiling point, and V_{air}^o is 20.1×10^{-6} ($\mathrm{m}^3/\mathrm{mol}$). T is the air temperature (in K), M_{air} and M_x are the molar masses of air and the tracer, respectively. $k = 101325$ Pa $\mathrm{m}^4\mathrm{g}^{0.5}\mathrm{s}^{-1}\mathrm{mol}^{-0.167}\mathrm{K}^{-1.75}$ is a constant used to obtain the right unit system. From the diffusivity of a tracer and the kinematic viscosity of air, Sc_{air} is calculated.

3.1.4.2 neutral stable atmosphere

Carpenter et al. (2004) suggested also an alternative parameterisation of R_a and R_{qbr}. Assuming a neutrally stable atmospheric surface layer (Garland, 1977):

$$R_a = \frac{U(z)}{u_*^2} \; , \tag{3.36}$$

where $U(z)$ is the wind speed at the height z of the lowest model layer and u_* is the friction velocity (both in $\mathrm{m/s}$).

The gas phase resistance is (Wesely, 1989a)

$$R_{qbr} = \left(\frac{5}{u_*}\right) Sc_{air}^{2/3} \; , \tag{3.37}$$

where Sc_{air} is the dimensionless Schmidt number in air.

This parametrisation shows the importance of the friction velocity in the calculation of the air-sea transfer for soluble gases (i.e. with transfer velocity dominated by the air side transfer velocity): being u_* generally proportional to $U(z)$ over the ocean, it is the most important term in Eq. 3.36 and hence in Eq. 3.28.

3.2 Evaluation of the AIRSEA submodel

As shown in Sect. 3.1, the submodel **AIRSEA** has been implemented to described the air-sea exchange of a large variety of gases, with only few restrictions: gases for which aqueous phase dissociation is important or acids and bases with a pH-dependent solubility. Thanks to different parametrisations, a calculation of the transfer velocity is possible. However (see Eq. 3.7), an equally important term (i.e. the difference in concentration between gas phase and liquid phase of the tracer $(C_w - HC_g)$) is required. While the concentrations of the tracer in the gas phase (C_g) can be easily obtained from *ECHAM5/MESSy1*, the concentration of the tracer in the liquid phase (C_w) is required as input from external sources. C_w can be taken from available climatologies, parameterised, or derived directly from field studies. In this section, the model is tested with three different trace gases, namely CO_2, DMS and isoprene. Global climatologies of the liquid phase concentration in the ocean for these gases are available from the literature, and the emission/deposition fluxes in the ocean have been subject of numerous studies.

3.2.1 Dimethylsulfide (DMS)

Dimethylsulfide (DMS, C_2H_6S) is an important sulfur compound. It is a biogenically emitted sulfur tracer, and it is exclusively produced in water. The outgassing of DMS from oceans accounts for $\approx 95\%$ of the total biogenic sulfur emissions (Mihalopoulos et al., 1992; Khalil and Rasmussen, 1984). In the atmosphere DMS is oxidized into SO_2 and methyl peroxy radical (CH_3O_2). SO_2 can be further oxidized to H_2SO_4, which can contribute to **C**loud **C**ondensation **N**uclei (**CCN**). Hence, the emission of DMS and the following production of H_2SO_4 can affect the cloud microphysical and consequently optical properties and hence modifies the radiation budget of the Earth (Charlson et al., 1987; Andreae and Crutzen, 1997).

A global climatology of DMS concentrations near the sea surface has been compiled by Kettle et al. (1999, and references therein)[3], based on 15617 measurements. With the use of the submodel **AIRSEA**, the simulation of the air-sea exchange for this tracer is straightforward.

A test simulation has been performed, with the same setup of the evaluation simulation *S1* as described in Sect. 2.1.2.1. Differently from *S1*, in this test simulation the emissions of DMS have been deactivated in the submodel **ONLEM**, to avoid double counting, and the submodel **AIRSEA** has been activated. The constants needed for the simulation of the DMS fluxes (Molar mass, henry's law coefficient and molar volume at boiling point) have been introduced as input for the submodel **AIRSEA** and are listed in Appendix C. The climatology of the DMS liquid phase concentrations has been imported through the submodel **OFFLEM**. Only the year 2000 of the model results has been taken into account for the budget calculations.

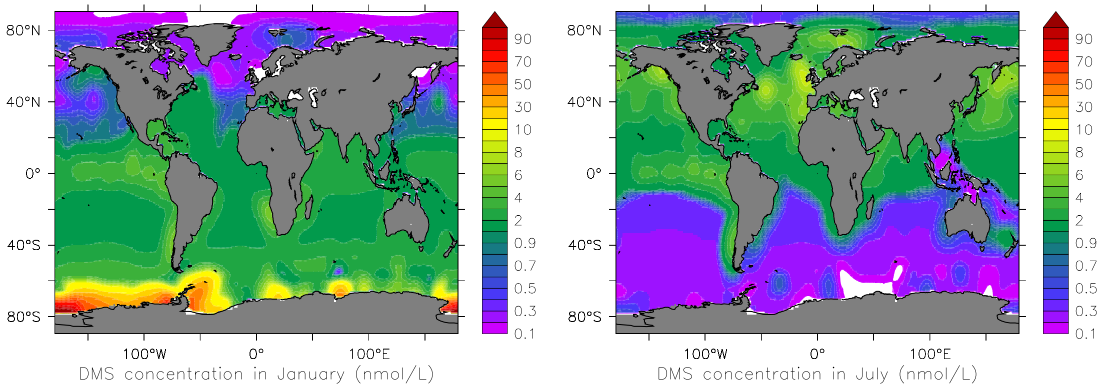

Figure 3.7: Climatological aqueous phase concentration of DMS in nmol/L for January and July, from Kettle et al. (1999).

Reference	annual DMS emission TgS/yr
Nguyen et al. (1978)	26
Andreae and Raemdonck (1983)	38.5
Bates et al. (1987)	16
Andreae (1990)	19-54
Bürgermeister et al. (1990)	24.8-28.3
Erickson et al. (1990)	15
Staubes and Georgii (1993)	26.8
Tarrasón et al. (1995)	15.5
Putaud and Nguyen (1996)	17-21
Kettle and Andreae (2000)	15-33
*ECHAM5/MESSy1*with **ONLEM** (*S1*)	7.7
*ECHAM5/MESSy1*with **AIRSEA** (This work)	14

Table 3.2: Global integrated DMS fluxes from oceans (from Kettle and Andreae,2000)

---

[3] http://dss.ucar.edu/datasets/ds289.2/

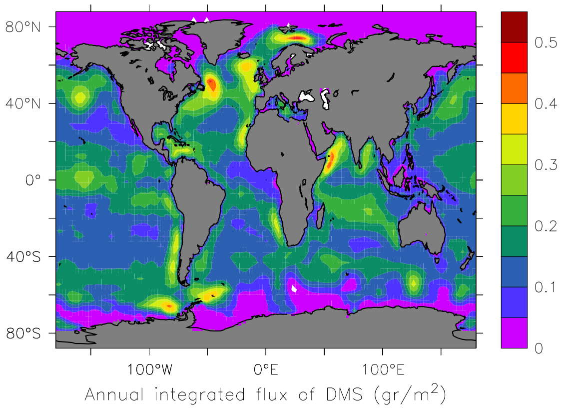

Figure 3.8: Annually integrated DMS flux from the oceans.

The global emission calculated with **AIRSEA** (14 $\mathrm{TgS/yr}$) is at the low end of the suggested values in the literature (see Tab. 3.2), but it is comparable with the other values previously calculated with different methods. Compared to Kettle and Andreae (2000), who used the same approach as in this work, the global integrated flux calculated is lower. However, Kettle and Andreae (2000) assumed a negligible DMS concentration in the gas phase, due to its high reactivity. Here, the simulated gas phase concentration for DMS has been taken in account (see Fig. 3.9), which decreases the magnitude of the flux(see Eq. 3.7).

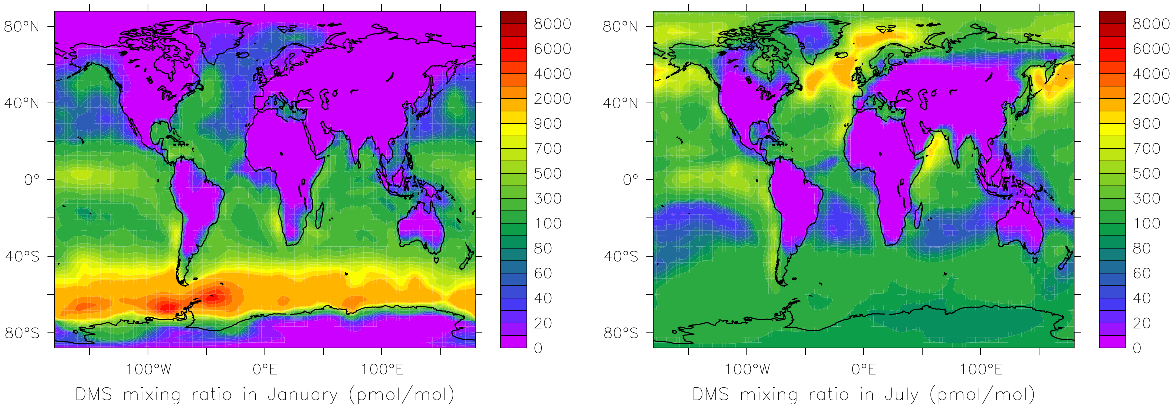

Figure 3.9: Gas phase concentration of DMS in $\mathrm{pmol/mol}$ for January and July, from *ECHAM5/MESSy1*calculated with the **AIRSEA** submodel

Nevertheless the model realistically simulates the emission patterns and the magnitude of the flux, and compared to **ONLEM** submodel, is closer to the values present in the literature.

3.2.2 ISOPRENE

Isoprene (C_5H_8) is a reactive biogenic hydrocarbon that affects the photo-chemistry in the troposphere. Terrestrial isoprene is emitted from the vegetation (most strongly by the tropical rainforest) with an annual flux of $\approx 500\mathrm{TgC/yr}$. Isoprene is also emitted from the sea, from phytoplankton production. Although this oceanic emission ($\approx 0.1 - 1.2$ TgC/yr) is of several orders of magnitude lower than the terrestrial source, the high reactivity of this tracer implies that marine emissions can have a local impact in remote regions (Donahue and Prinn (1990); Lewis et al. (2001)).

In the simulation *S1*, the emissions of isoprene from oceans have been neglected, due to its assumed small impact in comparison to the terrestrial source. Based on the work of Broadgate et al. (2000, and references therein), the liquid phase concentration fields of isoprene can be obtained from the amount of chlorophyll using the linear relationship

$$\frac{[\text{Isoprene}]}{[pmol/L]} = \frac{6.43}{[pmol/\mu g]} \times \frac{[\text{Chlorophyll}]}{[\mu g/L]} + \frac{1.2}{[pmol/L]}. \tag{3.38}$$

The seasonal global chlorophyll distribution used in this work is from the **W**orld **O**cean **A**tlas (**WOA**, Conkright et al. (2002)). We adopted this dataset, despite the too low temporal resolution to be coherent with the **WOA** salinity dataset (see Sect. 3.1.2). The resulting liquid phase concentrations of isoprene are shown in Fig. 3.10.

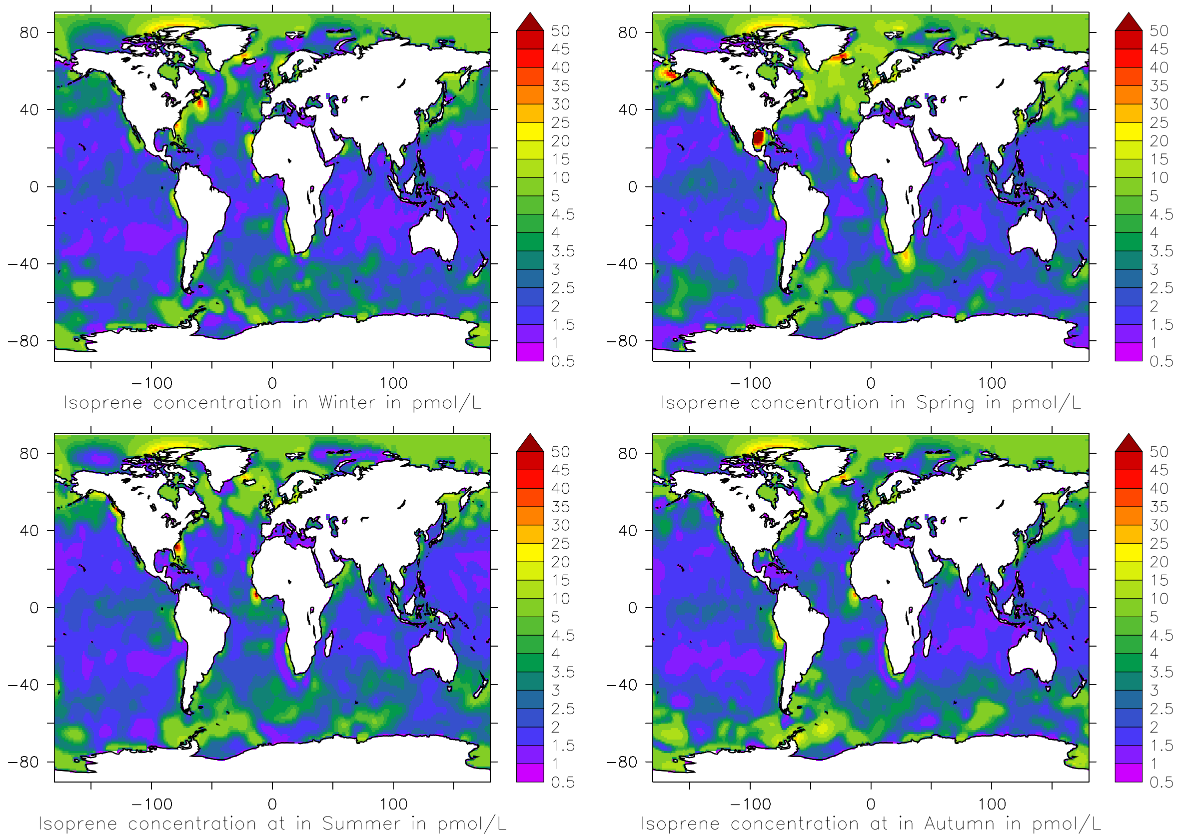

Figure 3.10: Liquid phase concentration of isoprene (in pmol/L) as calculated following Eq. 3.38 using the **WOA** global field of chlorophyll distribution.

*ECHAM5/MESSy1*has been integrated three years (1999-2001) with the same set-up of the simulation *S1* (see Sect. 2.1.2.1). The submodel **AIRSEA** has been activated to simulate the emissions of isoprene. Molar mass, Henry's law coefficient and molar volume at boiling point of isoprene, needed by the **AIRSEA** for the simulation of this tracer, have been introduced trough a namelist file, and the values used are reported in Appendix C. Finally, the liquid phase concentrations have been imported through the submodel **OFFLEM**.

month	Palmer and Shaw (2005) Tg/month		This work Tg/month		month	Palmer and Shaw (2005) Tg/month		This work Tg/month	
	NH	SH	NH	SH		NH	SH	NH	SH
Jan	0.004	0.005	0.004	0.004	Jul	0.002	0.004	0.003	0.005
Feb	0.004	0.005	0.003	0.004	Aug	0.002	0.008	0.003	0.005
Mar	0.005	0.005	0.003	0.004	Sep	0.002	0.010	0.003	0.005
Apr	0.005	0.005	0.004	0.004	Oct	0.003	0.008	0.003	0.005
May	0.005	0.004	0.003	0.005	Nov	0.003	0.008	0.003	0.004
Jun	0.003	0.003	0.003	0.004	Dec	0.003	0.006	0.004	0.004
				Palmer and Shaw (2005)			This work		
Annual global isoprene emission				0.11 Tg/yr			0.96 Tg/yr		

Table 3.3: Monthly and annually integrated hemispheric oceanic isoprene fluxes simulated with *ECHAM5/MESSy1*and **AIRSEA** compared with Palmer and Shaw (2005)

Month	global integrated flux in Tg/month Erickson and Hernandez (2002)	global integrated flux in Tg/month This work	Month	global integrated flux Tg/month Erickson and Hernandez (2002)	global integrated flux Tg/month This work
Jan	0.0071	0.0078	Jul	0.0070	0.0083
Feb	0.0068	0.0072	Aug	0.0075	0.0078
Mar	0.0069	0.0076	Sep	0.0072	0.0076
Apr	0.0067	0.0083	Oct	0.0076	0.0078
May	0.0068	0.0082	Nov	0.0075	0.0073
Jun	0.0071	0.0076	Dec	0.0073	0.0078
annual global integrated flux in Tg/yr					
	Erickson and Hernandez (2002)			This work	
	0.085			0.096	

Table 3.4: Global integrated isoprene fluxes from the oceans simulated with *ECHAM5/MESSy1*and **AIRSEA** compared with Erickson and Hernandez (2002).

In Tab. 3.3 the integrated hemispheric oceanic isoprene fluxes for the year 2001 are listed, together with the values obtained by Palmer and Shaw (2005) for the same year. Although the calculated emission fluxes are comparable, the seasonal cycle is smaller. The calculations of Palmer and Shaw (2005) are based on chlorophyll fields obtained from the MODIS instrument (Carder et al., 2004) on the Terra satellite. The difference can hence be due to a too simple representation of the liquid phase concentration of chlorophyll (and hence isoprene) in *ECHAM5/MESSy1* model. In Tab. 3.4, a comparison with the values obtained by Erickson and Hernandez (2002) is shown. Erickson and Hernandez (2002) based their work on chlorophyll fields obtained for the year 1998 from the **SEA** **W**ide **F**ield-of-view **S**ensor (Sea-WiFS[4]) Transfer Radiome-

---

[4] http://oceancolor.gsfc.nasa.gov/SeaWiFS/

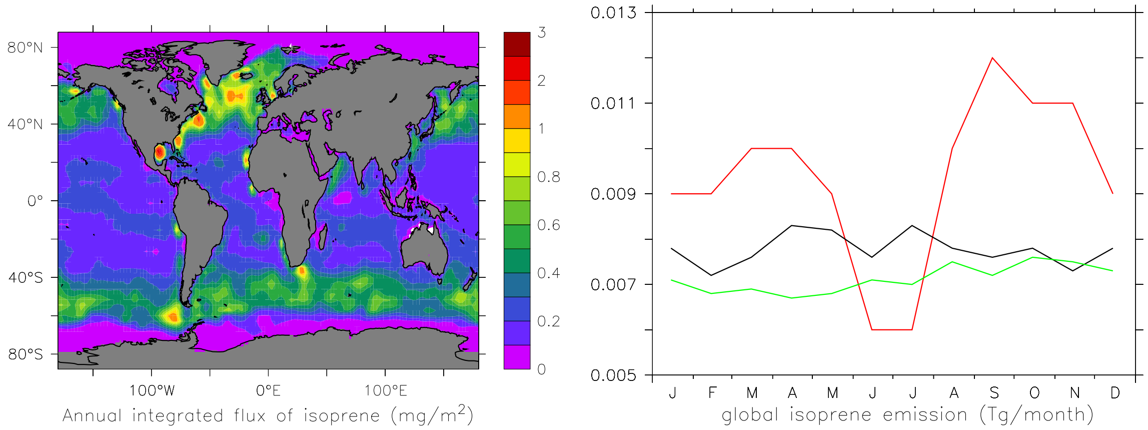

Figure 3.11: Left: Annually integrated isoprene fluxes from oceans. Right: global monthly integrated flux of isoprene. The black line represents this work, the red is obtained from the data of Palmer and Shaw (2005) and the green from the data of Erickson and Hernandez (2002)

ter, on the GeoEye's OrbView-2 (AKA SeaStar) satellite. In this case the fluxes calculated by the **AIRSEA** are slightly higher.

Figure 3.11 (right), depicts the results in Tabs. 3.3 and 3.4. Although *ECHAM5/MESSy1* does not reproduce a seasonal cycle (due to the use of seasonal fields), the simulated global emission fluxes are comparable to previous studies. Nevertheless, the annual global isoprene emission is equivalent in magnitude to both datasets (Palmer and Shaw (2005) and Erickson and Hernandez (2002)) obtained from satellite measurements. This shows that the submodel **AIRSEA** accurate describes the process of air-sea exchange, also for the complex organic tracer isoprene, whereas the overall results may improved by adopting more recent chlorophyll dataset.

3.2.3 Carbon dioxide (CO_2)

In the previous chapters some tests have been conducted for DMS and isoprene to verify the correct implementation of the **AIRSEA** submodel (Sect. 3.1). The gases tested, however, have the characteristic to be *only* emitted from the ocean, i.e. they have only mono-directional fluxes from ocean to air. In the case of CO_2, instead, deposition and emission fluxes are presents simultaneously in different regions of the globe. The capability of the submodel **AIRSEA** to reproduce such fluxes can hence be tested with this gas.

CO_2 is one of the most important greenhouse gases, and the impact of oceans on the atmospheric CO_2 budget is of great importance. Sabine et al. (2004) show that the oceans have been a true net sink for the anthropogenic CO_2 over the last 200 years, sequestering around 30% of the emitted CO_2. Moreover, the oceans have the potential to absorb $\approx 80\%$ of the emitted CO_2 on a time scale of millennia (Feely et al., 2001).

Numerous measurements are present in literature since 1955, and a well established climatology for concentrations in both liquid and gas phases has been compiled for different years by Takahashi et al. (1997, 2002). The climatology used in this work (Takahashi et al. (2002), from now on called "Takahashi climatology"), is based on more than 940000 measurements and represent a mean non-El niño year.

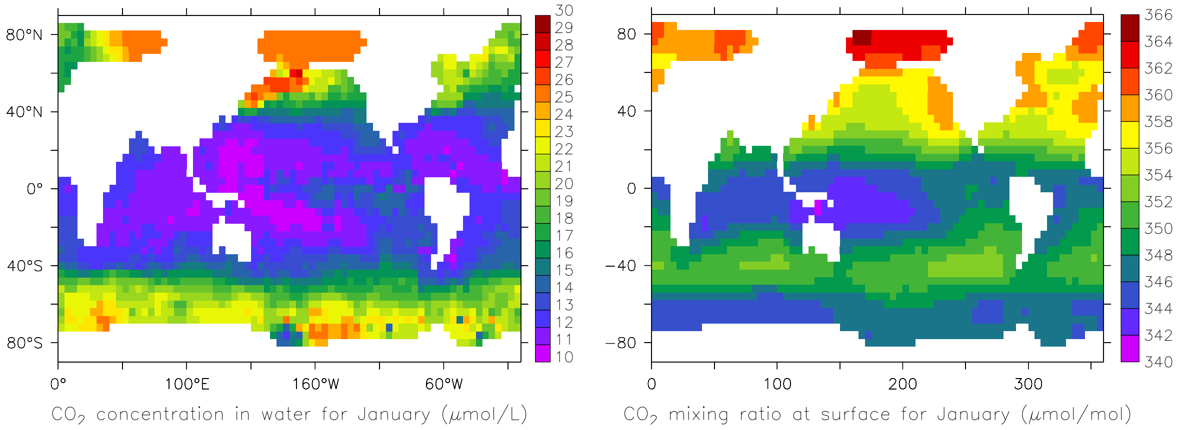

Figure 3.12: Liquid phase concentrations (left) and gas phase mixing ratio (right) of CO_2 as compiled by Takahashi et al. (2002) for January

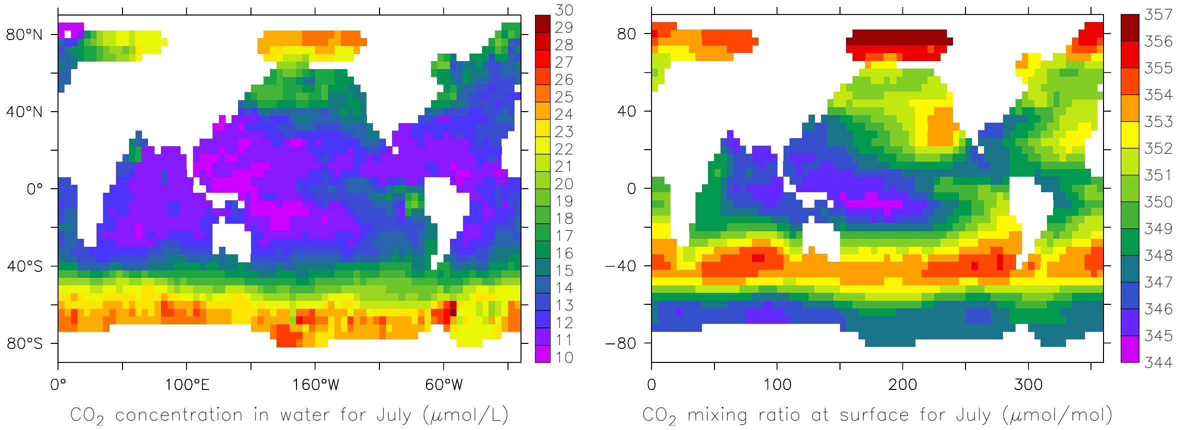

Figure 3.13: Liquid phase concentrations (left) and gas phase mixing ratio (right) of CO_2 as compiled by Takahashi et al. (2002) for July

Many studies of the global emission/deposition of this gas are available from literature, based both on experimental work and on modeling studies (see Sect. 3.2.3.2).

For the simulation of CO_2 air-sea exchanges, the following configuration of *ECHAM5/MESSy1* has been used. AN horizontal resolution of T63 and a vertical resolution of 31 levels has been applied. *ECHAM5* has been forced by the surface temperature climatology obtained from the years 1979-2001 (Taylor et al., 2000), without any nudging of meteorological parameters. The aim is to obtain a climatology for the air-sea exchange based on a climatological simulation of the *ECHAM5/MESSy1* model.

Thanks to the high modularity of *MESSy* , only few submodels needed to be activated to obtain a gas and liquid phase concentration of CO_2:

- **AIRSEA** which controls the air-sea gas transfer;
- **OFFLEM** which has been used to import the so called “Takahashi” climatology;
- **TNUDGE** which nudges the mixing ratio of CO_2 in the lowest level of the model to the Thakahashi climatology. The nudging coefficient was chosen to be the inverse of model time-step (so called "hard-nudging").
- **PTRAC** which introduces CO_2 as tracer in the model. Hence no chemistry module has been selected for this study.

Three other submodels have been also active (**CLOUD**,**CONVECT** and **RAD4ALL**) in their default configuration. With this set-up the year 2000 has been integrated. Since the gas phase of CO_2 has been “hard nudged” and the liquid phase of CO_2 was used as input for **AIRSEA**, the air-sea fluxes calculated with Eq. 3.7 depend only on the Henry’s law coefficient (H) and the transfer velocity K_{tot}, both calculated by the submodel **AIRSEA**.

3.2.3.1 Transfer velocity

The transfer velocity of CO_2 (K_{tot}) depends for more than 99% on the liquid phase transfer velocity (K_w), representing the classical approximation for modelling the exchange rates of this tracer.

Figure 3.14 depicts the annual average transfer velocity K_{tot} calculated from the model results. As expected, the highest values of the transfer velocity occur in regions with highest wind speed (i.e. $\approx 40°$ S).

In Fig. 3.15 the annual zonal average transfer velocity (multiplied by the Henry’s law coefficient) is presented. The model results are similar to the climatology obtained from satellite measurements (Boutin and Etcheto, 1997; Carr et al., 2002).

Compared to satellite measurements, in fact, the overall patterns are well reproduced. The highest transfer velocity is predicted at absolute latitudes higher than 40^o, while the minimum is located at the equator. However, differences can be found at low wind speed (equator): due to the use of instantaneous values of the wind speed in *ECHAM5/MESSy1* , the model predicts much higher transfer velocities than Carr et al. (2002). As pointed out by Chapman et al. (2002), the use of non-averaged wind fields can increase the transfer velocity (and the resulting fluxes) of about $10\% - 60\%$, with peaks up to $\approx 200\%$. This is confirmed by the comparison with the climatology calculated by Boutin and Etcheto (1997), who obtained an annual global average CO_2 transfer velocity of $3.15 \times 10^{-2}\ \mathrm{mol\,m^{-2}yr^{-1}\mu atm^{-1}}$. This value

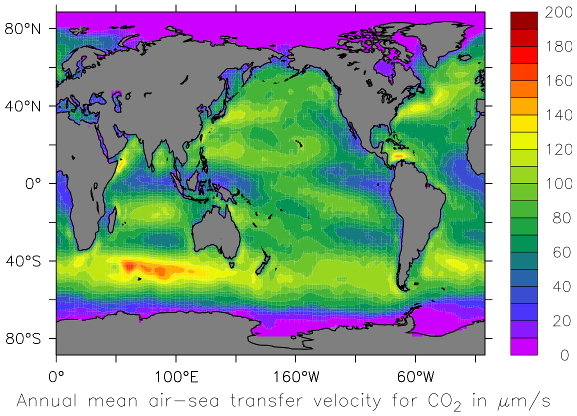

Figure 3.14: Simulated annual average transfer velocity of CO_2 (in $\mu m/s$) calculated with the Wanninkhof (1992) parameterisation.

is 40% lower than 5.24×10^{-2} $mol\,m^{-2}yr^{-1}\mu atm^{-1}$ obtained by averaging the calculated transfer velocity by the **AIRSEA** submodel.

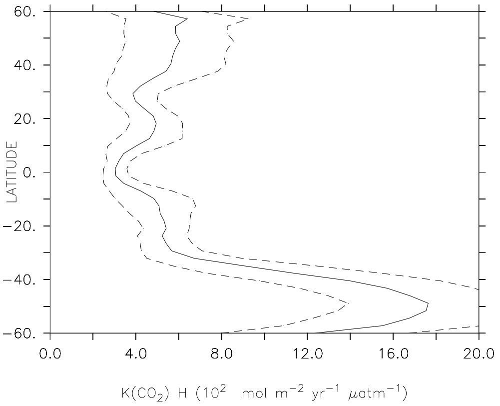

Figure 3.15: Simulated annual zonal average transfer velocity of CO_2 (in $mol\,m^{-2}yr^{-1}\mu atm^{-1}$) based on the Wanninkhof (1992) parameterisation. The results are not weighted by ocean surface.

The results confirm that the transfer velocity, calculated for this important greenhouse gas, is realistic and directly comparable with values obtained from different sources (i.e., satellite measurements).

3.2.3.2 CO_2 fluxes

Because **AIRSEA** realistically simulates the transfer velocity K_{tot}, a direct comparison of the CO_2 fluxes with the original Takahashi calculations is possible. In Tab. 3.5 the global annually integrated fluxes from the model results and values calculated by Takahashi et al. (2002) (based on the NCEP monthly averaged wind fields) are listed.

The Takahashi climatology is well reproduced with temperate oceans being a major source of CO_2 and the southern temperate oceans the major sink. However, the values simulated by the submodel **AIRSEA**

Zones	Takahashi et al. (1997)[a]	Takahashi et al. (2002)[a]	*AIRSEA*[a]	*AIRSEA*[b]
N of 50^{o}N (Arctic)	-0.45	-0.39	-0.65	-0.44
14^{o}N-50^{o}N (Nort. temperate)	-0.72	-0.92	-1.20	-0.84
14^{o}N-14^{o}S (Temperate)	1.04	1.07	2.06	1.35
14^{o}S-50^{o}S (Sout. Temperate)	-0.92	-1.51	-2.02	-1.29
S of 50^{o}S (Antarctic)	-0.30	-0.47	-0.20	-0.13
Global oceans	-1.34	-2.22	-2.01	-1.35

---

[a] based on Wanninkhof (1992) parameterisation

[b] based on Ho et al. (2006a) parameterisation

Table 3.5: Flux of $\mathrm{CO_2}$ in $\mathrm{Pg(C)/yr}$.

are slightly higher than the original calculation of Takahashi et al. (2002). As noted before, this is due to the use of instantaneous wind velocities instead of monthly averages. Nevertheless, the global flux is correctly reproduced with a global exchange flux (sink) of $2.01\ \mathrm{Pg(C)/yr}$, consistently with other studies, also based on different methods (see Tab. 3.6).

In Fig. 3.16 the net flux calculated for one year is presented. The distribution of the annual average net sea-air $\mathrm{CO_2}$ flux shows the same patterns as the calculation by Takahashi et al. (2002), presented in Fig. 3.17. The region between 40° and 60° latitude in both hemispheres represents major sink for atmospheric $\mathrm{CO_2}$, together with the north Atlantic. The eastern equatorial Pacific and the northwestern Arabian Sea are the most intense $\mathrm{CO_2}$ source areas, followed by the tropical Atlantic, the Indian Ocean and the northwestern subarctic Pacific.

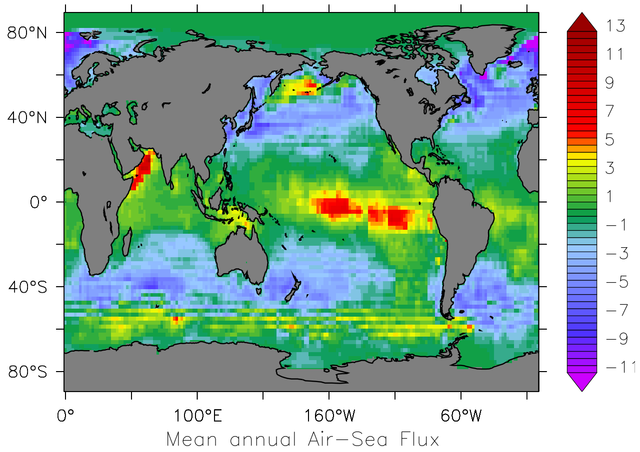

Figure 3.16: Annual mean net air-sea flux of $\mathrm{CO_2}$ in $\mathrm{mol(CO_2)m^{-2}yr^{-1}}$ for one year calculated by **AIRSEA** with instantaneous wind fields from *ECHAM5/MESSy1* and the Wanninkhof (1992) parameterisation of the water phase transfer velocity.

These source/sink patterns are coherent not only with the original Takahashi climatology but also with

Method	Reference	Net global uptake of CO_2 in $\mathrm{Pg(C)/yr}$
Airsea ΔCO_2 disequilibrium[a]	Liss and Merlivat (1986)[b]	0.9 ± 0.2
	Wanninkhof (1992)[b]	1.6 ± 0.3
	Wanninkhof and McGills (1999)[b]	1.9 ± 0.4
	Nightingale et al. (2000)[b]	1.2 ± 0.2
	Ho et al. (2006a)[b]	1.3 ± 0.3
	This work: Wanninkhof (1992)[c]	2.0 ± 0.2
	This work: Ho et al. (2006a)[c]	1.4 ± 0.2
Model based, OGCM	Matsumoto et al. (2004)	1.7 ± 0.2
	Wetzel et al. (2005)	1.74 ± 0.5
Model based, Inversion method	Gurney et al. (2004)	1.3 ± 1.0
	Mikaloff et al. (2006)	2.2 ± 0.2
	multimodel ensemble, Patra et al. (2006)	2.3 ± 0.5
Data based	Ocean inventory, McNeil et al. (2003)	1.5 ± 0.4
	O_2/N_2, Bender et al. (2005)	1.2 ± 0.5
	O_2/N_2, Keeling et al. (1996)	1.7 ± 0.9
	O_2 and $\delta^{13}C$, Battle et al. (2000)	2.0 ± 0.6

---

[a] based on Takahashi et al. (2002)

[b] calculated by Ho et al. (2006a)

[c] Uncertainties based on the standard deviation of simulated wind fields

Table 3.6: Selected estimates of the global CO_2 ocean uptake

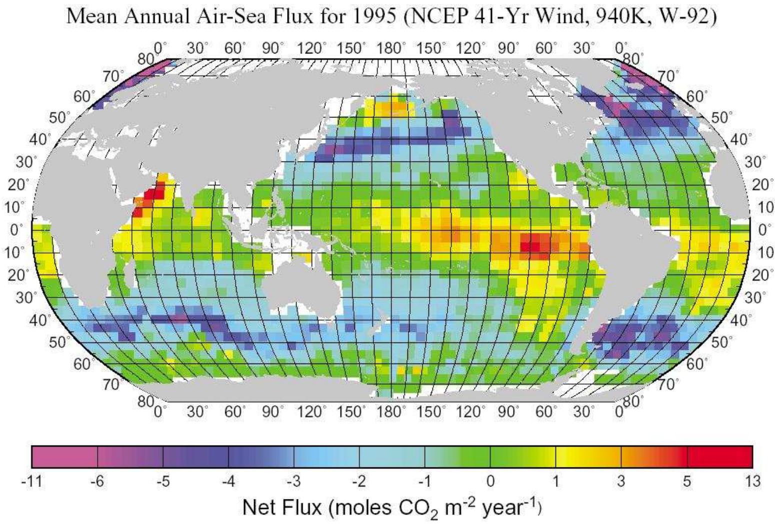

Figure 3.17: Mean annual net air-sea flux of CO_2 in $\mathrm{mol\,(CO_2)\,m^{-2}\,yr^{-1}}$ for a climatological year calculated by Takahashi et al. (2002), using NCEP wind fields and the Wanninkhof (1992) parameterisation of the transfer velocity.

the results obtained from an intercomparison study applying inversion method based on different models (Gurney et al., 2002, 2004).

In summary, the submodel **AIRSEA** realistically simulates the fluxes of CO_2 which is both emitted and deposited from/to the oceans.

3.3 Conclusions and outlook

In this chapter a new submodel **AIRSEA** of the *ECHAM5/MESSy1* model has been presented. **AIRSEA** has been coded following the rigorous coding standard of the *MESSy* interface. With the input of few constants **AIRSEA** calculates the transfer velocity of different gases. To calculate the fluxes, however, the submodel requires also the information about the tracer concentrations in the aqueous phase, which can be

- provided by the user as constant value,
- provided from prescribed maps (e.g., climatologies) imported via the MESSy submodel OFFLEM (Kerkweg et al., 2006b), or
- provided directly (“on-line”) by ocean biogeochemistry submodels.

Only the first two options are implemented in the code at the moment. Future improvements in the applicability of **AIRSEA** is the implementation of a ocean biogeochemistry submodel into the *MESSy* interface, with the possibility of on-line calculations of the aqueous phase concentrations. This will be an important next step in the development of an interactive Earth System model; and the present work may be used as benchmark in the model development.

Chapter 4

Lagrangian representation in MESSy

In the framework of *MESSy* a Lagrangian frame of reference has been implemented and some submodels have been coded to be included also in this representation. This enables using *ECHAM5/MESSy1* not only as a traditional “grid point” model, but also as Lagrangian model, combining the potential of the two approaches in one single model. In this chapter a description of this new feature is given followed by a mathematical description of the implementation of **DRYDEP** and **MECCA** in the Lagrangian frame, with the discussion of some case studies.

4.1 ECHAM5/MESSy in Lagrangian representation

Two frameworks are commonly used to described the dynamic of the atmosphere, based on the *Eulerian* and the *Lagrangian* perspectives (Byers, 1974; Dutton, 1986). The Eulerian approach considers fixed points in space through which the air flows, while the Lagrangian approach considers individual air parcels as they move in time and space (i.e. the trajectories of air parcels). *MESSy* has been developed for an *Eulerian* representation; the submodels change the tracer concentrations at fixed points in the atmosphere. However, with new code developments (still in progress) a *Lagrangian* frame of reference is also possible in *MESSy* ; this means that the changes in the tracer concentrations occur following the air parcel along the trajectory. The core of this representation is the submodel **A**tmospheric **T**racer **T**ransport **I**n a **LA**grangian model (**ATTILA**) (Reithmeier, 2001; Traub, 2004). **ATTILA** calculates the trajectories of air parcels, based on the wind field provided by the *ECHAM5* model. Hence, only the dynamical core of this Lagrangian representation is computed by **ATTILA**. The differential equations describing the displacements of an air parcel are solved using an interactive Runge Kutta 4^{th} order method. The locations of the air parcels are updated every time step, and information about latitude, longitude and pressure height of each parcel is available in all the *MESSy* submodels through the interface layer (see Sect. 2.1.2). No chemistry (or emission/deposition process) is directly calculated by **ATTILA**; for that purpose, additional submodels have to be activated.

In this chapter, the subscripts gp and lg denote the grid point (or Eulerian) and the Lagrangian representation, respectively. Moreover, if not explicitly indicated, it is implicitly assumed that an Eulerian frame of reference is used.

4.2 DRYDEP in Lagrangian representation

In *ECHAM5/MESSy1* (in Eulerian representation) the dry deposition flux $F_{ddep,gp}(X)$ is calculated by (Kerkweg et al., 2006a):

$$F_{ddep,gp}(X) = \mu_{gp}(X) \times \rho_{gp} \times v_{d,\mathit{eff},gp}(X), \tag{4.1}$$

with $\mu_{gp}(X)$ being the gas phase mixing ratio of species X in $\mathrm{mol/mol}$, ρ_{gp} the dry air density and $v_{d,\mathit{eff},gp}(X)$ the effective dry deposition velocity calculated with the following equation:

$$v_{d,\mathit{eff},gp} = \frac{\Delta z_{gp}}{\Delta t} \times \left[1 - \exp\left(v_d \, \frac{\Delta t}{\Delta z_{gp}}\right)\right]. \tag{4.2}$$

Here Δz_{gp} and Δp_{gp} are the grid box thicknesses in m and Pa respectively. Being *ECHAM5* an hydrostatic model, the dry air density can be calculated as

$$\rho_{gp} \quad = \quad \frac{\Delta p_{gp}}{g \Delta z_{gp}}. \tag{4.3}$$

Hence Eq. 4.1 becomes:

$$F_{ddep,gp}(X) \quad = \quad \mu_{gp}(X) \times \frac{\Delta p_{gp}}{g \, \Delta z_{gp}} \times v_{d,\mathit{eff},gp}(X), \tag{4.4}$$

where g is the gravitational acceleration ($\mathrm{m\,s^{-2}}$).

In both cases $F_{ddep,gp}(X)$ is in $\frac{\mathrm{mol}}{\mathrm{mol}} \frac{\mathrm{Kg}}{\mathrm{m^2 s}}$. From Eq. 4.4 is possible to calculate:

- The dry deposition flux $F(X)$, in $\mathrm{kg/(m^2 s)}$ (as seen in Eq. 2.7) can be obtained multiplying Eq. 4.4 by $\frac{M(X)}{M_{air}}$:

$$\begin{aligned} F_{gp}(X) &= F_{ddep,gp}(X) \times \frac{M(X)}{M_{air}} && (4.5) \\ &= \mu_{gp}(X) \times \frac{M(X)}{M_{air}} \times \frac{\Delta p_{gp}}{g \, \Delta z_{gp}} \times v_{d,eff,gp}(X) && (4.6) \end{aligned}$$

  This dry deposition flux is used to budget the gas species.

- The tracer tendencies ($\frac{\Delta \mu_{gp}(X)}{\Delta t}$, in $\mathrm{mol/(mol\,s)}$) are calculated by multiplying Eq. 4.4 by $\frac{g}{\Delta p_{gp}}$:

$$\begin{aligned} \frac{\Delta \mu_{gp}(X)}{\Delta t} &= \mu_{gp}(X) \times \rho_{gp} \frac{g}{\Delta p_{gp}} \times v_{d,\mathit{eff},gp}(X) && (4.7) \\ &= \mu_{gp}(X) \times \frac{\Delta p_{gp}}{g \, \Delta z_{gp}} \times \frac{g}{\Delta p_{gp}} \times v_{d,\mathit{eff},gp}(X) && (4.8) \\ &= \mu_{gp}(X) \times \frac{1}{\Delta z_{gp}} \times v_{d,\mathit{eff},gp}(X) \end{aligned}$$

  The tracer tendencies are used by the model for updating the trace gas mixing ratios. This is preformed sequentially with other processes due by the operator splitting used in combination with the "leapfrog" time-integration scheme (Seinfeld and Pandis, 1997; Jacobson, 1999).

Because the approach contained in Eq. 4.7 and 4.6 has been developed for an Eulerian representation, the implementation of this process in the Lagrangian representation is not straightforward. In fact, only information of the center of mass of the air parcels (and the mass of the parcels) are available in **ATTILA** and hence the grid box height does not reflect the heigh of the parcel in the Lagrangian representation. The parcels are randomly located in the grid box and the grid box height is only an upper limit of the air parcel displacements.

For the implementation a "Lagrangian" dry deposition a few assumptions have to be made:

- all parcels located in the lowest layer of the model are in contact with the Earth surface;
- only air parcels touching the ground are involved in the dry deposition processes (i.e. located in the lowest level of the model);
- the dry air density of an air parcel is the same as the dry air density of the grid box where the air parcel is located. This means that $\rho_{lg} = \rho_{gp} = \rho$.

Because the deposition velocity (v_d) depends only on surface and atmospheric characteristics, the value of v_d calculated in the Eulerian representation can be converted into the Lagrangian representation.

In the Lagrangian representation four methods have been developed to take into account the changes in the tracer tendencies of each air parcel.

1. The simplest approach is to assume that in an air parcel the change in mixing ratios is the same as in the Eulerian representation

$$\frac{\Delta\mu_{lg}(X)}{\Delta t} = \mu_{lg}(X) \times \rho \times \frac{g}{\Delta p_{gp}} \times v_{d,eff,gp}(X) \tag{4.9}$$

   This approach gives the same tendencies as the Eulerian frame of reference. Nevertheless, because only the mixing ratios are calculated in the Lagrangian representation, this calculation could yield negative values for gases which are rapidly deposited.

2. A more sophisticated approach is to assume that each parcel covers the entire surface area of the grid box where it is located:

$$\frac{\Delta\mu_{lg}(X)}{\Delta t} = \mu_{lg}(X) \times \rho \times \frac{g \times A_{gp}}{M_{lg}} \times v_{d,eff,gp}(X) \tag{4.10}$$

   Where A_{gp} is the grid box area and M_{lg} the mass of an air parcel, which is provided by **ATTILA**. This approach is a mixture between Eulerian and Lagrangian representation. Nevertheless the effective deposition velocity is not calculated in the Lagrangian representation and could be too high.

3. A completely self consistent Lagrangian deposition is also possible. The vertical displacement of an air parcel can be calculated with :

$$\rho_{lg} = \rho_{gp} \tag{4.11}$$

$$g\frac{\Delta p_{lg}}{\Delta z_{lg}} = g\frac{\Delta p_{gp}}{\Delta p_{gp}} \tag{4.12}$$

$$\Delta z_{lg} = \Delta z_{gp}\frac{\Delta p_{lg}}{\Delta p_{gp}} \tag{4.13}$$

   Because the air parcel is located within one grid box, $\Delta p_{lg} \leq \Delta p_{gp}$, which implies that Δz_{lg} is always less than the thickness of the grid box, i.e. $\Delta z_{lg} \leq \Delta z_{gp}$. Δz_{lg} can be defined as the height (in m) of the center of mass of the air parcel. In this case, $v_{d,eff,lg}(X)$ for an air parcel is:

$$v_{d,eff,lg} = \frac{\Delta z_{lg}}{\Delta t} \times \left[1 - \exp\left(v_d \,\frac{\Delta t}{\Delta z_{lg}}\right)\right]$$

Then new dry deposition fluxes can be defined, using the values calculated :

$$\begin{aligned}
F_{ddep,lg}(X) &= \mu_{lg}(X) \times \rho \times_{d,eff,lg}(X), && (4.14)\\
F_{lg}(X) &= F_{ddep,lg}(X) \times \frac{M(X)}{M_{air}}, && (4.15)\\
&= \mu_{lg}(X) \times \frac{M(X)}{M_{air}} \times \frac{\Delta p}{g\,\Delta z} \times v_{d,eff,lg}(X). && (4.16)
\end{aligned}$$

A tracer tendency can be obtained with the same approach used for the Eulerian representation:

$$\begin{aligned}
\frac{\Delta\mu_{lg}(X)}{\Delta t} &= \mu_{lg}(X) \times \rho \times \frac{g}{\Delta p_{lg}} \times v_{d,eff,lg}(X) && (4.17)\\
&= \mu_{lg}(X) \times \frac{\Delta p_{lg}}{g\,\Delta z_{lg}} \times \frac{g}{\Delta p_{lg}} \times v_{d,eff,lg}(X) && (4.18)\\
&= \mu_{lg}(X) \times \frac{1}{\Delta z_{lg}} \times v_{d,eff,lg}(X)
\end{aligned}$$

This approach calculates all the values needed in a Lagrangian representation, which is more self consistent. Because the air parcels have a constant mass, the pressure of each air parcels defines also the surface covered. However the vertical displacement of the parcel of air calculated with Δp_{lg} is not equal to the total vertical displacement, but only to the location of the center of mass. This could still give some imprecision in the calculation of the tracer tendencies.

4. In the last method developed, it is assumed that the average tracer mixing ratios of the air parcel located in a grid box represents the observed tracer mixing ratio of that box.

$$\mu'_{gp} = \frac{1}{N}\sum_{i}^{N} \mu_{lg} \qquad (4.19)$$

With N the number of air parcel located in the box. μ'_{gp} is then used in Eq. 4.7 to calculate the tracer tendencies ($\frac{\Delta\mu'_{gp}(X)}{\Delta t}$), following the Eulerian approach. The tracer tendencies are then assigned to the air parcels located in that box, weighted with the relative contribution to μ'_{gp}:

$$\frac{\Delta\mu_{lg}(X)}{\Delta t} = \frac{\Delta\mu'_{gp}(X)}{\Delta t} \times \frac{\mu_{lg}}{N \times \mu'_{gp}} \qquad (4.20)$$

The first three methods described are implicitly assuming a certain geometry of the air parcel, information that is not available “a priori”.

To test the four approaches described here, a simulation with idealized tracers has been performed. *ECHAM5/MESSy1* with a resolution of T42L19 has been integrated for one months, forced by a climatological sea surface temperature for the years 1979-2001 (Taylor et al., 2000), without any nudging. The idealized tracers (NH, SH and V1) have been initialized equally in the Eulerian and Lagrangian representation.

- V1 has been initialised with a horizontally homogeneous mixing ratio and a vertical gradient (see Fig. 4.1). V1 has a molar mass of $50\ \mathrm{g/mol}$, a Henry’s law coefficient of $1000\ \mathrm{M/(atmL)}$ and dry deposition reaction coefficient of 0.1.

- NH as been initialised with vertically homogeneous mixing ratio only in the Northern Hemisphere. NH has a molar mass of $50\ \mathrm{g/mol}$, a Henry's law coefficient of $100\ \mathrm{M/(atmL)}$ and dry deposition reaction coefficient of 0.1.
- SH as been initialised with vertically homogeneous mixing ratio only in the Southern Hemisphere. SH has the same molecular characteristic as NH.

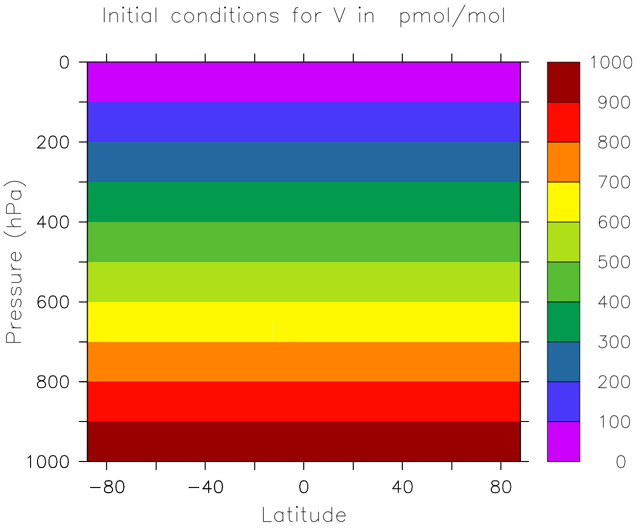

Figure 4.1: Initialisation field for the idealised tracer V, zonally averaged.

The dry deposition of these tracers has been activated in both Eulerian and Lagrangian representations; this process is the unique sink of these tracers, which have no sources. Four different simulations have then been performed with the same set up, changing only the dry deposition method for the Lagrangian representation.

In Fig. 4.2 (left) the global mass of the tracers are presented, in the case of the Eulerian representation (black line), and the Lagrangian representation, with the four dry deposition methods (red, green, blue and purple). Although all four methods seems to give reasonable results, the third and fourth methods (blue and purple line) are more tightly correlated with the Eulerian results also after one months of integration. The global mass ratios (Fig. 4.2, right) do not unequivocally indicate which method is preferable. Nevertheless the fourth deposition method seems to be more consistent with the Eulerian representation calculations, while the second dry deposition method yields the largest deviations. However still some improvements of the algorithm are possible and still more studies are needed to have a completely consistent dry deposition scheme in the Lagrangian representation.

4.3 MECCA in Lagrangian representation

In the Eulerian representation, the submodel **MECCA** calculates for each time step the changes of the mixing ratios due to chemical reactions. The partial differential equations are solved for each grid box in the domain of *ECHAM5/MESSy1*. The implementation of **MECCA** in the Lagrangian representation is

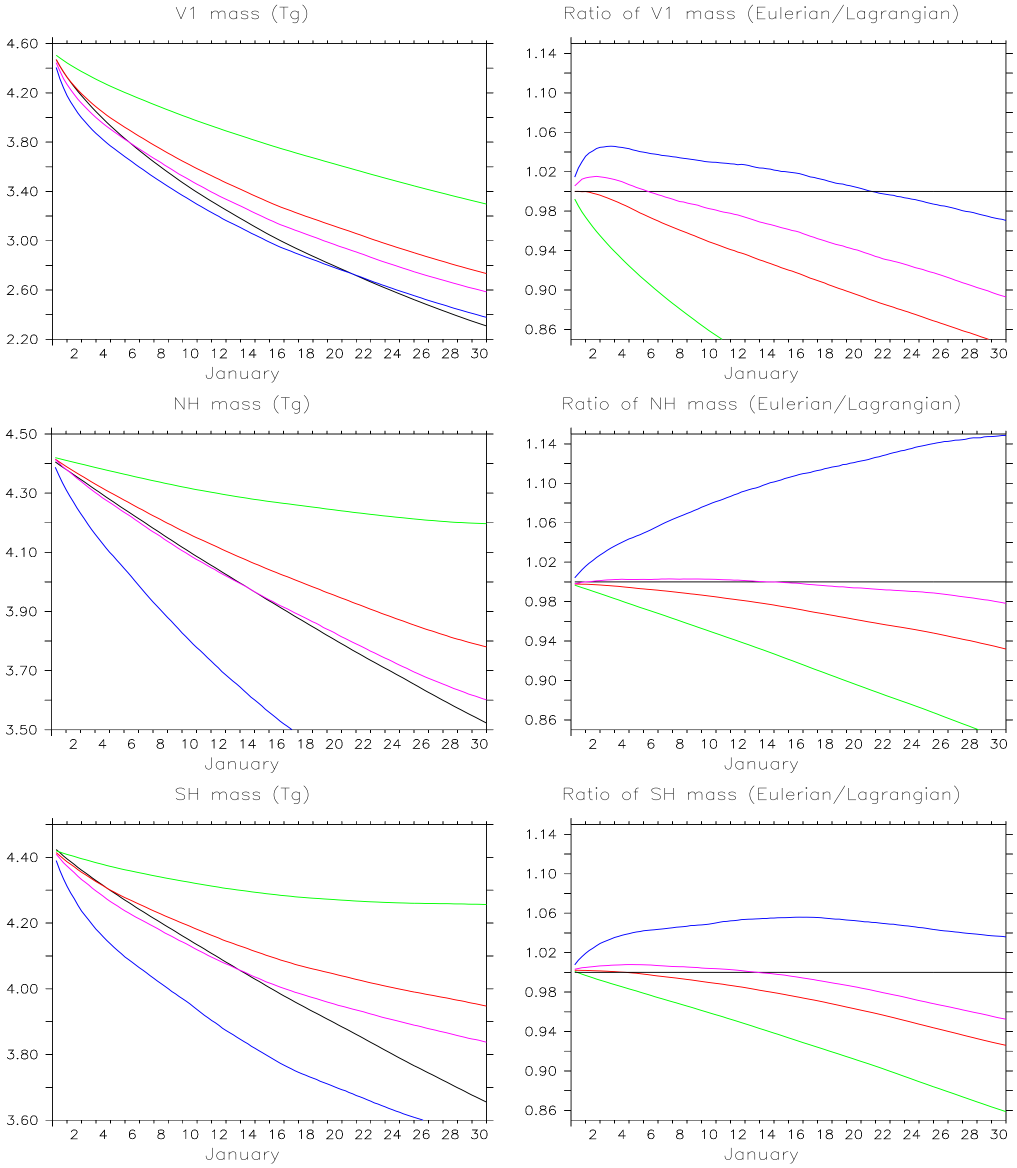

Figure 4.2: LEFT: Global mass in Tg. The black line is the global mass calculated from the Eulerian representation, while the other lines are obtained from the Lagrangian representation with different dry deposition methods (Red: dry deposition method 1; green: method 2; blue: method 3; purple: method 4). RIGHT: ratio between the global integrated mass in the Eulerian representation and in the Lagrangian representation. The colors denote the methods as before.

straightforward, solving the same set of equations for each air parcel present in the domain of **ATTILA**. The mixing ratios required for these calculations are known for each air parcel; moreover, because the locations of the parcels are known, temperature and humidity of an air parcel can be obtained from the global model *ECHAM5*. The pressure of the air parcel (the final physical parameter needed) is directly imported from **ATTILA**.

To test the chemistry, a similar simulation as described in Sect. 4.2 has been integrated, solely with the activation of the submodel **MECCA** in the Eulerian and Lagrangian representations. The chemical mechanism chosen was simple without photolysis reactions and not including any sulfur or halogen compounds.

In Fig. 4.3, the global masses of some selected tracers, calculated in the Lagrangian representation, are shown together with the one calculated by the Eulerian representation. In Fig. 4.4 the ratios of the masses are shown. Generally, less than 2% disagreement between the global masses calculated with the two representation is obtained. Although more test have to be conducted, these preliminary results suggest the correct implementation of the chemistry also in the Lagrangian representation.

4.4 Conclusions and outlook

In this chapter, the implementation of the submodels **DRYDEP** and **MECCA** in a Lagrangian representation has been presented. The sensitivity simulations suggest that the processes have been correctly implemented. However, a complete global chemical model operating in a Lagrangian frame of reference is still under development, and more tests (especially long term runs) have to be performed. With such a model, numerous studies are possible, with a particular focus on applications for field measurements campaigns. With a comprehensive “Lagrangian” chemical model, in fact, not only the trajectories of the air parcels measured during a field campaign can be calculated, but also their chemical history. Moreover, this representation can give detailed information about fluxes through layers and defined boundaries, for example Stratosphere-Troposphere Exchange (STE). The Lagrangian representation of *MESSy* is therefore a valuable tools for future studies in atmospheric chemistry.

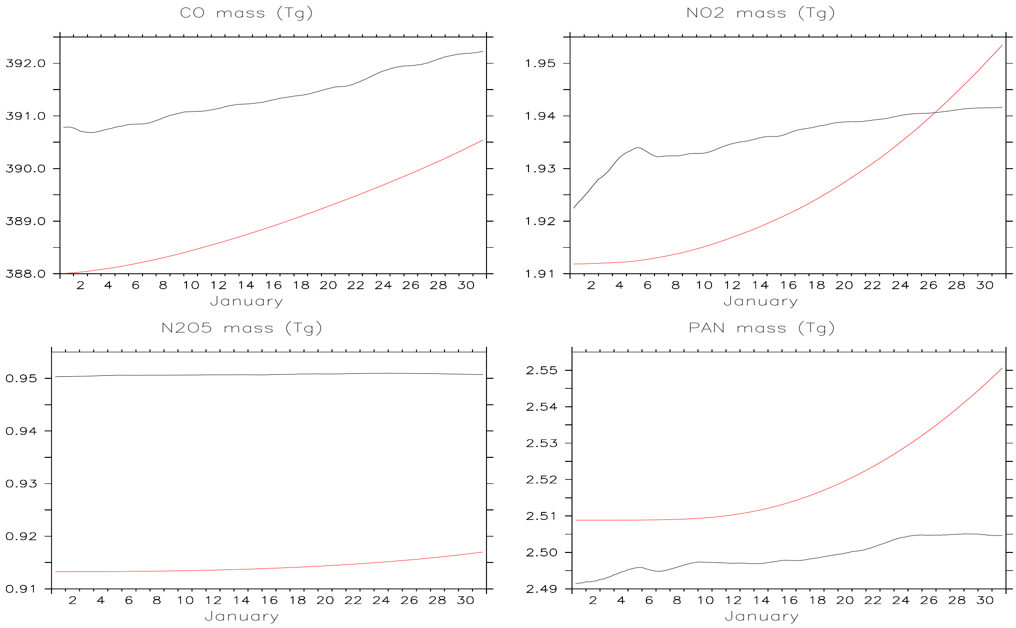

Figure 4.3: Global integrated mass of different tracers in Tg. The black line is the global integrated mass calculated from the Eulerian representation, while the red line is obtained from the Lagrangian representation.

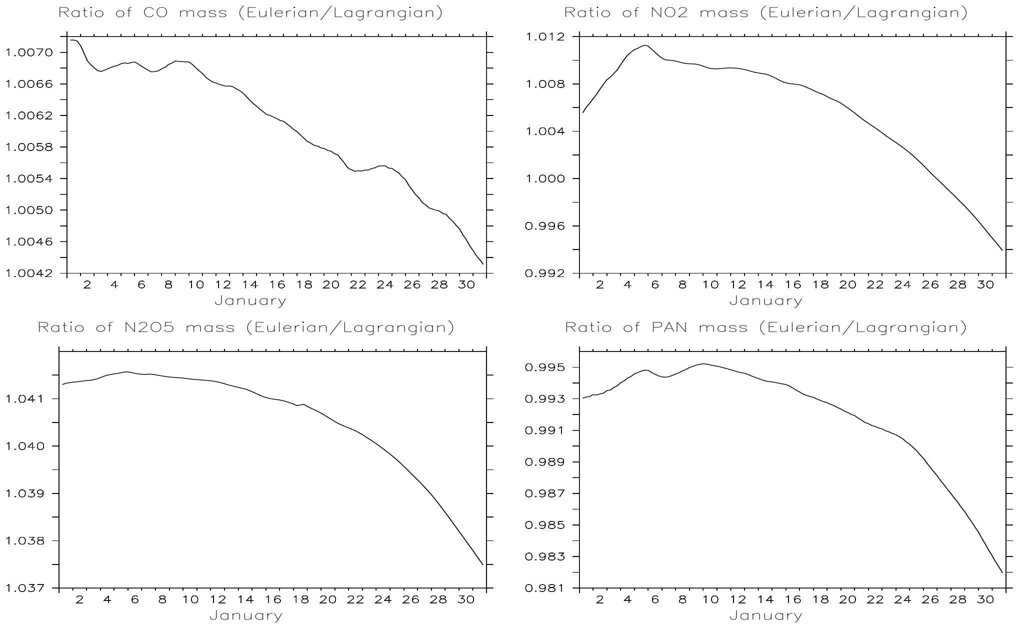

Figure 4.4: Ratio between the Eulerian and Lagrangian representation of the global integrated mass of different tracers

Chapter 5

Improvements of the VOC representation

In this chapter a series of sensitivity simulations is presented. These study options have been performed to improve the quality of the representation of the VOC in *ECHAM5/MESSy1* . In the first part of this chapter, some studies of VOC are presented (*S1A* , *S1B* , *S1C* and *S1D*). In the second part , the effects of the submodel **AIRSEA** are analysed (simulations *S1E* and *S1F*).

All the sensitivity simulations focused on the year 2000, since the emissions set-up was compiled for this year (Sect. 2).

5.1 Sensitivity studies

5.1.1 Updates of the model setup

To test the hypotheses derived in Sect. 2.3.2, a sensitivity simulation *S1A* has been integrated. This simulation is based on the reference simulation *S1* and contains the following modifications:

- The process of dry deposition of CO based on few available measurements (Conrad and Seiler, 1985; Sanhueza et al., 1998) was included. We used a constant soil deposition velocity of 0.04 $\mathrm{cm/s}$ limited to regions where the temperature is higher than 5 °C and the relative humidity is higher than 40% to exclude cold tundra and desert soils (Lawrence et al., 1999b);
- Increase of the CO fossil fuel emission over China by 45 % according to Kiley et al. (2003); The new total amount of CO emission is 1130 $\mathrm{Tg/yr}$, with 314 $\mathrm{Tg/yr}$ due to fossil fuel usage;
- Changed reaction coefficient for the reaction $\mathrm{C_3H_6 + OH}$ as described in Sect. 2.3.4.2 (Atkinson et al., 2005b);
- Decrease of oceanic emission of $\mathrm{C_2H_4}$ as suggested by Plass-Dülmer et al. (1995);
- Increase of $\mathrm{CH_3OH}$ biogenic emissions to 151 $\mathrm{Tg/yr}$ (Jacob et al., 2005);

- Increase of biogenic emissions of CH_3COCH_3 to 55.93 Tg/yr following Folberth et al. (2006);
- New photolysis of CH_3COCH_3 as described by Blitz et al. (2004), Arnold et al. (2004) and Arnold et al. (2005).

In addition to the simulation *S1A* a second simulation (named *S1B*) has been performed. In the simulation *S1B* dry deposition of CO (point 1 of *S1A*) is switched off, while the remaining set up is equivalent to *S1A*.

Table 5.1 lists the analysis and correlations between measurements and sensitivity simulations. With the exception of methanol, the model is performing better than in *S1*, although the improvement is in general not very substantial (see Sect. 2.3.2, Tab. 2.6).

tracer	num. obs.	bias	m	b	R^2
$C_2H_4(S1A)$	454	- 24.782	0.26	9.31	0.413
$C_3H_6(S1A)$	332	- 11.562	0.14	0.18	0.427
$CH_3COCH_3(S1A)$	246	- 211.95	0.57	52.00	0.429
$CH_3OH(S1A)$	116	- 239.05	0.28	380.84	0.273
$CO(S1A)$	456	- 6526.8	0.53	36585	0.660
$CO(S1B)$	456	- 4003.1	0.54	37864	0.651

Table 5.1: Correlation coefficients and linear regression of the comparison of the sensitivity simulations with aircraft observations (model = $m\times$ obs + b). “num. obs.” is the number of observations. Bias and b coefficient in pmol/mol. Bias= model-observations.

The dry deposition of CO, as implemented in *S1A*, yields a total deposition of 74 Tg/yr. This is outside the range suggested in literature by Moxley and Cape (1997) and Sanhueza et al. (1998) and strongly exceeds the dry deposition calculated by Horowitz et al. (2003) of 2 Tg/yr.

In Fig. 5.1, the relative changes between the sensitivity study *S1A* and the evaluation simulation (*S1*) are shown. For the remote regions the decrease in CO mixing ratio is very small (a few percent). No significant improvements of the simulation with respect to the measurements are obtained for remote locations and at the North America stations (see Fig. 5.2). From Fig. 5.2 we can also see that dry deposition of CO slightly decreases the ability of the model to reproduce the CO mixing ratio at high northern latitudes (Zeppelin, (ZEP) and Alert, (ALT)).

In simulation *S1A*, the Chinese emissions of CO (bio-fuel and fossil fuel usage) have been additionally increased from the originally 80.81 Tg/yr to 116.9 Tg/yr. This is in agreement with the value of 116 Tg/yr calculated by Streets et al. (2006) based on the TRACE-P campaign for the year 2000. Despite this drastic increase of the CO emissions over China, the impact on the CO mixing ratios at the surface, over the ocean downwind is small (Fig. 5.1).

Although dry deposition is obviously higher where more CO is emitted (Fig. 5.3), from Tab. 5.1 it is concluded that the impact of this process on CO mixing ratios is generally marginal. The simulation *S1B*, in fact, does not yield significantly different results compared to *S1A*. Moreover, as seen in Fig. 5.4, *S1B*

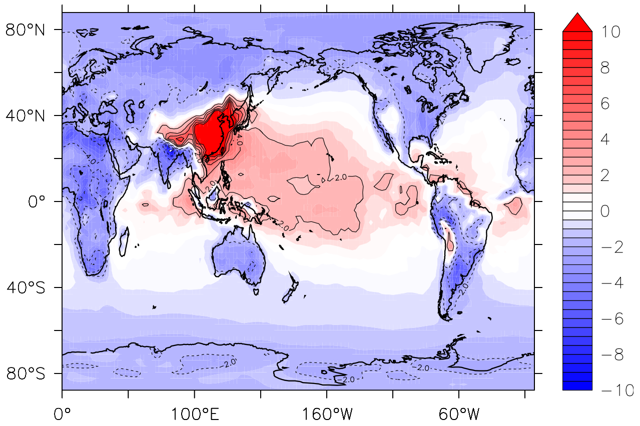

Figure 5.1: Relative difference of the annual average CO mixing ratio at the surface (in %) between sensitivity simulation *S1A* (including dry deposition of CO) and reference simulation *S1* (without dry deposition of CO).

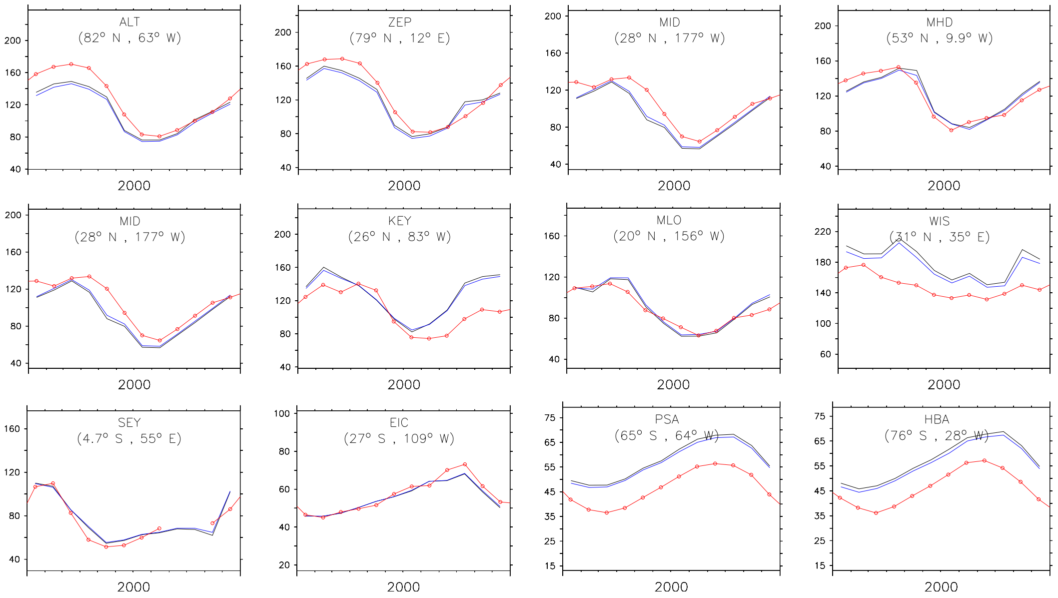

Figure 5.2: Comparison of CO mixing ratios (in $\mathrm{nmol/mol}$): observations are in red, model results are in black (reference simulation *S1*) and blue (sensitivity simulation *S1A*). For the locations Florida (KEY) the model results are sampled one grid-box upwind (see Sect.2.3.3).

does not show an improvement of the vertical profiles of CO compared to observations. Nevertheless, there is strong evidence that the Chinese emissions of CO are underestimated. However, the amount (and the geographic distribution) of the additional unknown sources are not clearly quantifiable (Fig. 5.4).

Furthermore, as shown in Tab. 5.1 and Fig. 5.2, the dry deposition of CO only weakly influences the results, and decreases the correlation between the model results and the measurements. The conclusion is that dry deposition of CO, as implemented for simulation *S1A*, is not suited for future studies.

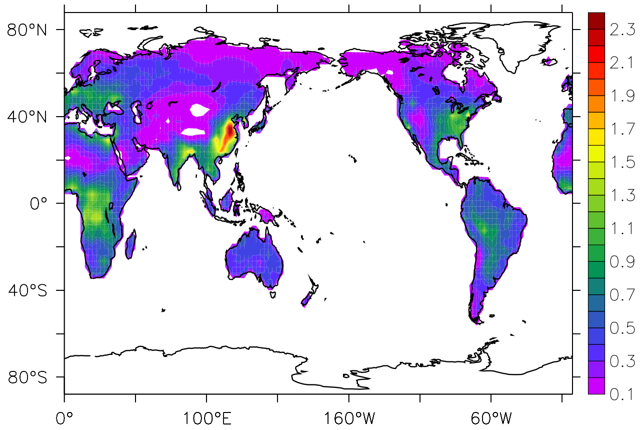

Figure 5.3: Annually integrated dry deposition of CO (simulation *S1A*) in $\mathrm{g/m^2}$.

The changed reaction rate for C_3H_6 slightly improves the correlation of this simulated trace gas (see Tab. 5.1, $R^2 = 0.427$) with aircraft observations. However, the model still simulates strong depletion in the free troposphere (see Fig. 5.5), and at relatively high temperatures (i.e. near the surface) there is virtually no difference between the simulations applying the two different reaction rates (Atkinson et al., 1999b, 2005b). The wrong vertical profile implies that the chemical processes related to this tracer are not well understood; more studies on this tracer (especially on its reaction with OH) are required. However, since the mixing ratios are very low, in the low ppt range close to the observational sensitivity, it cannot be excluded that the measurements are biased.

The decrease of oceanic emissions of C_2H_4 marginally improves the correlation at a few locations (see Fig. 5.6) over the ocean and in the marine boundary layer, but overall the resulting differences between *S1* and *S1A* are not significant ($R^2 = 0.413$ for *S1A*). It is concluded that the major problem is the high uncertainty of the terrestrial C_2H_4 sources.

For methanol, Tab. 5.1 shows a decrease in the correlation between model results and observations for *S1A* compared to *S1*. This is due to an increased scatter of the model results for *S1A* compared to *S1* (Fig. 5.7). Nevertheless, the overall bias is lower in *S1A* (≈ 239 $\mathrm{pmol/mol}$) than in *S1*. The dry deposition of methanol increased from 24.20Tg/yr in the reference simulation *S1* to 82.76 $\mathrm{Tg/yr}$ in the sensitivity simulation *S1A*. In comparison, Jacob et al. (2005) calculated 55 $\mathrm{Tg/yr}$ dry deposition of methanol and Heikes et al. (2002) and Tie et al. (2003) suggested the ranges 35-210 $\mathrm{Tg/yr}$ and 32-85 $\mathrm{Tg/yr}$, respectively. In conclusion, it is recommended to apply the increased amount of biogenic methanol emissions (i.e.,151 $\mathrm{Tg/yr}$) of the *S1a* simulation for future studies.

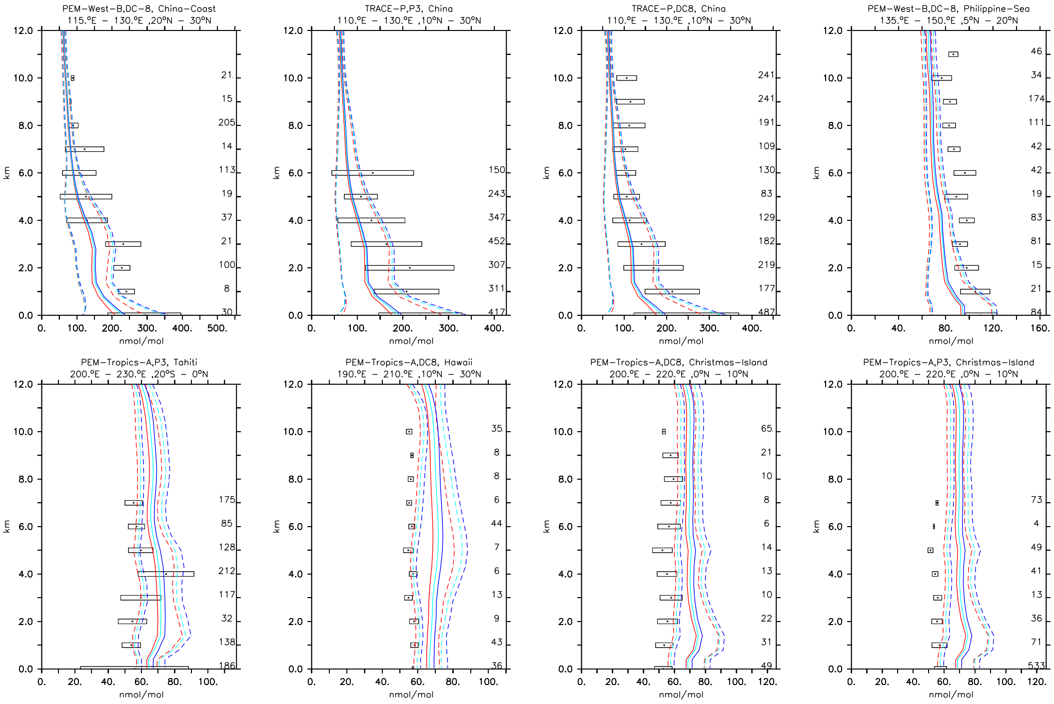

Figure 5.4: Vertical profiles of CO (in $\mathrm{nmol/mol}$) for some selected campaigns from Emmons et al. (2000). Asterisks and boxes represent the average and the standard deviation (w.r.t. space and time) of the measurements in the region, respectively. Red is the reference simulation *S1*, light blue the simulation *S1A*, and dark blue the simulation *S1B*. The corresponding standard deviations w.r.t. time and space are indicted by the dashed lines.

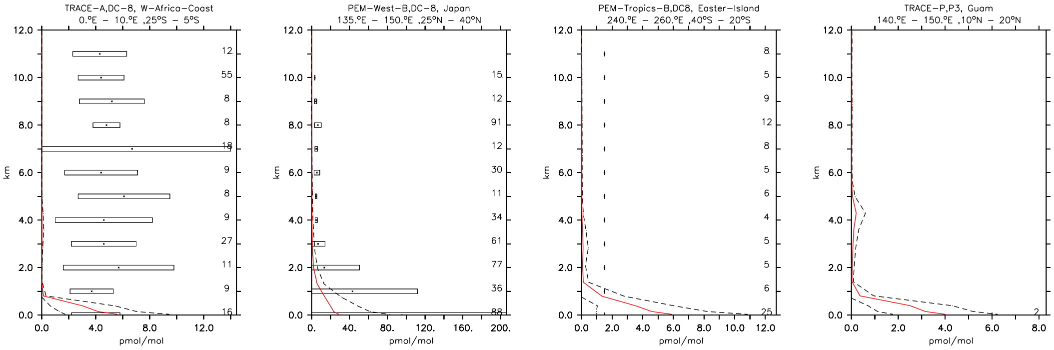

Figure 5.5: Vertical profiles of C_3H_6 (in $\mathrm{pmol/mol}$) for some selected campaigns and for the sensitivity simulation *S1A*. Symbols and colours as in Fig. 2.20.

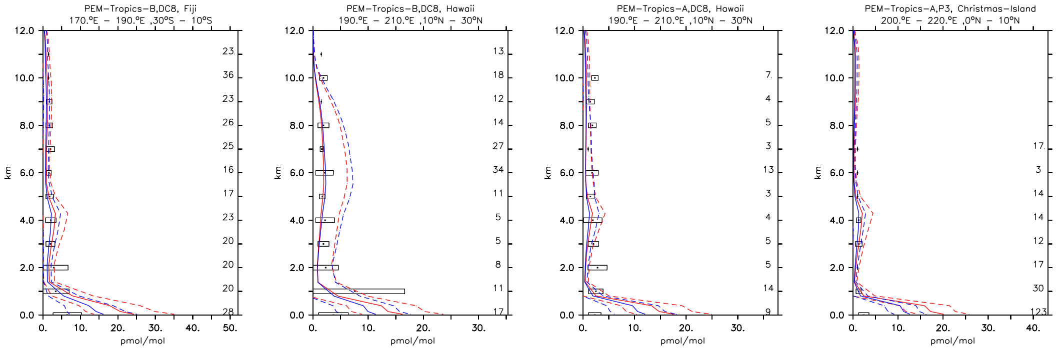

Figure 5.6: Vertical profiles of C_2H_4 (in pmol/mol) for some selected campaigns. The red line shows the results of the reference simulation (*S1*), the blue line the results of the sensitivity simulation *S1A*. Symbols as in Fig. 2.20.

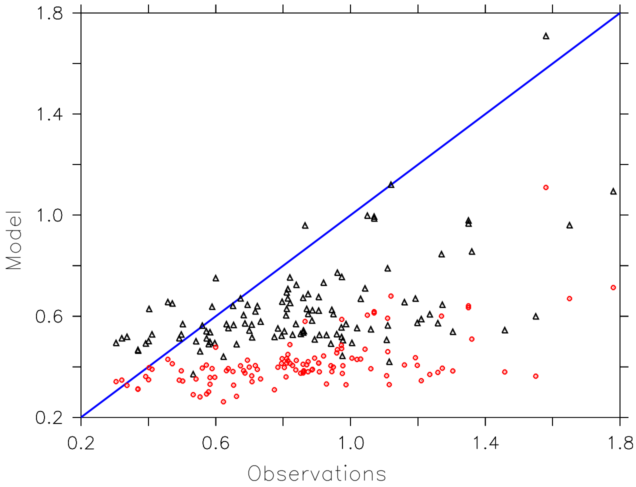

Figure 5.7: Scatter plot of model results versus observations of CH_3OH (both in nmol/mol). The red circles represent the results of the reference simulation (*S1*), the black triangles those of the sensitivity simulation (*S1A*).

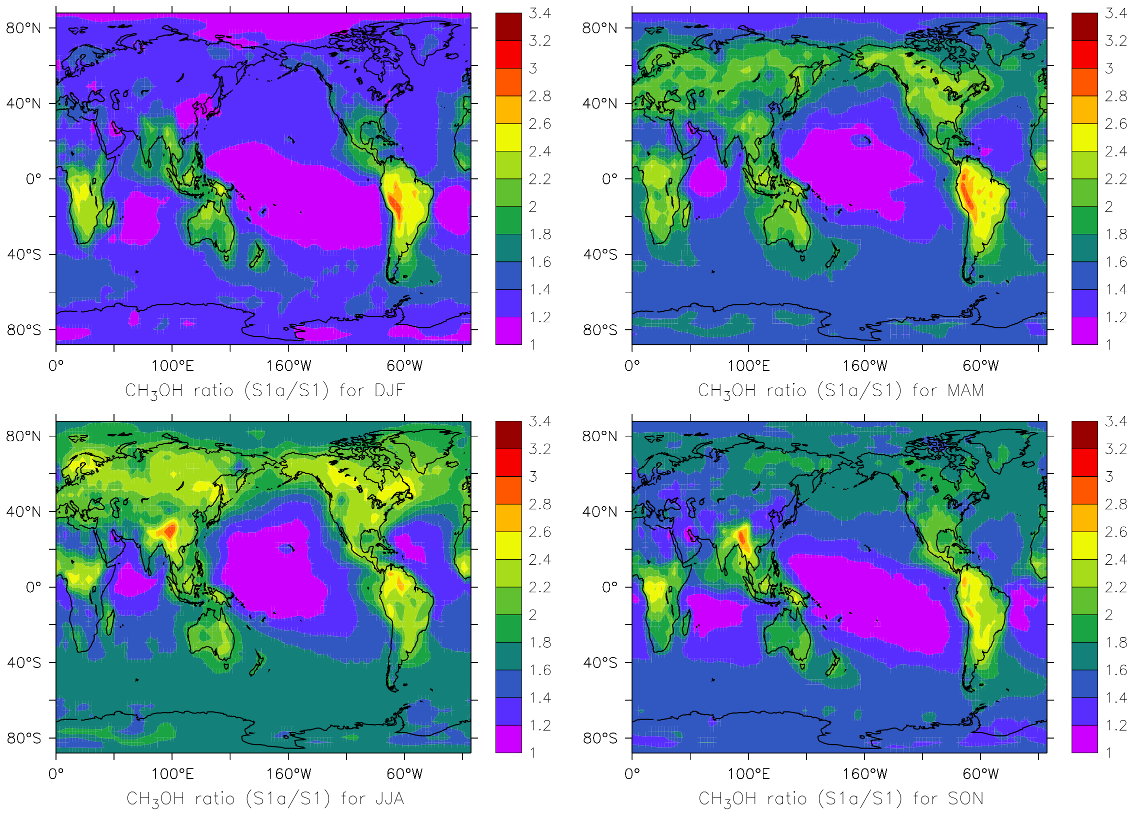

Figure 5.8: Ratio of methanol (CH_3OH) mixing ratio between simulation *S1A* and the reference simulation *S1* at the surface. The simulations are seasonally averaged.

For the photolysis of acetone (CH_3COCH_3) the new quantum yield (Blitz et al., 2004) has been used in simulation *S1A*. The corrected quantum yield is directly applied in the calculation of the photolysis rate (Eq. 2.4):

$$J_X \approx J^a_{1,X} + \sum_{i=2}^{8} J^a_{i,X} \cdot \delta_i \cdot \alpha_{i,X} \tag{5.1}$$

α is the ratio of the old quantum yield (OQY) and the new quantum yield (NQY) calculated in the 8 wavelength intervals $\left(\frac{NQY_{i,X}}{OQY_{i,X}}\right)$.

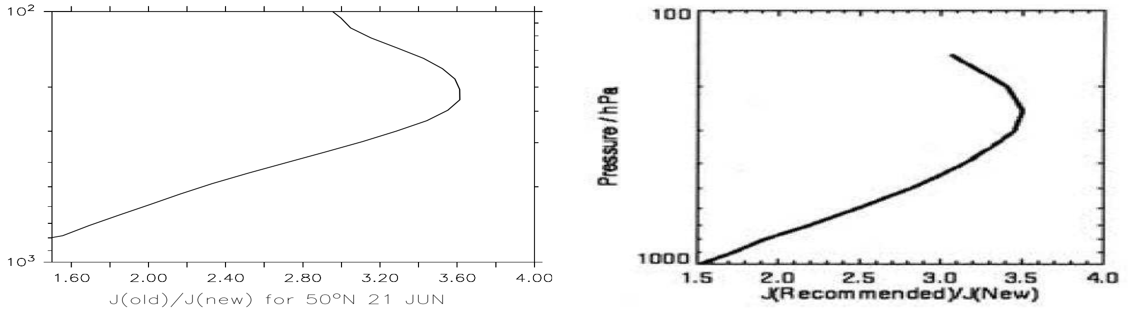

Figure 5.9: Ratio of J(Recommended)/J(New) as a function of altitude calculated for June 21 at 50°N (equinox). The left figure has been calculated with *ECHAM5/MESSy1*, while the right figure is from Blitz et al. (2004).

The correct implementation can be confirmed by Figs. 5.9 and 5.10, where the calculated new photolysis rate is graphically compared wit the work of Blitz et al. (2004).

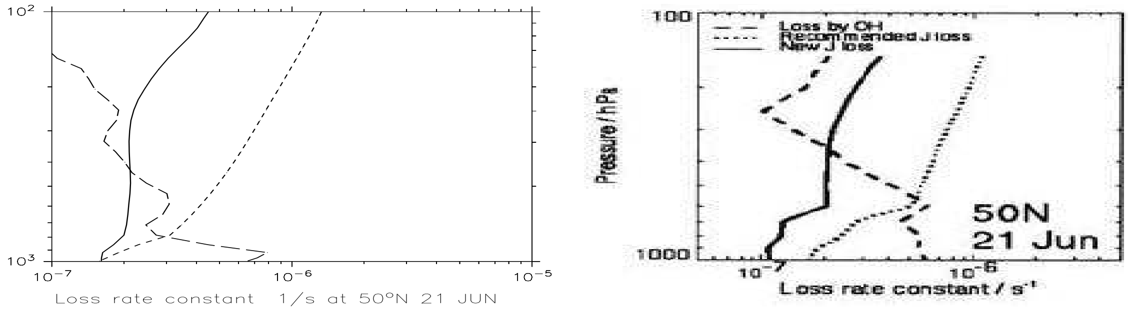

Figure 5.10: Loss rate of acetone by photolysis and reaction with OH calculated as a function of altitude for June 21 at 50°N. The left figure has been calculated with *ECHAM5/MESSy1* , while the right figure is from Blitz et al. (2004). In both figures, the continuous line in the loss rate due to photolysis with the "new" quantum yield; the dotted line is the loss rate due to photolysis with the "old" quantum yield and the dashed line is the loss rate due to reaction with OH.

This modification of the model setup improved the model results w.r.t. the observations (Tab. 5.1). Fig. 5.11, for example, clearly shows for the TRACE-P campaign (Japan) that the results of the *S1A* simulation are closer to the observations than those of the *S1* simulation. This is quantitatively confirmed by the correlation analysis between the different model results and the observations. For the sensitivity simulation

S1A the correlation coefficient increased (from $R^2 = 0.385$ to $R^2 = 0.429$) and the overall bias decreased (from -376.85 to -211.95 pmol/mol) based on the reference simulation. However, compared with station data, the *S1A* simulation shows a decrease in the correlation and an increased bias (see Tab. 5.2). This implies that the value of ≈ 56 Tg/yr suggested by Folberth et al. (2006) for the biogenic emissions likely is too high. Discrepancies between the model results and the observations remain, especially over the oceans and in the upper troposphere (Fig. 5.11). This is probably related to an oversimplified representation of the deposition / emission of acetone from oceans, an issue under debate (Singh et al., 2001; Jacob et al., 2002; Singh et al., 2003; Marandino et al., 2005) that will be further analysed in Sect. 5.1.3.

CH_3COCH_3	bias	m	b	R^2
S1	- 0.078	0.528	459.67	0.508
S1A	-0.15	0.67	525.9	0.435

Table 5.2: Correlation coefficients and linear regression analysis of model results versus station observations (model = $m\times$ measurement + b). Bias and b are in pmol/mol; bias = model results minus observations.

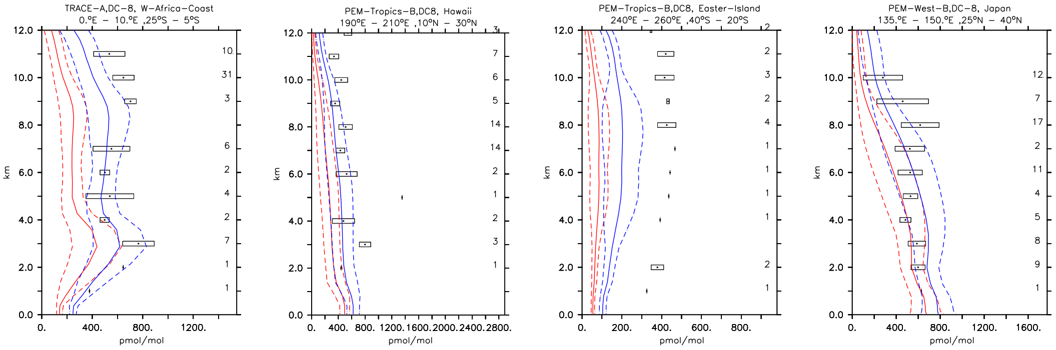

Figure 5.11: Vertical profiles of CH_3COCH_3 (in pmol/mol) for some selected campaigns. The red line shows the results of the reference simulation *S1*, the blue line the results of the sensitivity simulation *S1A*. Symbols as in Fig. 2.20.

5.1.2 Importance of dry deposition

Because a remarkably low sensitivity of CO mixing ratios to the emissions from China and dry deposition (see Sect. 5.1.1) has been found, it is desirable to rule out potential systematic errors connected to the operator splitting as applied in our model. In the standard *ECHAM5/MESSy1* set up, emission tendencies are calculated before the dry deposition tendencies of trace gases. Therefore, an additional sensitivity simulation (*S1C*) has been performed, in which the order of processes has been changed, such that the dry deposition tendency is calculated before emission tendencies and chemical tendencies. The model setup is the same as for *S1A*.

As shown in Tab. 5.3, the change in the annually averaged dry deposited tracer mass is 5% at maximum.

From this it is concluded that the systematic error due to the applied operator splitting is small (as for instance compared to uncertainties in emission estimates) and that the low sensitivity mentioned above is a robust result.

tracer	*S1A*Tg/yr	*S1C*Tg/yr	difference (%)
CO	74.	73.6	-0.5
CH_3OH	82.76	78.14	-5.5
CH_3COCH_3	31.25	29.82	-4.57

Table 5.3: Annual average dry deposition of different tracers as calculated by the different sensitivity simulations.

Because it has been ruled out that the operator splitting strongly influences the simulation, a simple change in the big-leaf approach for dry deposition has been tested, to evaluate the sensitivity of OVOC to this process. Only a few measurements are available of the dry deposition of OVOC. For methanol some indications can be obtained from Goldstein et al. (1995), Riemer et al. (1998), Holzinger et al. (2001) and Karl et al. (2004). Nevertheless, acetone has been used for this purpose because of its intermediate chemical characteristics w.r.t. solubility and reactivity. The big leaf approach is expected to have the highest uncertainties for trace gases which are partially soluble (see Sect. 2.1.2.6). Additionally, for this tracer the calculated dry deposition in *ECHAM5/MESSy1* (24.48 Tg/yr) is outside the range present in the literature (8.8-13 Tg/yr), as shown in Tab. 2.4.

Microbial activity in the terrestrial biosphere is both a source and a sink for acetone. Diurnal cycles of atmospheric acetone concentrations at eastern North American sites in summer show typically a 20% decrease from sunset to sunrise (Shepson et al., 1991; Goldan et al., 1995; Lee et al., 1995; Jacob et al., 2002) which could reflect microbial uptake. Nevertheless, Shade and Goldstein (2000) measured a weak net emission flux from the soil at night. As implemented in other models (e.g. GEOS-CHEM, Bey et al. (2001)), a constant dry deposition velocity of 0.1 cm/s has been used in the additional simulation *S1D*. This constant dry deposition velocity is applied only over ice-free land and gives $\approx$ 20 % decrease in concentration from sunset to sunrise for a 100 meter deep mixed layer (in absence of compensating emissions). Furthermore the role of snow in the acetone budget is still unclear. Grannas et al. (2002) and Guimbaud et al. (2002) showed that in the Arctic spring snow is a daytime source and a nighttime sink for acetone, which largely cancel each other over time. This process has hence been neglected in the *S1D* simulation.

The simulation *S1D* has been performed with the same set up as the evaluation simulation *S1A* but with the alternative dry deposition for CH_3COCH_3.

The total CH_3COCH_3 yearly deposited with this new approach is 22 Tg/yr, which is very close to the value obtained with the big leaf approach in the simulation *S1* and $\approx 27\%$ lower as calculated in simulation *S1A*. As shown in Fig. 5.12, while the dry deposition decreased over land, it increased over the ocean.

The regression analysis (Tab. 5.4) clearly shows that, although the agreement between the results of simulation *S1D* and aircraft observations increased with respect to the simulations *S1*, they decreased with respect to the simulations *S1A*. As shown in Fig. 5.13, the improvements in the simulated vertical profile of CH_3COCH_3 are not substantial. On the other hand, the comparison with station measurements does

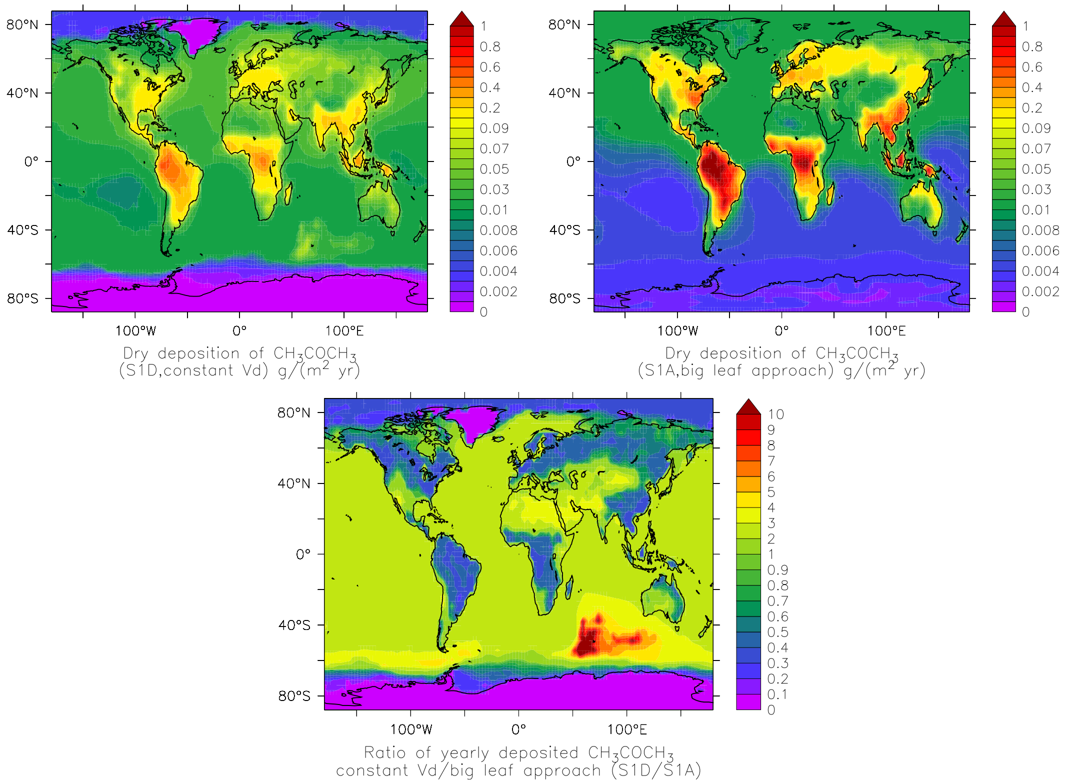

Dry deposition of CH_3COCH_3 (S1D,constant Vd) g/(m^2 yr)

Dry deposition of CH_3COCH_3 (S1A,big leaf approach) g/(m^2 yr)

Ratio of yearly deposited CH_3COCH_3 constant Vd/big leaf approach (S1D/S1A)

Figure 5.12: annualy integrated CH_3COCH_3 dry deposited in simulation *S1D* (upper left), simulation*S1A* (upper right) and the ratio of the two (bottom).

not give satisfactory results and the decreased agreement of simulation *S1D* with respect to simulations *S1* and *S1A* implies that this process is not correctly parameterised. It is concluded that the big leaf approach used in *ECHAM5/MESSy1* gives a reasonable dry deposition, and probably more effort should be invested to constrain uncertainties of the emissions, to which the model is more sensitive. The few measurements available of acetone uptake, in fact, are too sparse to estimate any deposition velocity that could decrease the uncertainties related to this process. The theoretical approach with all its limitations is still the most reliable technique that can be used to calculated the dry deposition of acetone and, most probably, of other organic compounds. Nevertheless, measurements in this fields that can give additional information, are strongly needed.

CH_3COCH_3 (*S1D*)	bias	m	b	R^2
aircraft observations	-259	0.57	77	0.46
stations observations	-145	0.80	367	0.44

Table 5.4: Correlation coefficients and linear regression analysis of model results versus observations (model = $m\times$ measurement + b) for the simulation *S1D*. Bias and b are in $\mathrm{pmol/mol}$; bias = model results minus observations.

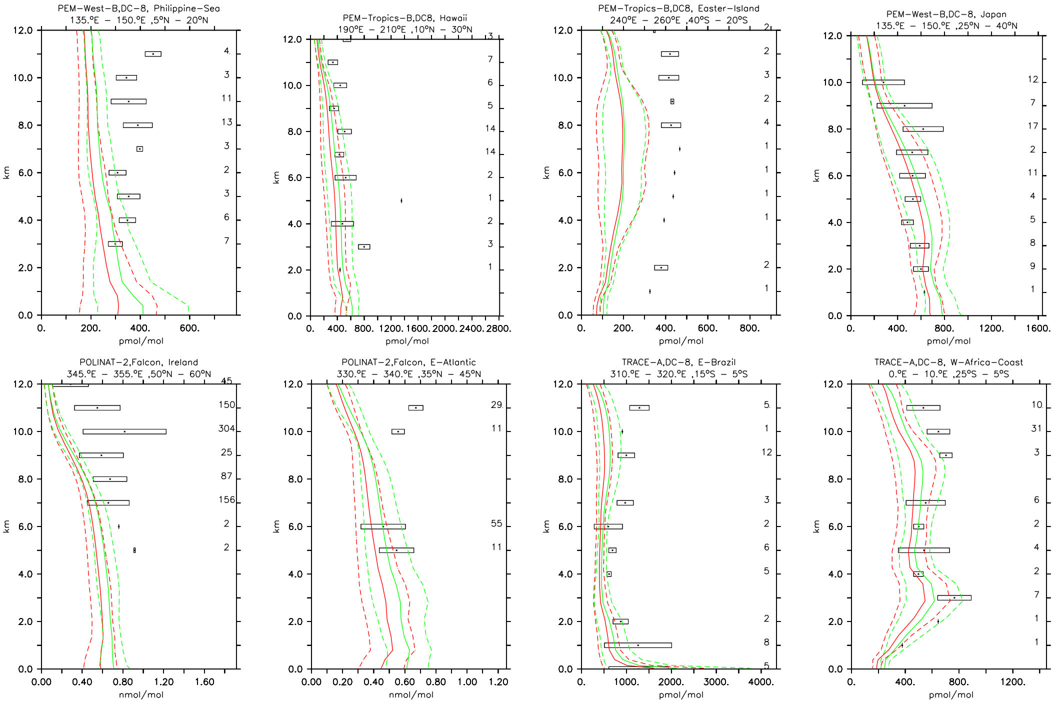

Figure 5.13: Vertical profiles of CH_3COCH_3 (in $\mathrm{pmol/mol}$) for some selected campaigns. The red line shows the results of the sensitivity simulation *S1D*, the green line the results of the sensitivity simulation *S1A*. Symbols as in Fig. 2.20.

5.1.3 The AIRSEA submodel and the OVOC

From the results obtained with the previous simulations, the following changes result in a clear improvement in the model simulation of NMHC:

- Increase of CH_3OH biogenic emissions to $151\ \mathrm{Tg/yr}$ (Jacob et al., 2005);
- New photolysis of CH_3COCH_3 as described by Blitz et al. (2004), Arnold et al. (2004) and Arnold et al. (2005).

These changes have been adopted into the two simulation *S1E* and *S1F*, which are used to investigate more specifically the effects of the **AIRSEA** submodel on the simulation of OVOC.

5.1.3.1 Liquid phase concentrations of CH_3CHO and CH_3COCH_3

As shown in Sect. 3.2, the submodel **AIRSEA** can be applied for different gases, giving realistic results. The submodel **AIRSEA**, however, has been designed to simulate in particular the exchange of OVOC. The simple NMVOC (i.e. C_2H_6, C_2H_4, C_3H_8 and C_3H_6) are generally emitted to the atmosphere, and the **OFFLEM** submodel describes this sufficiently accurate. In fact, the offline emissions of these trace gases have been pre-calculated using an ocean model, following the same algorithm as described in Sect. 3.2 for **AIRSEA**. In absence of an ocean model coupled to *ECHAM5/MESSy1*, **AIRSEA** would obtain the same results with additional calculations; hence, for computational reasons, the focus is only on oxygenated organic compounds, where no ocean effect was implemented, so far.

The submodel **AIRSEA** will hence be used only to compute the exchange rates of only oxygenated organic compounds (CH_3OH, CH_3CHO and CH_3COCH_3). Unfortunately, measurements of these organic species in the ocean are still scarce and the very limited knowledge of the liquid phase concentration of the OVOC in the oceans currently represents the most important limitation in the application of this submodel. In fact, as pointed out in Sect. 3.2, the concentration of the studied gas in the liquid phase is a critical parameter for the application of the **AIRSEA** submodel.

While numerous measurements of liquid phase concentrations are available for C_2H_6, C_2H_4, C_3H_8 and C_3H_6 (Plass-Dülmer et al. (1995, and references therein), Broadgate et al. (2000, and references therein)), for OVOC (specifically, acetone (CH_3COCH_3), methanol (CH_3OH) and acetaldehyde (CH_3CHO)) only a few studies are present in literature. In case of oxygenated compounds, in fact, these measurements are difficult, and only in the last few years, after the importance of the oceans has been recognized more field campaigns have been planned specifically for these measurements. In Tab. 5.5 a resume of the measurements available from literature is presented.

Based on Tab. 5.5 for methanol a simple saturation coefficient has been used to calculate the concentrations in the liquid phase on-line (automatically done by **AIRSEA**) with the following equation:

$$C^{liquid}_{\mathrm{CH_3OH}} = SHC^{gas}_{\mathrm{CH_3OH}} , \tag{5.2}$$

where $C^{liquid}_{\mathrm{CH_3OH}}$ is the concentration in the liquid phase for methanol, H the henry's law coefficient, S the saturation coefficient (in this case 0.94, according to Singh et al. (2003)), and $C^{gas}_{\mathrm{CH_3OH}}$ the concentration of methanol in the gas phase.

	Average water conc. nmol/L	Location	Reference
Acetone, CH_3COCH_3	17.6	Tropical Atlantic	Williams et al. (2004)
	14.5	North Pacific Ocean	Marandino et al. (2005)
	54.8	Carribean Sea	Zhou and Mopper (1993)
	12	- (model study)	Jacob et al. (2002)
	10	Pacific Ocean	Singh et al. (2003)
	balanced with atmosphere	Mace Head	Lewis et al. (2005)
Methanol, CH_3OH	118.4	Tropical Atlantic	Williams et al. (2004)
	100	Pacific Ocean	Singh et al. (2003)
	300	- (model study)	Galbally and Kirstine (2002)
	100 (94% saturation)	Mace Head	Carpenter et al. (2004)
	100	- (model study)	Heikes et al. (2002)
Acetaldehyde, CH_3CHO	15.7	Carribean Sea	Zhou and Mopper (1993)
	7	Pacific Ocean	Singh et al. (2003)

Table 5.5: Measurements of liquid phase concentrations of different oxygenated compound present in literature

In contrast to methanol, for acetaldehyde and acetone a more sophisticated approach has been used. To derived reasonable water concentration fields for these two tracers, the emission fields produced by Guenther et al. (1995) have been used. These fields are based on chlorophyll measurements together with model calculations of **P**hotosyntetically **A**ctive **R**adiance (**PAR**) at the sea surface, which shows a linear correlation with OVOC concentrations (Sinha et al., 2006). Chlorophyll is used as a proxy for the **D**issolved **O**rganic **M**atter (**DOM**), which has been found to correlate linearly with the VOC concentration in the water (Ratte et al., 1994, 1998; Riemer et al., 2000).

Williams et al. (2004) showed clearly that a North-South gradient for the liquid phase of these tracers is present, due to the shorter lifetime of these compounds in the liquid phase with respect to the air-sea transfer time scale (Zhou and Mopper, 1997, 1993). To simulate this gradient, the Guenther et al. (1995) fields have been scaled with a normalised multi-year (2000-2005) zonal average of the concentrations of these gases in the gas phase, calculated from the model results of *S1* and for the lowest level of the model.

Finally the results have been multiplied by a constant to obtain (within an error of 5%) the observed values listed in 5.5. These fields are only a first "order" approximation and no quantification of the relative errors is possible. Nevertheless, due to the absence of an ocean submodel in *ECHAM5/MESSy1* for the on-line calculation of these parameters, only this approach based on reasonable assumptions is possible. In Figs. 5.15 and 5.14 the calculated concentration fields are shown for January and July for acetaldehyde and acetone.

5.1.3.2 The Effect of the AIRSEA submodel

In the simulation *S1E* the submodel **AIRSEA** has been activated for CH_3COCH_3,CH_3OH and CH_3CHO, the liquid phase concentrations of these tracers have been prescribed as explained in Sect. 5.1.3.1. In

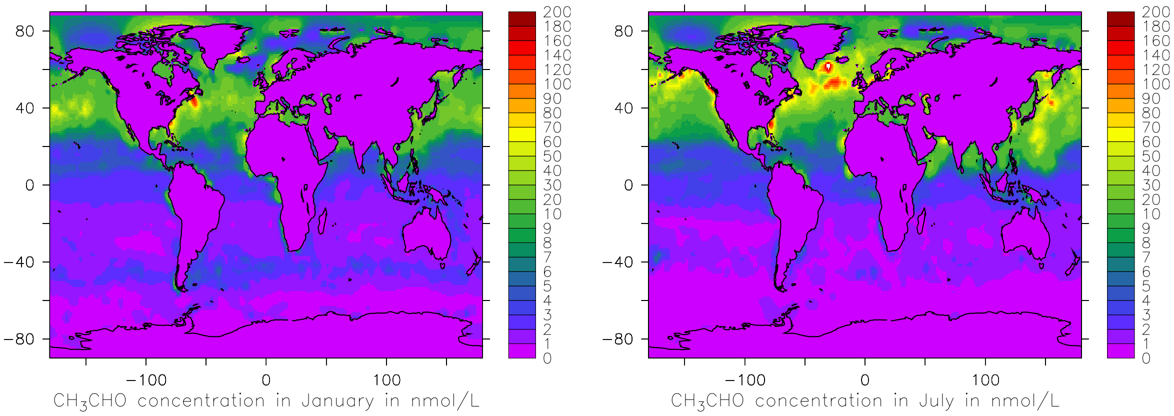

Figure 5.14: Pre-calculated liquid phase concentrations of CH_3CHO for January (left) and July (right)

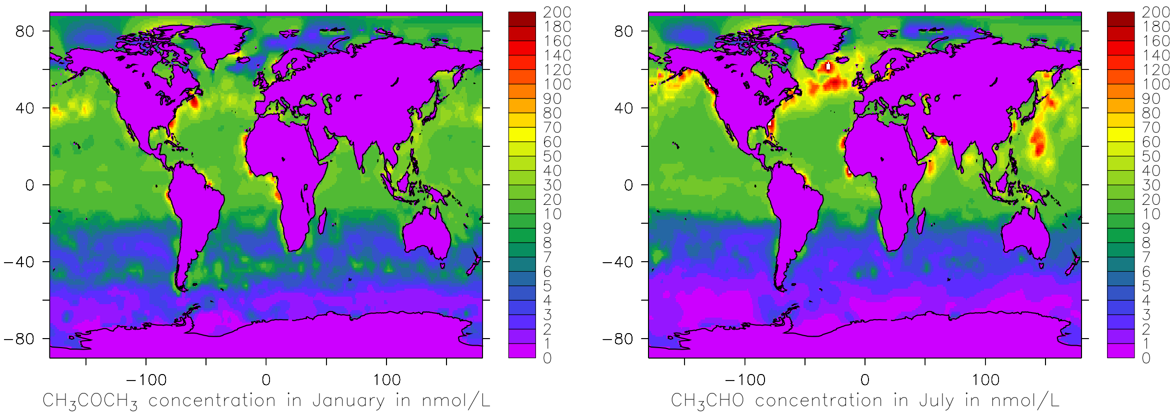

Figure 5.15: Pre-calculated liquid phase concentrations of CH_3COCH_3 for January (left) and July (right)

appendix C the constants used in the submodel are listed.

The few measurements available for CH_3CHO over the ocean (see Sect. 2) have been performed during the PEM-TROPICS-B campaign (Singh et al., 2001). During this campaign, mixing ratios between 60 and 100 pmol/mol have been measured. We note, however that CH_3CHO measurements by aircraft at the MPI for chemistry indicate that upper troposphere mixing ratios can be overestimated due to a yet unresolved artifact in the inlet system at lower pressure (J.Williams, personal comm.). Therefore, is cannot be excluded that some of the measuremetns in the upper troposphere, as presented in fig 5.16, may suffer from the same problem.

The improvement in the model of the simulation *S1E* with respect to the reference simulation *S1* are shown in Fig. 5.16. Although both simulations underestimate the mixing ratio of this tracer in the troposphere, the error decreased from a factor of 10 (in *S1*) to a factor of 3 (in *S1E*) or less in the lower troposphere.

Nevertheless, with the small number of data available, a global picture is not possible, and no further information about the reliability of the calculated liquid phase concentration of this trace gas can be obtained.

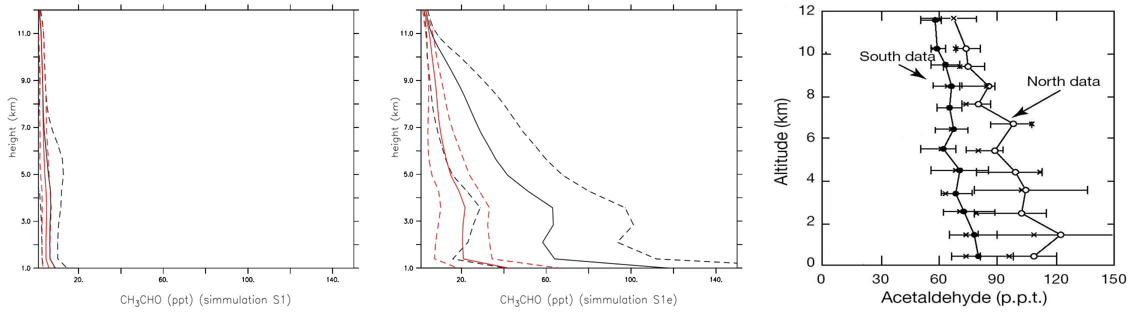

Figure 5.16: Left: acetaldehyde mixing ratios in ppt w.r.t time and space in the region of the PEM-TROPICS-B campaign (simulation *S1*). Red is calculated for the SH and black for the NH. The dashed lines represent the simulated standard deviation w.r.t. time and space. Center: as the left picture but from simulation *S1E*. Right: The observations of the PEM-TROPICS-B from Singh et al. (2001).

In case of methanol (CH_3OH) the global oceanic sink is 4.3 Tg/yr which is within the range of the values suggested in literature (50 Tg/yr Heikes et al. (2002), 0.3 Tg/yr Galbally and Kirstine (2002) and 10 Tg/yr Jacob et al. (2005)). The regression analysis between simulation *S1E* and aircraft observations is listed in Tab. 5.6. Compared to the simulation *S1A*, the improvements are negligible.

Nevertheless, the normalised standard deviation between observations and simulations increased from 0.546 (*S1A*) to 0.606 (*S1E*). This implies that the vertical gradients of CH_3OH are somewhat better simulated in *S1E*.

The improvement in the methanol vertical profiles is shown in Fig. 5.17 (PEM-TROPICS-B, all locations). The decrease of the ocean sink, with respect to the big leaf approach used before, improved the representation, in particular in the free troposphere. The air-sea exchange process is hence important to obtain the correct representation of methanol not only in the marine boundary layer, but especially in the free/upper troposphere.

These results are summarised in the Taylor diagram in Fig. 5.18; with this diagram the improvement

tracer	num. obs.	bias	m	b	R^2
$CH_3OH(S1E)$	116	- 317.93	0.32	268.68	0.284
$CH_3OH(S1A)$	116	- 239.05	0.28	380.84	0.273
$CH_3COCH_3(S1E)$	246	- 201.95	0.59	45.02	0.479
$CH_3COCH_3(S1A)$	246	- 211.95	0.57	52.00	0.429

Table 5.6: Correlation coefficients and linear regression of the comparison of the sensitivity simulations with aircraft observations (model = $m\times$ meas + b). Bias and b coefficient in pmol/mol. Bias= model-observations.

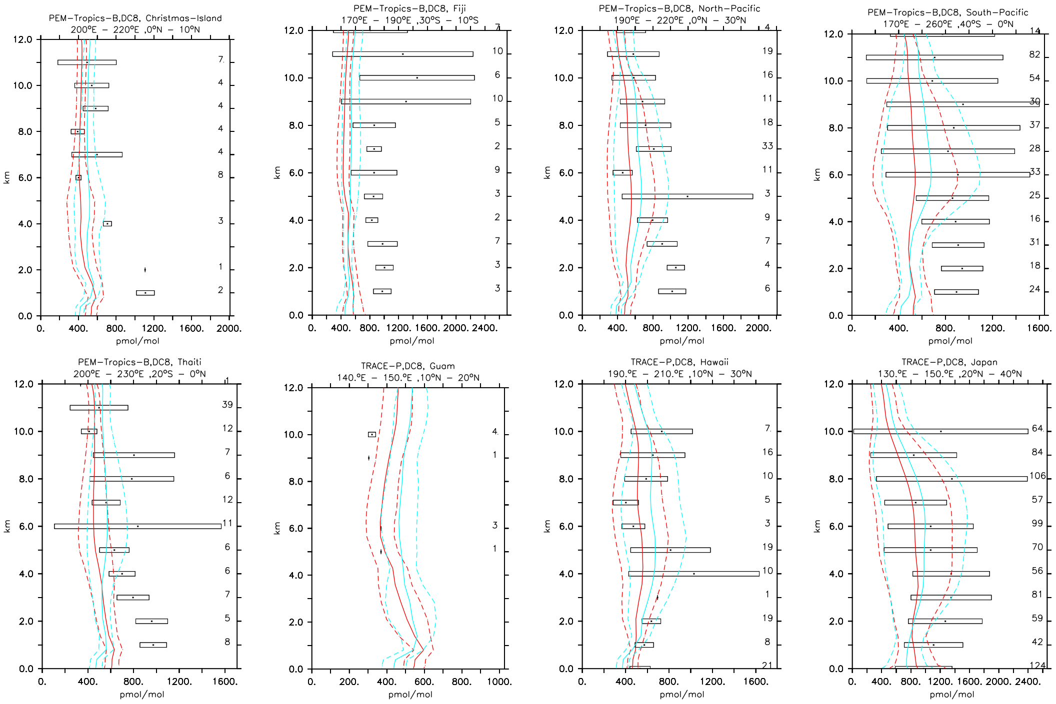

Figure 5.17: Vertical profiles of CH_3OH (in $\mathrm{pmol/mol}$) for some selected campaigns. The red lines show the results of the reference simulation *S1A* and the light blue lines the results of the sensitivity simulation *S1E*. Symbols as in Fig. 2.20.

obtained with an oceanic sink for CH_3OH are better quantifiable. It has to be emphasized that the calculations are generally biased by the uncertainties in the biogenic emissions which, as seen in Sect. 2 (Tab. 2.4), are the strongest component in the budget of this tracer.

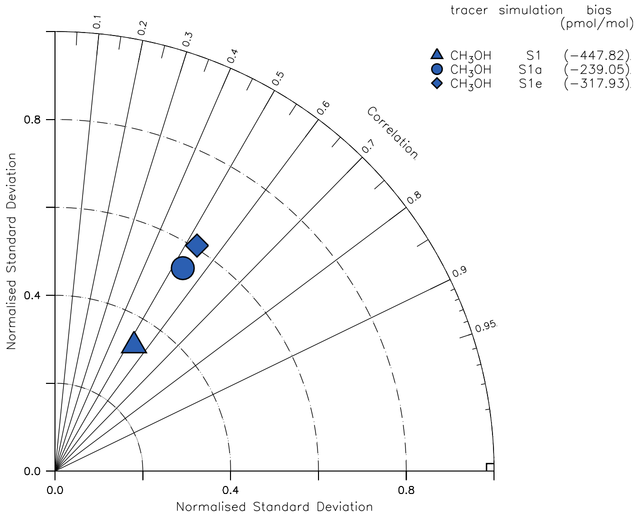

Figure 5.18: Taylor diagram of the comparison between aircraft measurements and model results for methanol. The symbols denote the different sensitivity simulations, respectively. The biases are listed in parentheses (in pmol/mol).

Also in the case of acetone the effects of using **AIRSEA** seems negligible. As listed in Tab. 5.6 and shown in Fig 5.19, the comparison with the aircraft observations improves only marginally (PEM-TROPICS-B, Fiji and Thaiti) and the results remain largely unchanged from the simulation *S1A*. Nevertheless, the increase in correlation and the decreased bias indicate that the submodel **AIRSEA** is acting in the right direction, although it still needs to be improved.

5.1.3.3 Special case: constant liquid phase concentration

Because the effect of the air-sea exchange is very low in the case of CH_3COCH_3, a further simulation (named *S1F*) has been performed. The objective of this analysis is to see if the low impact of the submodel **AIRSEA** on the representation of acetone is due to an incorrect representation of the liquid phase concentrations. The set-up of *S1F* is the same as that of simulation *S1E*. The unique change is the use of a constant concentration of 14 $\mathrm{nmol/L}$ for the liquid phase concentration of CH_3COCH_3 as input for the submodel **AIRSEA**.

The regression analysis (see Tab. 5.7) shows a decrease of the agreement between model simulation and aircraft measurements; also the normalised standard deviation decreased from 0.86 (*S1E*) to 0.75 (*S1F*).

This provides an additional confirmation of the finding described in Sect. 5.1.3.2. The simulated vertical profiles of CH_3COCH_3 are very sensitive to the liquid phase concentrations used in the **AIRSEA** submodel. This is confirmed by Fig. 5.20, which further indicates the decreased agreement between simulation *S1F* and aircraft observations with respect to the simulation *S1E*, especially over the ocean (PEM-TROPICS-B, Fiji or Thaiti).

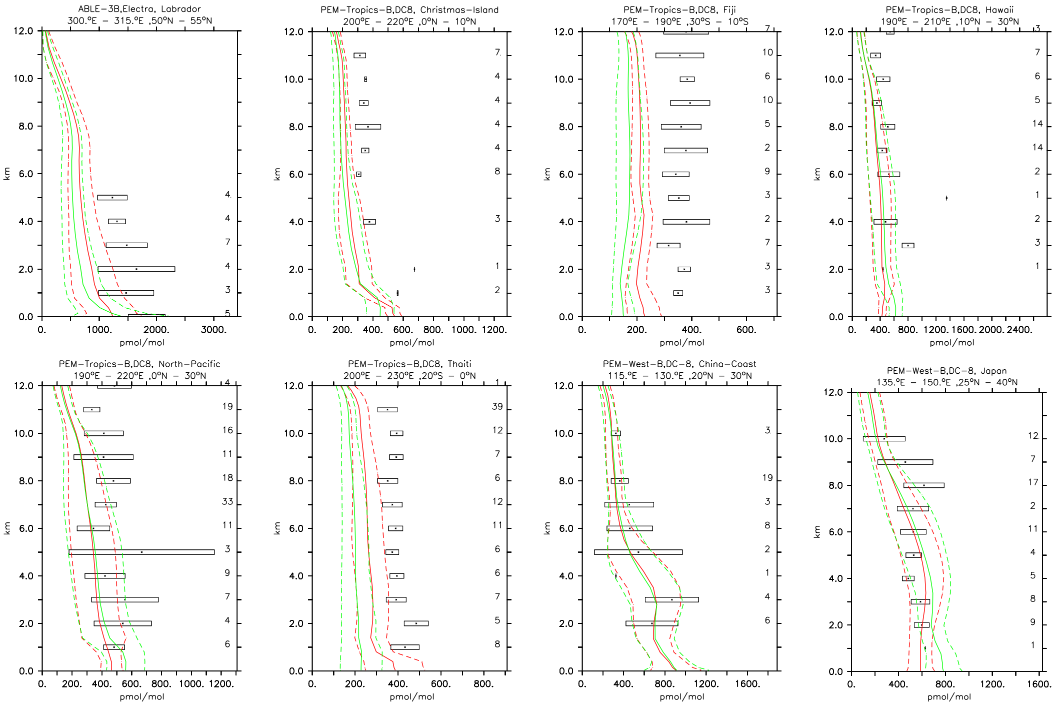

Figure 5.19: Vertical profiles of CH_3COCH_3 (in pmol/mol) for some selected campaigns. The red lines show the results of the reference simulation *S1E* and the green lines the results of the sensitivity simulation *S1A*. Symbols as in Fig. 2.20.

tracer	num. obs.	bias	m	b	R^2
$CH_3COCH_3(S1E)$	246	- 201.95	0.59	45.02	0.479
$CH_3COCH_3(S1F)$	246	- 231.35	0.49	73.69	0.434

Table 5.7: Correlation coefficients and linear regression of the comparison of the sensitivity simulations *S1E* and *S1F* with aircraft observations for acetone (model = $m\times$ meas + b). Bias and b coefficient in pmol/mol. Bias= model-observations

The same conclusion drawn for methanol is hence valid: The exchange through the ocean interface for gases close to Henry's equilibrium between gas phase and liquid phase (which is the case of many oxygenated compounds) is important for a correct representation of the vertical profile of these gases. The low impact of **AIRSEA** in *S1E* is due to the use of a liquid phase concentration of $\mathrm{CH_3COCH_3}$ which is very close to balance with the gas phase concentration of the same trace gas.

This analysis furthermore confirms that the upscale technique applied with only one meaningful value is not reliable for processes depending on biological activity. In the case of *S1F* in fact, the use of one single measurement to fix the liquid phase concentration yields a decrease in the agreement between the simulation and the observations.

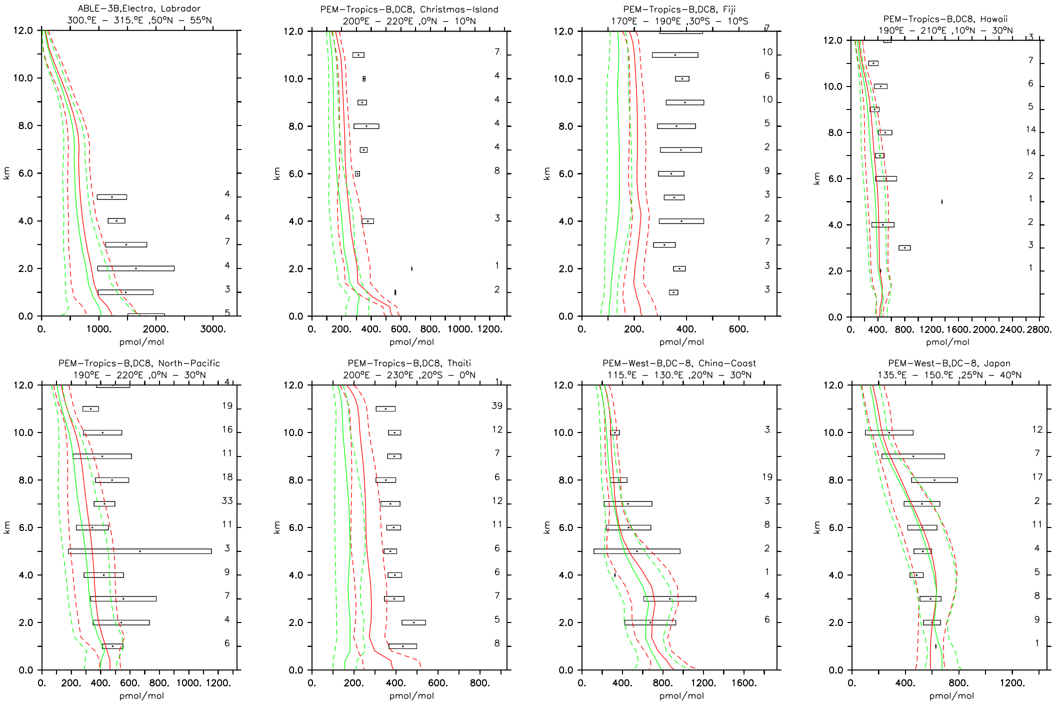

Figure 5.20: Vertical profiles of $\mathrm{CH_3COCH_3}$ (in $\mathrm{pmol/mol}$) for some selected campaigns. The red lines show the results of the reference simulation *S1E* and the green lines the results of the sensitivity simulation *S1F*. Symbols as in Fig. 2.20.

5.2 Conclusions

In this chapter some sensitivity simulations have been presented to improve the representation of organic compounds in the model. Table 5.8 summarised the changes applied in each simulation analysed with respect to the reference simulation *S1*,as described in Sect. 2. The Taylor diagram in Fig. 5.21 shows the overall results of the sensitivity studies.

The sensitivity simulations performed support the recent finding (Horowitz et al., 2003) that dry deposition of CO has been overestimated in many modelling studies so far. The agreement of CO simulations

Different set up with respect to *S1*	*S1A*	*S1B*	*S1C*	*S1D*	*S1E*	*S1F*
Dry deposition of CO	√		√	√		
Increase CO emission from China	√	√	√	√		
Reduced reaction coefficient between C_3H_6 and OH	√	√	√	√		
Decrease oceanic emission of C_2H_4	√	√	√	√		
Increase of CH_3OH biogenic emission	√	√	√	√	√	√
Increase of CH_3COCH_3 biogenic emission	√	√	√	√		
New photolysis rate of CH_3COCH_3	√	√	√	√	√	√
Inversion of operator splitting (emission/deposition)			√			
Constant dry deposition velocity for CH_3COCH_3				√		
AIRSEA application with variable liquid phase concentration for CH_3CHO					√	
AIRSEA application with a saturation value for CH_3OH					√	√
AIRSEA application with variable liquid phase concentration for CH_3COCH_3					√	
AIRSEA application with constant liquid phase concentration for CH_3COCH_3						√

Table 5.8: Summary of the changes applied in the different sensitivity simulations with respect to the reference simulation *S1*.

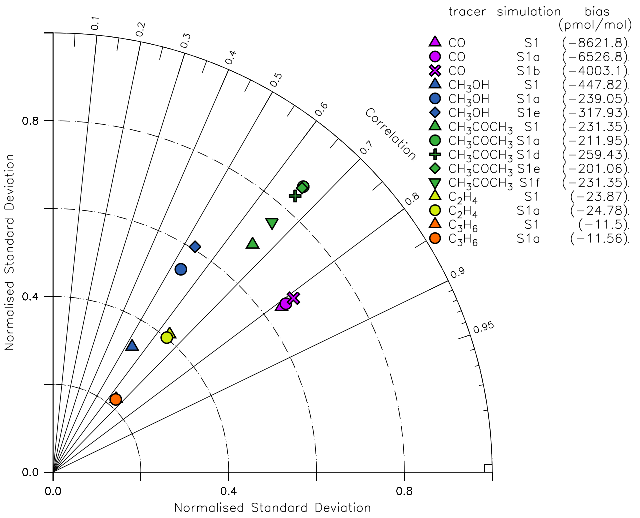

Figure 5.21: Taylor diagram of the comparison between aircraft measurements and model results. The color code denotes the tracers and the symbol the different sensitivity simulations, respectively. The biases are listed in parentheses (in pmol/mol).

with observations is best if the dry deposition of CO represents none or only a negligible contribution to the global CO budget. For alkenes, the results of the simulation *S1A* strongly indicate that the terrestrial emissions of C_2H_4 are significant (though largely unknown) and that the photochemistry of C_3H_6 is not yet fully understood. The same simulation also indicates that an increase of the methanol biogenic emissions to $151\ \mathrm{Tg/yr}$ decreases the discrepancies between model results and observations; however, the results are still not satisfactory.

An update of the photolysis rate calculation for acetone according to more recent estimates (Blitz et al., 2004) results in a higher correlation of model results with measurements, and reduces the problem in the upper troposphere.

The sensitivity study *S1D* showed that the big leaf approach used to parameterise the dry deposition process gives reasonable results and that the attempt to constrain the model with a “single observed values” is not improving the representation of CH_3COCH_3.

Finally, the inclusion of an ocean-atmosphere gas exchange process improved only marginally the overall correlation between model and observations. In the case of acetone, in fact, the near equilibrium between gas phase and liquid phase limits the sensitivity of the model to this process. Additionally, the emissions/deposition of this tracer from the oceans is of at least one order of magnitude lower than biogenic emissions.

Nevertheless, the vertical profiles of methanol, acetone and acetaldehyde improve consistently from the marine boundary layer to the upper troposphere when this process is accounted for, especially over oceanic regions. It is confirmed that this process is essential for a correct representation of oxygenated organic compounds in the model.

Most probably this process also strongly improves the correlations between observations and model simulations once the biogenic emissions are correctly constrained. Finally, a correct parametrisation of the air-sea exchange process, as implemented in *ECHAM5/MESSy1* , can further be improved if additional information about the liquid phase concentrations of the specific gases is available.

Chapter 6

Conclusions and Outlook

6.1 Conclusions

The atmospheric chemistry general circulation model *ECHAM5/MESSy1* has been used to study organic compounds in the atmosphere, with a special focus on small organic compounds. The chemical scheme applied includes NMVOCs up to three carbons, with a detailed degradation scheme for ethane, propane and simplifications for ethene and propene. The model has been extensively evaluated with the use of field campaign and station observations. Generally, the transport and the photochemistry of the analysed trace gases are well simulated and the highest uncertainties are related to emissions and deposition processes. The biogenic emissions, especially, are associated with large uncertainties whereas the anthropogenic emissions are better constrained.

The model is able to reproduce the seasonal cycle of ozone, both in magnitude and phase. Almost all discrepancies between the simulations and the observations can be explained by uncertainties in the observations and model variability. Stratosphere-troposphere exchange is realistically reproduced by the model, and the simulated vertical gradients of ozone are very close to the observations.

For carbon monoxide (CO) the agreement with station observations is good in terms of its seasonal cycle and magnitude. The model sampling technique strongly influences the results and in polluted regions the CO mixing ratios are generally biased by local sources that cannot be resolved by the coarse grid resolution. Nevertheless, the model results can be sampled upwind and the bias between model simulation and observation generally disappears. However, an overestimation for background CO in NH is present during the NH winter due to too strong emissions from anthropogenic sources. Also in the SH extra-tropics an overestimation is present. No single reason for the too high CO concentrations in these locations could be identified, and a combination of several factors appears to be responsible, requiring additional studies. Emissions of NO_x from snow (Wang et al., 2006), neglected in the evaluation simulation, could improve the correlation between observations and model results (i.e. correct amplitude of the seasonal cycle) although the bias may not disappear.

The sensitivity analyses conducted show that dry deposition does not play a significant role in the CO budget and can be neglected in further studies. Furthermore, the model seems to have a low sensitivity to the changes in the Chinese CO emissions. The applied increased emissions of fossil fuel from China (from

80 $\mathrm{Tg(CO)/yr}$ to 117 $\mathrm{Tg(CO)/yr}$) slightly improved the model performance; nevertheless, the correct amount to be used still has to be further quantified. Possibly, the Chinese CO emissions have been even more strongly underestimated.

Hydrogenperoxide (H_2O_2) is realistically reproduced by the model, which implies a generally accurate representation of peroxy radicals, although a detailed comparison is not feasible due to the high variability of this tracer. Nevertheless, the agreement between simulation and observations corroborates the realistic representation of HO_2 in the model.

For organics an overall slight underestimation of mixing ratios in the upper troposphere is present for all gases investigated, probably due to an underestimation of convective transport. More specifically, the alkanes are well reproduced. This improvement with respect to other models is mainly due to the different distribution of emissions, no longer heavily concentrated in Eurasia as in previous work. Particularly, the simulation of propene (C_3H_8) agrees very well with observations. This is mainly due to a decrease emissions from the Saudi Arabia and Siberia regions which were unrealistically high in the previous versions of the emission (EDGAR) database. This shows that, for this short lived species, the distribution pattern of the emissions are equally important as their magnitude.

For the alkenes the simulations are associated with several problems. In the case of ethene (C_2H_4), the sensitivity studies show that the simulation is not very sensitive to oceanic emissions, and hence the uncertainties in the terrestrial emissions greatly influence this trace gas. In the case of propene (C_3H_6) the mixing ratios at the surface over terrestrial sites are generally correct or higher than the observed one, while the comparison with aircraft measurements shows strong underestimations. This indicates an erroneous representation of the photochemistry of this trace gases which has to be improved in the future. Nevertheless, because the sensitivity simulation with a more recent rate coefficient for the reaction of C_3H_6 with OH did not show any difference with the reference simulations, a more detailed analysis of the measurement quality has to be conducted. In fact, since the mixing ratios in the upper troposphere are very low, in the low ppt range close to the observational sensitivity, it cannot be excluded that the measurements are biased. Further modelling and observational studies are hence needed to better constrain these tracers, which are precursors for several other important gases (e.g. glycolaldehyde). Moreover, the role of the ocean in the budget of these tracers is also important, which should be addressed in greater detail, with a better quantification (and distribution) of the emissions.

For the oxygenated organic compounds the results strongly differ for the specific species studied. Methanol is generally underestimated, and an increase of biogenic methanol emissions (i.e.,151 $\mathrm{Tg/yr}$) improves the simulation of this gas. The biogenic emissions have hence been strongly underestimated in previous studies, and the simulation performed showed that an improved match between observations and model simulations can be obtained if these emissions are further increased. The role of the ocean in the budget of this tracer still has to be defined, and it is conceivable that the oceanic deposition included (94% saturation) is not realistic. Formaldehyde, in contrast, is well reproduced with respect to the vertical observed profiles; this underscores the minor role of methanol oxidation in the budget of HCHO, which is largely produced by oxidation of methane. Because this tracer is mainly chemically produced, its correct representation shows that the chemistry of such compounds is relatively well understood and that the models are generally able to simulate their mixing ratios if the sources are well constrained.

Acetone is a critical trace gas for a correct representation of the hydroxyl radical in the upper troposphere. As a results of its photolysis it can greatly enhance the presence of HO_x and it is essential for a correct representation of ozone chemistry in this region. Model simulated acetone, whose mixing ratios in the boundary layer over land compare well with observations, is less well reproduced in the free troposphere. This indicates that the terrestrial emissions of this tracer have been well quantified and that photochemical process are probably responsible for the unrealistic representation of vertical profiles in the model. This disagreement has partially been corrected through the use of a more recent photolysis rate coefficient, which increased the lifetime of acetone in the upper troposphere and it is recommended to adopt the new photolysis rate in future studies. Nevertheless this increase in the mixing ratios in the upper troposphere is still insufficient to match the observations. Additionally, for this tracer large discrepancies between model simulations and observations are present especially over the ocean. The inclusion of air-sea gas exchange somewhat improved the model simulation of this tracer, although more measurements are needed. In fact, the highest uncertainties in the budget of acetone are connected with the ocean emission/deposition process, and better information about the acetone distribution in surface seawater are essential to understand this process. A good representation of the oceanic emission/deposition should improve the model results and produce not only the correct profiles but also a realistic global mass which has been largely underestimated by many studies so far.

In the case of PAN, no firm conclusion can be drawn due to the high variability of this tracer. Nevertheless the simulated vertical profiles do not agree with the observations, mainly due to wrong representation of PAN precursors (i.e. acetone). A more detailed analysis can be performed only after that all the precursors have been more accurately constrained in the model.

Sensitivity runs showed that the results are robust with respect to the operator splitting approach. The inversion of the emission and deposition processes during a model time-step does not significantly change the results, and it is confirmed that the sequence of the process in a model time-step does not influence the model results. This implies that *ECHAM5/MESSy1* is a valuable tool that can be used to study the effects of these processes.

Additionally, the theoretical calculation of the dry deposition of the tracers is generally preferable than the use of a single measured value, an often applied method in atmospheric chemistry modelling. In the case of acetone, the simulation which included a constant dry deposition velocity performed worse than the simulations which used a theoretical value calculation.

Finally acetaldehyde model results are underestimated by up to a factor of 10 or more with respect to the observations. The use of an air-sea exchange submodel improved significantly its simulation, giving realistic results in the marine boundary layer. In the upper troposphere the model still substantially underestimates the observed concentration substantially, although systematic errors in the measured values cannot be excluded.

To more realistically simulate the ocean-atmosphere gas exchange as mentioned before, the submodel **AIRSEA** has been developed. The tests conducted showed that the two layer model is sufficiently accurate for global modeling and that the same algorithm can simulate exchange rates for trace gases within a wide solubility range. While for some gases this process is essential, for OVOC the close balance between liquid phase and gas phase implies a low impact in the overall budget of these trace gases, which is mainly determined by terrestrial biogenic emissions. Nevertheless, for these gases the effect of this process is important in remote regions and, generally, the role of the ocean is needed for a correct representation of the vertical profiles. The performed simulations, in fact, showed that the simulated vertical profiles of these tracers are very sensitive to the liquid phase concentrations used in the submodel **AIRSEA**, which are poorly known.

Still more work has to be done to have a correct simulation of some trace gases here analysed. It has been shown that the systematic use of statistical tools (in conjunction with observational data) and sensitivity studies are essential to achieve significant improvements. This method, in fact, gives useful indications where and how the model has to be improved.

6.2 Outlook

Many questions have been raised by this thesis. Specifically, more studies are needed to better understand the behaviour of some organic tracers, notably alkenes, which are not correctly reproduced by the model. Improved additional measurements are needed for the background atmosphere. As noticed in Chapter 5, the disagreements between simulations and observations cannot be explained only with an erroneous compilation of the sources. Hence more studies (i.e., a more complete chemistry description in the model and laboratory studies of the relevant reaction coefficients) are required.

Organic compounds are largely emitted biogenically and the response of the biosphere (and its emission) to changes in the Earth's climate (Houghton, 1996) should receive increased attention. Through their photochemical impact on ozone and OH, in fact, the biogenic emissions could provide a positive feedback in the oxidation capacity of the troposphere. This mechanism has been suggested for isoprene (Shallcross and Monks, 2000), whose emissions are known to depend mainly on temperature and solar irradiance, but it can also be extended to other compounds and a more general view on biosphere-atmosphere feedbacks (Fuentes et al., 2001). More research is needed to better understand the effects of environmental conditions on VOC emissions and the effects of VOCs on the atmosphere, with a particular focus on the possible feedbacks. Further research requires the application of a coupled Earth system model which includes a realistic representation of the biosphere.

Another interesting topic is the role of oceans in atmospheric chemistry. As shown in this thesis, oceans play a central role in the budget of many trace gases. Moreover, emissions from oceans can have a big impact on the meteorology and cloud properties through the formation of aerosol particles, as shown by Meskhidze and Nenes (2006).

The implementation of a biogeochemical ocean model (with a comprehensive feedbacks between ocean and atmosphere) could help to solve many open questions. This biogeochemical model would also give the opportunity to exploit the capability of the **AIRSEA** submodel, with a realistic on-line calculated liquid phase concentration of many gases. However more measurements are also needed to better constrain and test such as coupled model; the few available measurements do not suffice for a detailed comparison. These indications for future research point towards the need of a comprehensive Earth System Model, in which feedbacks between system components (i.e. atmosphere, oceans, biosphere, cryosphere ...) are represented. This is essential for a better understanding of the large impact of mankind on the Earth's climate and living environment, including risks for human health.

Appendix A

Statistical tools

In this appendix the description of the simple statisticals equations used in this work is given

A.1 Basic statistic

Having two dataset, the simulated value m_i and the observed value o_i, some definition commonly used in statistics can be given:

- the differences of the two dataset:

$$d_i = m_i - o_i \; , d_i = f(o_i, m_i) \tag{A.1}$$

- average of m_i and o_i:

$$\overline{m} = \frac{1}{N}\sum_{i=1}^{N}(m_i) \; , \overline{o} = \frac{1}{N}\sum_{i=1}^{N}(o_i) \tag{A.2}$$

- bias:

$$\overline{E} = \overline{d} = \frac{1}{N}\sum_{i=1}^{N}(d_i) = \frac{1}{N}\sum_{i=1}^{N}(m_i - o_i) = \frac{1}{N}\sum_{i=1}^{N}(m_i) - \frac{1}{N}\sum_{i=1}^{N}(o_i) = \overline{m} - \overline{o} \tag{A.3}$$

- standard deviations:

$$\sigma_m = \left[\frac{1}{N}\sum_{i=1}^{N}(m_i - \overline{m})^2\right]^{1/2} \tag{A.4}$$

$$\sigma_o = \left[\frac{1}{N}\sum_{i=1}^{N}(o_i - \overline{o})^2\right]^{1/2} \tag{A.5}$$

- Root Mean Square (RMS)

$$E = \left[\frac{1}{N}\sum_{i=1}^{N}(m_i - o_i)^2\right]^{1/2} = \left[\frac{1}{N}\sum_{i=1}^{N}(d_i)^2\right]^{1/2} \tag{A.6}$$

- Correlation coefficient

$$R = \frac{\frac{1}{N}\sum_{i=1}^{N}\left((m_n - \overline{m})(o_n - \overline{o})\right)}{\sigma_m \sigma_o} \tag{A.7}$$

- Centred pattern RMS difference

$$E' = \left[\frac{1}{N}\sum_{i=1}^{N}\left[(m_i - m_i) - (o_i - o_i)\right]^2\right]^{1/2} \tag{A.8}$$

To notice is the relationship $\overline{E}^2 + {E'}^2 = E^2$.

A.2 Taylor diagram

Following Taylor (2001), the information contained in eq. A.4 A.5 A.7 A.6 can be resumed in one single chart. Infact, these statistical quatities are related in the following way:

$${E'}^2 = {\sigma_m}^2 + {\sigma_o}^2 - 2\sigma_m \sigma_o R \tag{A.9}$$

which is the law of cosines:

$$c^2 = a^2 + b^2 - 2ab\cos\phi \tag{A.10}$$

where a, b, and c are the lengths of the sides of a triangle and ϕ is the angle opposite side c. Following this approach in fig.A.1 the relationship contained in eq.A.9 is plotted.

It is immediate now to construct a diagram containing all this imformation. In figA.1, this diagram is presented.

A further improvement in this kind of diagram is to normalised the plotted values by the standard deviation of the observed field. In this case we have:

$$\hat{E'} = E'/\sigma_o \tag{A.11}$$

$$\hat{\sigma_m} = \sigma_m/\sigma_o$$

$$\hat{\sigma_o} = \sigma_m/\sigma_o = 1$$

The construction of the Taylor diagram is still valid, and in this case the observation lies in the point with correlation equal to 1 and $\hat{\sigma_o} = 1$. A perfect model which reproduces exactly the observed measures, will have as well 1 and $\hat{\sigma_m} = 1$. Obviously this is and ideal case, and the model should try to be as closest as possible to this point ($R = 1$, $\hat{\sigma_m} = 1$).

If not explicitly written, in the Tayor diagrams presented in this work, $\hat{\sigma_m}$, $\hat{\sigma_o}$ and $\hat{E'}$ *have always been used.*

A.2.1 Weighting factor

We suppouse that the simulated value m_i and the observed value o_i and the relatives errors δ_i^m and δ_i^o are given. In this work, if not esplicitiliy written, the model error is the variability calculated from the averaged

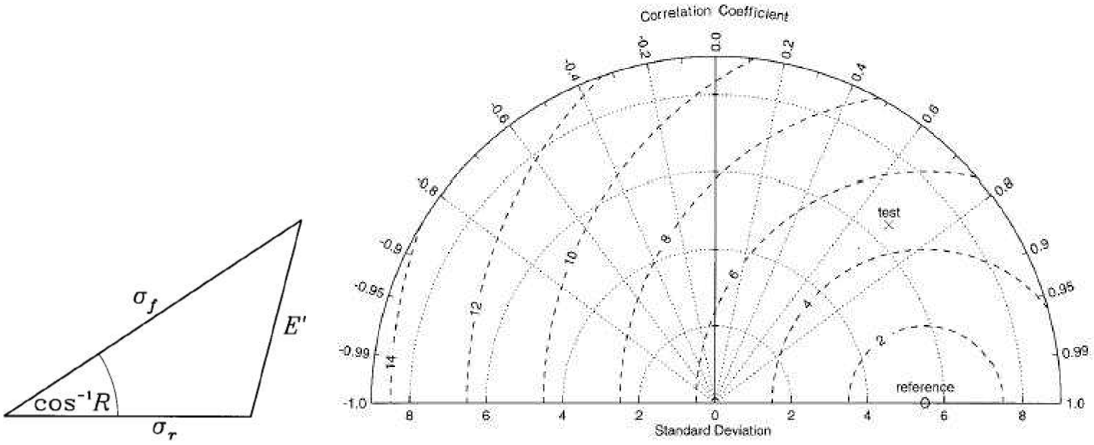

Figure A.1: Relationship between corelation, standard deviations and centered pattern root mean squared (left) and the relative taylor diagram built on this relationship; the circles sourrounding the "reference" point aren unit of "observation standard deviation". From Taylor (2001)

values and the measurements errors is a combination of instrumental error and variance (as it is given from any measuremts).

Any classical statistical calculation can be weighted using $1/\epsilon_i$ as weighting factor, where

$$\epsilon_i = \sqrt{\delta_i^{m2} + \delta_i^{o2}} \tag{A.12}$$

This allowed a more reasonable statistical analysis, where every value is scaled with the geometrical sum of the errors.

Using A.12 new definitions for the traditional statistical functions used in the study can be given:

- standard deviations:

$$\sigma_m = \left[\frac{1}{N} \sum_{i=1}^{N} \left(\frac{m_i - \overline{m}}{\epsilon_i} \right)^2 \right]^{1/2} \tag{A.13}$$

$$\sigma_o = \left[\frac{1}{N} \sum_{i=1}^{N} \left(\frac{o_i - \overline{o}}{\epsilon_i} \right)^2 \right]^{1/2} \tag{A.14}$$

- Root Mean Square (RMS)

$$E = \left[\frac{1}{N} \sum_{i=1}^{N} \left(\frac{m_i - o_i}{\epsilon_i} \right)^2 \right]^{1/2} = \left[\frac{1}{N} \sum_{i=1}^{N} \left(\frac{d_i}{\epsilon_i} \right)^2 \right]^{1/2} \tag{A.15}$$

- Correlation coefficient

$$R = \frac{\frac{1}{N} \sum_{i=1}^{N} \left(\frac{(m_n - \overline{m})(o_n - \overline{o})}{\epsilon_i^2} \right)}{\sigma_m \sigma_o} \tag{A.16}$$

- Centred pattern RMS difference

$$E' = \left[\frac{1}{N} \sum_{i=1}^{N} \left[\left(\frac{m_i - m_i}{\epsilon_i} \right) - \left(\frac{o_i - o_i}{\epsilon_i} \right) \right]^2 \right]^{1/2} \tag{A.17}$$

In order to apply this approach to the Taylor diagrams (Taylor, 2001), the basic relationship between the variables E', σ_m, σ_o and R must hold:

$$E'^2 = \sigma_m^2 + \sigma_o^2 - 2\sigma_m\sigma_o R \tag{A.18}$$

From the definitions A.14, A.13, A.6 a simple substitution can be made:

$$\begin{aligned} &\frac{1}{N}\left[\sum_{i=1}^{N}\left(\frac{m_i-\overline{m}}{\epsilon_i}\right)^2 + \sum_{i=1}^{N}\left(\frac{o_i-\overline{o}}{\epsilon_i}\right)^2 \right. \\ &\qquad \left. -2\sum_{i=1}^{N}\left(\frac{m_i-\overline{m}}{\epsilon_i}\right)\left(\frac{o_i-\overline{o}}{\epsilon_i}\right)\right] = \\ &\qquad \frac{1}{N}\sum_{i=1}^{N}\left[\left(\frac{m_i-\overline{m}}{\epsilon_i}\right) - \left(\frac{o_i-\overline{o}}{\epsilon_i}\right)\right]^2 \end{aligned} \tag{A.19}$$

hence (from A.19):

$$\frac{1}{N}\sum_{i=1}^{N}\left(\frac{d_i-\overline{d}}{\epsilon_i}\right)^2 = E'^2 \text{ as in eq. A.17} \tag{A.20}$$

This approach can be applied in different data analysis, like time-series or vertical profile analysis.

In all this analysis we obtain that average and RMS are unitless (they are normalised to ϵ_i). If we want to obtain a not normalised value we have to multiply all the statistic functions for an average of the weighting factor:

$$\widehat{\epsilon} = \left[\frac{1}{N}\sum_{i=1}^{N}{\epsilon_i}^2\right]^{1/2} = \left[\frac{1}{N}\sum_{i=1}^{N}(\delta_i^{m2} + \delta_i^{o2})\right]^{1/2} \tag{A.21}$$

Appendix B

Mecca reaction tables

The reactions used in the evaluation run (Sec. (2.1.2.1)) are here listed.

Table B.1: Gas phase reactions

#	reaction	rate coefficient	reference
G1000	$O_2 + O(^1D) \rightarrow O(^3P) + O_2$	`3.2E-11*EXP(70./temp)`	Sander et al. (2003)
G1001	$O_2 + O(^3P) \rightarrow O_3$	`6.E-34*((temp/300.)**(-2.4))*cair`	Sander et al. (2003)
G1002	$O_3 + O(^1D) \rightarrow 2\ O_2$	`1.2E-10`	Sander et al. (2003)*
G1003	$O_3 + O(^3P) \rightarrow 2\ O_2$	`8.E-12*EXP(-2060./temp)`	Sander et al. (2003)
G01Diag	$O_3(s) \rightarrow LO_3(s)$	`k_O3s`	Roelofs and Lelieveld (1997)*
G2100	$H + O_2 \rightarrow HO_2$	`k_3rd(temp,cair,5.7E-32,1.6,7.5E-11,0.,0.6)`	Sander et al. (2003)
G2101	$H + O_3 \rightarrow OH$	`1.4E-10*EXP(-470./temp)`	Sander et al. (2003)
G2102	$H_2 + O(^1D) \rightarrow H + OH$	`1.1E-10`	Sander et al. (2003)
G2103	$OH + O(^3P) \rightarrow H$	`2.2E-11*EXP(120./temp)`	Sander et al. (2003)
G2104	$OH + O_3 \rightarrow HO_2$	`1.7E-12*EXP(-940./temp)`	Sander et al. (2003)
G2105	$OH + H_2 \rightarrow H_2O + H$	`5.5E-12*EXP(-2000./temp)`	Sander et al. (2003)
G2106	$HO_2 + O(^3P) \rightarrow OH$	`3.E-11*EXP(200./temp)`	Sander et al. (2003)
G2107	$HO_2 + O_3 \rightarrow OH$	`1.E-14*EXP(-490./temp)`	Sander et al. (2003)
G2108a	$HO_2 + H \rightarrow 2\ OH$	`0.69*8.1E-11`	Sander et al. (2003)*
G2108b	$HO_2 + H \rightarrow H_2$	`0.29*8.1E-11`	Sander et al. (2003)*
G2108c	$HO_2 + H \rightarrow O(^3P) + H_2O$	`0.02*8.1E-11`	Sander et al. (2003)*
G2109	$HO_2 + OH \rightarrow H_2O$	`4.8E-11*EXP(250./temp)`	Sander et al. (2003)
G2110	$HO_2 + HO_2 \rightarrow H_2O_2$	`k_HO2_HO2`	Christensen et al. (2002), Kircher and Sander (1984)*
G2111	$H_2O + O(^1D) \rightarrow 2\ OH$	`2.2E-10`	Sander et al. (2003)
G2112	$H_2O_2 + OH \rightarrow H_2O + HO_2$	`2.9E-12*EXP(-160./temp)`	Sander et al. (2003)
G3100	$N + O_2 \rightarrow NO + O(^3P)$	`1.5E-11*EXP(-3600./temp)`	Sander et al. (2003)

Table B.1: Gas phase reactions (... continued)

#	reaction	rate coefficient	reference
G3101	$N_2 + O(^1D) \rightarrow O(^3P) + N_2$	`1.8E-11*EXP(110./temp)`	Sander et al. (2003)
G3102a	$N_2O + O(^1D) \rightarrow 2\ NO$	`6.7E-11`	Sander et al. (2003)
G3102b	$N_2O + O(^1D) \rightarrow N_2 + O_2$	`4.9E-11`	Sander et al. (2003)
G3103	$NO + O_3 \rightarrow NO_2 + O_2$	`3.E-12*EXP(-1500./temp)`	Sander et al. (2003)
G3104	$NO + N \rightarrow O(^3P) + N_2$	`2.1E-11*EXP(100./temp)`	Sander et al. (2003)
G3105	$NO_2 + O(^3P) \rightarrow NO + O_2$	`5.6E-12*EXP(180./temp)`	Sander et al. (2003)
G3106	$NO_2 + O_3 \rightarrow NO_3 + O_2$	`1.2E-13*EXP(-2450./temp)`	Sander et al. (2003)
G3107	$NO_2 + N \rightarrow N_2O + O(^3P)$	`5.8E-12*EXP(220./temp)`	Sander et al. (2003)
G3108	$NO_3 + NO \rightarrow 2\ NO_2$	`1.5E-11*EXP(170./temp)`	Sander et al. (2003)
G3109	$NO_3 + NO_2 \rightarrow N_2O_5$	`k_NO3_NO2`	Sander et al. (2003)*
G3110	$N_2O_5 \rightarrow NO_2 + NO_3$	`k_NO3_NO2/(3.E-27*EXP(10990./temp))`	Sander et al. (2003)*
G3200	$NO + OH \rightarrow HONO$	`k_3rd(temp,cair,7.E-31,2.6,3.6E-11,0.1,0.6)`	Sander et al. (2003)
G3201	$NO + HO_2 \rightarrow NO_2 + OH$	`3.5E-12*EXP(250./temp)`	Sander et al. (2003)
G3202	$NO_2 + OH \rightarrow HNO_3$	`k_3rd(temp,cair,2.E-30,3.,2.5E-11,0.,0.6)`	Sander et al. (2003)
G3203	$NO_2 + HO_2 \rightarrow HNO_4$	`k_NO2_HO2`	Sander et al. (2003)
G3204	$NO_3 + HO_2 \rightarrow NO_2 + OH + O_2$	`3.5E-12`	Sander et al. (2003)
G3205	$HONO + OH \rightarrow NO_2 + H_2O$	`1.8E-11*EXP(-390./temp)`	Sander et al. (2003)
G3206	$HNO_3 + OH \rightarrow H_2O + NO_3$	`k_HNO3_OH`	Sander et al. (2003)*
G3207	$HNO_4 \rightarrow NO_2 + HO_2$	`k_NO2_HO2/(2.1E-27*EXP(10900./temp))`	Sander et al. (2003)*
G3208	$HNO_4 + OH \rightarrow NO_2 + H_2O$	`1.3E-12*EXP(380./temp)`	Sander et al. (2003)
G4100	$CH_4 + O(^1D) \rightarrow .75\ CH_3O_2 + .75\ OH + .25\ HCHO + .4\ H + .05\ H_2$	`1.5E-10`	Sander et al. (2003)
G4101	$CH_4 + OH \rightarrow CH_3O_2 + H_2O$	`1.85E-20*EXP(2.82*log(temp)-987./temp)`	Atkinson (2003)*
G4102	$CH_3OH + OH \rightarrow HCHO + HO_2$	`7.3E-12*EXP(-620./temp)`	Sander et al. (2003)
G4103aG	$CH_3O_2 + HO_2 \rightarrow CH_3OOH$	`4.1E-13*EXP(750./temp)/(1.+1./497.7*EXP(1160./temp))`	Sander et al. (2003)*
G4103bG	$CH_3O_2 + HO_2 \rightarrow HCHO + H_2O + O_2$	`4.1E-13*EXP(750./temp)/(1.+497.7*EXP(-1160./temp))`	Sander et al. (2003)*
G4104 N	$CH_3O_2 + NO \rightarrow HCHO + NO_2 + HO_2$	`2.8E-12*EXP(300./temp)`	Sander et al. (2003)
G4105	$CH_3O_2 + NO_3 \rightarrow HCHO + HO_2 + NO_2$	`1.3E-12`	Atkinson et al. (1999a)
G4106aG	$CH_3O_2 + CH_3O_2 \rightarrow 2\ HCHO + 2\ HO_2$	`9.5E-14*EXP(390./temp)/(1.+1./26.2*EXP(1130./temp))`	Sander et al. (2003)
G4106bG	$CH_3O_2 + CH_3O_2 \rightarrow HCHO + CH_3OH$	`9.5E-14*EXP(390./temp)/(1.+26.2*EXP(-1130./temp))`	Sander et al. (2003)

Table B.1: Gas phase reactions (... continued)

#	reaction	rate coefficient	reference
G4107	$CH_3OOH + OH \rightarrow .7\ CH_3O_2 + .3\ HCHO + .3\ OH + H_2O$	`k_CH3OOH_OH`	Sander et al. (2003)*
G4108	$HCHO + OH \rightarrow CO + H_2O + HO_2$	`9.52E-18*EXP(2.03*log(temp) +636./temp)`	Sivakumaran et al. (2003)
G4109	$HCHO + NO_3 \rightarrow HNO_3 + CO + HO_2$	`3.4E-13*EXP(-1900./temp)`	Sander et al. (2003)*
G4110	$CO + OH \rightarrow H + CO_2$	`1.57E-13+cair*3.54E-33`	McCabe et al. (2001)
G4111	$HCOOH + OH \rightarrow HO_2$	`4.E-13`	Sander et al. (2003)
G4200	$C_2H_6 + OH \rightarrow C_2H_5O_2 + H_2O$	`1.49E-17*temp*temp*EXP(-499./temp)`	Atkinson (2003)
G4201	$C_2H_4 + O_3 \rightarrow HCHO + .22\ HO_2 + .12\ OH + .23\ CO + .54\ HCOOH + .1\ H_2$	`1.2E-14*EXP(-2630./temp)`	Sander et al. (2003)*
G4202	$C_2H_4 + OH \rightarrow .6666667\ CH_3CH(O_2)CH_2OH$	`k_3rd(temp,cair,1.E-28,0.8, 8.8E-12,0.,0.6)`	Sander et al. (2003)
G4203	$C_2H_5O_2 + HO_2 \rightarrow C_2H_5OOH$	`7.5E-13*EXP(700./temp)`	Sander et al. (2003)
G4204	$C_2H_5O_2 + NO \rightarrow CH_3CHO + HO_2 + NO_2$	`2.6E-12*EXP(365./temp)`	Sander et al. (2003)
G4205	$C_2H_5O_2 + NO_3 \rightarrow CH_3CHO + HO_2 + NO_2$	`2.3E-12`	Atkinson et al. (1999a)
G4206	$C_2H_5O_2 + CH_3O_2 \rightarrow .75\ HCHO + HO_2 + .75\ CH_3CHO + .25\ CH_3OH$	`1.6E-13*EXP(195./temp)`	see note
G4207	$C_2H_5OOH + OH \rightarrow .3\ C_2H_5O_2 + .7\ CH_3CHO + .7\ OH$	`k_CH3OOH_OH`	see note
G4208	$CH_3CHO + OH \rightarrow CH_3C(O)OO + H_2O$	`5.6E-12*EXP(270./temp)`	Sander et al. (2003)
G4209	$CH_3CHO + NO_3 \rightarrow CH_3C(O)OO + HNO_3$	`1.4E-12*EXP(-1900./temp)`	Sander et al. (2003)
G4210	$CH_3COOH + OH \rightarrow CH_3O_2$	`4.E-13*EXP(200./temp)`	Sander et al. (2003)
G4211a	$CH_3C(O)OO + HO_2 \rightarrow CH_3C(O)OOH$	`4.3E-13*EXP(1040./temp) /(1.+1./37.*EXP(660./temp))`	Tyndall et al. (2001)
G4211b	$CH_3C(O)OO + HO_2 \rightarrow CH_3COOH + O_3$	`4.3E-13*EXP(1040./temp) /(1.+37.*EXP(-660./temp))`	Tyndall et al. (2001)
G4212	$CH_3C(O)OO + NO \rightarrow CH_3O_2 + NO_2$	`8.1E-12*EXP(270./temp)`	Tyndall et al. (2001)
G4213	$CH_3C(O)OO + NO_2 \rightarrow PAN$	`k_PA_NO2`	Tyndall et al. (2001)
G4214	$CH_3C(O)OO + NO_3 \rightarrow CH_3O_2 + NO_2$	`4.E-12`	Canosa-Mas et al. (1996)
G4215a	$CH_3C(O)OO + CH_3O_2 \rightarrow HCHO + HO_2 + CH_3O_2 + CO_2$	`0.9*2.E-12*EXP(500./temp)`	Sander et al. (2003)
G4215b	$CH_3C(O)OO + CH_3O_2 \rightarrow CH_3COOH + HCHO + CO_2$	`0.1*2.E-12*EXP(500./temp)`	Sander et al. (2003)

Table B.1: Gas phase reactions (... continued)

#	reaction	rate coefficient	reference
G4216	$CH_3C(O)OO + C_2H_5O_2 \rightarrow .82\ CH_3O_2 + CH_3CHO + .82\ HO_2 + .18\ CH_3COOH$	`4.9E-12*EXP(211./temp)`	Atkinson et al. (1999a), Kirchner and Stockwell (1996)*
G4217	$CH_3C(O)OO + CH_3C(O)OO \rightarrow 2\ CH_3O_2 + 2\ CO_2 + O_2$	`2.5E-12*EXP(500./temp)`	Tyndall et al. (2001)
G4218	$CH_3C(O)OOH + OH \rightarrow CH_3C(O)OO$	`k_CH3OOH_OH`	see note
G4219	$NACA + OH \rightarrow NO_2 + HCHO + CO$	`5.6E-12*EXP(270./temp)`	see note
G4220	$PAN + OH \rightarrow HCHO + NO_2$	`2.E-14`	see note
G4221	$PAN \rightarrow CH_3C(O)OO + NO_2$	`k_PAN_M`	Sander et al. (2003)*
G4300	$C_3H_8 + OH \rightarrow .82\ C_3H_7O_2 + .18\ C_2H_5O_2 + H_2O$	`1.65E-17*temp*temp*EXP(-87./temp)`	Atkinson (2003)
G4301	$C_3H_6 + O_3 \rightarrow .57\ HCHO + .47\ CH_3CHO + .33\ OH + .26\ HO_2 + .07\ CH_3O_2 + .06\ C_2H_5O_2 + .23\ CH_3C(O)OO + .04\ CH_3COCHO + .06\ CH_4 + .31\ CO + .22\ HCOOH + .03\ CH_3OH$	`6.5E-15*EXP(-1900./temp)`	Sander et al. (2003)*
G4302	$C_3H_6 + OH \rightarrow CH_3CH(O_2)CH_2OH$	`k_3rd(temp,cair,8.E-27,3.5,3.E-11,0.,0.5)`	Atkinson et al. (1999a)
G4303	$C_3H_6 + NO_3 \rightarrow ONIT$	`4.6E-13*EXP(-1155./temp)`	Atkinson et al. (1999a)
G4304	$C_3H_7O_2 + HO_2 \rightarrow C_3H_7OOH$	`k_PrO2_HO2`	Atkinson (1997)*
G4305	$C_3H_7O_2 + NO \rightarrow .96\ CH_3COCH_3 + .96\ HO_2 + .96\ NO_2 + .04\ C_3H_7ONO_2$	`k_PrO2_NO`	Atkinson et al. (1999a)*
G4306	$C_3H_7O_2 + CH_3O_2 \rightarrow CH_3COCH_3 + .8\ HCHO + .8\ HO_2 + .2\ CH_3OH$	`k_PrO2_CH3O2`	Kirchner and Stockwell (1996)
G4307	$C_3H_7OOH + OH \rightarrow .3\ C_3H_7O_2 + .7\ CH_3COCH_3 + .7\ OH$	`k_CH3OOH_OH`	see note
G4308	$CH_3CH(O_2)CH_2OH + HO_2 \rightarrow CH_3CH(OOH)CH_2OH$	`6.5E-13*EXP(650./temp)`	Müller and Brasseur (1995)
G4309	$CH_3CH(O_2)CH_2OH + NO \rightarrow .98\ CH_3CHO + .98\ HCHO + .98\ HO_2 + .98\ NO_2 + .02\ ONIT$	`4.2E-12*EXP(180./temp)`	Müller and Brasseur (1995)*
G4310	$CH_3CH(OOH)CH_2OH + OH \rightarrow .5\ CH_3CH(O_2)CH_2OH + .5\ CH_3COCH_2OH + .5\ OH + H_2O$	`3.8E-12*EXP(200./temp)`	Müller and Brasseur (1995)
G4311	$CH_3COCH_3 + OH \rightarrow CH_3COCH_2O_2 + H_2O$	`1.33E-13+3.82E-11*EXP(-2000./temp)`	Sander et al. (2003)
G4312	$CH_3COCH_2O_2 + HO_2 \rightarrow CH_3COCH_2O_2H$	`8.6E-13*EXP(700./temp)`	Tyndall et al. (2001)
G4313	$CH_3COCH_2O_2 + NO \rightarrow NO_2 + CH_3C(O)OO + HCHO$	`2.9E-12*EXP(300./temp)`	Sander et al. (2003)

Table B.1: Gas phase reactions (... continued)

#	reaction	rate coefficient	reference
G4314	$CH_3COCH_2O_2 + CH_3O_2 \rightarrow .5\ CH_3COCHO + .5\ CH_3OH + .3\ CH_3C(O)OO + .8\ HCHO + .3\ HO_2 + .2\ CH_3COCH_2OH$	`7.5E-13*EXP(500./temp)`	Tyndall et al. (2001)
G4315	$CH_3COCH_2O_2H + OH \rightarrow .3\ CH_3COCH_2O_2 + .7\ CH_3COCHO + .7\ OH$	`k_CH3OOH_OH`	see note
G4316	$CH_3COCH_2OH + OH \rightarrow CH_3COCHO + HO_2$	`3.E-12`	Atkinson et al. (1999a)
G4317	$CH_3COCHO + OH \rightarrow CH_3C(O)OO + CO$	`8.4E-13*EXP(830./temp)`	Tyndall et al. (1995)
G4318	$MPAN + OH \rightarrow CH_3COCH_2OH + NO_2$	`3.2E-11`	Orlando et al. (2002)
G4319	$MPAN \rightarrow MVKO2 + NO_2$	`k_PAN_M`	see note
G4320	$C_3H_7ONO_2 + OH \rightarrow CH_3COCH_3 + NO_2$	`6.2E-13*EXP(-230./temp)`	Atkinson et al. (1999a)
G4400	$C_4H_{10} + OH \rightarrow C_4H_9O_2 + H_2O$	`1.81E-17*temp*temp*EXP(114./temp)`	Atkinson (2003)
G4401	$C_4H_9O_2 + CH_3O_2 \rightarrow .88\ CH_3COC_2H_5 + .68\ HCHO + 1.23\ HO_2 + .12\ CH_3CHO + .12\ C_2H_5O_2 + .18\ CH_3OH$	`k_PrO2_CH3O2`	see note
G4402	$C_4H_9O_2 + HO_2 \rightarrow C_4H_9OOH$	`k_PrO2_HO2`	see note
G4403	$C_4H_9O_2 + NO \rightarrow .84\ NO_2 + .56\ CH_3COC_2H_5 + .56\ HO_2 + .28\ C_2H_5O_2 + .84\ CH_3CHO + .16\ ONIT$	`k_PrO2_NO`	see note
G4404	$C_4H_9OOH + OH \rightarrow .15\ C_4H_9O_2 + .85\ CH_3COC_2H_5 + .85\ OH + .85\ H_2O$	`k_CH3OOH_OH`	see note
G4405	$MVK + O_3 \rightarrow .45\ HCOOH + .9\ CH_3COCHO + .1\ CH_3C(O)OO + .19\ OH + .22\ CO + .32\ HO_2$	`.5*(1.36E-15*EXP(-2112./temp) +7.51E-16*EXP(-1521./temp))`	Pöschl et al. (2000)
G4406	$MVK + OH \rightarrow MVKO2$	`.5*(4.1E-12*EXP(452./temp) +1.9E-11*EXP(175./temp))`	Pöschl et al. (2000)
G4407	$MVKO2 + HO_2 \rightarrow MVKOOH$	`1.82E-13*EXP(1300./temp)`	Pöschl et al. (2000)
G4408	$MVKO2 + NO \rightarrow NO_2 + .25\ CH_3C(O)OO + .25\ CH_3COCH_2OH + .75\ HCHO + .25\ CO + .75\ HO_2 + .5\ CH_3COCHO$	`2.54E-12*EXP(360./temp)`	Pöschl et al. (2000)
G4409	$MVKO2 + NO_2 \rightarrow MPAN$	`.25*k_3rd(temp,cair,9.7E-29,5.6,9.3E-12,1.5,0.6)`	Pöschl et al. (2000)*

Table B.1: Gas phase reactions (... continued)

#	reaction	rate coefficient	reference
G4410	MVKO2 + CH_3O_2 → .5 CH_3COCHO + .375 CH_3COCH_2OH + .125 $CH_3C(O)OO$ + 1.125 HCHO + .875 HO_2 + .125 CO + .25 CH_3OH	`2.E-12`	von Kuhlmann (2001a)
G4411	MVKO2 + MVKO2 → CH_3COCH_2OH + CH_3COCHO + .5 CO + .5 HCHO + HO_2	`2.E-12`	Pöschl et al. (2000)
G4412	MVKOOH + OH → MVKO2	`3.E-11`	Pöschl et al. (2000)
G4413	$CH_3COC_2H_5$ + OH → MEKO2	`1.3E-12*EXP(-25./temp)`	Atkinson et al. (1999a)
G4414	MEKO2 + HO_2 → MEKOOH	`k_PrO2_HO2`	see note
G4415	MEKO2 + NO → .985 CH_3CHO + .985 $CH_3C(O)OO$ + .985 NO_2 + .015 ONIT	`k_PrO2_NO`	see note
G4416	MEKOOH + OH → .8 MeCOCO + .8 OH + .2 MEKO2	`k_CH3OOH_OH`	see note
G4417	ONIT + OH → $CH_3COC_2H_5$ + NO_2 + H_2O	`1.7E-12`	Atkinson et al. (1999a)*
G4500	ISOP + O_3 → .28 HCOOH + .65 MVK + .1 MVKO2 + .1 $CH_3C(O)OO$ + .14 CO + .58 HCHO + .09 H_2O_2 + .08 CH_3O_2 + .25 OH + .25 HO_2	`7.86E-15*EXP(-1913./temp)`	Pöschl et al. (2000)
G4501	ISOP + OH → ISO2	`2.54E-11*EXP(410./temp)`	Pöschl et al. (2000)
G4502	ISOP + NO_3 → ISON	`3.03E-12*EXP(-446./temp)`	Pöschl et al. (2000)
G4503	ISO2 + HO_2 → ISOOH	`2.22E-13*EXP(1300./temp)`	Boyd et al. (2003)*
G4504	ISO2 + NO → .88 NO_2 + .88 MVK + .88 HCHO + .88 HO_2 + .12 ISON	`2.54E-12*EXP(360./temp)`	Pöschl et al. (2000)*
G4505	ISO2 + CH_3O_2 → .5 MVK + 1.25 HCHO + HO_2 + .25 CH_3COCHO + .25 CH_3COCH_2OH + .25 CH_3OH	`2.E-12`	von Kuhlmann (2001a)
G4506	ISO2 + ISO2 → 2 MVK + HCHO + HO_2	`2.E-12`	Pöschl et al. (2000)
G4507	ISOOH + OH → MVK + OH	`1.E-10`	Pöschl et al. (2000)
G4508	ISON + OH → CH_3COCH_2OH + NACA	`1.3E-11`	Pöschl et al. (2000)
G6100	Cl + O_3 → ClO	`2.3E-11*EXP(-200./temp)`	Sander et al. (2003)
G6101	ClO + $O(^3P)$ → Cl	`3.E-11*EXP(70./temp)`	Sander et al. (2003)
G6102	ClO + ClO → Cl_2O_2	`k_ClO_ClO`	Atkinson et al. (2005a)
G6103	Cl_2O_2 → ClO + ClO	`k_ClO_ClO/ (1.27E-27*EXP(8744./temp))`	Sander et al. (2003)*
G6200	Cl + H_2 → HCl + H	`3.7E-11*EXP(-2300./temp)`	Sander et al. (2003)
G6201a	Cl + HO_2 → HCl	`1.8E-11*EXP(170./temp)`	Sander et al. (2003)

Table B.1: Gas phase reactions (... continued)

#	reaction	rate coefficient	reference
G6201b	$Cl + HO_2 \rightarrow ClO + OH$	`4.1E-11*EXP(-450./temp)`	Sander et al. (2003)
G6202	$Cl + H_2O_2 \rightarrow HCl + HO_2$	`1.1E-11*EXP(-980./temp)`	Sander et al. (2003)
G6203a	$ClO + OH \rightarrow Cl + HO_2$	`7.4E-12*EXP(270./temp)`	Sander et al. (2003)
G6203b	$ClO + OH \rightarrow HCl$	`6.E-13*EXP(230./temp)`	Sander et al. (2003)
G6204	$ClO + HO_2 \rightarrow HOCl$	`2.7E-12*EXP(220./temp)`	Sander et al. (2003)
G6205	$HCl + OH \rightarrow Cl + H_2O$	`2.6E-12*EXP(-350./temp)`	Sander et al. (2003)
G6206	$HOCl + OH \rightarrow ClO + H_2O$	`3.E-12*EXP(-500./temp)`	Sander et al. (2003)
G6300	$ClO + NO \rightarrow NO_2 + Cl$	`6.4E-12*EXP(290./temp)`	Sander et al. (2003)
G6301	$ClO + NO_2 \rightarrow ClNO_3$	`k_3rd(temp,cair,1.8E-31,3.4, 1.5E-11,1.9,0.6)`	Sander et al. (2003)
G6303	$ClNO_3 + O(^3P) \rightarrow ClO + NO_3$	`2.9E-12*EXP(-800./temp)`	Sander et al. (2003)
G6304	$ClNO_3 + Cl \rightarrow Cl_2 + NO_3$	`6.5E-12*EXP(135./temp)`	Sander et al. (2003)
G6400	$Cl + CH_4 \rightarrow HCl + CH_3O_2$	`9.6E-12*EXP(-1360./temp)`	Sander et al. (2003)
G6401	$Cl + HCHO \rightarrow HCl + CO + HO_2$	`8.1E-11*EXP(-30./temp)`	Sander et al. (2003)
G6402	$Cl + CH_3OOH \rightarrow CH_3O_2 + HCl$	`5.7E-11`	Sander et al. (2003)
G6403	$ClO + CH_3O_2 \rightarrow HO_2 + Cl + HCHO$	`3.3E-12*EXP(-115./temp)`	Sander et al. (2003)
G6404	$CCl_4 + O(^1D) \rightarrow ClO + 3\ Cl$	`3.3E-10`	Sander et al. (2003)
G6405	$CH_3Cl + O(^1D) \rightarrow OH + Cl$	`1.65E-10`	Sander et al. (2003)*
G6406	$CH_3Cl + OH \rightarrow H_2O + Cl$	`2.4E-12*EXP(-1250./temp)`	Sander et al. (2003)
G6407	$CH_3CCl_3 + O(^1D) \rightarrow OH + 3\ Cl$	`3.E-10`	Sander et al. (2003)*
G6408	$CH_3CCl_3 + OH \rightarrow H_2O + 3\ Cl$	`1.6E-12*EXP(-1520./temp)`	Sander et al. (2003)
G6500	$CF_2Cl_2 + O(^1D) \rightarrow ClO + Cl$	`1.4E-10`	Sander et al. (2003)
G6501	$CFCl_3 + O(^1D) \rightarrow ClO + 2\ Cl$	`2.3E-10`	Sander et al. (2003)
G7100	$Br + O_3 \rightarrow BrO$	`1.7E-11*EXP(-800./temp)`	Sander et al. (2003)
G7101	$BrO + O(^3P) \rightarrow Br + O_2$	`1.9E-11*EXP(230./temp)`	Sander et al. (2003)
G7102a	$BrO + BrO \rightarrow Br + Br$	`2.4E-12*EXP(40./temp)`	Sander et al. (2003)
G7102b	$BrO + BrO \rightarrow Br_2$	`2.8E-14*EXP(869./temp)`	Sander et al. (2003)
G7200	$Br + HO_2 \rightarrow HBr$	`1.5E-11*EXP(-600./temp)`	Sander et al. (2003)
G7201	$BrO + HO_2 \rightarrow HOBr$	`3.4E-12*EXP(540./temp)`	Sander et al. (2003)
G7202	$HBr + OH \rightarrow Br + H_2O$	`1.1E-11`	Sander et al. (2003)
G7203	$HOBr + O(^3P) \rightarrow OH + BrO$	`1.2E-10*EXP(-430./temp)`	Sander et al. (2003)
G7301	$BrO + NO \rightarrow Br + NO_2$	`8.8E-12*EXP(260./temp)`	Sander et al. (2003)
G7302	$BrO + NO_2 \rightarrow BrNO_3$	`k_BrO_NO2`	Sander et al. (2003)*
G7400	$Br + HCHO \rightarrow HBr + CO + HO_2$	`1.7E-11*EXP(-800./temp)`	Sander et al. (2003)
G7403	$CH_3Br + OH \rightarrow H_2O + Br$	`2.35E-12*EXP(-1300./temp)`	Sander et al. (2003)
G7603a	$BrO + ClO \rightarrow Br + OClO$	`9.5E-13*EXP(550./temp)`	Sander et al. (2003)
G7603b	$BrO + ClO \rightarrow Br + Cl$	`2.3E-12*EXP(260./temp)`	Sander et al. (2003)
G7603c	$BrO + ClO \rightarrow BrCl$	`4.1E-13*EXP(290./temp)`	Sander et al. (2003)
G9200	$SO_2 + OH \rightarrow H_2SO_4 + HO_2$	`k_3rd(temp,cair,3.E-31,3.3, 1.5E-12,0.,0.6)`	Sander et al. (2003)
G9400a	$DMS + OH \rightarrow CH_3SO_2 + HCHO$	`1.13E-11*EXP(-253./temp)`	Atkinson et al. (2003)*
G9400b	$DMS + OH \rightarrow DMSO + HO_2$	`k_DMS_OH`	Atkinson et al. (2003)*

Table B.1: Gas phase reactions (... continued)

#	reaction	rate coefficient	reference
G9401	DMS + NO_3 → CH_3SO_2 + HNO_3 + HCHO	`1.9E-13*EXP(520./temp)`	Atkinson et al. (2003)
G9402	DMSO + OH → .6 SO_2 + HCHO + .6 CH_3O_2 + .4 HO_2 + .4 CH_3SO_3H	`1.E-10`	Hynes and Wine (1996)
G9403	CH_3SO_2 → SO_2 + CH_3O_2	`1.9E13*EXP(-8661./temp)`	Barone et al. (1995)
G9404	CH_3SO_2 + O_3 → CH_3SO_3	`3.E-13`	Barone et al. (1995)
G9405	CH_3SO_3 + HO_2 → CH_3SO_3H	`5.E-11`	Barone et al. (1995)

*Notes:

Rate coefficients for three-body reactions are defined via the function `k_3rd`(T, M, k_0^{300}, n, $k_{\rm inf}^{300}$, m, $f_{\rm c}$). In the code, the temperature T is called `temp` and the concentration of "air molecules" M is called `cair`. Using the auxiliary variables $k_0(T)$, $k_{\rm inf}(T)$, and $k_{\rm ratio}$, `k_3rd` is defined as:

$$
\begin{aligned}
k_0(T) &= k_0^{300} \times \left(\frac{300\mathrm{K}}{T}\right)^n && \text{(B.1)}\\
k_{\rm inf}(T) &= k_{\rm inf}^{300} \times \left(\frac{300\mathrm{K}}{T}\right)^m && \text{(B.2)}\\
k_{\rm ratio} &= \frac{k_0(T)M}{k_{\rm inf}(T)} && \text{(B.3)}\\
\texttt{k\_3rd} &= \frac{k_0(T)M}{1+k_{\rm ratio}} \times f_{\rm c}^{\left(\frac{1}{1+(\log_{10}(k_{\rm ratio}))^2}\right)} && \text{(B.4)}
\end{aligned}
$$

A similar function, called `k_3rd_iupac` here, is used by Atkinson et al. (2005a) for three-body reactions. It has the same function parameters as `k_3rd` and it is defined as:

$$
\begin{aligned}
k_0(T) &= k_0^{300} \times \left(\frac{300\mathrm{K}}{T}\right)^n && \text{(B.5)}\\
k_{\rm inf}(T) &= k_{\rm inf}^{300} \times \left(\frac{300\mathrm{K}}{T}\right)^m && \text{(B.6)}\\
k_{\rm ratio} &= \frac{k_0(T)M}{k_{\rm inf}(T)} && \text{(B.7)}\\
N &= 0.75 - 1.27 \times \log_{10}(f_{\rm c}) && \text{(B.8)}\\
\texttt{k\_3rd\_iupac} &= \frac{k_0(T)M}{1+k_{\rm ratio}} \times f_{\rm c}^{\left(\frac{1}{1+(\log_{10}(k_{\rm ratio})/N)^2}\right)} && \text{(B.9)}
\end{aligned}
$$

G1002: path leading to 2 O(^{3}P) + O_2 neglected

G01Diag: `k_O3s = (1.7E-12*EXP(-940./temp))*C(KPP_OH)+(1.E-14*EXP(-490./temp))*C(KPP_HO2)+J_O1D*2.2E-10*C(KPP_H2O)/(3.2E-11*EXP(70./temp)*C(KPP_O2)+1.8E-11*EXP(110./temp)*C(KPP_N2)+2.2E-10*C(KPP_H2O))`

G2108: branching ratio from Hack et al., see note B5 of Sander et al. (2003)

G2110: The rate coefficient is: `k_HO2_HO2 = (1.5E-12*EXP(19./temp)+1.7E-33*EXP(1000./temp)*cair)*(1.+1.4E-21*EXP(2200./temp)*C(KPP_H2O))`. The value for the first (pressure-independent) part is from Christensen et al. (2002), the water term from Kircher and Sander (1984)

G3109: The rate coefficient is: `k_NO3_NO2 = k_3rd(temp,cair,2.E-30,4.4,1.4E-12,0.7,0.6)`.

G3110: The rate coefficient is defined as backward reaction divided by equilibrium constant.

G3203: The rate coefficient is: `k_NO2_HO2 = k_3rd(temp,cair,1.8E-31,3.2,4.7E-12,` `1.4,0.6)`.

G3206: The rate coefficient is: `k_HNO3_OH = 2.4E-14*EXP(460./temp)+1./(1./(6.5E-34*EXP(1335./temp)*cair)+1./(2.7E-17*EXP(2199./temp)))`

G3207: The rate coefficient is defined as backward reaction divided by equilibrium constant.

G4103: product distribution is from Elrod et al. (2001)

G4107: The rate coefficient is: `k_CH3OOH_OH = 3.8E-12*EXP(200./temp)`

G4109: same temperature dependence assumed as for CH_3CHO+NO_3

G4201: product distribution is from von Kuhlmann (2001a) (see also Neeb et al. (1998))

G4206: Rate coefficient calculated by von Kuhlmann (pers. comm. 2004) using self reactions of CH_3OO and C_2H_5OO from Sander et al. (2003) and geometric mean as suggested by Madronich and Calvert (1990) and Kirchner and Stockwell (1996). The product distribution (branching=0.5/0.25/0.25) is calculated by von Kuhlmann (pers. comm. 2004) based on Villenave and Lesclaux (1996) and Tyndall et al. (2001).

G4207: same value as for G4107: CH_3OOH+OH assumed

G4213: The rate coefficient is: `k_PA_NO2 = k_3rd(temp,cair,8.5E-29,6.5,1.1E-11,1.,0.6)`.

G4216: `1.0E-11` from Atkinson et al. (1999a), temperature dependence from Kirchner and Stockwell (1996)

G4218: same value as for G4107: CH_3OOH+OH assumed

G4219: according to Pöschl et al. (2000), the same value as for CH_3CHO+OH can be assumed

G4220: 50% of the upper limit given by Sander et al. (2003), as suggested by von Kuhlmann (2001a)

G4221: The rate coefficient is: `k_PAN_M = k_PA_NO2/9.E-29*EXP(-14000./temp)`, i.e. the rate coefficient is defined as backward reaction divided by equilibrium constant.

G4301: product distribution is for terminal olefin carbons from Zaveri and Peters (1999)

G4304: The rate coefficient is: `k_PrO2_HO2 = 1.9E-13*EXP(1300./temp)`. Value for generic RO_2 + HO_2 reaction from Atkinson (1997) is used.

G4305: The rate coefficient is: `k_PrO2_NO = 2.7E-12*EXP(360./temp)`

G4306: The rate coefficient is: `k_PrO2_CH3O2 = 9.46E-14*EXP(431./temp)`. The product distribution is from von Kuhlmann (2001a).

G4307: same value as for G4107: CH_3OOH+OH assumed

G4309: products are from von Kuhlmann (2001a)

G4315: same value as for G4107: CH_3OOH+OH assumed

G4319: same value as for PAN assumed

G4401: same value as for propyl group assumed (`k_PrO2_CH3O2`)

G4402: same value as for propyl group assumed (`k_PrO2_HO2`)

G4403: same value as for propyl group assumed (`k_PrO2_NO`)

G4404: same value as for G4107: CH_3OOH+OH assumed

G4409: The factor 0.25 was recommended by Uli Poeschl (pers. comm. 2004).

G4414: same value as for propyl group assumed (`k_PrO2_HO2`)

G4415: same value as for propyl group assumed (`k_PrO2_NO`)

G4416: same value as for G4107: CH_3OOH+OH assumed

G4417: value for $C_4H_9ONO_2$ used here

G4503: same temperature dependence assumed as for other RO_2+HO_2 reactions

G4504: Yield of 12 % $RONO_2$ assumed as suggested in Table 2 of Sprengnether et al. (2002).

G6102: The rate coefficient is: `k_ClO_ClO = k_3rd_iupac(temp,cair,2.E-32,4.,1.E-11,0.,0.45)`.

G6103: The rate coefficient is defined as backward reaction divided by equilibrium constant.

G6204: At low temperatures, there may be a minor reaction channel leading to O_3+HCl. See Finkbeiner et al. (1995) for details. It is neglected here.

G6405: average of reactions with CH_3Br and CH_3F (B. Steil, pers. comm., see also note A15 in Sander et al. (2003)).

G6407: extrapolated from reactions with CH_3CF_3, CH_3CClF_2, and CH_3CCl_2F (B. Steil, pers. comm., see also note A15 in Sander et al. (2003)).

G7302: The rate coefficient is: `k_BrO_NO2 = k_3rd(temp,cair,5.2E-31,3.2,6.9E-12, 2.9,0.6)`.

G7303: The rate coefficient is defined as backward reaction (Sander et al., 2003) divided by equilibrium constant (Orlando and Tyndall, 1996).

G8101: This value was assumed by Jimenez et al. (2003).

G8102: The product as well as the reaction were assumed by von Glasow et al. (2002). An alternative pathway is the formation of new particles. This reaction needs to be updated when laboratory measurements become available.

G8103: product distribution is from Bloss et al. (2001)

G8203: assumed (J. Crowley, pers. comm. 2004)

G8300: The rate coefficient is: `k_I_NO2 = k_3rd(temp,cair,3.E-31,1.,6.6E-11,0.,0.6)`.

G8304: J. Moldanova and J. Plane, pers. comm.

G8305: The rate coefficient is defined as backward reaction (Sander et al., 2003) divided by equilibrium constant (van den Bergh and Troe, 1976).

G8306: Note that in an earlier study by Jenkin et al. (1985), a value of 5E-3 s^{-1} was assumed.

G8600: Turnipseed et al. (1997) found a branching ratio of 14% for the sum of channels which do not produce `I` atoms. We assume that `OIO` and `Cl` are produced in this case.

G8701: Gilles et al. (1997) found an upper limit of 35% for I atom production. We assume 35% I and 65% OIO as products. See also Rowley et al. (2001) for info about products.

G9400a: Abstraction path. The assumed reaction sequence (omitting H_2O and O_2 as products) according to Yin et al. (1990) is:

$$\begin{array}{rcl}
\mathrm{DMS + OH} & \rightarrow & \mathrm{CH_3SCH_2} \\
\mathrm{CH_3SCH_2 + O_2} & \rightarrow & \mathrm{CH_3SCH_2OO} \\
\mathrm{CH_3SCH_2OO + NO} & \rightarrow & \mathrm{CH_3SCH_2O + NO_2} \\
\mathrm{CH_3SCH_2O} & \rightarrow & \mathrm{CH_3S + HCHO} \\
\mathrm{CH_3S + O_3} & \rightarrow & \mathrm{CH_3SO} \\
\mathrm{CH_3SO + O_3} & \rightarrow & \mathrm{CH_3SO_2} \\
\hline
\mathrm{DMS + OH + NO + 2O_3} & \rightarrow & \mathrm{CH_3SO_2 + HCHO + NO_2}
\end{array}$$

Neglecting the effect on O_3 and NO_x, the remaining reaction is:

$$\mathrm{DMS + OH + O_3 \rightarrow CH_3SO_2 + HCHO}$$

G9400b: Addition path. The rate coefficient is: `k_DMS_OH = 1.0E-39*EXP(5820./temp) *C(KPP_O2)/(1.+5.0E-30*EXP(6280./temp) *C(KPP_O2))`.

Table B.2: Photolysis reactions

#	reaction	rate coefficient	reference
J1000	$O_2 + h\nu \rightarrow O(^3P) + O(^3P)$	`JX(ip_O2)`	see note
J1001aJ	$O_3 + h\nu \rightarrow O(^1D)$	`JX(ip_O1D)`	see note
J1001bJ	$O_3 + h\nu \rightarrow O(^3P)$	`JX(ip_O3P)`	see note
J2100	$H_2O + h\nu \rightarrow H + OH$	`JX(ip_H2O)`	see note
J2101	$H_2O_2 + h\nu \rightarrow 2\ OH$	`JX(ip_H2O2)`	see note
J3100	$N_2O + h\nu \rightarrow O(^1D)$	`JX(ip_N2O)`	see note
J3101 J	$NO_2 + h\nu \rightarrow NO + O(^3P)$	`JX(ip_NO2)`	see note
J3102	$NO + h\nu \rightarrow N + O(^3P)$	`JX(ip_NO)`	see note
J3103aNJ	$NO_3 + h\nu \rightarrow NO_2 + O(^3P)$	`JX(ip_NO2O)`	see note
J3103bNJ	$NO_3 + h\nu \rightarrow NO$	`JX(ip_NOO2)`	see note
J3104 J	$N_2O_5 + h\nu \rightarrow NO_2 + NO_3$	`JX(ip_N2O5)`	see note
J3200	$HONO + h\nu \rightarrow NO + OH$	`JX(ip_HONO)`	see note
J3201 J	$HNO_3 + h\nu \rightarrow NO_2 + OH$	`JX(ip_HNO3)`	see note
J3202 J	$HNO_4 + h\nu \rightarrow .667\ NO_2 + .667\ HO_2 + .333\ NO_3 + .333\ OH$	`JX(ip_HNO4)`	see note
J4100	$CH_3OOH + h\nu \rightarrow HCHO + OH + HO_2$	`JX(ip_CH3OOH)`	see note
J4101aJ	$HCHO + h\nu \rightarrow H_2 + CO$	`JX(ip_COH2)`	see note
J4101bJ	$HCHO + h\nu \rightarrow H + CO + HO_2$	`JX(ip_CHOH)`	see note
J4102	$CO_2 + h\nu \rightarrow CO + O(^3P)$	`JX(ip_CO2)`	see note
J4200	$C_2H_5OOH + h\nu \rightarrow CH_3CHO + HO_2 + OH$	`JX(ip_CH3OOH)`	see note
J4201	$CH_3CHO + h\nu \rightarrow CH_3O_2 + HO_2 + CO$	`JX(ip_CH3CHO)`	see note
J4202	$CH_3C(O)OOH + h\nu \rightarrow CH_3O_2 + OH$	`JX(ip_PAA)`	see note
J4203	$NACA + h\nu \rightarrow NO_2 + HCHO + CO$	`0.19*JX(ip_CHOH)`	see note
J4204	$PAN + h\nu \rightarrow CH_3C(O)OO + NO_2$	`JX(ip_PAN)`	see note
J4300	$C_3H_7OOH + h\nu \rightarrow CH_3COCH_3 + HO_2 + OH$	`JX(ip_CH3OOH)`	see note
J4301	$CH_3COCH_3 + h\nu \rightarrow CH_3C(O)OO + CH_3O_2$	`JX(ip_CH3COCH3)`	see note
J4302	$CH_3COCH_2OH + h\nu \rightarrow CH_3C(O)OO + HCHO + HO_2$	`0.074*JX(ip_CHOH)`	see note
J4303	$CH_3COCHO + h\nu \rightarrow CH_3C(O)OO + CO + HO_2$	`JX(ip_CH3COCHO)`	see note
J4304	$CH_3COCH_2O_2H + h\nu \rightarrow CH_3C(O)OO + HO_2 + OH$	`JX(ip_CH3OOH)`	see note
J4305	$MPAN + h\nu \rightarrow CH_3COCH_2OH + NO_2$	`JX(ip_PAN)`	see note

Table B.2: Photolysis reactions (... continued)

#	reaction	rate coefficient	reference
J4306	$C_3H_7ONO_2 + h\nu \rightarrow CH_3COCH_3 + NO_2 + HO_2$	`3.7*JX(ip_PAN)`	see note
J4400	$C_4H_9OOH + h\nu \rightarrow OH + .67\ CH_3COC_2H_5 + .67\ HO_2 + .33\ C_2H_5O_2 + .33\ CH_3CHO$	`JX(ip_CH3OOH)`	see note
J4401	$MVK + h\nu \rightarrow CH_3C(O)OO + HCHO + CO + HO_2$	`0.019*JX(ip_COH2)` `+.015*JX(ip_CH3COCHO)`	see note
J4402	$MVKOOH + h\nu \rightarrow OH + .5\ CH_3COCHO + .25\ CH_3COCH_2OH + .75\ HCHO + .75\ HO_2 + .25\ CH_3C(O)OO + .25\ CO$	`JX(ip_CH3OOH)`	see note
J4403	$CH_3COC_2H_5 + h\nu \rightarrow CH_3C(O)OO + C_2H_5O_2$	`0.42*JX(ip_CHOH)`	see note
J4404	$MEKOOH + h\nu \rightarrow CH_3C(O)OO + CH_3CHO + OH$	`JX(ip_CH3OOH)`	see note
J4405	$MeCOCO + h\nu \rightarrow 2\ CH_3C(O)OO$	`2.15*JX(ip_CH3COCHO)`	see note
J4406	$ONIT + h\nu \rightarrow NO_2 + .67\ CH_3COC_2H_5 + .67\ HO_2 + .33\ C_2H_5O_2 + .33\ CH_3CHO$	`3.7*JX(ip_PAN)`	see note
J4500	$ISOOH + h\nu \rightarrow MVK + HCHO + HO_2 + OH$	`JX(ip_CH3OOH)`	see note
J4501	$ISON + h\nu \rightarrow MVK + HCHO + NO_2 + HO_2$	`3.7*JX(ip_PAN)`	see note
J6000	$Cl_2 + h\nu \rightarrow Cl + Cl$	`JX(ip_Cl2)`	see note
J6100	$Cl_2O_2 + h\nu \rightarrow 2\ Cl$	`1.4*JX(ip_Cl2O2)`	see note
J6101	$OClO + h\nu \rightarrow ClO + O(^3P)$	`JX(ip_OClO)`	see note
J6200	$HCl + h\nu \rightarrow Cl + H$	`JX(ip_HCl)`	see note
J6201	$HOCl + h\nu \rightarrow OH + Cl$	`JX(ip_HOCl)`	see note
J6301	$ClNO_3 + h\nu \rightarrow Cl + NO_3$	`JX(ip_ClNO3)`	see note
J6400	$CH_3Cl + h\nu \rightarrow Cl + CH_3O_2$	`JX(ip_CH3Cl)`	see note
J6401	$CCl_4 + h\nu \rightarrow 4\ Cl$	`JX(ip_CCl4)`	see note
J6402	$CH_3CCl_3 + h\nu \rightarrow 3\ Cl$	`JX(ip_CH3CCl3)`	see note
J6500	$CFCl_3 + h\nu \rightarrow 3\ Cl$	`JX(ip_CFCl3)`	see note
J6501	$CF_2Cl_2 + h\nu \rightarrow 2\ Cl$	`JX(ip_CF2Cl2)`	see note
J7000	$Br_2 + h\nu \rightarrow Br + Br$	`JX(ip_Br2)`	see note
J7200	$HOBr + h\nu \rightarrow Br + OH$	`JX(ip_HOBr)`	see note
J7301	$BrNO_3 + h\nu \rightarrow Br + NO_3$	`JX(ip_BrNO3)`	see note
J7400	$CH_3Br + h\nu \rightarrow Br + CH_3O_2$	`JX(ip_CH3Br)`	see note
J7401	$CH_2Br_2 + h\nu \rightarrow 2\ Br$	`JX(ip_CH2Br2)`	see note
J7402	$CHBr_3 + h\nu \rightarrow 3\ Br$	`JX(ip_CHBr3)`	see note
J7500	$CF_3Br + h\nu \rightarrow Br$	`JX(ip_CF3Br)`	see note
J7600	$BrCl + h\nu \rightarrow Br + Cl$	`JX(ip_BrCl)`	see note

Table B.2: Photolysis reactions (... continued)

#	reaction	rate coefficient	reference
J7601	$CF_2ClBr + h\nu \rightarrow Br + Cl$	`JX(ip_CF2ClBr)`	see note
J7602	$CH_2ClBr + h\nu \rightarrow Br + Cl$	`JX(ip_CH2ClBr)`	see note
J7603	$CHCl_2Br + h\nu \rightarrow Br + 2\ Cl$	`JX(ip_CHCl2Br)`	see note
J7604	$CHClBr_2 + h\nu \rightarrow 2\ Br + Cl$	`JX(ip_CHClBr2)`	see note

*Notes: J-values are calculated with an external module and then supplied to the MECCA chemistry

J6100: Stimpfle et al. (2004) claim that the combination of absorption cross sections from Burkholder et al. (1990) and the Cl_2O_2 formation rate coefficient by Sander et al. (2003) can approximately reproduce the observed Cl_2O_2/ClO ratios and ozone depletion. They give an almost zenith-angle independent ratio of 1.4 for Burkholder et al. (1990) to Sander et al. (2003) J-values. The IUPAC recommendation for the Cl_2O_2 formation rate is about 5 to 15 % less than the value by Sander et al. (2003) but more than 20 % larger than the value by Sander et al. (2000). The J-values by Burkholder et al. (1990) are within the uncertainty range of the IUPAC recommendation.

Appendix C

Constants used in the AIRSEA submodel

Tracer	Molar Mass $[\mathrm{g/mol}]$	Henry's Law coefficient [a]		Molar Volume at boiling point $[\mathrm{cm}^3/\mathrm{mol}]$	α	Setschenow constant $[\mathrm{L/mol}]$	main reference for liquid phase concentration
		$k_H^\ominus$ $[\mathrm{M/atm}]$	$\frac{\Delta_{soln}H}{R}$ $[\mathrm{K}]$				
DMS	62.13	0.48	3100	77.4[b]	1	0	Kettle and Andreae (2000)
$\mathrm{CO_2}$	44.0	3.6	2200	37.3[b]	1	0	Takahashi et al. (2002)
CH3OH	32.04	2.2×10^2	5600	42.5[c]	1	0	Singh et al. (2003)
$\mathrm{C_2H_4}$	28.05	4.8×10^{-3}	1800	49.4[c]	1	0.127[d]	Plass-Dülmer et al. (1995)
$\mathrm{C_2H_6}$	30.07	2.0×10^{-3}	2300	53.5[c]	1	0.162[d]	Plass-Dülmer et al. (1995)
$\mathrm{CH_3CHO}$	44.05	14	5600	51.8[b]	2	0	Singh et al. (2003)
$\mathrm{C_3H_6}$	42.08	4.8×10^{-3}	3400	69.0[c]	1	0	Plass-Dülmer et al. (1995)
$\mathrm{C_3H_8}$	44.09	1.5×10^{-3}	2700	74.5[c]	1	0	Plass-Dülmer et al. (1995)
$\mathrm{CH_3COCH_3}$	58.08	30	4600	74[c]	1	0.11[d]	Williams et al. (2004)
ISOPRENE	68.11	1.3×10^{-2}	0	103.6[b]	1	0	Broadgate et al. (2000)

---

[a] Sander (1999b, and references therein), with $H(T) = k_H^\ominus \times \exp\left(-\frac{\Delta_{soln}H}{R}\left(\frac{1}{T} - \frac{1}{T^\ominus}\right)\right)$, $T^\ominus = 298.15$ K

[b] LeBas method, LeBas (1915); Reid et al. (1984)

[c] Hayduk and Laudie (1974, and references therein)

[d] Ni et al. (2000, and references therein)

Table C.1: Table with constant used in the air-sea submodel

Bibliography

Andreae, M.: Ocean-atmosphere interactions in the global biogeochemical sulfur cycle, Mar. Chem., 30, 1–29, 1990. 62

Andreae, M. O. and Crutzen, P.: Atmospheric aerosol: Biogeochemical sources and role in atmospheric chemistry, Science, 276, 1052–11 058, 1997. 61

Andreae, M. O. and Raemdonck, H.: Dimethylsulfide in the surface ocean and the marine atmosphere, Science, 221, 744–747, 1983. 62

Andronache, C., Chameides, W. L., Rodgers, M. O., Martinez, J., Zimmerman, P., and Greenberg, J.: Vertical distribution of isoprene in the lower boundary layer of the rural and urban southern United States, J. Geophys. Res., 99, 16 989–16 999, 1994. 20

Anguelova, M. and Webster, F.: Whitecap coverage from satellite measurements: A first step toward modeling the variability of oceanic whitecaps, J. Geophys. Res., 111, doi:10.1029/2005JC003 158, 2006. 58

Arnold, S. R., Chipperfield, M. P., and Blitz, M.: Photodissociation of acetone: Atmospheric implications of temperature-dependent quantum yields, Geophys. Res. Lett., 31, doi:10.1029/2003GL019 099, 2004. 47, 82, 93

Arnold, S. R., Chipperfield, M. P., and Blitz, M.: A three-dimensional model study of the effect of new temperature-dependent quantum yields for acetone photolysis, Geophys. Res. Lett., 110, doi:10.1029/2005JD005 998, 2005. 19, 49, 82, 93

Asher, W. and Wanninkhof, R.: The effect of bubble-mediated gas transfer on purposeful gaseous tracer experiments, J. Geophys. Res., 103, 10 555–10 560, 1998a. 57, 58

Asher, W. and Wanninkhof, R.: Transient tracers and air-sea gas transfer, J. Geophys. Res., 103, 15 939–15 958, 1998b. 58

Asselin, R.: Frequency filter for time integrations, Mon. Weather Rev., 100, 487–490, 1972. 10

Atkinson, R.: Gas-phase tropospheric chemistry of volatile organic compounds: 1. Alkanes and alkenes, J. Phys. Chem. Ref. Data, 26, 215–290, 1997. 114, 119

Atkinson, R.: Atmospheric chemistry of VOCs and NO_x, Atmos. Environ., 34, 2063–2101, 2000. 5, 16

Atkinson, R.: Kinetics of the gas-phase reactions of OH radicals with alkanes and cycloalkanes, Atmos. Chem. Phys., 3, 2233–2307, 2003. 112, 113, 114, 115

Atkinson, R. and Arey, J.: Gas-Phase tropospheric chemistry of biogenic volatile compounds: a review, Atmos. Environ., 37, 197–297, 2003. 5, 6

Atkinson, R., Baulch, D. L., Cox, R. A., Hampson, Jr., R. F., Kerr, J. A., Rossi, M. J., and Troe, J.: Summary of evaluated kinetic and photochemical data for atmospheric chemistry: Web version August 1999, `http://www.iupac-kinetic.ch.cam.ac.uk/`, 1999a. 112, 113, 114, 115, 116, 119

Atkinson, R., Baulch, D. L., Cox, R. A., Hampson, Jr., R. F., Kerr, J. A., Rossi, M. J., and Troe, J.: Summary of evaluated kinetic and photochemical data for atmospheric chemistry: Web version August 1999, `http://www.iupac-kinetic.ch.cam.ac.uk/`, 1999b. 42, 43, 84

Atkinson, R., Baulch, D. L., Cox, R. A., Crowley, J. N., Hampson, R. F., Hynes, R. G., Jenkin, M. E., Rossi, M. J., and Troe, J.: Evaluated kinetic and photochemical data for atmospheric chemistry: Part 1 - gas phase reactions of O_x, HO_x, NO_x and SO_x species, Atmos. Chem. Phys. Discuss., 3, 6179–6699, 2003. 117, 118

Atkinson, R., Baulch, D. L., Cox, R. A., Crowley, J. N., Hampson, Jr., R. F., Hynes, R. G., Jenkin, M. E., Kerr, J. A., Rossi, M. J., and Troe, J.: Summary of evaluated kinetic and photochemical data for atmospheric chemistry: Web version March 2005, `http://www.iupac-kinetic.ch.cam.ac.uk/`, 2005a. 116, 118

Atkinson, R., Baulch, D. L., Cox, R. A., Crowley, J. N., Hampson, Jr., R. F., Hynes, R. G., Jenkin, M. E., Kerr, J. A., Rossi, M. J., and Troe, J.: Summary of evaluated kinetic and photochemical data for atmospheric chemistry: Web version March 2005, `http://www.iupac-kinetic.ch.cam.ac.uk/`, 2005b. 7, 42, 43, 81, 84

Atlas, E., Ridley, B., and Cantrell, C. A.: The Tropospheric Ozone Production about the Spring Equinox (TOPSE) Experiment: Introduction, J. Geophys. Res., 108, 8353, doi:10.1029/2002JD003 172, 2003. 20

Barone, S. B., Turnipseed, A. A., and Ravishankara, A. R.: Role of adducts in the atmospheric oxidation of dimethyl sulfide, Faraday Discuss., 100, 39–54, 1995. 118

Bates, T., Cline, J., Gammon, R., and Kelly-Hansen, S.: Regional and seasonal variation in the flux of oceanic dimethylsulfide, J. Geophys. Res., 92, 2930–2938, 1987. 62

Bates, T. S., Kelly, K. C., Johnson, J. E., and Gammon, R. H.: Regional and seasonal variations in the flux of oceanic carbon monoxide to the atmosphere, J. Geophys. Res., 100, 23 093–23 101, 1995. 33, 40

Bates, T. S., Huebert, B. J., Gras, J. L., Griffiths, F. B., and Durkee, P. A.: International Global Atmospheric Chemistry (IGAC) Project's First Aerosol Characterization Experiment (ACE 1): Overview, J. Geophys. Res., 103, 16 297–16 318, 1998. 20

Battle, M., Bender, M., Tans, P., White, J., Ellis, J., Conway, T., and Francey, R.: Global carbon sinks and their variability inferred from atmospheric O_2 and δ^{13}C, Science, 287, 2467 2470, 2000. 71

Bender, M., Ho, D., Hendricks, M., Mike, R., Battle, M., Tans, P., Conway, T., Sturtevant, B., and Cassar, N.: Atmospheric O2/N2 changes, 1993-2002: Implications for the partitioning of fossil fuel CO_2 sequestration, Global Biogeochem. Cycles, 19, doi:10.1029/2004GB002 410, 2005. 71

Bengtsson, L., Hodges, K., and Hagemann, S.: Sensitivity of large-scale atmospheric analysis to humidity observations and its impact on the global water cycle and tropical and extratropical weather systems in ERA40, Tellus, 56A, 202–217, 2004. 10

Bey, I., Jacob, D. J., Yantosca, R. M., Logan, J. A., Field, B. D., Fiore, A. M., Li, Q., Liu, H. Y., Mickley, L. J., and Schultz, M. G.: Global modeling of tropospheric chemistry with assimilated meteorology: Model description and evaluation, J. Geophys. Res., 106, 23 073–23 095, 2001. 19, 33, 38, 90

Blitz, M., Heard, D., Pilling, M., Arnold, S. R., and Chipperfield, M. P.: Pressure and temperature-dependent quantum yields for the photodissocuation od acetone between 279 and 327.5 nm, Geophys. Res. Lett., 31, doi:10.1029/2003GL018 793, 2004. 47, 82, 88, 93, 102

Bloss, W. J., Rowley, D. M., Cox, R. A., and Jones, R. L.: Kinetics and products of the IO self-reaction, J. Phys. Chem. A, 105, 7840–7854, 2001. 120

Bottenheim, J. W. and Shepherd, B. F.: C_2–C_6 hydrocarbon measurements at four rural locations across Canada, J. Geophys. Res., 29, 647–664, 1995. 20

Boutin, J. and Etcheto, J.: Long-term variability of the air-sea CO_2 exchange coefficient: Consequence for the CO_2 fuxes in the equatorial Pacific Ocean, Global Biogeochem. Cycles, 11, 453–470, 1997. 68

Boyd, A. A., Flaud, P.-M., Daugey, N., and Lesclaux, R.: Rate constants for $RO_2 + HO_2$ reactions measured under a large excess of HO_2, J. Phys. Chem. A, 107, 818–821, 2003. 116

Boyer, T., Stephens, C., Antonov, J., Conkright, M., Locarnini, R., O'Brien, T., and Garcia, H.: World Ocean Atlas 2001, Volume 2: Salinity, p. 167 pp., NOAA Atlas NESDIS 50, U.S. Government Printing Office, 2002. 54

Brasseur, G. P., Hauglustaine, D. A., Walters, S., Rasch, P. J., and Müller, J.-F.: MOZART, a global chemical transport model for ozone and related chemical tracers, 1. Model description, J. Geophys. Res., 103, 28 265–28 269, 1998. 13, 19, 33

Broadgate, W., Liss, P., and Penkett, A.: Seasonal emission of isoprene and other reactive hydrocarbon gases from the ocean, Geophys. Res. Lett., 24, 2675–2678, 2000. 64, 93, 125

Brühl, C., Pöschl, U., Crutzen, P. J., and Steil, B.: Acetone and PAN in the upper troposphere: impact on ozone production from aircraft emissions, Atmos. Environ., 34, 3931–3938, 2000. 8, 47

Bucholz, J.: Simulations of Physics and Chemistry of Polar Stratospheric Clouds with a General Circulation Model, Ph.D. thesis, Johannes Gutenberg Universität, Mainz, Germany, 2005. 10, 13

Bürgermeister, S., Zimmermann, S., Gerogii, H.-W., Bingemer, H., Kirst, G., Janssen, M., and Ernst, W.: On the biogenic origin of dimethylsulfide: Relation between chlorophyll, ATP, organismic DMPS, phytoplankton species, and DMS distribution in Atlantic surface wate and atmosphere, J. Geophys. Res., 95, 20 607–20 615, 1990. 62

Burkholder, J. B., Orlando, J. J., and Howard, C. J.: Ultraviolet absorption cross sections of $\mathrm{Cl_2O_2}$ between 210 and 410 nm, J. Phys. Chem., 94, 687–695, 1990. 123

Byers, H.: General Meteorology, McGraw-Hill, New York, USA, 1974. 73

Canosa-Mas, C. E., King, M. D., Lopez, R., Percival, C. J., Wayne, R. P., Shallcross, D. E., Pyle, J. A., and Daele, V.: Is the reaction between $\mathrm{CH_3(O)O_2}$ and $\mathrm{NO_3}$ important in the night-time troposphere?, J. Chem. Soc. Faraday Trans., 92, 2211–2222, 1996. 113

Carder, K., Chen, F. R., Cannizzaro, J. P., Campbell, J. W., and Mitchell, B. G.: Performance of the MODIS semi-analytical ocean color algorithm for chlorophyll-a, Adv. Space Res., 33, 1152–1159, 2004. 65

Carpenter, L., Alastair, C., and Hopkin, J.: Uptake of methanol to the North Atlantic Ocean surface, Global Biogeochem. Cycles, 18, doi:10.1029/2004GB002 294, 2004. 61, 94

Carr, M.-E., Wenquing, T., and Liu, W.: $\mathrm{CO_2}$ exchange coefficients from remotely sensed wind speed measurements: SSM/I versus QuikSCAT in 2000, Geophys. Res. Lett., 29, doi:10.1029/2002GL015 068, 2002. 68

Chameides, W. L. and Walker, J. C. G.: A photochemical theory of tropospheric ozone, J. Geophys. Res., 78, 8751–8760, 1973. 1

Chapman, E., Shaw, W. J., Easter, R. C., Bian, X., and Ghan, S. J.: Influence of wind speed averaging on estimates of dimethylsulfide emission fluxes, J. Geophys. Res., 107, doi:10.1029/2001JD001 564, 2002. 68

Charlson, R., Lovelock, J., Andreae, M. O., and Warren, S.: Oceanic phytoplankton, atmospheric sulphur, cloud albedo and climate, Nature, 326, 655–661, 1987. 61

Christensen, L. E., Okumura, M., Sander, S. P., Salawitch, R. J., Toon, G. C., Sen, B., Blavier, J.-F., and Jucks, K. W.: Kinetics of $\mathrm{HO_2 + HO_2 \rightarrow H_2O_2 + O_2}$: Implications for stratospheric $\mathrm{H_2O_2}$, Geophys. Res. Lett., 29, 2002. 111, 118

Clarkson, T. S., Martin, R. J., and Rudolph, J.: Ethane and propane in the southern marine troposphere, Atmos. Environ., 31, 3763–3771, 1997. 20

Collins, W. J., Stevenson, D. S., Johnson, C. E., and Derwent, R. G.: Tropospheric Ozone in a Global-Scale Three-Dimensional Lagrangian Model and Its Response to NO_x Emission Controls, J. Atmos. Chem., 26, 223–274, 1997. 8

Conkright, M., O'Brien, T., Stephens, C., Locarnini, R., Garcia, H., Boyer, T., and Antonov, J.: World Ocean Atlas 2001, Volume 6: Chlorophyll, p. 46 pp., NOOA Atlas NESDIS 52, U.S. Government Printing Office, 2002. 64

Conrad, R. and Seiler, W.: Influence of temperature, moisture, and organic carbon on the flux of H_2 and CO between soil and atmosphere: Field studies in subtropical regions, J. Geophys. Res., 90(D3), 5699–5709, 1985. 81

Conway, B., Desnoyers, J., and Smith, A.: Hydration of simple ions and polyions, Philos. Trans. R. Soc., 256, 256–389, 1964. 55

Conway, T., Tans, P., Waterman, L., Thoning, K., Kitzis, D., Masarie, K., and Zhang, N.: Evidence for interannual variability fo the carbon cycle from the NOAA/CMDL global air sampling network, J. Geophys. Res., 99, 22 831–22 855, 1994. 20

Courant, R., Friedrichs, K., and Lewy, H.: Über die partiellen Differenzengleichungen der mathematischen Physik, Mathematische Annalen, 100, 32–74, 1928. 9

Crutzen, P. and Zimmermann, P. H.: The changing photochemistry of the troposphere, Tellus, 43 AB, 136–151, 1991. 1

Crutzen, P. J.: Gas-phase nitrogen and methane chemistry in the atmosphere, Report AP-10, University of Stockholm, 1972. 1, 5

Crutzen, P. J.: A discussion of the chemistry of some minor constituents in the stratosphere and troposphere, Pure and Applied Geophysics, 106–108, 1385–1399, 1973. 1, 5

Crutzen, P. J.: Photochemical reactions initiated by and influencing ozone in unpolluted tropospheric air, Tellus, 16, 47–56, 1974. 1, 5

Crutzen, P. J.: The role of NO and NO_2 in the chemistry of the stratosphere and troposphere, Ann. Rev. Earth Planet Sci., 7, 443–472, 1979. 6

Damian, V., Sandu, A., Damian, M., Potra, F., and Carmichael, G. R.: The kinetic preprocessor KPP - a software environment for solving chemical kinetics, Computers and Chemical Engineering, 26, 1567 – 1579, 2002. 14

Debye, P. and MacAulay, I.: Das Elektrische Feld Der Ionen Und Die Neutralsalzwirking, Physic Z, 26, 22–29, 1925. 55

Diffey, B.: Solar ultraviolet radiation effects on biological systems, Physics in Medicine and Biology, 26, 299–328, 1991. 1

Donahue, N. M. and Prinn, R. G.: Non-methane Hydrocarbon Chemistry in the Remote Marine Boundary Layer, J. Geophys. Res., 95, 18 387–18 411, 1990. 64

Dutton, J.: The Ceaseless Wind. An Introduction to the Theory of Atmospheric Motion, Dover, New York, USA, 1986. 73

Elrod, M. J., Ranschaert, D. L., and Schneider, N. J.: Direct kinetics study of the temperature dependence of the CH_2O branching channel for the CH_3O_2 + HO_2 reaction, Int. J. Chem. Kinetics, 33, 363–376, 2001. 119

Emmons, L. K., Hauglustaine, D. A., Müller, J.-F., Carroll, M. A., Brasseur, G. P., Brunner, D., Staehelin, J., Thouret, V., and Marenco, A.: Data composites of airborne observations of tropospheric ozone and its precursors, J. Geophys. Res., 105, 20 497–20 538, 2000. 20, 35, 85

Erickson, D. and Hernandez, J.: A global, high resolution, satellite-based model of air-sea isoprene flux, in Gas transfer at water surface, edited by M. Donelan, W. Drennan, M. Saltzmann, and R. Wanninkhof, pp. 333–341, Geophysical Monograph, 2002. 65, 66

Erickson, D., Ghan, S., and Penner, J.: Global ocean to atmosphere dimethyl sulfide flux, J. Geophys. Res., 95, 7542–7552, 1990. 62

Feely, R., Sabine, C., Takahasi, T., and Wanninkhof, R.: Uptake and Storage of Carbon Dioxide in the Ocean: The Global CO_2 Survey, Oceanography, 14, 18–32, 2001. 66

Finkbeiner, M., Crowley, J. N., Horie, O., Müller, R., Moortgat, G. K., and Crutzen, P. J.: Reaction between HO_2 and ClO: Product formation between 210 and 300 K, J. Phys. Chem., 99, 16 264–16 275, 1995. 119

Fishman, J., Hoell, Jr., J. M., Bendura, R. D., Mc Neal, R. J., and Kirchhoff, V. W. J. H.: NASA GTE TRACE A Experiment (September October 1992): Overview, J. Geophys. Res., 101, 23 865–23 880, 1996. 20

Folberth, G., Hauglustaine, D., Lathiere, J., and Brocheton, F.: Interactive chemistry in the Laboratoire de Meteorologie Dynamique general circulation model: model description and impact analysis of biogenic hydrocarbons on tropospheric chemistry, Atmos. Chem. Phys., 6, 2273–2319, 2006. 19, 33, 47, 82, 89

Folkins, I. and Chatfield, R.: Impact of acetone on ozone production and OH in the upper troposphere at high NOx, J. Geophys. Res., 105, 11 585–11 599, 2000. 7, 47

Frank, D., Sackett, W., Hall, R., and Fredericks, A.: Methane, ethane, and propane concentrations in the Gulf of Mexico, Am. Assoc. Pet. Geol. Bull., 19, 1933–1938, 1970. 51

Fried, A., Wang, Y., Cantrell, C., Wert, B., Walega, J., Ridley, B., Atlas, E., Shetter, R., Lefer, B., Coffey, M. T., Hannigan, J., Blake, D., Blake, N., Meinardi, S., Talbot, B., Dibb, J., E.Scheuer, Wingenter, O., Snow, J., Heikes, B., and Ehhalt, D.: Tunable diode laser measurements of formaldehyde during the TOPSE 2000 study: Distributions, trends,, J. Geophys. Res., 108, doi:10.1029/2002JD002 208, 2003. 47

Fuentes, J. D., Hayden, B. P., Garstang, M., Lerdau, M., Fitzjarrald, D., Baldochi, D. D., Monson, R., Lamb, B., and Geron, C.: New Directions: VOCs and biosphere-atmosphere feedbacks, Atmos. Environ., 35, 189–191, 2001. 106

Galbally, I. E. and Kirstine, W.: The production of methanol by flowering plants and the global cycle of methanol, J. Atmos. Chem., 43, 195–229, 2002. 43, 45, 94, 96

Ganzeveld, L. and Lelieveld, J.: Dry Deposition parameterization in a chemical general circulation model and its influence on the distribution of reactive trace gases, J. Geophys. Res., 100, 20 999–21 012, 1995. 12, 18, 59

Ganzeveld, L., Lelieveld, J., and Roelofs, G.-J.: A dry deposition parameterization for sulfur oxides in a chemistry and general circulation model, J. Geophys. Res., 103, 5679–5694, 1998. 12, 17, 59

Ganzeveld, L., van Aardenne, J., Butler, T., Jöckel, P., Kerkweg, A., Lawrence, M., Metzger, S., Stier, P. Zimmerman, P., and Lelieveld, J.: Technical Note: Anthropogenic and natural offline emissions and the online EMissions and dry DEPosition (EMDEP) submodel of the Modular Earth Submodel system (MESSy), Atmos. Chem. Phys., submitted, 2006. 17, 30, 36

Garland, J.: The dry deposition of sulphur dioxide to land and water surfaces, Proc. R. Soc. London, 354, 245–268, 1977. 61

Gilles, M. K., Turnipseed, A. A., Burkholder, J. B., Ravishankara, A. R., and Solomon, S.: Kinetics of the IO radical. 2. Reaction of IO with BrO, J. Phys. Chem. A, 101, 5526–5534, 1997. 120

Giorgetta, M. and Bengtsson, L.: The potential role of the quasi-biennial oscillation in the stratosphere-troposphere exchange as found in water vapour in general circulation model experiments, J. Geophys. Res., 104, 6003–6019, 1999. 14

Goldan, P. D., Kuster, W., Fehsenfeld, F., and Montzka, S.: Hydrocarbon measurements in the southeastern United States: The Rural Oxidants in the Southern Environment (ROSE) program 1990, J. Geophys. Res., 100, 35 945–35 963, 1995. 20, 90

Goldstein, A. H., Wofsy, S. C., and Spivakovsky, C. M.: Seasonal variation of nonmethane hydrocarbons in rural New England: Constraints on OH concentrations in northern midlatitudes, J. Geophys. Res., 100, 21 023–21 033, 1995. 90

Grannas, A. M., Shepson, P., Guimbaud, C., Sumner, A., Albert, M., Simpson, W., Domine, F., Boudries, H., Bottenheim, J., Beine, H., Honrath, R., and Zhou, X.: A study of photochemical and physical processes affecting carbonyl compounds in the Arctic atmospheric boundary layer, Atmos. Environ., 36, 2733–2742, 2002. 90

Green, T. and Houk, D. F.: The Mixing of Rain with Near-Surface Water, J. Fluid. Mech., 90, 569 588, 1979. 59

Greenberg, J. P., Helmig, D., and Zimmerman, P. R.: Seasonal measurements of nonmethane hydrocarbons and carbon monoxide at the Mauna Loa Observatory during the Mauna Loa Observatory Photochemitry Experiment 2, J. Geophys. Res., 101, 14 581–14 598, 1996. 20

Guenther, A., Hewitt, C. N., Erickson, D., Fall, R., Geron, C., Graedel, T., Harley, P., Klinger, L., Lerdau, M., McKay, W. A., Pierce, T., Scholes, B., Steinbrecher, R., Tallamraju, R., Taylor, J., and Zimmerman, P.: A global model of natural volatile organic compound emissions, J. Geophys. Res., 100, 8873–8892, 1995. 16, 17, 94

Guenther, A., Geron, C., Pierce, T., Lamb, B., Harley, P., and Fall, R.: Natural emissions of non-methane volatile organic compounds, carbon monoxide, and oxides of nitrogen from North America, Atmos. Environ., 34, 2205–2230, 2000. 16

Guimbaud, C., Grannas, A., Shepson, P., Fuentes, J., Boudries, H., Bottenheim, J., Domine, F., Houdier, S., Perrier, S., Biesenthal, T., and Splawn, B.: Snowpack processing of acetaldehyde and acetone in the Arctic atmospheric boundary layer, Atmos. Environ., 36, 2743–2752, 2002. 90

Gurney, K., Law, R., Denning, A., Rayner, P.J.and Pak, B., Baker, D., Bousquet, P., Bruhwiler, L., Chen, Y.-H. Ciais, P., Fan, S., Fung, I., Gloor, M., Heimann, M., Higuchi, K., John, J., Maki, T., Maksyutov, S., Masarie, K., Peylin, P., Prather, M. Pak, B., Randerson, J., Sarmiento, J., Taguchi, S., Takahashi, T., and Yuen, C.-W.: Towards robust regional estimates of CO2 sources and sinks using atmospheric transport models, Nature, 415, 626–630, 2002. 72

Gurney, K., Law, R., Denning, A., Rayner, P.J.and Pak, B., Baker, D., Bousquet, P., Bruhwiler, L., Chen, Y.-H. Ciais, P., Fung, I., Heimann, M., John, J., Maki, T., Maksyutov, S., Peylin, P., Prather, M., and Taguchi, S.: Transcom 3 inversion intercomparison: Model mean results for the estimation of seasonal carbon sources and sinks, Global Biogeochem. Cycles, 18, doi:10.1029/2003GB002 111, 2004. 71, 72

Haagen-Smit, A. J.: Chemistry and physiology of Los Angeles smog, Ind. Eng. Chem., 44, 1342–1346, 1952. 1

Haas-Laursea, D. and Hartley, D.: Consistent sampling methods for comparing models to CO_2 flask data, J. Geophys. Res., 102, 19 059–19 071, 1997. 31

Hagemann, S., Arpe, K., Bengtsson, L., and Kirchner, I.: Parameterization of moist convection in the National Center for Atmospheric Research community climate model (CCM2), Technical report, 3. workshoop on re-analysis, 5-9 november 2001, ERA-40 Project report series, Reading, UK, 2002. 10

Hagemann, S., Arpe, K., and Roeckner, E.: Evaluation of the hydrological cycle in the ECHAM5 model, J. Clim., 19, 3810–3827, 2006. 9

Harris, R., Wosfy, S., Hoell, J., Bendura, R., Drewry, J., McNeal, R., Pierce, D., Rabine, V., and R.L., S.: The Arctic Boundary layer Expadition (ABLE-3B): July-August 19990, J. Geophys. Res., 99, 1635–1644, 1994. 20

Hauglustaine, D. A., Brasseur, G. P., Walters, S., Rasch, P. J., Müller, J.-F., Emmons, L. K., and Carroll, M. A.: MOZART, a global chemical transport model for ozone and related chemical tracers, 2: Model results and evaluation, J. Geophys. Res., 103, 28 291–28 335, 1998. 33

Hayduk, W. and Laudie, H.: Prediction of diffusion coefficients for nonelectrolytes in diluite aqueous solutions, AIChE J., 20, 611–615, 1974. 57, 125

Heikes, B. G., Chang, W., Pilson, M. E. Q., Swift, E., Singh, H. B., Guenther, A., Jacob, D. J., Field, B. D., Fall, R., Riemer, D., and Brand, L.: Atmospheric methanol budget and ocean implication, Global Biogeochem. Cycles, 16, 1133, doi:10.1029/2002GB001 895, 2002. 19, 43, 45, 84, 94, 96

Hein, R., Crutzen, P. J., and Heimann, M.: An inverse modelling approach to investigate the global atmospheric methane cycle, Global Biogeochem. Cycles, 11, 43–76, 1997. 16

Ho, D., Bliven, L., Wanninkhof, R., and Schlosser, P.: The effect of rain on air-water gas exchange, Tellus, 49, 149–158, 1997. 59

Ho, D., Cliff, S., Murray, A. L., Smith, J., Schlosser, P., Harvey, M., and Hill, P.: Measurements of air-sea gas exchange at high wind speeds in the Southern Ocean: Implications for global parameterizations, Geophys. Res. Lett., 33, doi:10.1029/2006GL026 817, 2006a. 55, 56, 57, 70, 71

Ho, D., Veron, F., Harrison, E., Bliven, L., Scott, N., and McGillis, W.: The combined effect of rain and wind on air-water gas exchange: A feasibility study, J. Mar. Syst., p. doi:10.1016/j.jmarsys.2006.1002.1012, 2006b. 59

Hoell, J. M., Davis, D. D., Liu, S. C., Newell, R., Shipham, M., Akimoto, H., McNeal, R. J., Bendura, R. J., and Drewry, J. W.: Pacific Exploratory Mission – West A (PEM–West A): September – October 1991, J. Geophys. Res., 101, 1641–1653, 1996. 20

Hoell, J. M., Davis, D. D., Liu, S. C., Newell, R., Akimoto, H., McNeal, R. J., and Bendura, R. J.: Pacific Exploratory Mission – West Phase B: February – March 1994, J. Geophys. Res., 102, 28 223–28 239, 1997. 20

Hoell, J. M., Davis, D. D., Jacob, D. J., Rodgers, M. O., Newell, R. E., Fuelberg, N. E., McNeal, R. J., Raper, J. L., and Bendura, R. J.: Pacific Exploratory Mission in the tropical Pacific: PEM-Tropics A, August–September 1996, J. Geophys. Res., 104, 5567–5583, 1999. 20

Holton, J. R., Haynes, P. H., McIntyre, M. E., Douglas, A. R., Rood, R. B., and Pfister, L.: Stratosphere-Troposphere Exchange, Rev. Geophys., 33, 403–439, 1995. 27

Holzinger, R., Jordan, A., Hansel, A., and Lindinger, W.: Methanol measurements in the lower troposphere near Innsbruck, Atmos. Environ., 35, 2525–2532, 2001. 90

Horowitz, L. W., Walters, S., Mauzerall, D. L., Emmons, L. K., Rasch, P. J., Granier, C., Tie, X., Lamarque, J.-F., Schultz, M. G., Tyndall, G. S., Orlando, J. J., and Brasseur, G. P.: A global simulation of tropospheric ozone and related tracers: Description and evaluation of MOZART, version 2, J. Geophys. Res., 108, 4784, doi:10.1029/2002JD002 853, 2003. 19, 30, 33, 82, 100

Houghton, J.: (Intergovernmental Panel on Climate Change), Climate Change 1995: The Science of Climate Change, Cambridge University Press, Cambridge, UK, 1996. 5, 106

Houghton, J. T., Ding, Y., Griggs, D. J., Nouger, M., van der Linden, P. J., Dai, X., Maskell, K., and Johnson, C. A.: IPCC - Climate Change 2001: The Scientific Basis. Contribution of Working Group I to the third Assessment Report of the Intergovernmental Panel on Climate Change, Cambridge University Press, 2001. 13

Houk, D. F. and Green, T.: A Note on Surface Waves Due to Rain, J. Geophys. Res., 81, 4482 4484, 1976. 58

Houweling, S., Dentener, F., and Lelieveld, J.: The impact of non-methane hydrocarbon compounds on tropospheric photochemistry, J. Geophys. Res., 103, 10 673–10 696, 1998. 13

Hynes, A. J. and Wine, P. H.: The atmospheric chemistry of dimethylsulfoxide (DMSO) kinetics and mechanism of the OH + DMSO reaction, J. Atmos. Chem., 24, 23–37, 1996. 118

Jacob, D., Field, B., Jin, E., Bey, I., Li, Q., Logan, J., and Yantosca, R.: Atmospheric budget of acetone, J. Geophys. Res., 107, 4100, doi:10.1029/2001JD000 694, 2002. 19, 36, 38, 89, 90, 94

Jacob, D., Crawford, J., Kleb, M., Connors, V., Bendura, R., Raper, J., Sachse, G., Gille, J., Emmons, L., and Heald, C.: Transport and Chemical Evolution over the Pacific (TRACE-P) aircraft mission: Design, execution, and first results, J. Geophys. Res., 108, doi:10.1029/2002JD003 276, 2003. 20

Jacob, D. J., Field, B. D., Li, Q., Blake, D. R., de Gouw, J., Warneke, C., Hansel, A., Wisthaler, A., Singh, H. B., and Guenther, A.: Global budget of methanol: Constraints from atmospheric observations, J. Geophys. Res., 110, doi:10.1029/2004JD005 172, 2005. 19, 43, 45, 81, 84, 93, 96

Jacobson, Z.: Foundamentals of Atmospheric modelling, Cambridge University press, 1999. 74

Jaeglé, L., Jacob, D. J., Wennberg, P. O., Spivakovsky, C. M., Hanisco, T. F., Lanzendorf, E. J., Hintsa, E. J., Fahey, D. W., Keim, E. R., Proffitt, M. H., Atlas, E. L., Flocke, F., Schauffler, S., McElroy, C. T., Midwinter, C., Pfister, L., and Wilson, J. C.: Observed OH and HO_2 in the upper troposphere suggest a major source from convective injection of peroxides, Geophys. Res. Lett., 24, 3181–3184, 1997. 8

Jaeglé, L., Jacob, D. J., Brune, W. H., Faloona, I., Tan, D., Heikes, B. G., Kondo, Y., Sachse, G. W., Anderson, B., Gregory, G. L., Singh, H. B., Pueschel, R., Ferry, G., Blake, D. R., and Shetter, R.: Photochemistry of HO_x in the upper troposphere at northern mid-latitudes, J. Geophys. Res., 105, 3877–3892, 2000. 8

Jaeglé, L., Jacob, D. J., Brune, W. H., and Wennberg, P. O.: Chemistry of HO_x radicals in the upper troposphere, Atmos. Environ., 35, 469–489, 2001. 7, 47

Jähne, B., Muennich, K., Boesinger, R., Dutzi, A., Huber, W., and Libner, P.: On parameter influencing the air-water gas exchange, J. Geophys. Res., 92, 1937–1949, 1987. 57

Jenkin, M. E. and Clemitshaw, K. C.: Ozone and other secondary photochemical pollutants: chemical processes governing their formation in the planetary boundary layer, Atmos. Environ., 34, 2499–2527, 2000. 5

Jenkin, M. E., Cox, R. A., and Candeland, D. E.: Photochemical aspects of tropospheric iodine behaviour, J. Atmos. Chem., 2, 359–375, 1985. 120

Jeuken, A., Siegmund, P., Heijboer, L., Feichter, J., and Bengtsson, L.: On the potential assimilating meteorological analyses in a global model for the purpose of model validation, J. Geophys. Res., 101, 16 939–16 950, 1996. 10

Jimenez, J. L., Bahreini, R., Cocker III, D. R., Zhuang, H., Varutbangkul, V., Flagan, R. C., Seinfeld, J. H., O'Dowd, C. D., and Hoffmann, T.: New particle formation from photooxidation of diiodomethane (CH_2I_2), J. Geophys. Res., 108D, 2003. 120

Jöckel, P., Sander, R., Kerkweg, A., Tost, H., and Lelieveld, J.: Technical Note: The Modular Earth Submodel System (MESSy) – a new approach towards Earth System Modeling, Atmos. Chem. Phys., 5, 433–444, 2005. 10, 11

Jöckel, P., Tost, H., Pozzer, A., Brühl, C., Bucholz, J., L., G., Hoor, P., Kerkweg, A., Lawrence, M., Sander, R., Steil, B., Stiller, G., Tanarhte, M., Taraborrelli, D., van Aardenne, J., and Lelieveld, J.: Evaluation of the atmospheric chemistry GCM ECHAM5/MESSy: Consistent simulation of ozone in the stratosphere and troposphere, Atmos. Chem. Phys., 6, 5067–5104, 2006. 1, 11

Junge, C. E.: Global ozone budget and exchange between stratosphere and troposphere, Tellus, 14, 363–377, 1962. 1

Karl, T., Potosnak, M., Guenther, A., Clark, D., Walker, J., Herrick, J., and Geron, C.: Exchange processes of volatile organic compounds above a tropical rain forest: Implications for modeling tropospheric chemistry above dense vegetation,, J. Geophys. Res., 109, doi:10.1029/2004JD004 738., 2004. 90

Katsaros, K. B.: Effects of Precipitation on the Eddy Exchange in a Wind-Driven Sea, Dyn. Atmosph. Oceans, 1, 99–126, 1976. 59

Keeling, R., Piper, S., and Heinmann, M.: Global and hemispheric CO2 sinks deduced from changes in atmospheric O2 concentration, Nature, 381, 218–221, 1996. 71

Kelly, K.: Rethinking the ozone problem in urban and regional air pollution, National Academy Press, Washington DC, USA, 1991. 7

Kentarchos, A. S. and Roelofs, G.: A model study of stratospheric ozone in the troposphere and its contribution to tropospheric OH formation, J. Geophys. Res., 108,D12, doi:10.1029/2002JD002 598, 2003. 1

Kerkweg, A.: Global Modelling of Atmospheric Halogen Chemistry in the Marine Boundary Layer, Ph.D. thesis, Rheinischen Friedrich-Wilhelms-Universität, Bonn, Germany, 2005. 13

Kerkweg, A., Buchholz, J., Ganzeveld, L., Pozzer, A., Tost, H., and Jöckel, P.: Technical Note: An implementation of the dry removal processes DRY DEPosition and SEDImentation in the Modular Earth Submodel System (MESSy), Atmos. Chem. Phys., 6, 4617–4632, 2006a. 12, 14, 18, 59, 74

Kerkweg, A., Sander, R., Tost, H., and Jöckel, P.: Technical Note: Implementation of prescribed (OFFLEM), calculated (ONLEM), and pseudo-emissions (TNUDGE) of chemical species in the Modular Earth Submodel System (MESSy), Atmos. Chem. Phys., 6, 3603–3609, 2006b. 13, 14, 16, 72

Kettle, A., Andreae, M., Amouroux, D., Andreae, T., Bates, T., Berresheim, H., Bingemer, H., Boniforti, R., Curran, M., DeTullio, G., Helas, G., Jones, G., Keller, M., Kiene, R., Leck, C., Levasseur, M., Maspero, M., Matraii, P., McTaggart, A., Mihalopoulos, N., Nguyen, B., Novo, A., J.P., P., Rapsomanikis, S., Roberts, G., Schebeske, G., Sharma, S., Simo, R., Staubes, R., Turner, S., and Uher, G.: A global database of sea surface dimethylsulfide (DMS) measurements and a simple model to predict sea surface DMS as a function of latitude, longitude and month, Global Biogeochem. Cycles, 13, 399–444, 1999. 62

Kettle, A. J. and Andreae, M.: Flux of dimethylsulfide from the oceans: A comparison of updated data set and flux models, J. Geophys. Res., 105, 26 793–26 808, 2000. 62, 63, 125

Khalil, M. and Rasmussen, R.: Global sources, lifetime and mass balances of carbonylsulfide (OCS) and carbon disulfide (CS_2) in the Earth's atmosphere, Atmos. Environ., 18, 1805–1813, 1984. 61

Kiley, C. M., Fuelberg, H. E., Palmer, P. I., Allen, D., Carmichael, G., Jacob, D., Mari, C., Pierce, R., Pickering, K., Tang, Y., Wild, O., Fairlie, T., Logan, J., Sachse, G., Shaack, T., and Streets, D.: An intercomparison and evaluation of aircraft-derived and simulated CO from seven chemical transport models during the TRACE-P experiment, J. Geophys. Res., 108, doi:10.1029/2002JD003 089, 2003. 34, 81

Kircher, C. C. and Sander, S. P.: Kinetics and mechanism of HO_2 and DO_2 disproportionations, J. Phys. Chem., 88, 2082–2091, 1984. 111, 118

Kirchner, F. and Stockwell, W. R.: Effect of peroxy radical reactions on the predicted concentrations of ozone, nitrogenous compounds, and radicals, J. Geophys. Res., 101D, 21 007–21 022, 1996. 114, 119

Lamb, B., Gay, D., Westberg, H., and Pierce, T.: A biogenic hydrocarbon emission inventory for the U.S.A. using a simple forest canopy model, Atmos. Environ., 27A, 1673–1690, 1993. 17

Lamontagne, R., Swinnerton, J., and Linnebom, V.: C_1 - C_4 hydrocarbons in the North and South Pacific, Tellus, 26, 71–77, 1974. 51

Landgraf, J. and Crutzen, P. J.: An Efficient Method for Online Calculations of Photolysis and Heating Rates, J. Atmos. Chem., 25, 863–878, 1998. 13, 15, 16

Lang, P., Steele, L., Waterman, L. S., R.C., M., K.A., M., and E.J., D.: NOAA/CMDL atmospheric methane data for the period 1983-1990 from shipboard flask sampling, Noaa tech. memo, ERL CMDL-4, 1992. 20

Lawrence, M. and Rasch, P.: Tracer transport in deep convective updrafts: plume ensemble versus bulk formulations, J. Aerosol Sci., 62, 2880–2894, 2005. 12

Lawrence, M. G., Crutzen, P. J., and Rasch, P. J.: Analysis of the CEPEX ozone data using a 3D chemistry-meteorology model, Q. J. R. Meteorol. Soc., 125, 2987–3009, 1999a. 15

Lawrence, M. G., Crutzen, P. J., Rasch, P. J., Eaton, B. E., and Mahowald, N. M.: A model for studies of tropospheric photochemistry: Description, global distributions, and evaluation, J. Geophys. Res., 104, 26 245–26 277, 1999b. 81

LeBas, G.: The Molecular Volumes of Liquid Chemical Compounds, in The Properties of Gases and Liquids, Monograph Longmans, Green, 1915. 55, 125

Lee, M., Heikes, B., Jacob, D., Sachse, G., and Anderson, B.: Atmospheric carbonyl compounds at a rural southeastern United States site, J. Geophys. Res., 100, 25 933–25 944, 1995. 90

Leighton, P. A.: Photochemistry of air pollution, Academic Press, 1961. 1

Lelieveld, J. and Dentener, F. J.: What controls tropospheric ozone?, J. Geophys. Res., 105, 3531–3551, 2000. 1

Lelieveld, J., Peters, W., Dentener, F., and Krol, M.: Stability of tropospheric hydroxyl chemistry, J. Geophys. Res., 107, doi:10.1029/2002JD002 272, 2002. 3, 4, 30

Lelieveld, J., Brühl, C., Steil, B., Crutzen, P., Fischer, H., Giorgietta, M., Hoor, P., Milz, M., Sausen, R., Stiller, G., and Tost, H.: Stratosphereic dryness, Atmos. Chem. Phys. Discuss., submitted, 2006. 10

Levy, H.: Normal Atmosphere: Large radical and formaldehyde concentrations predicted, Sci. China, 173, 141–143, 1971. 1, 3

Lewis, A. C., Carpenter, L. J., and Pilling, M. J.: Nonmethane hydrocarbons in Southern Ocean boundary layer air, J. Geophys. Res., 106, 4987–4994, 2001. 64

Lewis, A. C., Hopkins, J., Carpenter, L. J., Stanton, J., Read, K. A., and Pilling, M.: Sources and sinks of acetone, methanol, and acetaldehyde in North Atlantic marine air, Atmos. Chem. Phys., 5, 1963–1974, 2005. 43, 94

Lin, S.-J. and Rood, R. B.: Multidimensional Flux-Form Semi-Lagrangian Transport Schemes, Mon. Weather Rev., 124, 2026–2070, 1996. 9

Lindskog, A. and Moldanová, J.: The Influence of the Origin, Season and Time of the day on the Distribution of Individual NMHC Measured at Rörvik, Sweden, Atmos. Environ., 28, 2383–2398, 1994. 20

Lippmann, M.: Health effects of ozone. A critical review., JAPCA, 39, 672–695, 1989. 1

Liss, P. and Merlivat, L.: Air-sea gas exchange rates: Introduction and synthesis, in The Role of Air-Sea Exchange in Geochemical Cycling, pp. 113–127, P. Buat-Menard, 1986. 55, 56, 57, 71

Liss, P. and Slater, P.: Flux of gases across the air-sea interface, Nature, 247, 181–184, 1974. 51

Logan, J. A.: An analysis of ozone-sonde data for the troposphere: Recommendations for testing 3-D models and development of a gridded climatology for tropospheric ozone, J. Geophys. Res., 104, 16 115–16 149, 1999a. 18

Logan, J. A.: An analysis of ozone-sonde data for the the lower stratosphere, J. Geophys. Res., 104, 16 151–16 170, 1999b. 18

Logan, J. A., Prather, M. J., Wofsy, S. C., and McElroy, M. B.: Tropospheric chemistry: A global perspective, J. Geophys. Res., 86, 7210–7254, 1981. 3, 30

Lohmann, U. and Roeckner, E.: Design and performance of a new cloud microphysics scheme developed for the ECHAM general circulation model, Climate Dynamics, 12, 557–572, 1996. 12

Longstreth, J. D., deGruijl, F. R., Kripke, M. L., Takizawa, Y., and Vanderleun, J. C.: Effects of increased solar ultraviolet radiation on human health, Ambio, 24, 153–165, 1995. 1

Lyman, W., Reehl, W., and Rosenblatt, D.: Handbook of chemical property estimation mehods, American Chemical Society, Washington DC, USA, 1990. 60

Madronich, S. and Calvert, J. G.: Permutation reactions of organic peroxy radicals in the troposphere, J. Geophys. Res., 95D, 5697–5715, 1990. 119

Manzini, E., Giorgetta, M., Esch, M., Kornblueh, L., and Roeckner, E.: The influence of sea surface temperatures on the northern winter stratosphere: Ensemble simulations with the MAECHAM5 model, J. Clim., 19, 3863–3881, 2006. 9

Marandino, C., De Bruyn, W., Miller, S., Prather, M., and Saltzmann, E.: Oceanic uptake and the global atmospheric acetone budget, Geophys. Res. Lett., 32, doi:10.1029/2005GL023 285, 2005. 89, 94

Masterton, W. and Lee, T.: Salting coefficients from scaled particle theory, J. Phys. Chem., 74, 1776, 1970. 55

Matsumoto, K., Sarmiento, J., Key, R., Aumont, O., Bullister, J., Caldeira, K., Campin, J.-M., Doney, S. C., Drange, H., Dutay, J.-C., Follows, M., Gao, Y., Gnanadesikan, A., Gruber, N., Ishida, A., Joos, F., Lindsay, K., Maier-Reimer, E., Marshall, J. C., Matear, R. J., Monfray, P., Mouchet, A., Nar, R., Plattner, G.-K., cSchlitzer, R., Slater, R., Swathi, P. S., Totterdell, I. J., Weirig, M.-F., Yamanaka, Y., Yool, A., and Orr, J. C.: Evaluation of ocean carbon cycle models with data-based metrics, Geophys. Res. Lett., 31, doi:10.1029/2003GL018 970, 2004. 71

McCabe, D. C., Gierczak, T., Talukdar, R. K., and Ravishankara, A. R.: Kinetics of the reaction OH + CO under atmospheric conditions, Geophys. Res. Lett., 28, 3135–3138, 2001. 113

McDevitt, W. and Long, F.: The activity coefficient of benzene in aqueous salt solutions, J. Am. Chem. Soc., 74, 1773 1777, 1952. 55

McKee, D. J., ed.: Tropospheric Ozone, Human Health and Agricultural Impacts, Lewis, Boca Raton, Fla., 1993. 1

McKeen, S. A., Gierczak, T., Burkholder, J. B., Wennberg, P. O., Hanisco, T. F., Keim, E. R., Gao, R.-S., Liu, S. C., Ravishankara, A. R., and Fahey, D. W.: The photochemistry of acetone in the upper troposphere: A source of odd-hydrogen radicals, Geophys. Res. Lett., 24, 3177–3180, 1997. 47

McNeil, B. I., Matear, R., Key, R., Bullister, J., and Sarmiento, J.: Anthropogenic CO2 uptake by the ocean using the global chlorofluorocarbon dataset, Science, 299, 235–239, 2003. 71

Meilinger, S. K.: Heterogeneous Chemistry in the Tropopause Region: Impact of Aircraft Emissions, Ph.D. thesis, ETH Zürich, Switzerland, `http://e-collection.ethbib.ethz.ch/show?type=diss&nr=13819`, 2000. 13

Meskhidze, N. and Nenes, A.: Phytoplankton and Cloudiness in the Southern Ocean, Science, 314, 1419 – 1423, doi:10.1126/science.1131 779, 2006. 106

Mihalopoulos, N., Ngyen, B., Putand, J., and Belviso, S.: The oceanic source of carbonyl sulfide (COS), Atmos. Environ., 26A, 1383–1394, 1992. 61

Mikaloff, S., Gruber, N., Jacobson, A. R., Doney, S. C., Dutkiewicz, S., Gerber, M., Follows, M., Joos, F., Lindsay, K., Menemenlis, D., Mouchet, A., Müller, S., and Sarmiento, J.: Inverse estimates of anthropogenic CO2 uptake, transport, and storage by the ocean, Global Biogeochem. Cycles, 20, doi:10.1029/2005GB002 530, 2006. 71

Monahan, E.: Occurrence and evolution of acustically relevant sub surface bubble plumes and their associated, remotely monitorable, surface withecaps, in Natural Physical Sources of Underwater Sound, edited by B. Kerman, pp. 503–517, Kluwer Acad., 1993. 58

Moxim, W. J., Levy, H., and Kasibhatla, P. S.: Simulated global tropospheric PAN: Its transport and impact on NO_x, J. Geophys. Res., 101, 12 621–12 638, 1996. 6

Moxley, J. M. and Cape, J. N.: Depletion of carbon monoxide from the nocturnal boundary layer, Atmos. Environ., 31, 1147–1155, 1997. 30, 82

Müller, J.-F. and Brasseur, G.: IMAGES: A three-dimensional chemical transport model of the global troposphere, J. Geophys. Res., 100D, 16 445–16 490, 1995. 114

Müller, J.-F. and Brasseur, G.: IMAGES: A three-dimensional chemical transport model of the global troposphere, J. Geophys. Res., 100, 16 445–16 490, 1995. 8, 47

Naujokat, B.: An update of the observed quasi biennial oscillation of the stratospheric winds over the tropics, J. Aerosol Sci., 43, 1873–1877, 1986. 14

Neeb, P., Horie, O., and Moortgat, G. K.: The ethene-ozone reaction in the gas phase, J. Phys. Chem. A, 102, 6778–6785, 1998. 119

Nguyen, B., Gaudry, A., Bonsang, B., and Lambert, G.: Reevaluation of the role of dimethylsulfide in the sulfur budget, Nature, 275, 637–639, 1978. 62

Ni, N., El-Sayed, M., Sanghvi, T., and Yalkowsky, S.: Estimation of the effect of NaCl on the solubility of organic compounds in aqueous solutions, J. Pharm. Sci., 89, 1620–1625, 2000. 55, 125

Nightingale, P. D., Malin, G., Law, C. S., Watson, A. J., Liss, P. S., Liddicoat, M. I., Boutin, J., and Upstill-Goddard, R. C.: In situ evaluation of air-sea gas exchange parametrizations using novel conservsative and volatile tracers, Global Biogeochem. Cycles, 14, 373–387, 2000. 55, 56, 57, 71

Nordeng, T. E.: Extended versions of the convective parametrization scheme at ECMWF and their impact on the mean and transient activity of the model in the tropics, Tech. Rep. 206, ECWMF, 1994. 9

Novelli, P. C., Steele, L. P., and Tans, P.: The mixing ratios of carbon monoxide in the troposphere, J. Geophys. Res., 97, 13 109–13 121, 1992. 20

Novelli, P. C., Masarie, K. A., and Lang, P. M.: Distribution and recent changes of carbon monoxide in the lower troposphere, J. Geophys. Res., 103, 19 015–19 033, 1998. 20, 31, 32

Olivier, J. G. J., Bouwman, A. F., van der Maas, C. W. M., Berdowski, J. J. M., Veldt, C., Bloos, J. P. J., Visschedijk, A. J. J., Zandveld, P. Y. J., and Haverlag, J. L.: Description of EDGAR Version 2.0: A set of global inventories of greenhouse gases and ozone-depleting substances for all anthrophogenic and most natural sources on a per country $1^\circ \times 1^\circ$ grid, RIVM Rep. 771060002, Rijksinstituut, Bilthoven, Netherlands, 1996. 16

Olivier, J. G. J., Bloos, J. P. J., Berdowski, J. J. M., Visschedijk, A. J. H., and Bouwman, A. F.: A 1990 global emission inventory of anthropogenic sources of carbon monoxide on $1^\circ \times 1^\circ$ developed in the framework of EDGAR/GEIA, Chemosphere, 1, 1–17, 1999. 16

Orlando, J. J. and Tyndall, G. S.: Rate coefficients for the thermal decomposition of $\mathrm{BrONO_2}$ and the heat of formation of $\mathrm{BrONO_2}$, J. Phys. Chem., 100, 19 398–19 405, 1996. 120

Orlando, J. J., Tyndall, G. S., Bertman, S. B., Chen, W., and Burkholder, J. B.: Rate coefficient for the reaction of OH with $\mathrm{CH_2{=}C(CH_3)C(O)OONO_2}$ (MPAN), Atmos. Environ., 36, 1895–1900, 2002. 115

Ostapoff, F., Tarbeyev, Y., and Worthem, S.: Heat Flux and Precipitation Estimates from Oceanographic Observations, Science, 180, 960–962, 1973. 59

Palmer, P. and Shaw, S.: Quantifying global marine isoprene fluxes using MODIS chlorophyll observations, J. Geophys. Res., 32, doi:10.1029/2005GL022 592, 2005. 65, 66

Palmer, P. I., Jacob, D. J., Fiore, A. M., Martin, R. V., Chance, K., and Kurosu, T. P.: Mapping isoprene emissions over North America using formaldehyde column observations from space, J. Geophys. Res., 108, 4180, doi:10.1029/2002JD002 153, 2003. 43

Park, R., Pickering, K., Allen, D., Stenchikov, G., and Fox-Rabinovitz, M.: Global simulation of tropospheric ozone using the University of Maryland Chemical Transport Model (UMD-CTM): 1. Model description and evaluation, J. Geophys. Res., 109, doi:10.1029/2003JD004 266, 2004a. 19, 33

Park, R., Pickering, K., Allen, D., Stenchikov, G., and Fox-Rabinovitz, M.: Global simulation of tropospheric ozone using the University of Maryland Chemical Transport Model (UMD-CTM): 2. Regional transport and chemistry over the central United States using a stretched grid, J. Geophys. Res., 109, doi:10.1029/2003JD004 269, 2004b. 33

Patra, P., Gurney, K. R., Denning, A. S., Maksyutov, S., Nakazawa, T., Baker, D., Bousquet, P., Bruhwiler, L., Chen, Y.-H., Ciais, P., Fan, S., Fung, I., Gloor, M., Heimann, M., Higuchi, K., John, J., Law, R., Maki, T., Pak, B., Peylin, P., Prather, M., Rayner, P., Sarmiento, J., Taguchi, S., Takahashi, T., and Yuen, C.-W.: Sensitivity of inverse estimation of annual mean CO2 sources and sinks to ocean-only sites versus all-sites observational networks, J. Geophys. Res., 33, doi:10.1029/2005GL025 403, 2006. 71

Pickering, K. E., Thompson, A. M., Wang, Y., Tao, W.-K., McNamara, E. P., Kichhoff, V. W. J. H., Heikes, B. G., Sachse, G. W., Bradshaw, J. D., Gregory, G. L., and Blake, D. R.: Convective transport of biomass burning emissions over Brazil during TRACE A, J. Geophys. Res., 101, 23 993–24 012, 1996. 38

Pickering, K. E., Wang, Y., Tao, W. K., Price, C., and Müller, J.-F.: Vertical distributions of lightning NO_x for use in regional and global chemical transport models, J. Geophys. Res., 103, 31 203–31 216, 1998. 13

Pitzer, K.: Activity coefficients in electrolyte solutions, 2nd Edition, CRC Press Inc.,Boca Raton, FL., 1991. 54

Placet, M., Mann, C., R.O., G., and Niefer, M.: Emissions of ozone precursors from stationary sources, Atmos. Environ., 34, 2183–2204, doi:10.1016/S1352–2310(99)00 464–1, 2000. 16

Plass-Dülmer, C., Koppman, R., Ratte, M., and Rudolph, J.: Light nonmethane hydrocarbons in seawater, Global Biogeochem. Cycles, 9, 79–100, 1995. 51, 93, 125

Plass-Dülmer, C., Koppmann, R., Ratte, M., and Rudolph, J.: Light non-methane hydrocarbons in seawater, Global Biogeochem. Cycles, 9, 79–100, 1995. 81

Poisson, N., Kanakidou, M., and Crutzen, P. J.: Impact of non-methane hydrocarbons on tropospheric chemistry and the oxidizing power of the global troposphere: 3-dimensional modelling results, J. Atmos. Chem., 36, 157–230, 2000. 36

Pöschl, U., von Kuhlmann, R., Poisson, N., and Crutzen, P. J.: Development and intercomparison of condensed isoprene oxidation mechanisms for global atmospheric modeling, J. Atmos. Chem., 37, 29–52, 2000. 115, 116, 119

Pozzer, A., Tost, H., Jöckel, P., Sander, R., Ganzeveld, L., Kerkweg, A., and Lelieveld, J.: Simulating organic species with the global chemistry-climate model ECHAM5/MESSy: a comparison of model results and observations, Atmos. Chem. Phys., (in preparation), 2006. 11

Prather, M. J. and Jacob, D. J.: A persistent imbalance in HO_x and NO_x photochemistry of the upper troposphere driven by deep convection, Geophys. Res. Lett., 24, 3189–3192, 1997. 8

Price, C. and Rind, D.: A simple lightning parameterization for calculating global lightning distributions, J. Geophys. Res., 97, 9919–9933, 1992. 13

Prinn, R. G., Weiss, R. F., Fraser, P. J., Simmonds, P. G., Cunnold, D. M., Alyea, F. N., O Doherty, S., Salameh, P., Miller, B. R., Huang, J., Wang, R. H. J., Hartley, D. E., Harth, C., Steele, L. P., Sturrock, G., Midgley, P. M., and McCulloch, A.: A history of chemically and radiatively important gases in air deduced from ALE/GAGE/AGAGE, J. Geophys. Res., 1051, 17 751–17 792, 2000. 14

Putaud, J.-P. and Nguyen, B.: Assessment of dimethylsulfide sea-air exchange rate, J. Geophys. Res., 101, 4403–4411, 1996. 62

Raper, J., Kleb, M., Jacob, D., Davis, D., Newell, R., Fuelberg, H., Bendura, R., Hoell, J., and McNeal, R.: Pacific Exploratory Mission in the Tropical Pacific: PEM-Tropics B, March-April 1999, J. Geophys. Res., 106, 32 401–32 425, 2001. 20

Ratte, M., Bujok, O., Spitzy, A., and Rudelph, J.: Laboratory experiments on the origin of C_2 -C_3 alkenes in seawater, in CACGP/IGAC symposium, Fuji-Yoshida, Japan, Sept. 5-9, 1994. 94

Ratte, M., Bujok, O., Spitzy, A., and Rudolph, J.: Photochemical alkene formation in seawater from dissolved organic carbon: Results from laboratory experiments, J. Geophys. Res., 103, 5707–5717, 1998. 94

Regener, V. H.: Vertical flux of atmospheric ozone, J. Geophys. Res., 62, 221–228, 1957. 1

Reid, R., Pransnitz, J., and Poling, B.: The Molecular Volumes of Liquid Chemical Compounds, in The Properties of Gases and Liquids, 3rd edition, McGraw Hill, New York, 1984. 55, 125

Reithmeier, C.: Untersuchungen zum global Spurenstofftranport und Stratosphären-Troposphären Austausch mit dem Lagrangeschen Modell ECHAM4/ATTILA, Ph.D. thesis, Ludwig-Maximilians-Universität, München, 2001. 73

Ridley, B., Walega, J., and adn F.E.Grahek, J. D.: Distribution of NO,NO_x,NO_y and O_3 to 12 km aktitude during the summer monsoon season over New Mexico, J. Geophys. Res., 99, 25 519–25 534, 1994. 20

Riedel, K., Allan, W., Weller, R., and Schrems, O.: Discrepancies between formaldehyde measurements and methane oxidation model predictions in the Antarctic troposphere: An assessment of other possible formaldehyde sources, J. Geophys. Res., 110, doi:10.1029/2005JD005 859, 2005. 47

Riemer, D., Pos, W., Milne, P., Farmer, C., Zika, R., Apel, E., Olszyna, K., Kliendienst, T., Lonneman, W., Bertman, S., Shepson, P., and Starn, T.: Observations of nonmethane hydrocarbons and oxygenated volatile organic compounds at a rural site in the southeastern United States, J. Geophys. Res., 103, 28 111–28 128, doi:10.1029/98JD02 677, 1998. 90

Riemer, D. D., Milne, P. J., and Zika, R. G.: Photoproduction of nonmethane hydrocarbons (NMHCs) in seawater, Mar. Chem., 71, 177–198, 2000. 94

Robert, A.: The integration of a sp[ectral model of the atmosphere by the implicit method, in WMO/IUGG Japan Meteorological society, Tokyo, Japan, pp. 19–24, 1969. 10

Roeckner, E., Bäuml, G., Bonaventura, L., Brokopf, R., Esch, M., Giorgetta, M., Hagemann, S., Kirchner, I., Kornblueh, L., Manzini, E., Rhodin, A., Schlese, U., Schulzweida, U., and Tompkins, A.: The atmospheric general circulation model ECHAM5.PART I: Model description, Technical report, Max Planck Institute for Meteorology, 2003. 9

Roeckner, E., Brokopf, R., Esch, M., Giorgetta, M., Hagemann, S., Kornblueh, L., Manzini, E., Schlese, U., and Schulzweida, U.: Sensitivity of simulated climate to horizontal and vertical resolution in the ECHAM5 atmosphere model, J. Clim., 19, 3771–3791, 2006. 9

Roelofs, G.-J. and Lelieveld, J.: Model study of the influence of cross-tropopause O_3 transports of tropospheric O_3 levels, Tellus, 49B, 38–55, 1997. 111

Roesch, A. and Roeckner, E.: Assessment of snow cover and surface albedo in the ECHAM5 general circulation model, J. Clim., 19, 3828–3843, 2006. 9

Rowley, D. M., Bloss, W. J., Cox, R. A., and Jones, R. L.: Kinetics and products of the IO + BrO reaction, J. Phys. Chem. A, 105, 7855–7864, 2001. 120

Rudolph, J., Khedim, A., and Wagenbach, E.: The Seasonal Variation of Light Non-methane Hydrocarbons in the Antarctic Troposphere, J. Geophys. Res., 94, 13 039–13 044, 1989. 20

Sabine, C., Feely, R., Gruber, N., Key, R., Lee, K., Bullister, J., Wanninkhof, R., Wong, C., Wallace, D., Tilbrook, B., Millero, F., Peng, T.-H., Kozyr, A., Ono, T., and Rios, A.: The Oceanic Sink for Anthropogenic CO_2, Nature, 305, 367–371, 2004. 66

Saltzmann, E., King, D., K., H., and C., L.: Experimental determination of the diffusion coefficient of dimethylsulfide in water, J. Geophys. Res., 98, 16 481–16 486, 1993. 57

Sander, R.: Modeling atmospheric chemistry: Interactions between gas-phase species and liquid cloud/-aerosol particles, Surv. Geophys., 20, 1–31, 1999a. 56

Sander, R.: Compilation of Henry's law constant for inorganic and organic species of potential importance in environmental chemistry, `http://www.henrys-law.org`, 1999b. 54, 125

Sander, R., Jöckel, P., Kerkweg, A., and Lelieveld, J.: Technical Note: The new comprehensive atmospheric chemistry module MECCA, Atmos. Chem. Phys., 5, 445–450, 2005. 13, 14

Sander, S. P., Friedl, R. R., DeMore, W. B., Golden, D. M., Kurylo, M. J., Hampson, R. F., Huie, R. E., Moortgat, G. K., Ravishankara, A. R., Kolb, C. E., and Molina, M. J.: Chemical kinetics and photochemical data for use in stratospheric modeling. Supplement to evaluation 12: Update of key reactions. Evaluation number 13, JPL Publication 00-3, Jet Propulsion Laboratory, Pasadena, CA, `http://jpldataeval.jpl.nasa.gov/`, 2000. 123

Sander, S. P., Finlayson-Pitts, B. J., Friedl, R. R., Golden, D. M., Huie, R. E., Kolb, C. E., Kurylo, M. J., Molina, M. J., Moortgat, G. K., Orkin, V. L., and Ravishankara, A. R.: Chemical Kinetics and Photochemical Data for Use in Atmospheric Studies, Evaluation Number 14, JPL Publication 02-25, Jet Propulsion Laboratory, Pasadena, CA, 2003. 111, 112, 113, 114, 116, 117, 118, 119, 120, 123

Sandu, A. and Sander, R.: Technical Note: Simulating chemical systems in Fortran90 and Matlab with the kinetic preprocessor KPP-2.1, Atmos. Chem. Phys., 6, 187–195, 2006. 14

Sanhueza, E., Dong, Y., Scharffe, D., Lobert, J. M., and Crutzen, P. J.: Carbon monoxide uptake by temperate forest soils: The effects of leaves and humus layers, Tellus, 50 B, 51–58, 1998. 30, 81, 82

Schlüssel, P., Soloviev, A., and Emery, W.: Cool and freshwater skin of the ocean during rainfall, Boundary-Layer Meteorology, 82, 437–472, 1997. 58

Schoeberl, M. and Toon, O.: Tropical Ozone Transport Experiment (TOTE) and Vortex Ozone Transport Experiment (VOTE), `http://code916.gsfc.nasa.gov/Public/Analysis/aircraft/tote/vote_doc.html`, 2002. 20

Seinfeld, J. H. and Pandis, S.: Atmospheric Chemistry and Physics: From Air Pollution to Climate Change, Wiley-Interscience, 1997. 74

Shade, G. W. and Goldstein, A.: Fluxes of oxygenated volatile organic compounds from a ponderosa pine plantation, J. Geophys. Res., 106, 3111–3123, 2000. 90

Shallcross, D. E. and Monks, P. S.: New Directions: A role for isoprene in biosphere-climate-chemistry feedbacks, Atmos. Environ., 34, 1659–1660, 2000. 106

Shepson, P., Hastie, D., Schiff, H., Polizzi, M., Bottenheim, J., Anlauf, K., Mackay, G., and Karecki, D. R.: Atmospheric concentrations and temporal variations of C1 C3 carbonyl compounds at two rural sites in central Ontario, Atmos. Environ., 25, 2001–2016, 1991. 90

Singh, H., Chen, Y., Tabazadeh, A., Fukui, Y., Bey, I., Yantosca, R., Jacob, D., Arnold, F., Wohlfrom, K., Atlas, D., Flocke, F., Blake, D., Blake, N., Heikes, B., Snow, J., Talbot, R., Gregory, G., Sachse, G., Vay, S., and Kondo, Y.: Distribution and fate of selected oxygenated organic species in the troposphere and lower stratosphere over the Atlantic, J. Geophys. Res., 105, 3795–3805, 2000. 43

Singh, H., Salas, l., Chatfield, R., Czech, E., Fried, A., Walega, J., Evans, M., Field, B., Jacob, D., Blake, D., Heikes, B., Talbot, R. andSachse, G., Crawford, J., Avery, M., Sandholm, S., and Fuelberg, H.: Analysis of the atmospheric distriburion, sources, and sinks of oxygenated volatile orhanic chemicals based in measurements over the Pacific during TRACE-P, J. Geophys. Res., 105(D3), doi:10.1029/2003JD003 883, 2004. 43

Singh, H. B. and Hanst, P. L.: Peroxyacetyl nitrate (PAN) in the unpolluted atmosphere: An important reservoir for nitrogen oxides, Geophys. Res. Lett., 8, 941–944, 1981. 6

Singh, H. B., O'Hara, D., Herlth, D., Bradshaw, J. D., Sandholm, S. T., Gregory, G. L., Sachse, G. W., Blake, D. R., Crutzen, P. J., and Kanakidou, M.: Atmospheric measurements of peroxy acetyl nitrate and other organic nitrates at high latitudes: possible sources and sinks, J. Geophys. Res., 97, 16 511–16 522, 1992. 6

Singh, H. B., O'Hara, D., Herlth, D., Sachse, W., Blake, D. R., Bradshaw, J. D., Kanakidou, M., and Crutzen, P. J.: Acetone in the atmosphere: Distribution, source, and sinks, J. Geophys. Res., 99, 1805–1819, 1994. 20

Singh, H. B., Kanakidou, M., Crutzen, P. J., and Jacob, D. J.: High concentrations and photochemical fate of oxygenated hydrocarbons in the global troposphere, Nature, 378, 50–54, 1995. 47

Singh, H. B., Chen, Y., Staudt, A. C., Jacob, D. J., Blake, D. R., Heikes, B. G., and Snow, J.: Evidence from the Pacific troposphere for large global sources of oxygenated organic compounds, Nature, 410, 1078–1081, 2001. 43, 51, 89, 96

Singh, H. B., Tabazadeh, A., Evans, M. J., Field, B. D., Jacob, D. J., Sachse, G., Crawford, J. H., Shetter, R., and Brune, W. H.: Oxygenated volatile organic chemicals in the oceans: Inferences and implications based on atmospheric observations and air-sea exchange models, Geophys. Res. Lett., 30, 1862, doi:10.1029/2003GL017 933, 2003. 43, 89, 93, 94, 125

Singh, H. B. et al.: Relationship between peroxyacetyl nitrate (PAN) and nitrogen oxides in the clean troposphere, Nature, 318, 347–349, 1985. 6

Sinha, V., Williams, J., Meyerhöfer, M., Riebesell, U., Paulino, A. I., and Larsen, A.: Air-sea fluxes of methanol, acetone, acetaldehyde, isoprene and DMS from a Norwegian fjord following a phytoplankton bloom in a mesocosm experiment, Atmos. Chem. Phys. Discuss., 6, 9907 9935, 2006. 94

Sivakumaran, V., Hölscher, D., Dillon, T. J., and Crowley, J. N.: Reaction between OH and HCHO: temperature dependent rate coefficients (202-399 K) and product pathways (298 K), Phys. Chem. Chem. Phys., 5, 4821–4827, 2003. 113

Solberg, S., Dye, C., Schmidbauer, N., Herzog, A., and Gehrig, R.: Carbonyls and nonmethane hydrocarbons at rural European sites from the Mediterranean to the Arctic, J. Atmos. Chem., 25, 33–66, 1996. 20, 37, 39

Soloviev, A. and Schluessel, P.: A model of air-sea gas exchange incorporating physics of the turbulent boundary layer and the properties of the sea surface, in Gas transfer at water surface, edited by M. Donelan, W. Drennan, M. Saltzmann, and R. Wanninkhof, pp. 141–146, Geophysical Monograph, 2002. 58

Sprengnether, M., Demerjian, K. L., Donahue, N. M., and Anderson, J. G.: Product analysis of the OH oxidation of isoprene and 1,3-butadiene in the presence of NO, J. Geophys. Res., 107D, 2002. 119

Staubes, R. and Georgii, H.-W.: Biogenic sulfur compounds in seawater and the atmosphere of the Antarctic region, Tellus, 45, 127–137, 1993. 62

Steil, B., Dameris, M., Brühl, C., Crutzen, P. J., Grewe, V., Ponater, M., and Sausen, R.: Development of a chemistry module for GCMs: First results of a multiannual integration, Ann. Geophys., 16, 205–228, 1998. 13

Stickler, A., Fischer, H., Williams, J., de Reus, M., Sander, R., Lawrence, M., Crowley, J., and Lelieveld, J.: Influence of summertime deep convection on formaldehyde in the middle and upper troposphere over Europe, J. Geophys. Res., 111, doi:10.1029/2005JD007 001, 2006. 46

Stimpfle, R. M., Wilmouth, D. M., Salawitch, R. J., and Anderson, J. G.: First measurements of ClOOCl in the stratosphere: The coupling of ClOOCl and ClO in the Arctic polar vortex, J. Geophys. Res., 109, 2004. 123

Streets, D., Bond, T. C., Carmichael, G. R., Fernandes, S. D., Fu, Q., He, D., Klimont, Z., Nelson, S. M., Tsai, N. Y., Wang, M. Q., Woo, J. H., and Yarber, K. F.: An inventory of gaseous and primary aerosol emission in Asia in the year 2000, J. Geophys. Res., 108, doi:10.1029/2002JD003 093, 2003. 34

Streets, D., Zhang, Q., Wang, L. He, K., Hao, J., Wu, Y., Tang, Y., and Carmichael, G.: Revisiting China's CO emissions after the Transport and Chemical Evolution over the Pacific (TRACE-P) mission: Synthesis of inventories, atmospheric modeling, and observations, J. Geophys. Res., 111, doi:10.1029/2006JD007 118, 2006. 34, 82

Stull, R.: An introduction to Boundary layer Meteorology, Kluwer Academic Publisher, 1998. 60

Takahashi, T., Feely, R., Weiss, R., Wanninkhof, R., Chipman, D. W., Sutherland, S. C., and Takahashi, T.: Global air-sea flux of CO2: An estimate based on measurements of sea air pCO2 difference, Proc. Natl. Acad. Sci., 94, 8292 8299, 1997. 51, 66, 70

Takahashi, T., Sutherland, S. C., Sweeney, C., Poisson, A., Metzl, N., Tilbrook, B., Bates, N., Wanninkhof, R., Feely, R. A., Sabine, C., Olafsson, J., and Nojiri, Y.: Global sea air CO_2 flux based on climatological surface ocean pCO_2, and seasonal biological and temperature effects, Deep-Sea Res. II, 49, 1601 1622, 2002. 66, 67, 69, 70, 71, 125

Tanre, D., Geleyn, J.-F., and Slingo, J. M.: First results of the introduction of an advanced aerosol-radiation interaction in the ECMWF low resolution global model, in Aerosols and their climatic e effects, edited by H. Gerber and A. Deepak, pp. 133–177, A. Deepak, Hampton, VA, 1984. 14

Tarrasón, L., Turner, S., and Floisand, I.: Estimation of seasonal dimethyl sulphide fluxes over the North atlantic Ocean and their contribution to European pollution levels, J. Geophys. Res., 100, 11 623–11 639, 1995. 62

Taylor, K.: Summarizing multiple aspects of model performance in a single diagram, J. Geophys. Res., 106, 7183–7192, 2001. 27, 108, 109, 110

Taylor, K., Williamson, D., and Zwiers, F.: The sea surface temperature and sea ice concentration boundary conditions for AMIP II simulations; PCMDI Report, Tech. Rep. 60, Program for Climate Model Diagnosis and Intercomparison, 2000. 54, 68, 76

Thompson, A.: The oxidizing capacity of the Earth's atmosphere: Probable past and future changes, Science, 256, 1157–1165, 1992. 3, 30

Thompson, A. M., Singh, H., and Schlager, H.: Introduction to special section: Subsonic Assessment Ozone and Nitrogen Oxide Experiment (SONEX)and Pollution from Aircraft Emissions in the North Atlantic Flight Corridor (POLINAT 2), J. Geophys. Res., 105, 3595–3603, 2000. 20

Thompson, A. M., Witte, J. C., McPeters, R. D., Oltmans, S. J., Schmidlin, F. J., Logan, J. A., Fujiwara, M., Kirchhoff, V. W. J. H., Psny, F., Coetzee, G. J. R., Hoegger, B., Kawakami, S., Ogawa, T., Johnson, B. J., Vömel, H., and Labow, G.: Southern Hemisphere Aditional Ozonesondes SHADOZ 1998–2000 tropical ozone climatology: Comparison with Total Ozone Mapping Spectrometer (TOMS) and ground-based measurements, J. Geophys. Res., 108, 8238, doi:10.1029/2001JD000 967, 2003a. 18

Thompson, A. M., Witte, J. C., Oltmans, S. J., Schmidlin, F. J., Logan, J. A., Fujiwara, M., Kirchhoff, V. W. J. H., Posny, F., Coetzee, G. J. R., Hoegger, B., Kawakami, S., Ogawa, T., Fortuin, J. P. F., and Kelder, H. M.: Southern Hemisphere Aditional Ozonesondes SHADOZ 1998–2000 tropical ozone climatology: 2. Tropospheric variability and the zonal wave-one, J. Geophys. Res., 108, 8241, doi:10.1029/2002JD002 241, 2003b. 18

Tie, X., Guenther, A., and Holland, E.: Biogenic methanol and its impacts on tropospheric oxydants, Geophys. Res. Lett., 17, doi:10.1029/2003GL017 167, 2003. 43, 45, 84

Tiedtke, M.: A Comprehensive Mass Flux Scheme for Cumulus Parametrization in Large-Scale Models, Mon. Weather Rev., 117, 1779–1800, 1989. 9, 12

Tompkins, A. M.: A prognostic parameterization for the subgrid-scale variability of water vapor and clouds in large-scale models and its use to diagnose cloud cover, J. Atmos. Sci., 59, 1917–1942, 2002. 12

Tost, H.: Global Modelling of Cloud, Convection and Precipitation Influences on Trace Gases and Aerosols, Ph.D. thesis, Rheinischen Friedrich-Wilhelms-Universität, Bonn, Germany, 2006. 12, 14

Tost, H., Jöckel, P., Kerkweg, A., Sander, R., and Lelieveld, J.: Technical Note: A new comprehensive SCAVenging submodel for global atmospheric chemistry modelling, Atmos. Chem. Phys., 6, 565–574, 2006. 42, 45

Touaty, M., Bonsang, B., Kanakidou, M., and Poisson, N.: Monitoring and model comparison of the seasonal variation of tropospheric light hydrocarbons at Amsterdam Island, in Proceeding of the EUROTRAC Symposium 1996, pp. 613–619, Computational Mechanism Publications, Southampton, 1996. 20

Traub, M.: Global Modelling of Atmospheric Halogen Chemistry in the Marine Boundary Layer, Ph.D. thesis, Johannes Gutenberg-Universität in Mainz, 2004. 73

Turnipseed, A. A., Gilles, M. K., Burkholder, J. B., and Ravishankara, A. R.: Kinetics of the IO radical. 1. Reaction of IO with ClO, J. Phys. Chem. A, 101, 5517–5525, 1997. 120

Tyndall, G. S., Staffelbach, T. A., Orlando, J. J., and Calvert, J. G.: Rate coefficients for the reactions of OH radicals with methylglyoxal and acetaldehyde, Int. J. Chem. Kinetics, 27, 1009–1020, 1995. 115

Tyndall, G. S., Cox, R. A., Granier, C., Lesclaux, R., Moortgat, G. K., Pilling, M. J., Ravishankara, A. R., and Wallington, T. J.: The atmospheric chemistry of small organic peroxy radicals, J. Geophys. Res., 106D, 12 157–12 182, 2001. 113, 114, 115, 119

Vakhtin, A., Murphy, J., and Leone, S.: Low-Temperature Kinetics of Reactions of OH Radical with Ethene, Propene, and 1-Butene, J. Phys. Chem., 107, 10 055–10 062, 2003. 42

van Aalst, M. K., van den Broek, M. M. P., Bregman, A., Brühl, C., Steil, B., Toon, G. C., Garcelon, S., Hansford, G. M., Jones, R. L., Gardiner, T. D., Roelofs, G.-J., Lelieveld, J., and Crutzen, P. J.: Trace gas transport in the 1999/2000 Arctic; comparison of nudged GCM runs with observations, Atmos. Chem. Phys., 4, 81–93, sRef-ID: 1680-7324/acp/2004-4-81/, 2004. 10

van Aardenne, J., Dentener, F., Olivier, J., Peters, J., and Ganzeveld, L.: The EDGAR 3.2 Fast Track 2000 dataset (32FT2000), http://www.mnp.nl/edgar/model/v32ft2000edgar/docv32ft2000/, 2005. 17

van den Bergh, H. and Troe, J.: Kinetic and thermodynamic properties of INO and INO_2 intermediate complexes in iodine recombination, J. Chem. Phys., 64, 736–742, 1976. 120

van der Leun, J. and de Gruijl, F.: Climate change and skin cancer, Photochem. Photobiol. Sci., 1, 324–326, 2002. 1

Villenave, E. and Lesclaux, R.: Kinetics of the cross reactions of CH_3O_2 and $C_2H_5O_2$ radicals with selected peroxy radicals, J. Phys. Chem., 100, 14 372–14 382, 1996. 119

Volz, A. and Kley, D.: Evaluation of the Montsouris series of ozone measurements made in the 19th-century, Nature, 332, 240–242, 1988. 1

von Glasow, R., Sander, R., Bott, A., and Crutzen, P. J.: Modeling halogen chemistry in the marine boundary layer. 1. Cloud-free MBL, J. Geophys. Res., 107D, 2002. 120

von Kuhlmann, R.: Tropospheric photochemistry of ozone, its precursors and the hydroxyl radical: A 3D-modeling study considering non-methane hydrocarbons, Ph.D. thesis, Johannes Gutenberg-Universität, Mainz, Germany, 2001a. 116, 119

von Kuhlmann, R.: Tropospheric Photochemistry of Ozone, its Precursors and the Hydroxyl Radical: A 3D-Modeling Study Considering Non-Methane Hydrocarbons, Ph.D. thesis, Johannes Gutenberg-Universität Mainz, Mainz, Germany, `http://www.mpch-mainz.mpg.de/~kuhlmann/rvkdisshtml`, 2001b. 15

von Kuhlmann, R., Lawrence, M. G., Crutzen, P. J., and Rasch, P. J.: A model for studies of tropospheric ozone and nonmethane hydrocarbons: Model description and ozone results, J. Geophys. Res., 108, 4294, doi:10.1029/2002JD002 893, 2003a. 15, 33, 36

von Kuhlmann, R., Lawrence, M. G., Crutzen, P. J., and Rasch, P. J.: A Model for Studies of Tropospheric Ozone and Non-Methane Hydrocarbons: Model Evaluation of Ozone Related Species, J. Geophys. Res., 108, 4729, doi:10.1029/2002JD003 348, 2003b. 13, 15, 19, 20, 30, 33, 45, 46

von Kuhlmann, R., Lawrence, M. G., Pöschl, U., and Crutzen, P. J.: Sensitivities in global scale modeling of isoprene, Atmos. Chem. Phys., 4, 1–17, 2004. 13

Wang, X., McElroy, M., Wang, T., and Palmer, P.: Asian emission of CO and NO_x: Constrain from aircraft and Chinese station data, J. Geophys. Res., 109, doi:10.1029/2004JD005 250, 2004. 34

Wang, Y. and Zeng, T.: On tracer correlations in the troposphere: The case of ethane and propane, J. Geophys. Res., 109, doi:10.1029/2004JD005 023, 2004. 38

Wang, Y., Jacob, D. J., and Logan, J. A.: Global simulation of tropospheric O_3-NO_x-hydrocarbon chemistry, 3. Origin of tropospheric ozone and effects of non-methane hydrocarbons, J. Geophys. Res., 103, 10 757–10 767, 1998a. 20

Wang, Y., Logan, J. A., and Jacob, D. J.: Global simulation of tropospheric O_3-NO_x-hydrocarbon chemistry, 2. Model evaluation and global ozone budget, J. Geophys. Res., 103, 10 727–10 755, 1998b. 33

Wang, Y., Choi, Y., Zeng, T., Davis, D., Buhr, M., Huey, L. G., and Neff, W.: Assessing the photochemical impact of snow NO_x emissions over Antarctica during ANTCI 2003, Atmos. Environ., p. submitted, 2006. 103

Wanninkhof, R.: Relationship between wind speed and gas exchange over the ocean, J. Geophys. Res., 97, 7373–7382, 1992. 55, 56, 57, 69, 70, 71

Wanninkhof, R. and McGills, W. R.: A cubic relationship between air-sea CO_2 exchange and wind speed, Geophys. Res. Lett., 26, 1889–1892, 1999. 55, 56, 57, 71

Wennberg, P. O., Hanisco, T. F., Jaeglé, L., Jacob, D., Hintsa, E. J., Lanzendorf, E. J., Anderson, J. G., Gao, R.-S., Keim, E. R., Donnelly, S. G., Negro, L. A. D., Fahey, D. W., McKeen, S. A., Salawitch, R. J., Webster, C. R., May, R. D., Herman, R. L., Proffitt, M. H., Margitan, J. J., Atlas, E. L., Schauffler, S. M., Flocke, F., McElroy, C. T., and Bui, T. P.: Hydrogen radicals, nitrogen radicals, and the production of O_3 in the upper troposphere, Sci. China, 279, 49–53, 1998. 7, 47

Wesely, M.: Paramatrization of surface resistances to gaseous dry deposition in regional-scale numerical models, Atmos. Environ., 23, 1293–1304, 1989a. 59, 61

Wesely, M. L.: Parameterization of surface resistances to gaseous dry deposition in regional-scale numerical models, Atmos. Environ., 23, 1293–1304, 1989b. 18

Wetzel, P., Winguth, A., and Maier-Reimer, E.: Sea-to-air CO_2 flux from 1948 to 2003: A model study, Global Biogeochem. Cycles, 19, doi:10.1029/2004GB002 339, 2005. 71

Wild, M. and Roeckner, E.: Radiative fluxes in the ECHAM5 general circulation model, J. Clim., 19, 3792–3809, 2006. 9

Wilke, C. and Chang, P.: Correlation of diffusion coefficients in diluite solutions, AIChE J., 1, 264–270, 1955. 57

Williams, J., Pöschl, U., Crutzen, P. J., Hansel, A., Holzinger, R., Warneke, C., Lindinger, W., and Lelieveld, J.: An atmospheric chemistry interpretation of mass scans obtained from a proton transfer mass spectrometer flown over the tropical rainforest of Surinam, J. Atmos. Chem., 38, 133–166, 2001. 43

Williams, J., Holzinger, R., Gros, V., Xu, X., Atlas, E., and Wallace, D.: Measuremets of organic species in air and seawater from the tropical Atlantic, Geophys. Res. Lett., 31, doi:10.1029/2004GL02 001, 2004. 94, 125

WMO: International meteorological vocabulary, ISBN: 92-63-02182-1, 1992. 14

World Meteorological Organization, W.: Assessement of trends in the vertical distribution of ozone, Sparc report no.1, global ozone res. and monit. proj., WMO Rep.43, Geneva, 1998. 18

Xie, W., Ji, H., and Li, W.: The calculation method of a modified equation of the internal pressure salt effect theory, in Acta Physicochim. Sin., vol. 74, pp. 1–304, 1985. 55

Xie, W., Su, J., and Xie, X.: Studies on the activity coefficients of benzene an its derivatives in aqueous salt solution., Thermochimica Acta, 169, 271–286, 1990. 55

Xie, W., Shiu, W., and Mackay, D.: A review of the effect of salt on the solubility of organic compounds in seawater, Mar. Environ. Res., 44, 429–444, 1997. 54, 55

Yin, F., Grosjean, D., and Seinfeld, J. H.: Photooxidation of dimethyl sulfide and dimethyl disulfide. I: Mechanism development, J. Atmos. Chem., 11, 309–364, 1990. 120

Zaveri, R. A. and Peters, L. K.: A new lumped structure photochemical mechanism for large-scale applications, J. Geophys. Res., 104D, 30 387–30 415, 1999. 119

Zhou, X. and Mopper, K.: Carbonyl compounds in the lower marine troposphere over the Carribean sea and Bahamas, J. Geophys. Res., 98, 2385–2392, 1993. 94

Zhou, X. and Mopper, K.: Photochemical production of low-molecular weight compounds in seawater and surface microlayer and their air-sea exchange, Mar. Chem., 56, 201–213, 1997. 43, 94

Ziereis, H., Schlager, H., Schulte, P., van Velthoven P.F.J., and Slemr, F.: Distributions of NO, NO_x, and NO_y in the upper troposphere and lower stratosphere between $28°N$ and $61°N$ during POLINAT 2, J. Geophys. Res., 105, 3653, 2000. 20